May 30th, 10:45 AM - May 31st, 3:00 PM

Full Proceedings: IJREWHS 2016

International Association for Hydro-Environmental Engineering and Research

Local Organizing Committee IJREWHS2016

Mario Oertel, Prof. Dr.-Ing. habil. (Chairman)
Full Professor
Hydraulic Engineering Section
Luebeck University of Applied Sciences

Daniel B. Bung, Prof. Dr.-Ing. (Vice-Chairman)
Full Professor
Hydraulic Engineering Section
Aachen University of Applied Sciences

Jessica Klein, M. Eng.
Research Assistant
Hydraulic Engineering Section
Luebeck University of Applied Sciences

Daniel Valero, M. Sc.
Research Assistant
Hydraulic Engineering Section
Aachen University of Applied Sciences

Keynote Lectures and Short Lecture:

Daniel B. Bung, Prof. Dr.-Ing.
Full Professor
Hydraulic Engineering Section
Aachen University of Applied Sciences

"Application of imaging techniques to laboratory investigations of aerated flows"

Carsten Thorenz, Dr.-Ing.
Head of Section
Hydraulics at Structures
Federal Waterways Engineering and Research Institute (BAW)

"Hydraulic Structures at Federal Waterways"

Blake P. Tullis, Prof. PhD
Full Professor
Utah Water Research Laboratory
Utah State University

"How to write a good scientific paper"

Program:

IJREWHS 2016 Program - May 30th to June 1st 2016 - Lübeck University of Applied Sciences Germany,

	Sunday May 29th		Monday May 30th		Tuesday May 31st		Wednesday Juni 1st	
8		Arrival and Check-In	08:00-09:00	Registration and Welcome Coffee			07:30	Departure
9			09:00-09:30	Welcome and Introduction	09:00-09:30	Good Morning Coffee	09:00	Ship Lift Scharnebeck
10			09:30-10:15	Keynote Lecture 1 - Prof. Dr.-Ing. Daniel B. Bung	09:30-10:30	Keynote Lecture 2 - Dr.-Ing. Carsten Thorenz		
			10:15-10:45	Coffee Break	10:30-11:00	Coffee Break		
11			10:45-12:15	Technical Session 1	11:00-12:30	Technical Session 3	11:15	Weir Geesthacht
12							12:00	Fish Step Geesthacht
			12:15-13:15	Lunch	12:30-13:30	Lunch		
13			13:15-13:45	Short Lecture - Prof. Blake P. Tullis, PhD	13:30-15:00	Technical Session 4		
14			13:45-15:00	Technical Session 2			14:00	Boat Trip Hamburg
15					15:00-15:30	Coffee Break		
			15:00-15:30	Coffee Break	15:30-16:30	Workshop 2: Round Table Discussions (Technical Sessions 3 and 4)		
16			15:30-16:30	Workshop 1: Round Table Discussions (Technical Sessions 1 and 2)			16:00	End of Workshop
					16:30-17:00	Presentation Round Table Results		
17			16:30-17:00	Presentation Round Table Results	17:00-17:30	Conclusions		
18			18:00-19:00	Boat Trip around Lübeck (Trave River)				
19	19:00	Registration and Welcome Reception	19:00	"Open" Dinner at Inner City	19:00	Official Workshop Dinner		
20								

Presentations:

Monday, May 30th 2016

Room 14-0.07	Chair:	**Daniel Valero, Barbara Stachurska**
Technical Session 1		Title / Author
1	10:45 - 11:00	Investigation of the Flow Field inside a Drainage System: Gully – Pipe – Manhole Beg, Carvalho and Leandro
2	11:05 - 11:20	Increasing Piano Key Weir Efficiency by Fractal Elements Bremer and Oertel
3	11:25 - 11:40	Numerical investigation of the pressure on a spillway crest Goffin, Erpicum, Archambeau, Dewals and Pirotton
4	11:45 - 12:00	Prediction of Hydraulic Jump location in Some Types of Prismatic Channels using Numerical Modelling Hafnaoui, Carvalho and Debabeche

Room 14-0.07	Chair:	**Louis Goffin, Pedro Ramos**
Technical Session 2		Title
5	13:45 - 14:00	Inlet capacity of street inlets with partial severed grate openings Kemper and Schlenkhoff
6	14:05 -14:20	Vertical Slot Fishway: Evaluation of numerical model quality Klein and Oertel
7	14:25 - 14:40	Nappe Vibration Characteristics for Free-overfall Structures Lodomez, Archambeau, Dewals, Pirotton and Erpicum
8	14:45 - 15:00	Water waves measurements at Bellsund in the western Spitsbergen Majewski, Sulisz, Paprota, Szmytkiewicz and Reda

Tuesday, May 31st 2016

Room 14-0.07	Chair:	**Maurine Lodomez, Jessica Klein**
Technical Session 3		Title / Author
9	11:00 - 11:15	Large Eddy Simulation of the water flow around a cylindrical pier mounted in a flat and fixed bed Ramos, Maia, Schindfessel, De Mulder and Pêgo
10	11:20 - 11:35	Coupling Process for 1D-2D Numerical Flash Flood Simulation: A Parameter Study of Involved Variables for Gullies and Manholes; Schlauß and Grottker
11	11:40 - 11:55	Analysis of clearance gap losses on the hydraulic pressure machine Schwyzer and Saenger
12	12:00 - 12:15	Experimental and theoretical studies on the formation of freak waves over a sloping bottom Sorek, Zdolska, Bieliński and Sulisz

Room 14-0.07	Chair:	**Svenja Kemper, Dawid Majewski**
Technical Session 4		Title
13	13:30 - 13:45	An investigation of the velocity field over rippled sand bottom Stachurska and Staroszczyk
14	13:50 - 14:05	Feasibility Study and Optimization of the Structural – Design of Locks made out of Plain Concrete Tahir, Kunz and Terheiden
15	14:10 - 14:25	Interfacial velocity estimation in highly aerated stepped spillway flows with a single tip fibre optical probe and Artificial Neural Networks; Valero and Bung
16	14:30 - 14:45	Soil-Water-Structure Interaction on Diaphragm Quay-Walls Adesoga

Field Trip:

Ship lift Scharnebeck (Elbe side canal)

Weir Geesthacht (Elbe River)

Double vertical slot fish pass Geesthacht (Elbe River)

Boat trip Hamburg

Venue:

Founded in 1134, the Hanseatic City of Luebeck is situated near the Baltic Sea. With its approximately 210.000 inhabitants, it is a center of commerce, industry, and higher education that is playing an increasingly important role in bringing together the people of Denmark, Sweden, Finland, Russia, the Baltic States and Poland. Much of its architecture, dating back to the Middle Ages, is still intact in the older portion of town, which is a UNESCO World Heritage Site. With its many restaurants, cinemas, theaters, and clubs, the city offers a variety of recreation opportunities for young people. Luebeck offers a lively art scene, plays host to Northern Film Days and is the main venue for the world-famous Schleswig-Holstein Music Festival. Because of its closeness to the Baltic Sea, Luebeck offers a wide variety of cultural and sporting activities.

Luebeck's location on the Baltic Sea is also of international significance. Long-existing contacts to the Scandinavian countries expand cultural, economic and scientific opportunities, and strengthen Luebeck as a site for higher education within the framework of indispensable international cooperation. Among students the Hanseatic City of Luebeck is considered a well-kept secret, since living and studying here take place in easily accessible surroundings, in contrast to cities with "mass universities".

The regional economy, with its connections to the universities, offers further good reasons for studying in Luebeck. The close cooperation between the universities and companies in and around Luebeck becomes obvious in many ways. The availability of traineeships, the cooperative formulation and implementation of diploma theses, research projects and possible subsequent job offers make higher education in Luebeck extremely attractive. Companies in Luebeck seek and establish contacts to the universities.

Workshop Proceedings:

All papers published in the Proceedings and have been thoroughly peer-reviewed for technical quality and presented at IJREWHS2016. The Proceedings were published by Utah State University and is available open access. Each manuscript includes the ISBN of the Proceedings as well individual direct object identifiers (DOI). Each manuscript is indexed by Scopus and Compendex. Each manuscript is available to users through the USU digital commons portal pursuant to a Creative Commons Attribution-NonCommercial CC BY 4.0 license.

Papers:

DOI:10.15142/T3859Z

Investigation of the Flow Field inside a Drainage System: Gully – Pipe – Manhole

Md N. A. Beg[1], R. F. Carvalho[1], J. Leandro[1], P. Lopes[1] and L. Cartaxo[1]
[1]MARE - Marine and environmental research center
Department of Civil Engineering, University of Coimbra,
Coimbra, Portugal
E-mail: mnabeg@uc.pt

ABSTRACT

Gully drop connected with manhole is one crucial structural part in several urban drainage systems. This paper analyses the flow pattern and flow hydraulics of a gully-manhole drainage structure. Analysis is done numerically using computational fluid dynamics CFD tools OpenFOAM®. Data from the Dual Drainage / Multi Link Element installation (DD-MLE) at the University of Coimbra hydraulic lab is used to validate the numerical simulations. The experimental model setup consists of a 0.5 m wide channel, a 0.6 × 0.24 × 0.32 m (L × W × D) gully, a gully outlet with an 80 mm diameter pipe and a manhole of 1 m diameter with a 300 mm inlet and outlet pipe connected. The flow pattern is observed under drainage flow conditions with different surcharge heights of the manhole. It has been observed that the intercepted flow through the gully decreases with the increase of surcharge in the manhole. The shear stress at the gully floor is found much higher than that of manhole floor. This indicates the probability that bigger sediment particle can be transported through gully but will remain deposited at the manhole floor. The flow pattern in the manhole changes with the change of surcharge height. The flow through the manhole inlet seems to disperse less at higher surcharge.

Keywords: *Computational Fluid Dynamics (CFD), Urban drainage, OpenFOAM®, Gully-Manhole*

1. INTRODUCTION

Urban flooding is one of the biggest issues for a large city. Predicting urban drainage flows accurately is an important way in preventing or minimizing flood risks. In most cities, urban drainage system is the only pathway to convey the flood water from urban areas. The system is usually described as two different sets of components; the major system or overland system is composed of surface paths and temporary storage areas and the minor system or below ground system is composed of pipes and manholes. Gullies work as the connectors between the two systems. They collect the runoff from paved and unpaved system and supply manholes. During a high flood event, pressurized flow may occur and create back flow from the manhole to the surface (Butler and Davies 2011; Djordjević et al. 2013; Lopes et al. 2015). To assess the flood risk in a city, evaluation of the drainage efficiency of a gully is necessary.

Some works have been done by different authors to characterize individually gully and manhole hydraulics. Galambos (2012) used ANSYS Fluent CFD tools to validate 3D and 2D/3D CFD models and a number of computational simulations on different gratings. His works also extended to better understand the effect of various geometric and road alignment on the intercepted flow. Lopes et al. (2016) used three dimensional model with VOF surface capturing technique using OpenFOAM® to analyse gully efficiency with the grate's slots aligned in the flow direction and compared with experimental data sets. Djordjević et al. (2013), Martins et al. (2014) and Leandro et al. (2014) presented both experimental and numerical investigation for drainage condition of a gully. On the other hand, Lopes et al. (2015) showed analysis of the flow field in a gully with surcharge condition. Romagnoli et al. (2013) measured the turbulence characteristics of gully for reverse flow. Several works have been done on manhole as well. Stovin et al. (2008) have showed a number of possible methods to validate CFD model, while Rubinato (2015) has showed uses of scaled models to quantify hydraulic losses in a manhole. Beg et al. (2016) used OpenFOAM® with VOF model to assess flow path line and manhole pressure variation in surcharged manhole and compared with experimental results.

In this work, both gully and manhole hydraulics were analysed together using three dimensional CFD model OpenFOAM®. The geometry of the numerical model was a replication of a real scale dual drainage experimental model setup installed at the hydraulic laboratory of University of Coimbra. The work focuses on

different hydraulic properties on of the gully-manhole structure while draining to a surcharged manhole. These results may be used to aid the simulation of pollutant transport model in the drainage system.

This paper starts presenting the experimental and numerical modelling methodologies in section 2, followed by presenting the comparison between the numerical and experimental results and some analysis using the numerical model results in section 3. Conclusion is made in section 4.

2. METHODOLOGY

2.1. Experimental Setup

The experimental facility installed at the hydraulic lab of University of Coimbra was used for this study. A detailed description of the facility can be found at Carvalho et al. (2013). The facility contains a quasi-real scale multi-link dual drainage network to observe different phenomena of an Urban Drainage Network. For the current study, a part of the setup was used, containing a rectangular surface drain (0.5 m wide), a rectangular gully pot (0.6 m × 0.24 m × 0.32 m) and a circular manhole (1 m diameter) (Figure 1). The surface drain has a slope of 1:1000. The manhole is connected with 300 mm diameter inlet and outlet pipes and does not have any guide channel inside. The inlet-outlet pipes are parallel to the surface and has no slope. The gully is connected to the manhole with an angular pipe of 80 mm diameter, at an angle of 63º in plan and 90º in vertical. The manhole did not have any inflow from its top, however no lid was loosely placed at its top ensuring equal pressure at both sides. A discharge flow meter is installed at the end of the pipe and that is represented by a small contraction in the numerical model. The gully-manhole size and the slope replicate a typical drainage system in Portugal. But the size of the gully outlet pipe is smaller that of the design recommendation. The Portuguese legislation recommends a 200 mm pipe for the gully outlet which drains a flow of 100 l/s approximately. This was exchanged for an 80 mm pipe due to different limitations of experimental model setup installed.

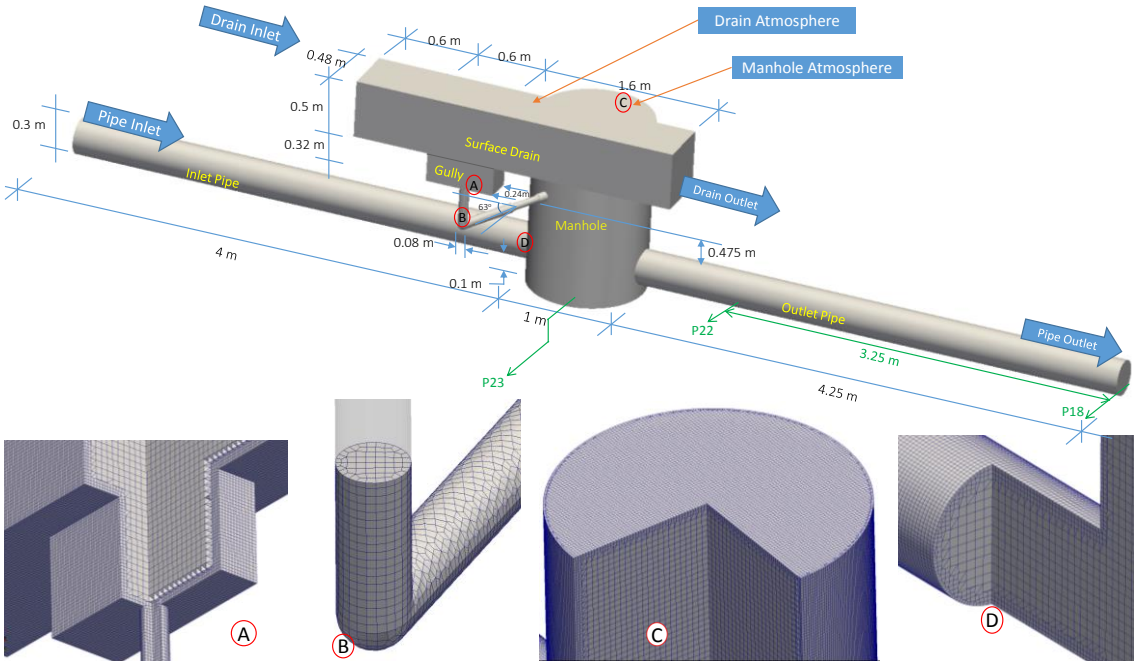

Figure 1: Upper Panel: Experimental setup; Lower panel: Computational mesh of different parts of the domain A: Gully with outlet pipe, B: Outlet Pipe, C: Manhole and D: Pipe connected with Manhole

The system is equipped with three electromagnetic flow meters (not shown in the figure). The first one is located at the drain inlet, the second one is the referred at the pipe between manhole and gully and the third is at the outlet pipe; from which different discharge at the drain, gully and manhole can be measured.

Two separate experimental study data have been used for the numerical simulation. In the first experimental work, only the manhole with inlet and outlet pipe were used; in which a flow of 43.7 l/s was applied through the

manhole inlet (SE1). The second set of experimental works, flow through the drain and gully was observed; in which 19.8 l/s flow was measured upstream of the drain inlet (SE2). The grate of the gully was removed. The flow through the rectangular drain was an open channel flow with a flow depth of 8 cm in the channel; which yielded a Froude number of 0.6. Some part of the incoming drain inlet flow passed through the gully outlet to the manhole and the rest overflowed through the gully and made a free fall to the reservoir tank through the drain outlet. As the discharge was overflowing the gully top, the location if the water surface was located in the drain above the gully. The intercepted flow by gully enters the manhole as a free fall plunging jet with a recirculation zone in the manhole. This flow accumulates with the inflow through manhole inlet and flows out through the manhole outlet. The gully was given special attention. The velocity field at the gully was measure at three vertical planes using ADV (Acoustic Doppler Velocimetry). The first and the third planes are at 5 cm distance from the two longitudinal walls of the gully; which made each of the plans 7 cm apart from the central line of the gully. The second plane is the central plane. Each plane had 121 point measurements, at an interval of 4.8 cm and 2.5 cm towards horizontal and vertical directions respectively (Figure 2). The velocity measurement was taken inside the gully only and was not extended to the water surface.

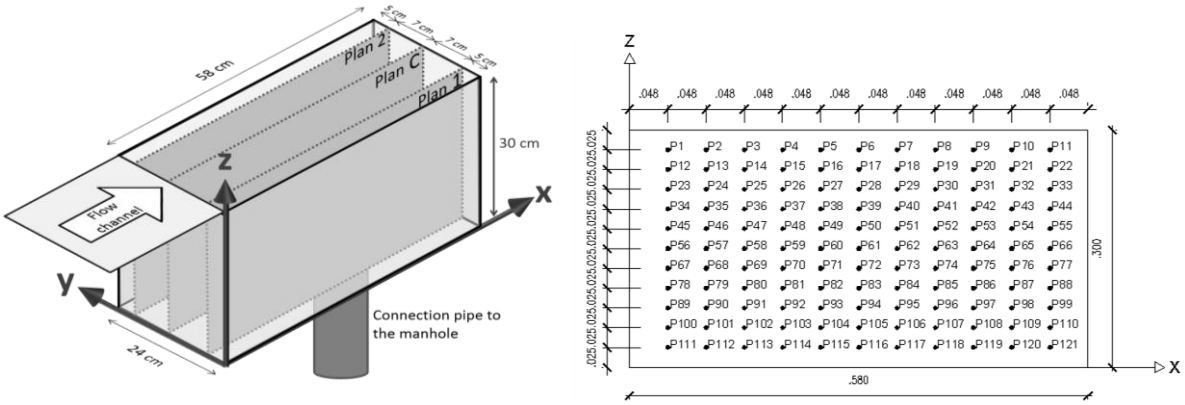

Figure 2: Velocity measurement locations using ADV. Left panel shows the location of the three planes and the right panel shows the point measurement locations at each plane

In the both experimental scenarios, the manhole was at surcharged condition and the manhole inlet-outlet pipe was pressurized. The surcharge height at the manhole was 0.67 m; which was 20.5 cm below the invert level of the gully outlet to the manhole.

2.2. Numerical Model Description

The objective of the numerical modelling is to characterize the incoming flow through the gully and check the flow path in the manhole during drainage condition. Open source three dimensional CFD model tools OpenFOAM® version 2.3.0 is used in this study. The solver *interFoam* is chosen which includes Volume of Fluid (VOF) method (Hirt and Nichols 1981) to track the free surface or interface location between two fluids. This method uses volume fraction indicator function α to determine the amount of liquid present in each cell. In case of $\alpha=0$ or 1, the cell volume is considered filled with air or water respectively; while $0<\alpha<1$ represents that the cell contains the free surface as it is partially filled with water.

The *interFoam* solver uses a single set of Navier-Stokes equations for the two fluids, water and air, and additional equations to describe free-surface where the velocity at free-surface is shared by both phases. The solver considers a system of isothermal, incompressible and immiscible two-phase flow. The model deals with Reynolds averaged conservation of mass and momentum,

$$\nabla.\boldsymbol{u} = 0 \tag{1}$$

$$\frac{\partial \rho \boldsymbol{u}}{\partial t} + \nabla.(\rho \boldsymbol{u}\boldsymbol{u}) = -\nabla p^* + \nabla.\boldsymbol{\tau} + \boldsymbol{g}.\boldsymbol{x}\nabla\rho + \boldsymbol{f_\sigma} \tag{2}$$

where $\boldsymbol{g}$ is the acceleration due to gravity, $\boldsymbol{u}$ is the velocity vector in the Cartesian coordinate, τ is the shear stress tensor, p* is the modified pressure adopted by removing the hydrostatic pressure ($\rho\boldsymbol{g}.\boldsymbol{x}$) from the total pressure and $\boldsymbol{f_\sigma}$ is the volumetric surface tension force.

The viscous stress term is defined by the incompressible Newton's law,

$$\nabla.\boldsymbol{\tau} = \nabla(\mu(\nabla\boldsymbol{u})) + (\nabla\boldsymbol{u}).\nabla\mu \tag{3}$$

The advection equation to describe free-surface in VOF method (Hirt and Nichols 1981), which uses an interfacial compressive term to keep the interface region confined in a small space (Rusche 2002; Weller 2002) is described as:

$$\frac{\partial\alpha}{\partial t} + \nabla.(\alpha\boldsymbol{u}) + \nabla.[\boldsymbol{u_c}\alpha(1-\alpha)] = 0 \tag{4}$$

The last term of equation (4) is the compressive term. The term $\alpha(1-\alpha)$ ensures that the compressive term or compressive velocity $\boldsymbol{u_c}$ is calculated only at the interphase (when $0< \alpha<1$). This velocity acts at the perpendicular direction to the interface and defined as:

$$\boldsymbol{u_c} = C_\alpha|\boldsymbol{u_c}|\frac{\nabla\alpha}{|\nabla\alpha|} \tag{5}$$

C_α is a Boolean term (value is 0 or 1) which activates (C_α =1) or deactivates (C_α =0) the interface compressive term. The volumetric surface tension $\boldsymbol{f_\sigma}$ is calculated by the Continuum Surface Force model (Brackbill et al. 1992).

$$\boldsymbol{f_\sigma} \approx \sigma\kappa\nabla\alpha \tag{6}$$

Here, κ is referred as the surface curvature.

To model the turbulence phenomena, k-ε turbulent modelling approach is used. This turbulence calculation approach uses two closure equations for k *(turbulent kinetic energy)* and ε (Energy dissipation). The unsteadiness in flow is averaged out in this model and regarded as part of the turbulence (Furbo et al. 2009).

The value of k is calculated along with ε using k- ε turbulent model. The dynamic viscosity (μ) is calculated as:

$$\mu = \rho(\nu_t + \nu_0) \tag{7}$$

where, ν_0 and ν_t are molecular viscosity and turbulent viscosity respectively.

2.3. Mesh Generation

Mesh generation is one of the most important issue in CFD modelling. The quality of mesh is the key to have quality result from the model. The construction of the computational mesh for this study, was done as follows: (1) the geometry was prepared using open source software SALOME v.7.5.1; (2) the geometry was exported to Stereolithography (STL) format. (3) another open source meshing tool *cfMesh* (Juretić 2015) was used to prepare the mesh. This tool prepares three dimensional hexahedral mesh in the Cartesian planes. The maximum mesh size is kept as 2 cm towards all the three directions. The mesh was further refined at the walls and joins of different geometrical shapes. The created computational mesh has 821,500 computational cells with a little more than 1.01 million nodes. Some of the mesh properties can be seen at Figure 1 and Table 1.

Table 1: Quality parameters of the computational mesh

Parameter Name	**Max. Aspect ratio**	**Max. skewness**	**Max. non-orthogonality**	**Avg. non-orthogonality**	**Min. face area (m^2)**	**Max. face area (m^2)**	**Min. volume (m^3)**	**Max. volume (m^3)**
Value	7.27	1.708	51.32	4.13	3.45×10^{-06}	4.72×10^{-04}	4.19×10^{-09}	1.06×10^{-05}

2.4. Boundary conditions

Six open boundaries were used for the computational domain. They are: Drain Inlet, Drain Atmosphere, Drain Outlet, Pipe Inlet, Pipe Atmosphere and Pipe Outlet. The drain inlet was further divided in to two parts for the incoming water and air phases respectively. The boundary data are calculated from the experimental model

completed before. The upstream boundaries were obtained from measured discharge data while the downstream pressure data were obtained from observed water depths in the drain and manhole.

As the simulation used *k-ε* turbulent approach, OpenFOAM® requires six types of Boundary Conditions (BC) for each boundary. They are *alpha.water* (water volume fraction in each cell), ***u*** (velocity vector in Cartesian domain), *p_rgh* (relative bottom pressure corresponding to datum), *k* (turbulent kinetic energy), *ε* (energy dissipation) and *nut* (turbulent viscosity). The first three BC's are required for hydraulic modelling while the last three are required for turbulence calculation.

For both inlets, fixed velocity/discharge were applied using *alpha.water* and *U*. Pressure data (*p_rgh*) were prescribed at the outlet boundaries. Both of the atmosphere boundaries were kept as *zeroGradient* velocity and relative air pressure as zero; so that air could be exchanged if needed. All the wall BC's were kept as no-slip condition (i.e. velocity = 0). For the turbulent approach, values of *k*, *ε* and *nut* were calculated using the equations in FLUENT manual (ANSYS Ins 2009), considering medium turbulence at the gully and manhole. All the walls are prescribed as *wallFunction* as this eliminates the necessity of fine layered boundary mesh and hence reduce the computational time (Greenshields 2015).

Three different numerical model setups were simulated using the same mesh. The setups are described in Table 2. The first scenario replicates the experimental setup while the second and the third scenarios use a higher surcharge level in the manhole, in a view of checking the change of flow condition in the gully due to the higher surcharge level in the manhole.

Table 2: Numerical model scenarios

	Drain inlet *Q* (l/s)	**Manhole inlet *Q* (l/s)**	**Manhole surcharge level (m)**	**Remarks**
Simulation 1	19.8	43.7	0.67	Experimental case scenario = SE1 & SE2
Simulation 2	19.8	43.7	1.16	Additional scenario 1
Simulation 3	19.8	43.7	1.47	Additional scenario 2

2.5. Simulation of the models

The model was ready to run after the boundary setup. During the simulation, *adjustableRunTime* was used keeping maximum CFL number to 0.8. Cluster computing system at the University of Coimbra was used to run the simulations using MPI mode with 16 processors. Each simulation took 40 sec to reach steady state. The computation time was 138 hours for each simulation. Results were obtained once the simulation reached steady state.

3. RESULTS AND DISCUSSION

3.1. Comparison with experimental work at the gully

The numerical model results are compared with the experimental study data of the velocity profiles at the gully obtained by the Vectrino acoustic velocimetry. Figure 3 shows s contours at the three different planes and Figure 4 shows comparison of longitudinal and vertical velocity profiles at different location of the gully.

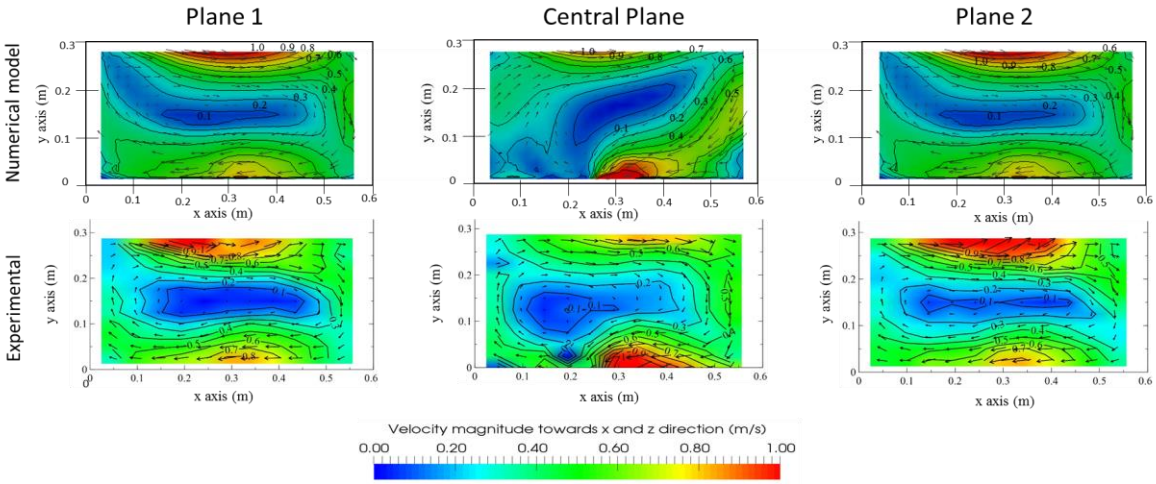

Figure 3: Comparison of velocity between numerical (upper panel) and experimental (bottom panel) study at three longitudinal planes of the gully

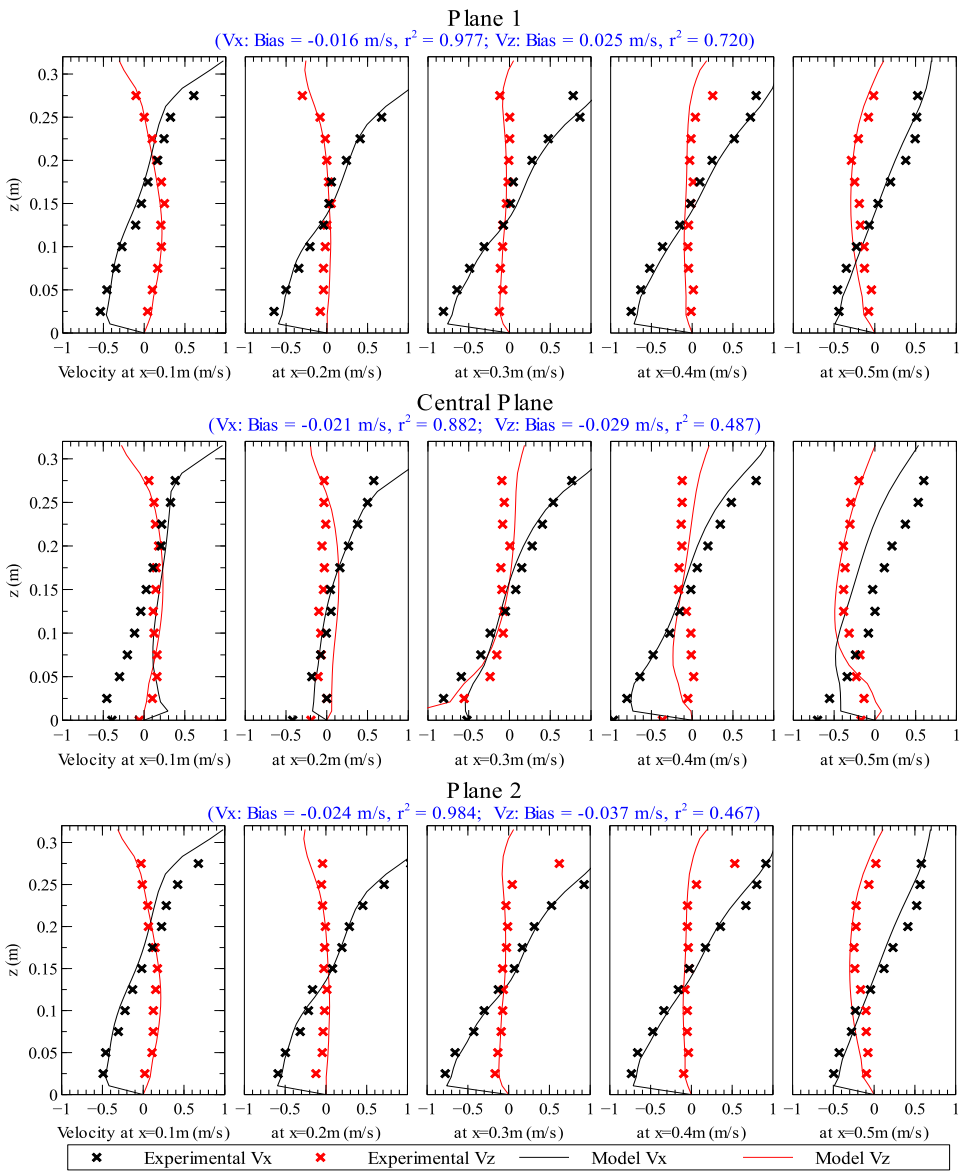

Figure 4: Velocity profile at different location of gully. Firm lines showing numerical model data and cross (x) markers showing data from experimental study

It can be seen from Figure 3 and Figure 4 that the numerical model shows good agreement with experimental data. The vertical vortex size and location created in the numerical result shows similarity to those observed in the experimental model data. Average statistical comparison between the two data can be shown in at Figure 4 and more detailed in Table 3. It shows that the model can reproduce the longitudinal velocity component (*Vx*) very well (average r^2 = 0.95 and BAIS = –0.004 m/s). The representation of vertical velocity component (*Vz*) in the gully is at satisfactory level (average BIAS 0.011 m/s and r^2 = 0.56).

Table 3: Statistical BIAS and correlation coefficient (r2)

		BIAS						r^2					
		***x*=0.1m**	***x*=0.2m**	***x*=0.3m**	***x*=0.4m**	***x*=0.5m**	**Avg.**	***x*=0.1m**	***x*=0.2m**	***x*=0.3m**	***x*=0.4m**	***x*=0.5m**	**Avg.**
P 1	***Vx***	0.060	0.014	-0.078	-0.068	-0.007	-0.016	0.99	0.97	0.98	0.99	0.96	0.98
P C		-0.223	-0.034	-0.024	-0.009	0.186	-0.021	0.67	0.93	0.95	1.00	0.87	0.88
P 2		0.096	0.023	-0.010	-0.016	0.028	0.024	0.99	0.99	0.99	0.98	0.97	0.98
Avg.		-0.023	0.001	-0.037	-0.031	0.069	**-0.004**	0.935	0.88	0.96	0.97	0.99	**0.95**
P 1	***Vz***	0.004	-0.031	0.009	0.072	0.073	0.025	0.87	0.70	0.53	0.79	0.71	0.72
P C		-0.020	-0.141	0.015	-0.020	0.021	-0.029	0.36	0.05	0.84	0.53	0.65	0.49
P 2		-0.029	-0.021	0.069	0.079	0.089	0.037	0.85	0.05	0.02	0.71	0.71	0.47
Avg.		-0.015	-0.064	0.031	0.044	0.061	**0.011**	0.69	0.27	0.46	0.68	0.69	**0.56**

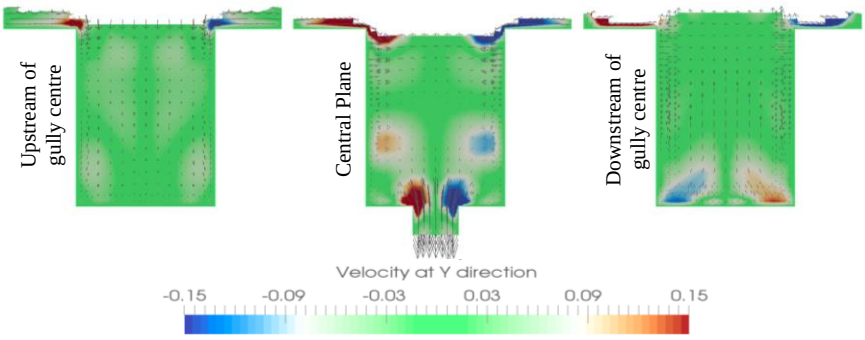

Figure 5: Transverse velocity (*Vy*) at the gully

Figure 5 shows the transverse velocity (*Vy*) in the gully at three different transects. It can be seen from Figure 5 that transverse velocity is very low, in the range of –3 cm/s to +3 cm/s. This velocity component was found insignificant to compare with experimental results.

3.2. Pressure and Shear stress

The pressure and the wall shear stress at the gully bottom were analyzed and can be seen in Figure 6. Similar plot have been made for the bottom of the manhole in Figure 7. In both of the figures, the water flows from the left to right.

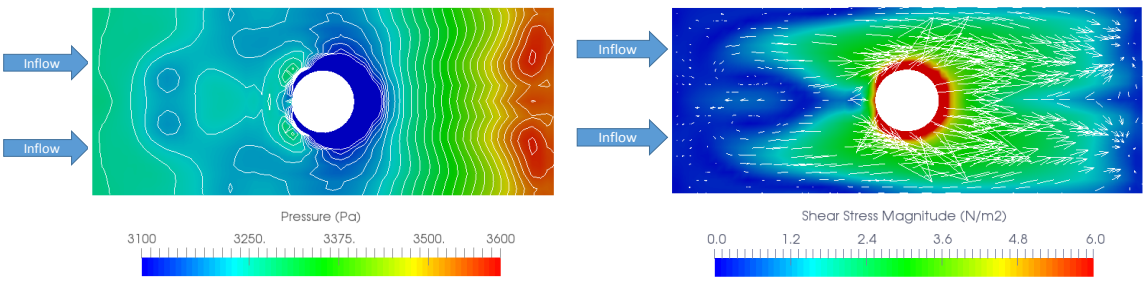

Figure 6: Pressure variation (left panel) and wall shear stress (right panel) at the bottom of the gully

It can be seen from Figure 6 that the bottom pressure at the gully is not uniform. Excluding the outlet location, the pressure gradually increases from upstream direction to the downstream direction. The deviation of the pressure at the gully bottom is in the range of 300 Pa. At the right panel of Figure 6, the wall shear stress at the gully bottom can be seen. The figure shows that the shear stress at the immediate upstream of the gully outlet is the highest. The shear stress direction can be seen towards the opposite direction of the flow.

From Figure 7, a similar view of bottom pressure and shear stress at the manhole bottom can be found. Like the gully bottom, the pressure at the manhole bottom also increases from the downstream to the upstream. Here the variation of bottom pressure is in the range of 200 Pa. The bottom shear stress shows higher value near the outlet. Both bottom shear stress and pressure diagram are asymmetric at the manhole bottom; whereas those diagrams showed symmetric pattern at the gully bottom. The influence of oblique flow from the gully outlet might be the reason of this asymmetric pattern.

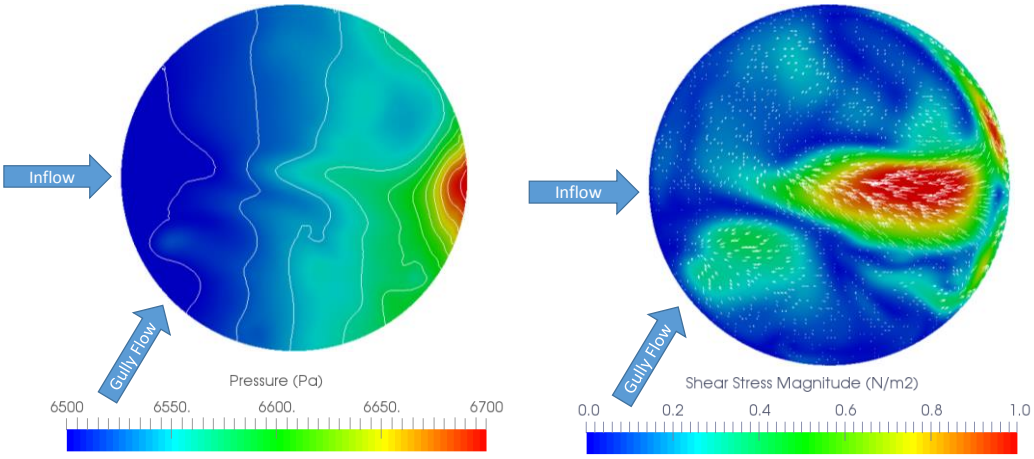

Figure 7: Pressure variation (left panel) and wall shear stress (right panel) at the bottom of the manhole

The pressure and shear stress diagrams at the bottom of the two structures might be useful in predicting sediment deposition pattern inside the structures. The pressure and shear stress diagrams at the bottom of the two structures might be useful in predicting sediment deposition pattern inside the structures. It is likely that in case of particulate transport in the system, the particles are more likely to be deposited at the region with higher pressure with lower shear stress and erosion may take place at the region with higher shear stress and lower pressure. A relation between critical shear stress and sediment particle size is given by Berenbrock and Tranmer (2008). The shear stresses at the gully bottom are in the range of 3 to 6 N/m^2. This stress is higher than the critical shear stress of fine gravel (D_{50} = 4-8 mm) While the shear stresses at the manhole bottom are in the range of 0.4 to 1.0 N/m^2, which is more than the critical shear stress of coarse sand (D_{50} = 1 to 2 mm). So it is likely that gully flow can transport sediment particles up to 8 mm; while the manhole flow can transport sediment particles of up to 2 mm. The bigger sediment particles are likely to be deposited at the manhole bottom.

3.3. Flow path line

During the experimental and numerical study, the following flow distribution (Table 4) was observed at different part of the domain.

Table 4: Flow distribution

Simulation	Drain Inlet (l/s)	Drain Outlet (l/s)	Gully Pipe (l/s)	Manhole Pipe Inlet (l/s)	Manhole Pipe Outlet (l/s)
Simulation 1	19.80	12.4	7.4	43.7	51.1
Simulation 2	19.80	13.4	6.4	43.7	50.1
Simulation 3	19.80	15.9	3.9	43.7	47.6

In all the three simulations, the inflows at the drain inlet were 19.80 l/s. The intercepted flow by the gully was 7.4 l/s (40 % of the inflow) at the experimental case scenario (Simulation 1). The remaining 12.4 l/s (60 % of the inflow) was over flown through the drain. The discharge at the manhole outlet was 51.7 l/s of which 15 % was coming through the gully and the remaining 85 % was coming through the manhole inlet pipe. At simulation 2 and 3, with the increase in manhole surcharge, the flow through the gully outlet decreases. Out of 19.8 l/s inflow through the drain inlet, only 6.4 l/s (32.3 %) and 3.9 l/s (19.7 %) flow were intercepted and drained out by the gully. The flow ratio between manhole inlet and gully pipe plays a significant role in determining the flow circulation pattern inside the manhole.

In this study, the flow path inside the manhole was analysed through the numerical model result. Figure 8 shows different streamline inside the manhole from the above mentioned three simulation results. The yellow streamlines show the flow path coming from the drain and gully whereas the red streamlines are showing the flow path coming through the manhole inlet pipe. The blue arrows show the direction of flow at each case.

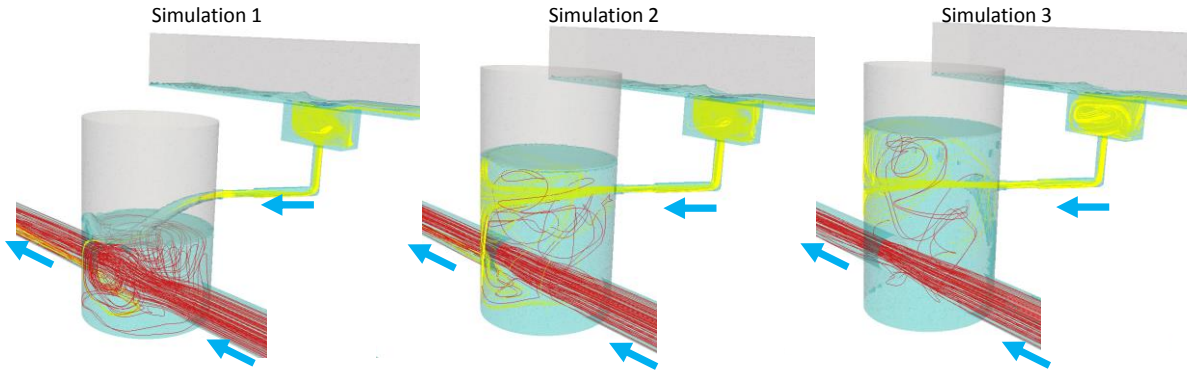

Figure 8: Flow path line / streamline inside the manhole and gully

It can be seen from Figure 8 that both of the flow coming from the gully and manhole inlet circulates inside the manhole and become well mixed. At the left panel, the streamline from simulation 1 shows that the flow from the gully enters the manhole as a plunging jet and recirculates around the manhole. In simulation 1, the flow from the manhole circulates with the manhole. With the increase of surcharge in simulation 2 and 3, the dispersion in manhole inlet flow decreases.

4. CONCLUSION

This study provides first step assessment of flow behaviour inside a gully-manhole linking structure in an urban drainage system. The manhole intakes flow from a gully and adjacent manhole through inlet pipes. A three dimensional CFD model of a quasi-real scale gully-manhole structure was produced using OpenFOAM®, which includes VOF through *interFoam* solver and *k-ε* turbulence modelling approach. The model shows good agreement with the observed velocity profiles at different plane of the gully.

The flow behaviour at the gully-manhole system was analysed from different surcharge conditions of the manhole. It shows that the intercepted flow by the gully decreases when the surcharge at the manhole. The shear stress at the manhole bottom is much lower than that of gully bottom. This indicates that all the sediment particle sizes transported by the gully will not be transported by this kind of manhole. Some bigger particles may be deposited at the manhole bed. The streamlines from the numerical model showed that the flow from the gully and from manhole inlet becomes well mixed in the manhole. The flow through the manhole inlet showed less depressive nature in higher surcharge.

The study described here is useful to calibrate/validate a numerical model created with the open-source toolbox OpenFOAM® and in characterizing the physical model setup. The work will be further continued to develop an experimental and numerical approach to better understand particulate transport phenomena inside the gully-manhole-pipe drainage. Datasets obtained in this study will be used to calibrate/validate a numerical model created with the open-source toolbox OpenFOAM®.

5. ACKNOWLEDGMENTS

The work presented is part of the QUICS (Quantifying Uncertainty in Integrated Catchment Studies) project. This project has received funding from the European Union's Seventh Framework Programme for research, technological development and demonstration under grant agreement No. 607000. The authors would also like to acknowledge for the support of FCT (Portuguese Foundation for Science and Technology) through the Project UID/MAR/04292/2013 financed by MEC (Portuguese Ministry of Education and Science) and FSE (European Social Fund), under the program POCH (Human Capital Operational Programme).

6. REFERENCES

ANSYS Ins. (2009). *ANSYS Fluent 12.0 User 's Guide*. *October*.

Beg, M. N. A., Carvalho, R., Lopes, P., Leandro, J., and Melo, N. (2016). "Numerical Investigation of the Flow Field inside a Manhole-Pipe Drainage System." *Hydraulic Structures and Water System Management. 6th IAHR International Symposium on Hydraulic Structures*, B. Crookston and B. Tullis, eds., Portland, Oregon, USA, 1–11.

Brackbill, J. U., Kothe, D. B., and Zemach, C. (1992). "A continuum method for modeling surface tension." *Journal of Computational Physics*, 100(2), 335–354.

Butler, D., and Davies, J. W. (2011). *Urban drainage*. *Taylor & Francis*, Spon Press, London.

Carvalho, R., Páscoa, P., Leandro, J., Abreu, J., Lopes, P., Quinteiro, R., and Lima, L. M. P. L. (2013). "Experimental investigation of the linking element gully - drop manhole." *Proceedings of 35th IAHR World Congress 2013*, 35th IAHR World Congress 2013.

Djordjević, S., Saul, A. J., Tabor, G. R., Blanksby, J., Galambos, I., Sabtu, N., and Sailor, G. (2013). "Experimental and numerical investigation of interactions between above and below ground drainage systems." *Water Science and Technology*, 67(3), 535–542.

Environmental, B., Commission, I., and Agency, U. S. E. P. (2008). *Simulation of Flow, Sediment Transport, and Sediment Mobility of the Lower Coeur d ' Alene River, Idaho*. *U.S. Geological Survey Scientific Investigations Report 2008–5093*, Reston, Virginia.

Furbo, E., Harju, J., and Nilsson, H. (2009). *Evaluation of turbulence models for prediction of flow separation at a smooth surface*. *Project Report - Uppsala Universitet*, Uppsala.

Galambos, I. (2012). "Improved Understanding of Performance of Local Controls Linking the above and below Ground Components of Urban Flood Flows." *PhD Thesis*, University of Exeter.

Greenshields, C. J. (2015). *OpenFOAM User Guide*.

Hirt, C. W., and Nichols, B. D. (1981). "Volume of fluid (VOF) method for the dynamics of free boundaries." *Journal of Computational Physics*, 39(1), 201–225.

Juretić, F. (2015). *cfMesh User Guide (v1.1)*. Zagreb, Croatia.

Leandro, J., Lopes, P., Carvalho, R., Páscoa, P., Martins, R., and Romagnoli, M. (2014). "Numerical and experimental characterization of the 2D vertical average-velocity plane at the center-profile and qualitative air entrainment inside a gully for drainage and reverse flow." *Computers & Fluids*, 102(June), 52–61.

Lopes, P., Leandro, J., Carvalho, R. F., Páscoa, P., and Martins, R. (2015). "Numerical and experimental investigation of a gully under surcharge conditions." *Urban Water Journal*, 12(6), 468–476.

Lopes, P., Leandro, J., Carvalho, R. F., Russo, B., and Gómez, M. (2016). "Assessment of a VOF Model Ability to Reproduce the Efficiency of a Continuous Transverse Gully with Grate." *Journal of Irrigation and Drainage Engineering*, (in production).

Martins, R., Leandro, J., and Carvalho, R. F. (2014). “Characterization of the hydraulic performance of a gully under drainage conditions.” *Water science and technology*, 69(12), 2423–30.

Romagnoli, M., Carvalho, R. F., and Leandro, J. (2013). “Turbulence characterization in a gully with reverse flow.” *Journal of Hydraulic Engineering-ASCE*, 139(7), 736–744.

Rubinato, M. (2015). “Physical scale modelling of urban flood systems.” University of Sheffield.

Rusche, H. (2002). “Computational Fluid Dynamics of Dispersed Two-Phase Flows at High Phase Fractions.” *PhD Thesis*, (December).

Stovin, V. R., Guymer, I., and Lau, S. D. (2008). “Approaches to validating a 3D CFD manhole model.” *11th International Conference on Urban Drainage (11ICUD)*, 1–10.

Weller, H. G. (2002). *Derivation modelling and solution of the conditionally averaged two-phase flow equations. Technical Report TR/HGW/02, Nabla Ltd.*

DOI:10.15142/T34G6P

Increasing Piano Key Weir Efficiency by Fractal Elements

F. L. Bremer[1] and M. Oertel[1]
[1] Hydraulic Engineering Section, Civil Engineering Department
Lübeck University of Applied Sciences
Lübeck, Germany
E-mail: frederik.bremer@fh-luebeck.de

ABSTRACT

Piano Key Weirs (PKW) are hydraulic structures which can be used for flood release systems on dams or for in-channel weir replacement. The efficiency can be increased compared to linear weirs, since the effective overfall length will be majorly increased by arranged piano keys. The present research investigation deals with experimental model results of scaled PKW models and compares resulting discharge coefficients and scale effects. One PKW geometry was manufactured with included fractal elements with the main aim to increase the structure's efficiency. The paper includes detailed information on the investigated experimental model. The concept of the fractal PKW has a major positive effect on PKW efficiency for very low energy heads. With increasing discharges this advantage gradually decreases. Additionally, the paper focuses on future concepts and possible PKW adaptions.

Keywords: *Piano Key Weir, PKW, discharge coefficient, efficiency, fractal elements*

1. INTRODUCTION

Piano Key Weirs (PKW) are nonlinear weir types. The general design was developed by Blanc and Lempérière (2001) and Lempérière and Ouamane (2003). The PKWs are used for improving flood release structures for reservoir systems. They can also be used as a weir replacement in regular flow channels. Because of the nonlinear geometry an increase of discharge capacity can be provided. In comparison to the total crest length the footprint size of a PKW is relatively small and it is ideal for top-of-dam spillway control structure (Oertel & Tullis 2014).

In general, PKWs are differentiated into three main classifications: Type A, Type B and Type C. A PKW Type A has symmetric upstream and downstream overhang lengths. A PKW Type B has only overhangs to the upstream direction and the PKW Type C is the opposite with only overhangs to the downstream. Figure 1 shows the inlet key has its overhangs downstream and the outlet key its overhangs upstream. A PKW is built out of PKW units W_u, which contains one inlet key and two half outlet keys. The main geometrical parameters are listed and visualized in Figure 1.

Previous studies within scaled physical models show that the hydraulics of PKWs depend on several geometrical parameters. Ribeiro et al. (2012) identified that primary and secondary parameters influence the discharge capacity considerably. The weir height P and the total weir width W are defined as primary parameters. The inlet and outlet width ratio $W_iW_o^{-1}$ and the height ratio $P_iP_o^{-1}$ are for example defined as secondary parameter. However, Machiels et al. (2014) defines the main influence factors as the weir heights P, the width ratio of the inlet and outlet $W_iW_o^{-1}$ and the overhang ratio B_iB^{-1}.

To determine discharge coefficients according to Poleni the upstream water surface level h_T above weir crest is necessary. By extending the Poleni formula with the velocity head the Du Buat formula can be developed:

$$Q = \frac{2}{3}\, C_d\, L\, (2g)^{0.5}\, H_T^{1.5} \tag{1}$$

with: Q = discharge, C_d = dimensionless discharge coefficient, L = total centerline crest length, g = acceleration due to gravity, H_T = total upstream energy head including the velocity head = $h_T + v_T^2(2g)^{-1}$. The required flow velocity v_T is averaged over the total upstream flow depth h.

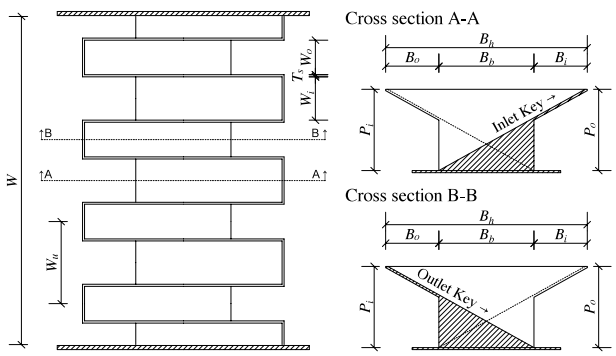

Parameter	Definition
P_i	upstream weir height
P_o	downstream weir height
W_i	inlet key width
W_o	outlet key width
N_u	No. of PKW units
B_h	side crest length
B_i	downstream overhang length
B_o	upstream overhang length
B_b	weir foot length
T_s	wall thickness
W_u	PKW unit width, $W_u = W_i + W_o + 2 \times T_s$
W	total weir width, $W = N_u \times W_u$
L_u	crest centerline length of PKW unit, $L_u = W_u + 2 \times B_h - 2 \times T_s$
L	total crest centerline length, $L = N_u \times L_u$.

Figure 1. Main geometric PKW notations (flow direction left to right), according to Pralong et al. (2011) and Oertel and Bremer (2016).

2. FRACTALIZATION PRINCIPLE

Objects that are similar to their constituents are called fractals. The term fractal was coined in 1970 by the French-American mathematician Benoit Mandelbrot. But already in 1926 the British physicist Fry Richardson discovered the phenomenon of fractal patterns (Lossau 2016).
With the propose to improve the PKW's discharge capacity a new concept of "fractalizing" the PKW crest was developed by Laugier et al. (2011). It consists of implementing small PKW units at the top side crest to majorly increase the developed total centerline crest length, since this parameter has a major influence on resulting PKW's discharge capacities, especially for small energy heads (Laugier et al. 2011).

3. EXPERIMENTAL MODEL

3.1. General remarks

The present paper focuses on water surface profiles and the resulting discharge coefficients and efficiency studies of two PKW geometries. A (1) Type A PKW and a (2) Type A PKW with fractal components were designed, based on Bremer (2016) and labeled as (1) PKW_A and (2) PKW_A_F.
The physical modeling data were produced by installing the two PKW geometries in a tilting flume (length L = 10.0 m, width W = 0.8 m, height H = 0.8 m) at Lübeck University of Applied Sciences' Water Research Laboratory.
The flow supply was provided by two frequency regulated pumps (fabricate: Grundfos NBE-150-250, each 11 kW) and a piping system containing a valve and a magnetic inductive flow meter (MID, fabricate: Krohe, model: Optiflux 2000, accurate to ±0.1 l/s). The flow depths were measured by using an ultrasonic sensor (USS, fabricate: general acoustics, model: USS635, accurate to ±1 mm) mounted on an automatic step motor (fabricate: isel, accurate better than 1 mm) for positioning the USS in 1 cm steps along the flow direction in the tilting flume.

3.2. PKW geometries

The most important geometric parameters for the two PKW geometries are shown in Figure 2. The PKWs are all designed with an inlet- and outlet key widths of W_i = 105 mm and W_o = 85 mm. This represents an inlet to outlet

ratio of $W_iW_o^{-1}$ = 1.25. The weir heights P, the weir widths W, the weir foot lengths B_b and the number of PKW units Nu are also equal in the two designed PKW geometries.

The PKW_A geometry (Figure 2 (a)) is a symmetric PKW with equal down- and upstream overhang lengths ($B_i = B_o$ =129.1 mm). The total crest centerline length is L = 4667.2 mm. It results in a weir width total crest centerline length ratio of LW^{-1} = 5.86.
The configuration PKW_A$_F$ (Figure 2 (b)) is based on the PKW_A geometry. Fractal elements were placed on the PKW side walls crest. In every side wall five orthogonal fractal elements after the model of a PKW B type were included, so the total crest centerline length increases up to L = 6691.2mm with a resulting ratio of LW^{-1} = 8.41.

(a) PKW_A
(b)

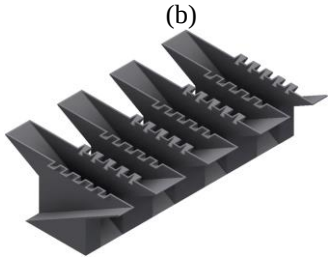

(b) PKW_A$_F$

Parameter	Unit	PKW_A	PKW_A$_F$
P	[mm]	196.9	196.9
L	[mm]	4667.2	6691.2
W	[mm]	800.0	800.0
W_i	[mm]	105.0	105.0
W_o	[mm]	84.0	84.0
B_b	[mm]	230.7	230.7
B_h	[mm]	488.9	741.9
B_i	[mm]	129.1	129.1
B_o	[mm]	129.1	129.1
T_s	[mm]	5.0	5.0
N_u	[−]	4	4
$W_iW_o^{-1}$	[−]	1.25	1.25
PT_s^{-1}	[−]	39.38	39.38
LW^{-1}	[−]	5.86	8.41
PT_s^{-1}	[−]	41.4	41.4

Figure 2. 3D visualization and dimensions of the manufactured PKW geometries (flow direction left to right) according to Oertel and Bremer (2016) .

3.3. Model runs

For the two investigated PKWs 18 model runs each, in total 36, were performed with varying discharges (specific discharges q = 2.50, 6.25, 10.00, 13.75, 17.50, 21.25, 25.00, 31.25, 37.50, 43.75, 50.00, 56.25, 62.50, 75.00, 87.50, 100.00, 112.50, 125.00 l(sm) $^{-1}$).
The water surface levels (WSL) were collected up to 2.5 m upstream and 0.3 m downstream of the PKW axis in 1 cm steps. The measuring time was set to 10 seconds. Outliners, which were identified using a standard deviation criterion (outlier of: $d > m + 2 \times s$ or $d < m - 2 \times s$, with: d = time dependent flow depth data point, m = mean time averaged flow depth and s = standard deviation), were removed from the data. The corrected time-averaged flow depths h was used for data analysis.
For calculating the upstream energy heads H_T the time-averaged upstream flow depth h was deducted by the weir height P ($h_T = h - P$). Also the velocity head $v_T(2g)^{-1}$ gets added. To fulfill the discharge coefficients formula by Du Buat (equation 1) the total upstream energy heads becomes $H_T = h_T + v_T(2g)^{-1}$. Oertel (2016) and Bremer (2016) both point out, that the distance to the weir geometry for the point on which the WSLs are taken has a great influence on calculating precise discharge coefficients C_d. Hence, for all 36 model runs the WSLs are taken at a distance of 5 × P upstream from the PKW axis to ensure a safe result production.

4. RESULTS

4.1. Water surface profiles

Figure 3 shows for the two investigated PKW models, the resulting time averaged water surface profiles in the flumes centerline for all tested specific discharges. The two plots show that a smooth water surface occurs for distances $xP^{-1} > 2$. Between $0 < xP^{-1} < 2$ flow will be accelerated and the WSL starts to decrease. In between $-1.5 < xP^{-1} < 0$ the structure's overflowing edges lead to an increase in the resistance forces of the PKW. The flow decreases and the WSL de- and increases to a waved surface. Figure 4 to 6 show detailed plots of the WSLs over the inlet cross section in a direct comparison of the PKW_A and PKW_A$_F$. Three exemplary specific discharges were selected (q = 13.75 l(sm)$^{-1}$, 50.00 l(sm)$^{-1}$, 125.00 l(sm)$^{-1}$). The considered discharges are also illustrated by photographs. Figure 4 (a) shows that the PKW_A$_F$ has a lower water surface profile than the PKW_A. Figure 5 (a) & 6 (a) illustrate that the water surface profile of PKW_A and PKW_A$_F$ have a similar height. Also the photographs in Figure 6 (Figure 6 (b) & (c)) show that, the outlet cross section of the PKW_A$_F$ is more filled with water. This indicates a lower hydraulic efficiency of the PKW_A$_F$ outlet cross section. In addition to these plots Figure 7 shows the water surface levels in direct comparison for PKW_A and PKW_A$_F$ geometries at measuring distance 5 × P up water. In general comparison the PKW_A$_F$ geometry has the lowest WSLs at the measuring distance 5 × P. In further consideration the PKW_A has for specific discharge q < 20 l(sm)$^{-1}$ higher WSLs in comparison to the PKW_A$_F$. Between the specific discharge 20 l(sm)$^{-1}$ < q < 40 l(sm)$^{-1}$ the PKW_A decreases its WSLs relative to the PKW_A$_F$. For discharge q > 40 l(sm)$^{-1}$ the WSLs of the PKW_A are approximately equal to the WSLs of the PKW_A$_F$.

Scale effects might influence the water surface profiles, which would have an effect on the calculated discharge coefficients. Scale effects in particular might affect the PKW_A$_F$ geometry and especially small discharges. To identify these scale effects further investigation in a large-scale model should be provided. In this paper the influence of scale effects is neglected.

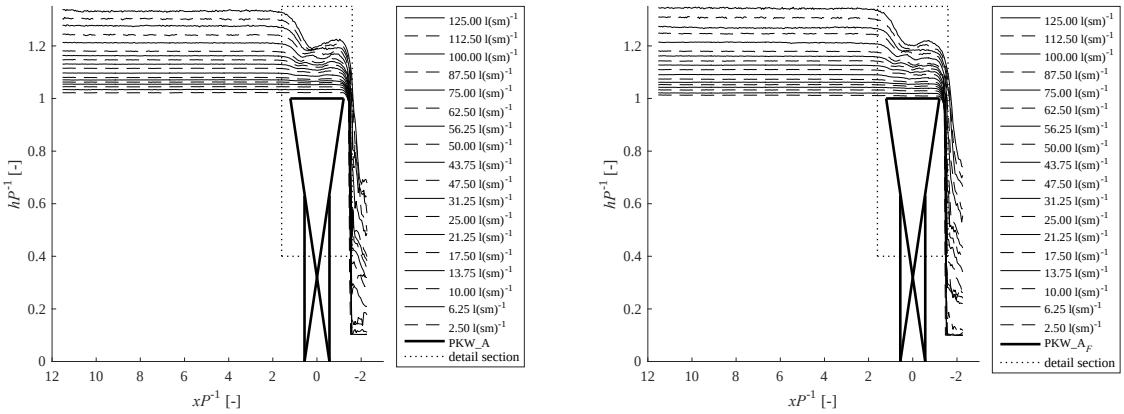

(a) PKW_A (b) PKW_A$_F$

Figure 3. WSL at flume's centerline for investigated discharges (inlet key section, exaggerated plot).

(a) WSL (b) PKW_A (c) PKW_A$_F$

Figure 4. Detail plot of the WSLs over the PKW cross section and photographs for a specific discharge q = 13.75 l(sm)$^{-1}$.

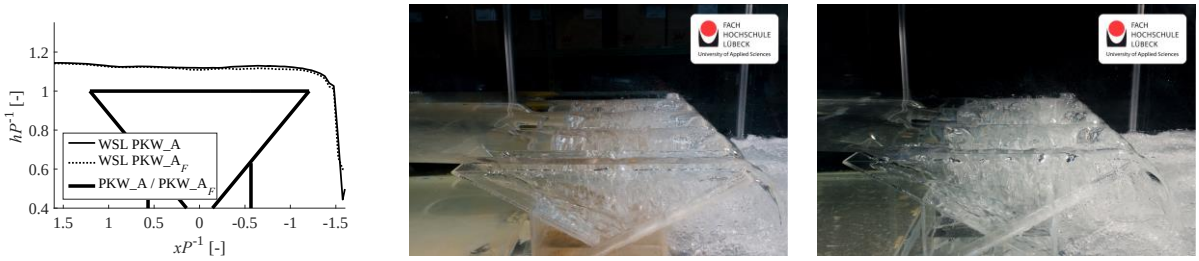

(a) WSL (b) PKW_A (c) PKW_A$_F$

Figure 5. Detail section of the WSLs over the PKW cross section and photographs for a specific discharge q = 50.00 l(sm)$^{-1}$.

(a) WSL (b) PKW_A (c) PKW_A$_F$

Figure 6. Detail section of the WSLs over the PKW cross section and photographs for a specific discharge q = 125.00 l(sm)$^{-1}$.

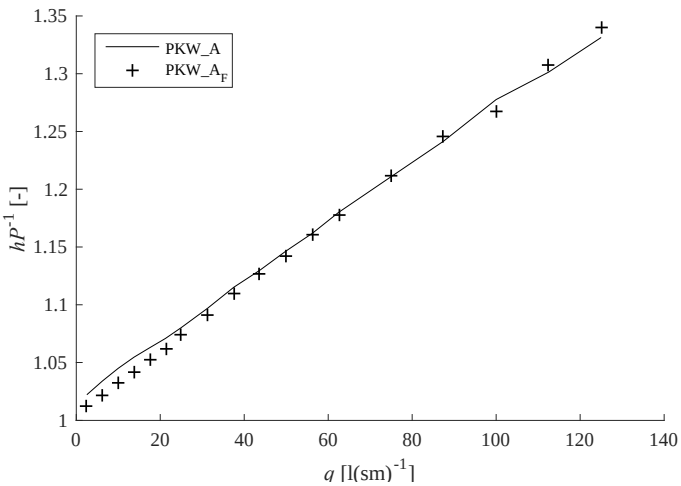

Figure 7. Direct comparison of water surface heights for PKW_A and PKW_A$_F$ geometries at measuring distance 5×P.

4.2. Discharge coefficients and PKW efficiency

Figure 8 (a) shows the calculated discharge coefficients C_d as absolute values. The discharge coefficients are calculated by using equation 1 including the velocity head $v_T(2g)^{-1}$. For comparing the two investigated PKW models the PKW_A will be taken as reference geometry. Figure 8 (b) shows the relative comparison of resulting C_d values for the investigated PKW geometries.

Figure 8 (a) show a typical development of discharge coefficients with larger C_d values for small discharges and for higher discharges with lower values. This is a result of the outlet cross section reduces its hydraulic efficiency with increasing discharges, so the discharge coefficients decreases.

Generally, the PKW_A geometry shows the largest C_d values. For a given ratio $H_TP^{-1} < 0.05$ the PKW_A$_F$ has larger C_d values than PKW_A. By increasing the energy heads the discharge coefficients of the fractal PKW rapidly decrease. For ratios $H_TP^{-1} < 0.05$ the PKW_A$_F$ C_d values are lower than the C_d values of the PKW_A.
By looking at Figure 8 with consideration that a large C_d value equals a good efficiency, the PKW_A seems to be in general the most efficient PKW per unit length of the two investigated geometries. From a ratio $H_TP^{-1} < 0.05$ (equals a specific discharge 13.75 l(sm)$^{-1}$ < q < 17.50 l(sm)$^{-1}$) the PKW_A has larger C_d values than the PKW_A$_F$ what might indicate a higher efficiency. Whereas Figure 7 shows that the PKW_A has for specific discharge q > 40 l(sm)$^{-1}$ approximately equal WSLs as the PKW_A$_F$. This concludes, that the PKW_A and the PKW_A$_F$ might have the same efficiency for specific discharges q > 40 l(sm)$^{-1}$ (equals an energy head $H_TP^{-1} \approx 0.14$). Consequently, the discharge coefficients C_d, calculated with using the total centerline crest length are not reasonable for useful PKW efficiency statements.

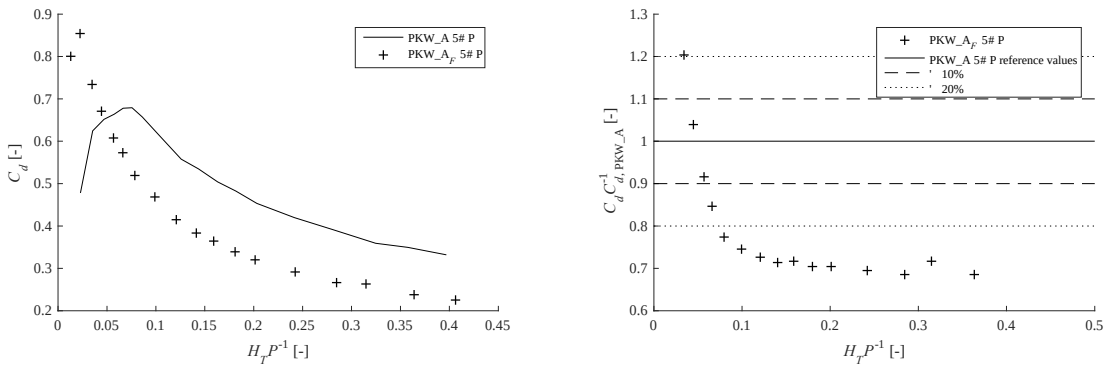

(a) absolute values (b) direct comparison

Figure 8. Discharge coefficients C_d for PKW_A and PKW_A$_F$ geometries.

Considering that the discharge coefficients C_d, calculated by using the total centerline crest length are not reasonable for useful PKW efficiency statements, it is necessary to provide a method for direct comparison. Indications of PKW efficiency are the upstream water surface levels on a specific measuring point or distance to the weir as shown in Figure 7. It is more accurate to determine the PKW efficiency by using a normalized discharge coefficient C_{dw}. The C_{dw} value allows analyzing and comparing PKW efficiency for PKWs with different centerline crest lengths. Therefore Equation 1 gets modified by replacing the total centerline crest lengths L with the fixed flume width W, as shown below:

$$Q = \frac{2}{3} C_{dw}\, W\, (2g)^{0.5}\, H_T^{1.5} \qquad (2)$$

with: C_{dw} = normalized discharge coefficient, W = fixed flume width = 0.8 m (for present investigation). If the purpose of the PKW is to produce a high efficiency, which equals a low upstream head the calculated C_d values, which includes the total centerline crest length L, does not allow a statement about the efficiency of the investigated weir geometry. Thus, the normalized C_{dw} value becomes necessary. Machiels et al. (2011) comes also to this conclusion.
Figure 9 shows resulting normalized discharge coefficients C_{dw} for PKW_A and PKW_A$_F$ as absolute values (Figure 9 (a)) and relative comparison (Figure 9 (b)). Now the not matching results between Figure 7 and Figure 6 are obvious. For low discharges $H_TP^{-1} < 0.05$ the PKW_A has a lower efficiency. The PKW_A$_F$ has by far the highest efficiency even up to $H_TP^{-1} \leq 0.10$. With increasing discharges $H_TP^{-1} > 0.10$ the efficiency of PKW_A and PKW_A$_F$ is similar. The large C_{dw} values of the PKW_A$_F$ for low discharges in comparison to the reference geometry might be a result of scale effects. Therefore, further investigations are necessary to examine data.

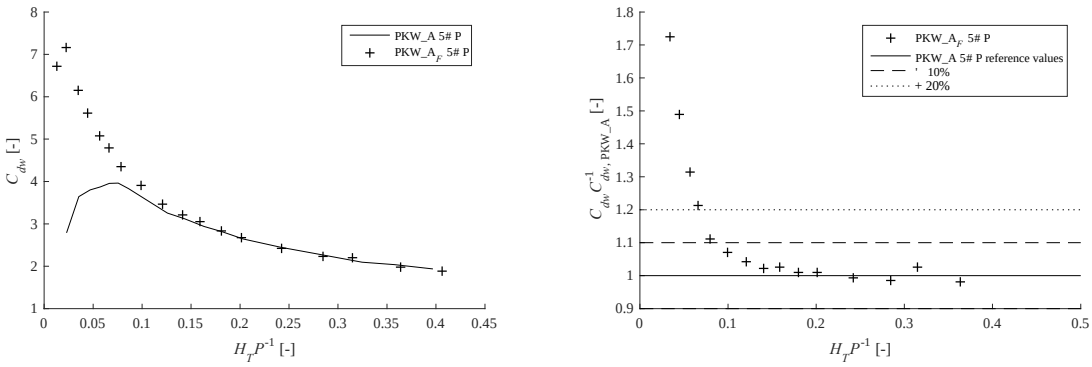

(a) absolute values (b) direct comparison

Figure 9. Normalized discharge coefficients C_{dw} for PKW_A and PKW_A$_F$ geometries.

5. RESULT ANALYSIS

The concept of the fractal PKW has a major positive influence on the discharge capacity for low energy heads. For the smallest tested discharge the PKW_A$_F$ has an up to over 70% increased efficiency. With increasing discharges the advantage gradually decreases and the PKW_A$_F$ has a similar efficiency as the tested reference geometry (PKW_A). For most practical PKW Applications, increasing efficiency at very small heads is likely of limited benefit compared to the cost associated with adding fractals.

In addition to this investigation larger scaled models, particularly of the fractal PKW is needed to determine scale effects. The PKW_A$_F$ will be influenced by scale effects especially for those low energy heads. It seems to be, that the surface tension has a negative influence on the results and the efficiency for small discharges might be even increased. Cicero et al. (2011) compares a 1/30 scaled physical model with a 1/60 scaled model to characterize the effect of surface tension for low energy heads for PKW structures. Therefore, the Weber number must be calculated by following equation:

$$We = \frac{\rho g H^2}{\sigma} \tag{3}$$

with: ρ = water density, g = gravitation due to gravity, H = total energy head, σ = surface tension.

The calculated and compared C_d values by Cicero et al. (2011) of both models show differences less than 8 %. This is lower than measurements uncertainties. Within low energy head the measurement uncertainties for the 1/60 models get larger. For energy heads $H_T P^{-1} > 0.2$ (equals H_T = 1.5 cm or We = 30 for the 1/60 scaled model) the calculated results match relatively precise (Cicero et al. 2011). In Figure 10 the calculated Weber numbers for the investigated PKW_A and PKW_A$_F$ are shown. The peak of the C_d values for the PKW_A is $H_T P^{-1} \approx 0.08$ and for the PKW_A$_F$ $H_T P^{-1} \approx 0.03$. A Weber number $We \approx 30$ is equal to $H_T P^{-1} \approx 0.08$. That means all tested discharges with an energy head $H_T P^{-1} > 0.08$ have no influence by scale effects. The discharges with low energy heads $H_T P^{-1} < 0.08$ must be reinvestigated with a larger scaled model to remove scale effects.

Figure 11 shows PKW_A and PKW_A$_F$ as exemplary photographs for specific discharges of q = 13.75 l(sm)$^{-1}$, q = 50.00 l(sm)$^{-1}$ and q = 125.00 l(sm)$^{-1}$.With increasing discharge the water amounts pass the weir more and more in longitudinal direction and with less 3D effects. So the total centerline crest length has for large discharges decreasing influence on the efficiency of the PKW.

In this investigation the fractal elements were designed as configuration PKW type B. These fractal elements are placed orthogonal to the side crest of the weir. For improving this design further investigation with different fractal elemental set ups are needed. For example, to place the fractal units in an angle so the incident flow is improved. Also this might influence the hydraulic efficiency of the outlet cross section. As in Figure 12 is shown the fractal elements guide the water orthogonal into the outlet cross section. That leads to a longer flow length and the water remains longer in the outlet cross section. A backwater of the descendant water is the result. With placing the fractal elements at an angle this problem might be less relevant. Also it's necessary not to reduce the outlet width by any fractal elements because that might influence the hydraulic efficiency as well.

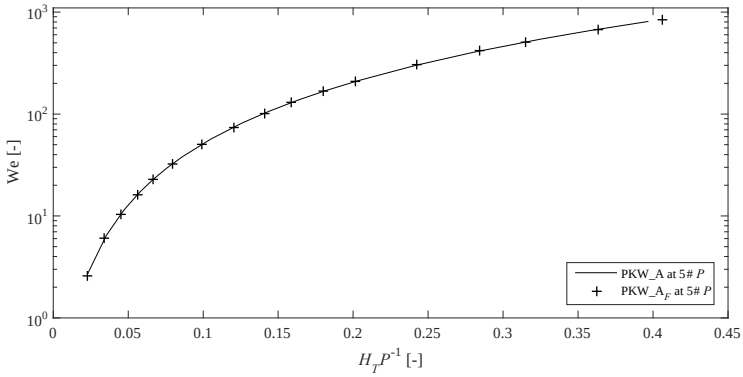

Figure 10. calculated Weber numbers for PKW_A and PKW_A$_F$.

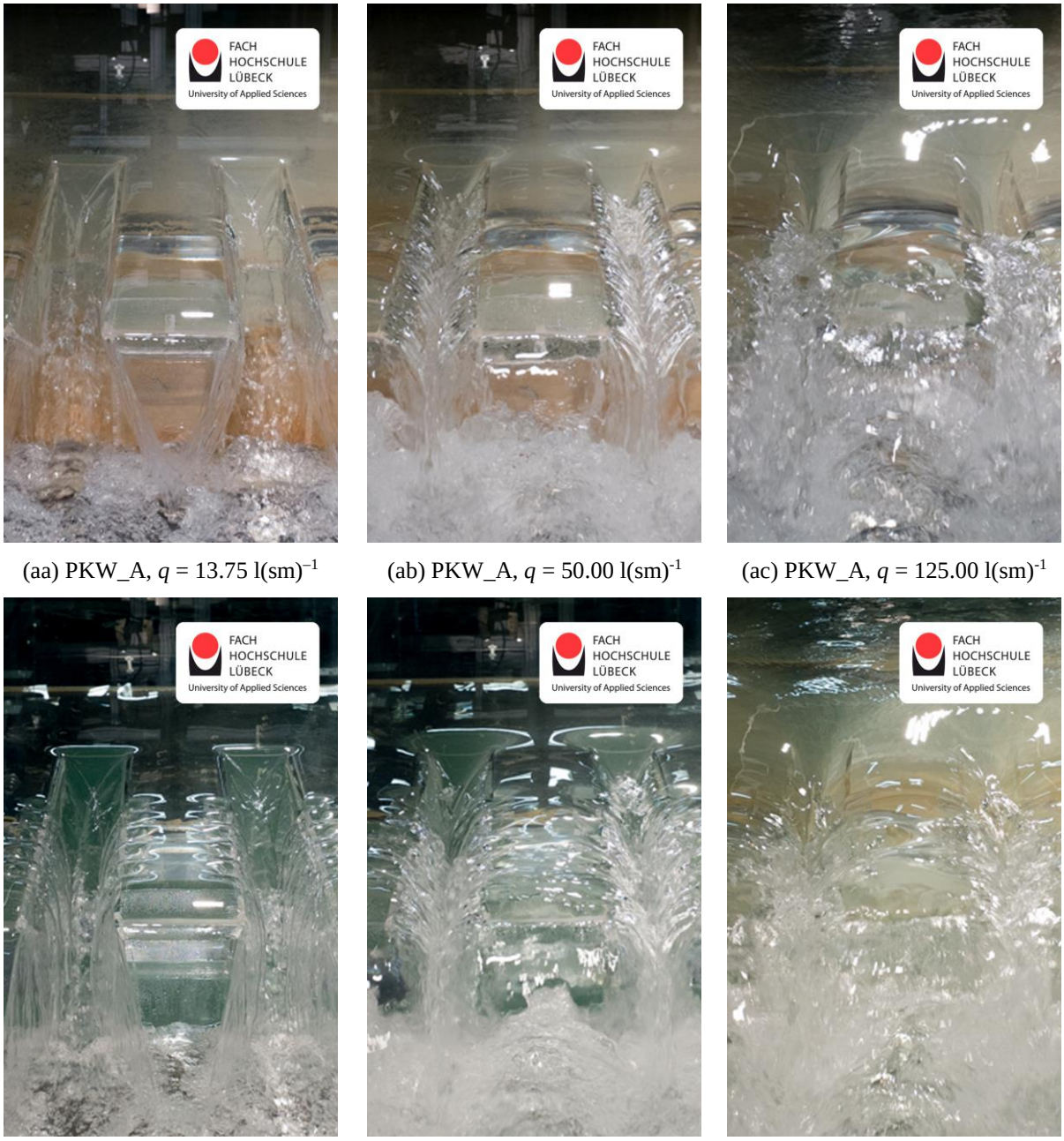

(aa) PKW_A, q = 13.75 l(sm)$^{-1}$ (ab) PKW_A, q = 50.00 l(sm)$^{-1}$ (ac) PKW_A, q = 125.00 l(sm)$^{-1}$

(ba) PKW_A, q = 50 l(sm)$^{-1}$ (bb) PKW_A$_F$, q = 50.00 l(sm)$^{-1}$ (bc) PKW_A$_F$, q = 125.00 l(sm)$^{-1}$

Figure 11. Detail Photograph of the inlet in centerline of the PKW_A and PKW_A$_F$.

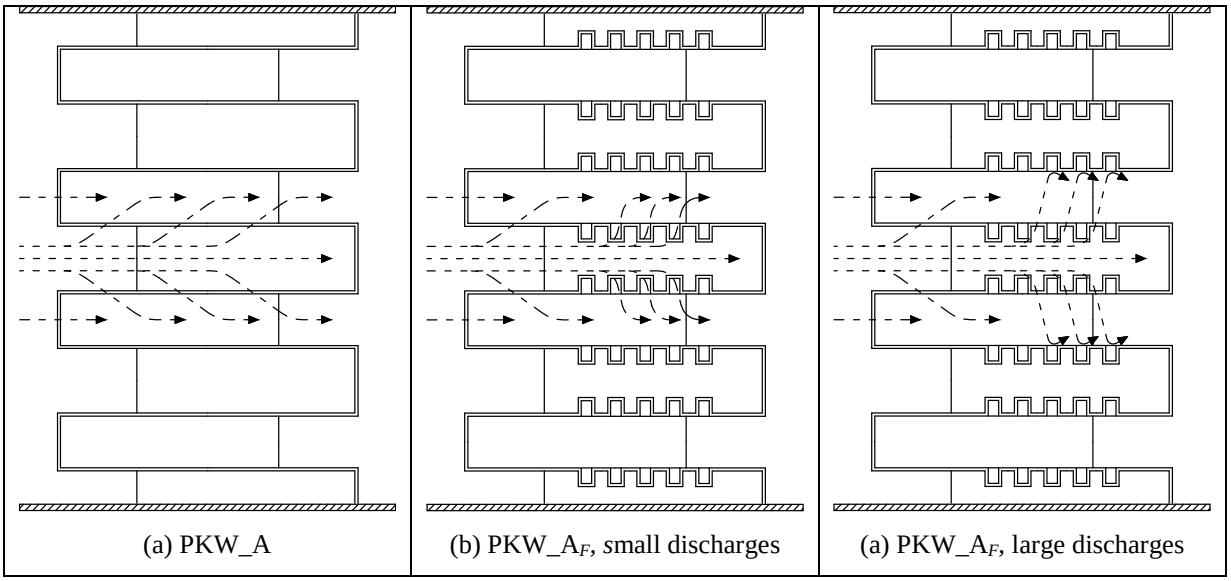

Figure 12. Idealized flow direction in comparison of PKW_A and PKW_A$_F$.

6. CONCLUSIONS

The present investigation is about PKWs with fractal elements and its structure efficiency, discharge coefficients and water surface profiles.

The water surface profiles show flow acceleration right in front of the upstream face of the PKW structure and the WSL decreases rapidly. Over the PKW structure the velocity decreases erratically and the WSL increases to a wavy surface. Within the inlet cross section three-dimensional flow effects cannot be excluded. Further investigation is needed.

Discharge coefficients resulting from the present investigation show a typical development with height C_d values for small discharges and with lower values for higher discharges. By increasing discharges the outlet cross section reduces its hydraulic efficiency and the discharge coefficients decrease. Also the effective total centerline crest length reduces with increasing discharges.

Comparing determined C_d values with measured water surface profiles shows that the discharge coefficients provide no reasonable information about the PKW efficiency. To determine the PKW efficiency a normalized discharge coefficient C_{dw} is necessary. Within the C_d value included total crest length gets replaced by the total weir width. Due to this calculation method it is possible to compare the efficiency of PKW with different total centerline crest length.

The PKW_A$_F$ shows a significant better efficiency for small discharges compared to reference geometry. The results for calculated C_d and C_{dw} values with an energy head $H_T P^{-1} < 0.08$ are influenced by scale effects and further investigation with larger scaled physical model is necessary to exclusionary scale effects. Within larger discharges the PKW_A$_F$ efficiency equals the efficiency of the reference geometry.

7. REFERENCES

Bremer, F. (2016). Piano-Key-Wehre mit fraktaler Geometrie – Strömungscharakteristika und Überfallbeiwerte. *Master Thesis*, Hydraulic Engineering Section, Lübeck University of Applied Sciences, Germany [in German].

Blanc, P. and Lempérière, F. (2001). Labyrinth spillways have a promising future. *Hydropower & Dams*, 8(4), 129–131.

Cicero, G. M., Menon, J. M., Luck, M. & Pinchard, T. (2011). Experimental study of side and scale effects on hydraulic performances of a Piano Key Weir. *Proc. 1st Workshop on Labyrinth and Piano Key Weirs*, PKW 2011, Taylor & Francis Group London, 167–172.

Laugier, F., Pralong, J., Blancher, B. and Montarros, F. (2011). Development o f a new concept of Piano Key Weir spillway to increase low head hydraulic efficiency: Fractal PKW. *Proc. 1st Workshop on Labyrinth and Piano Key Weirs*, PKW 2011, Taylor & Francis Group London, 281-288.

Lempérière, F. and Ouamane, A. (2003). The piano key weir: a new cost-effective solution for spillways. *Hydropower & Dams*, 10(5), 144–149.

Lossau, N. (2016). Geheimnisvolle Muster im Alten Testament entdeckt. *Die Welt*, http://www.welt.de/wissenschaft/article151474321/Geheimnisvolle-Muster-im-Alten-Testament-entdeckt.html (Mai 15., 2016)

Machiels, O., Erpicum, S., Archambeau, P., Dewals, B. & Pirotton, M. (2011). Piano Key Weir preliminary design method – Application to a new dam project. *Proc. 1st Workshop on Labyrinth and Piano Key Weirs*, PKW 2011, Liege, Belgium.

Machiels, O., Pirotton, M., Archambeau, P., Dewals, B. und Erpicum, S. (2014). Experimental parametric study and design of Piano Key Weirs. *J. Hydr. Res.* (Vol. 52, No. 3).

Oertel, M. (2016). Sensitivity Analysis for discharge coefficients of Piano Key Weirs. *6th International Symposium on Hydraulic Structures*, IAHR, Portland, USA.

Oertel, M. and Bremer, F. (2016). Analysis of Various Piano Key Weir Geometries concerning Discharge Coefficient Development. *Proc. 4th IAHR Europe Congress*, Liege, Belgium.

Oertel, M. and Tullis, B.-P. (2014). Comparison of Piano Key Weir Discharge Coefficients from experimental and numerical models. *Proc. 3rd IAHR Europe Congress*, Porto, Portugal.

Ouamane, A. and Lempérière, F. (2013). PK Weir, Design of a New Economic Shape Of Weir *Dams, Piano Keys Weirs, Tidal Energy & Energy Storage.*, http://www.hydrocoop.org/pk-weir-design-new- economic-shape-of-weir.

Pralong, J., Vermeulen, J., Blancher, B., Laugier, F., Erpicum, S., Machiels, O., Pirotton, M., Boillat, J. L., Leite Ribeiro, M., and Schleiss, A. J. (2011). A naming convention for the Piano Key weirs geometrical parameters. *Proc. 1st Workshop on Labyrinth and Piano Key Weirs,* PKW 2011, Liege, Belgium.

Ribeiro, M. L., Pfister, M., Schleiss, A. & Boillat, J.-L. (2012). Hydraulic design of A-type Piano Key Weirs. *J. Hydr. Res.*, 50(4), 400–408.

DOI:10.15142/T30P4R

Numerical investigation of the pressure on a round crested weir

L. Goffin[1], S. Erpicum[1] P. Archambeau[1], B. J. Dewals[1] and M. Pirotton[1]
[1]HECE, ArGEnCo
University of Liege (ULg)
Liège, Belgium
E-mail: l.goffin@ulg.ac.be

ABSTRACT

Understanding the pressure distribution on round crested weir can help to improve their design. In this frame, we propose a finite difference method for irrotational flows. Our method, based on a previous work, determines the free surface iteratively. For best results, the computation of the velocity at the free surface is done by a bi-dimensional function fitting. Knowing the velocity, the elevation and a reference energy level, the pressure can be derived. The evolution path is determined by numerical derivatives of the pressure at the surface. The iterative method is tested on a subcritical flow. The pressure computation is compared to experimental measurements of the pressure on a spillway crest (trans-critical flow). Both results are very encouraging: the free surface moves smoothly to an equilibrium state and the pressure on the structure is very close to experiment. For this last point, the method is also able to faithfully reproduce pressure drops.

Keywords: *Finite difference, Spillway, free surface, potential flow*

1. INTRODUCTION

Spillways are important structures that should provide sufficient safety during flood events. Understanding their behavior for discharges higher than design ones is a key point for innovative design and safer structures. To do so, experimental and numerical investigations should be led in parallel for collecting specific information about these structures. This paper focuses on the implementation of a new numerical method that aims to determine quickly the free surface position, velocity and pressure fields for trans-critical flows.

In hydraulics, the Finite Volumes Method (FVM) is traditionally used to simulate free-surface flows. However it doesn't allow to compute directly the pressure on the structure due to the assumptions directly linked to this method. Numerical methods such as Finite Elements (FE) (Chatila & Tabbara 2004), Smoothed Particle Hydrodynamics (SPH) (Goffin 2013; Goffin et al. 2016; Lodomez 2014; Lodomez et al. 2014) and Particle Finite Elements (PFEM) (Larese et al. 2008) implemented in 3-D or 2-D vertical slices can handle flows over round crested weirs with information about the pressure on the structure. However they require a large amount of computing resources in order to handle accurately the flow pattern at the interface with the structure. For ordinary desktop computers, a computation for a single discharge may reach several hours. Thus, optimizing a weir profile would require too many time with such methods.

A need for simpler and quicker methods is obvious. Castro-Orgaz (2013) solves the problem using a potential flow assumption. Equations are solved in the non-physical (x,ψ), where x is the horizontal direction and ψ the stream function. A more natural way would be to express the problem in the physical spatial plane (x, z). The method presented in this paper enhances the one introduced in Goffin et al. (2014) where the potential flow is solved in a physical plane (x,z). First, improvements from Goffin et al. (2014) method will be presented. Then, test cases and practical examples are explained for a bump and a flow over a round crested weir.

2. NUMERICAL METHOD

The method developed here is based on the assumption that the flow is irrotational. This was proved by Escande (1937) for flows over spillways. The Laplacian $\Delta = \nabla^2$ of the potential ϕ or the stream function ψ can be solved in such cases. The resulting field, once derived, yields to a velocity field.

Thanks to the energy conservation principle, the pressure p at a given point can be deduced for a given energy level E :

$$E = z + \frac{p}{\rho g} + \frac{\|\vec{u}\|^2}{2g} \tag{1}$$

where z is the altitude, ρ the density, g the acceleration of gravity and $\vec{u}$ the velocity vector.

The domain is discretized by using the finite difference approach. Irregular nodes are created at boundaries in order to represent accurately their geometry. Irregular nodes result from the intersection between the boundary contour and the grid lines. Regular nodes are created at the intersection of grid lines for the inner domain. An example of discretization is depicted in Figure 1.

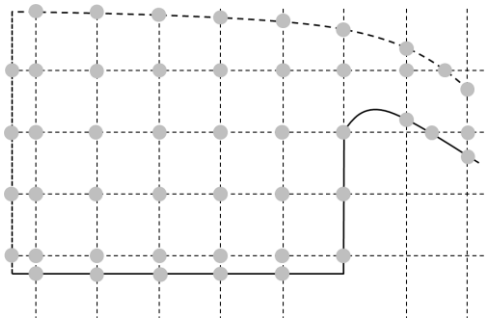

Figure 1: Schematic discretization of the computation domain

2.1. First approach and drawbacks

In Goffin et al. (2014), the Laplacian solved was based on the potential :

$$\Delta^2 \phi = 0 \tag{2}$$

This approach required to impose Neumann boundary conditions (BC), i.e. the value of a derivative is imposed at the boundary, for free surface and impervious boundaries. This was achieved by using the Green-Gauss theorem to compute derivatives at these boundaries. It led to a good approximation of the velocity at the boundary but some oscillations could be observed.

Determining the free surface requires iterations on the position of free surface nodes. This was done thanks to an approach based on curvilinear coordinates developments (Stilmant et al. 2013). The evolution of the pressure with the water depth dp/dH was linked to properties related to curvilinear cross sections and velocity profiles. The evolution of depth for each surface node ΔH was given by

$$\Delta z = \gamma \frac{p_{i+1} - p_i}{\frac{dp}{dH}} \tag{3}$$

with γ a relaxation coefficient. The derivative at the denominator is close to zero in the region of the critical section. This led to some instabilities in that area.

Main drawbacks of this method included:

- Oscillations due the velocity evaluation at boundaries
- Instabilities near the critical section
- Pressure evaluation at the free surface could present oscillations due to the velocity evaluation

2.2. New approach

The new approach described in this section aims to reduce previous method problems. The first problem that was tackled is the evaluation of velocity at boundaries. To do so, The Laplacian is now solved for the stream function ψ :

$$\nabla^2\psi = \frac{\partial^2\psi}{\partial x^2} + \frac{\partial^2\psi}{\partial z^2} \tag{4}$$

Only Dirichlet BC are now required which avoids to use a Green-Gauss derivative evaluation (Goffin et al. 2014) which led to approximations at the boundary. Velocities computed on the outer limits should be more accurate now using an imposed value for the unknown.

The second derivative is discretized according to a finite difference scheme on an irregular grid (see Figure 2):

$$\begin{aligned}\frac{\partial^2\psi}{\partial x^2} &\approx \frac{2}{a_1(a_1+a_2)}\psi_{i-1} - \frac{2}{a_1a_2}\psi_i + \frac{2}{a_2(a_1+a_2)}\psi_{i+1}\\ \frac{\partial^2\psi}{\partial z^2} &\approx \frac{2}{b_1(b_1+b_2)}\psi_{j-1} - \frac{2}{b_1b_2}\psi_j + \frac{2}{b_2(b_1+b_2)}\psi_{j+1}\end{aligned} \tag{5}$$

Where a_k are relative to horizontal distances and b_k are relative to vertical distances between nodes.

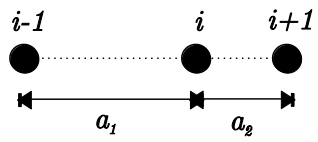

Figure 2 : Discretization scheme for a horizontal second derivative

When distances between nodes are equal, the discretization scheme has second order precision, while it is first order when nodes are not regularly spaced (Hirsch 2007).

After the computation of a given state, the velocities are evaluated for the inner nodes as a derivative of the stream function:

$$\vec{u} = \begin{pmatrix} u \\ v \end{pmatrix} = \begin{pmatrix} \dfrac{\partial\psi}{\partial z} \\ -\dfrac{\partial\psi}{\partial x} \end{pmatrix} \tag{6}$$

These derivatives are evaluated thanks to centered finite differences. For the nodes located on the boundaries, velocities are computed thanks to an interpolation from inner nodes. For a given boundary node, inner neighbors within a radius *r* are considered. The value

$$f_{i,j} = z_{i,j} + \frac{\left\|\vec{u}_{i,j}\right\|^2}{2g} \tag{7}$$

is computed for each of these nodes. Then, a bi-dimensional function is fitted by least squares on this set of points:

$$f(x,z) = c_1x^2 + c_2x + c_3z^2 + c_4z + c_5x^2z^2 + c_6x^2z + c_7xz^2 + c_8xz + c_9 \tag{8}$$

When coefficients c_i are determined, the value *f* of equation (7) can be computed using (8) for the boundary node. This method avoids velocity discontinuities at boundaries. Then, the pressure can be determined by means of (1) and a reference energy level *E*.

The approach adopted here for the free surface evolution is different from the previous paper. It is based on a Taylor development, second order accurate:

$$p_{i+1} = p_i + \frac{dp}{dH}\Delta z + \frac{1}{2}\frac{d^2 p}{dH^2}\Delta z^2 + O\left(\Delta z^3\right) \tag{9}$$

First, a classical Newton-Raphson approach (first order accurate) (Ypma 1995) is implemented by using only the first derivative:

$$\Delta z = \frac{p_{i+1} - p_i}{\frac{dp}{dH}} \tag{10}$$

Obviously, it can lead to indeterminate solution if $dp/dH = 0$. This is the case at the critical section. Nodes close to it are subject to large displacements since the pressure derivative is close to 0.

In order to avoid too large displacements of the free surface, a relaxing factor was used to limit displacements to a tenth of the discretization step. This relaxing factor was applied for the whole free surface.

Compared to a classical Newton-Raphson iteration scheme, solving the quadratic function (9) avoids to have infinite Δz since a second derivative is present. Equation (9) can be solved to find Δz that should be applied to free surface nodes:

$$\Delta z_{1,2} = \frac{-\frac{dp}{dH} \pm \sqrt{\left(\frac{dp}{dH}\right)^2 - 2\frac{d^2 p}{dH^2}\left(p_i - p_{i+1}\right)}}{\frac{d^2 p}{dH^2}} \tag{11}$$

The first root (+) was found to be the solution for supercritical flows and the second root (-) was found to be the one for subcritical flows.

In equations (10) and (11), first and second derivatives are evaluated numerically. Traditionally, this would require moving each node independently, leading to a large amount of intermediate computations. The method chosen in this approach is hybrid and consists in moving vertically the whole free surface by an increment ε. Derivatives are computed by moving the free surface upward and downward:

$$\begin{aligned} \frac{dp}{dH} &\approx \frac{p\left(H+\varepsilon\right) - p(H-\varepsilon)}{2\varepsilon} \\ \frac{d^2 p}{dH^2} &\approx \frac{p\left(H+\varepsilon\right) - 2p\left(H\right) + p(H-\varepsilon)}{\varepsilon^2} \end{aligned} \tag{12}$$

For subcritical and supercritical flows, the energy level and the pressure to reach are given as parameters. When the flow is transcritical, the energy level is set by the critical section (Castro-Orgaz & Montes 2015). This critical section tends to minimize the specific energy of the flow. The critical section can be determined by spotting the section were $dp/dH = 0$ and where the specific energy is minimized. Since the total energy of the flow is set by the user, the pressure at the critical section represents the target pressure that all nodes has to reach, which is p_{i+1} in (10) and (11).

3. TEST CASE

The test case in this section show first results of the currently implemented method for a subcritical flow on a bump. The bump has equation $0.3\left(1-x^2\right)$ in the range $\left[-1;1\right]$ m. In the range $\left[-5;-1\right[\cup \left]1;5\right]$ m, the bottom is

flat and at the altitude 0 m. The domain is discretized with a fine 2×2 mm² grid in order to concentrate on the results of the iterative method and not on the effects linked to a rough discretization.

The initial condition is a horizontal free surface set at 0.47 m. The target pressure is 0 m and the energy level is imposed at 0.4723 m. An analytical solution was computed. It considers a uniform vertical velocity profile and the energy is conserved on all free surface points. Given the energy conservation equation (1), a water level can be derived. The uniform vertical velocity profile assumption is not in total agreement with the model implemented here. Some differences may be noticed. The velocity and pressure on the free surface were computed according to the fit of function (8) and neighbors were taken in a radius $r = 8\Delta x$. The problem was solved with equation (10) leading to results given in Figure 3 where the initial condition as well as the final solution obtained by the model are depicted.

It can be seen that the free surface resulting from the computation fits closely the analytical solution in shape and in values. However, this analytical solution is computed for a uniform velocity profile, which is not representative above the bump. This inconsistence can be noticed in the rightmost plot in Figure 3.

These encouraging results show that this method is able to move a free surface. It should also be tested on different flow regimes.

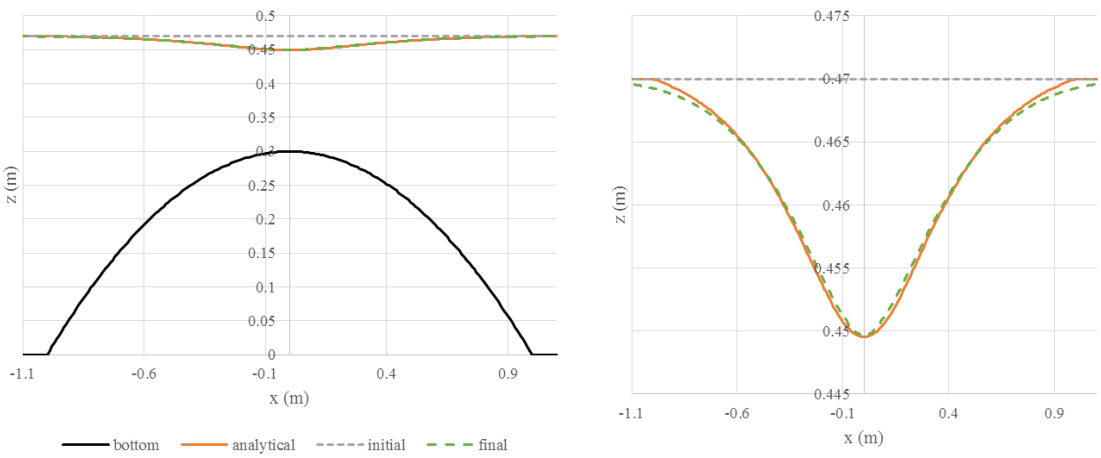

Figure 3: Free surface position for a subcritical flow over a bump

4. PRESSURE PROFILE ON A ROUND CRESTED WEIR

Once a free surface profile is determined, velocity fields and pressure fields can be computed. This section is focusing on the determination of the pressure on the structure with a free surface profile measured experimentally.

An experimental campaign was led about pressure diagrams on WES (USACE 1987) round crested weir for high head ratios (H / H_d), with a design head H_d = 15 cm. Numerical simulations were led for a domain spreading from the reservoir to the spillway itself. Results shown in Figure 4 were computed for $H / H_d = 2$ and are focusing only on the weir crest. Very good agreement between experimental measures and numerical results can be observed. This figure shows that the method implemented is able to faithfully reproduce the pressure on a weir crest. Even pressure drops can be reproduced with a high level of fidelity.

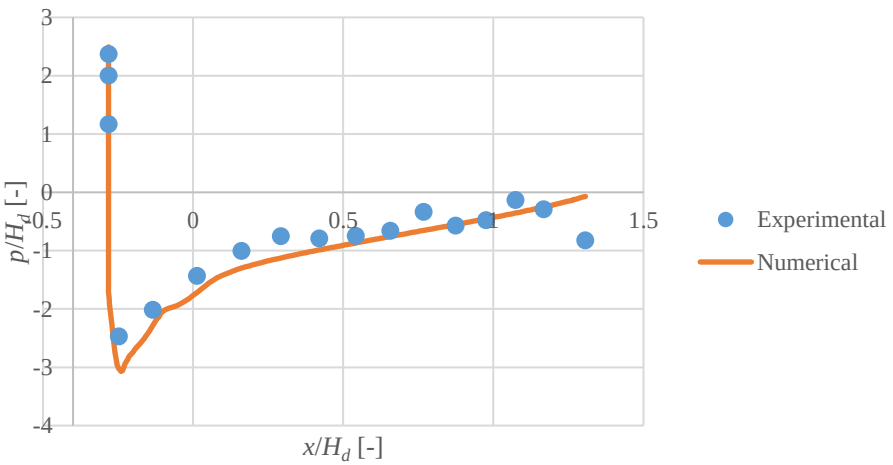

Figure 4: Comparison between experimental measurements and numerical computation of the pressure on a WES weir crest

5. CONCLUSIONS

In this paper, we presented an original method which goal is to determine the free surface profile of irrotational flows. This work was based on first developments presented in Goffin et al. (2014). Improvements were presented in order to reduce drawbacks noticed in the previous approach.

The Newton-Raphson scheme was successfully tested on a subcritical flow over a bump. A more advanced method was also proposed in order to deal with transcritical flows.

With a given free surface, the method showed that it was able to faithfully reproduce the pressure diagram on a round crested weir.

Further developments should focus on transcritical flows and the critical section issue. In this frame the second order method should bring benefits.

6. REFRENCES

Castro-Orgaz, O., 2013. Potential flow solution for open-channel flows and weir-crest overflow. *Journal of Irrigation and Drainage Engineering*, 139(7), pp.551–559.

Castro-Orgaz, O. & Montes, J.S., 2015. Minimum specific energy in open-channel flows: the Salas–Dominguez contribution. *Journal of Hydraulic Research*, 53(2), pp.151–160.

Chatila, J. & Tabbara, M., 2004. Computational modeling of flow over an ogee spillway. *Computers & structures*, 82(22), pp.1805–1812.

Escande, L., 1937. *Barrages* H. & Cie, ed., Hermann & Cie.

Goffin, L., 2013. *Development of a didactic SPH model*. University of Liege.

Goffin, L. et al., 2014. How to simulate quickly and efficiently a flow over a spillway? In *5th IAHR International Junior Researcher and Engineer Workshop on Hydraulic Structures*.

Goffin, L. et al., 2016. Validation and Test Cases for a Free Surface SPH Model. In *Advances in Hydroinformatics*. Springer, pp. 175–187.

Hirsch, C., 2007. *Numerical computation of internal and external flows: The fundamentals of computational fluid dynamics* E. Ltd, ed., Butterworth-Heinemann.

Larese, A. et al., 2008. Validation of the particle finite element method (PFEM) for simulation of free surface flows. *Engineering Computations (Swansea, Wales)*, 25(4), pp.385–425.

Lodomez, M. et al., 2014. Comparison between Experimental and SPH Models over a Sharp-crested Weir. In *5th IAHR International Junior Researcher and Engineer Workshop on Hydraulic Structures*.

Lodomez, M., 2014. *Determining the characteristics of a free jet in 2-D by the SPH method*. University of Liège.

Stilmant, F. et al., 2013. Depth-averaged flow modeling in curvilinear coordinates. In *2013 IAHR World Congress*.

USACE, 1987. *Hydraulic design criteria*,

Ypma, T.J., 1995. Historical Development of the Newton-Raphson Method. *SIAM Review*, 37(4).

DOI:10.15142/T3D01F

Prediction of Hydraulic Jump location in Some Types of Prismatic Channels using Numerical Modelling

M. A. Hafnaoui [1,2], R. F. Carvalho[3] and M. Debabeche[1]
[1]Research Laboratory of Civil Engineering, Hydraulics, Environment and Sustainable Development, - LARGHYDE -
University of Biskra
Biskra, Algeria
[2]Scientific and Technical Research Center on Arid Regions - CRSTRA -
Biskra, Algeria.
[3]MarineandEnvironmentalSciences Centre – MARE -
Universityof Coimbra
Coimbra, Portugal
E-mail: hafnaoui.amine@crstra.dz

ABSTRACT

The numerical modelling of free surface flows is important to understand their behaviour and predict undesired situations that may occur, as formation and location of hydraulic jump within irrigation channels. The Saint-Venant equations are most commonly used for practical modelling of this type of flows. There are many methods and numerical schemes used for the solution of these equations. The extension TVD plays an important role in minimizing the oscillations of the flow in the channels. In our work we used MATLAB® as a programming tool to develop a model based on 1D Saint-Venant equations and the MacCormack finite difference method with TVD extension scheme and after its validation we used it to calculate flow depth, velocity and predict the location of the hydraulic jump which is formed in prismatic sloped channels with different sections, such as rectangular and triangular sections.
Based on experimental trials at *LARHYSS laboratory, University of Biskra, Algeria that allowed us to impose different upstream water depth and velocity (Froude number), downstream water depth as well as hydraulic jump locations, we were able to analyse the accuracy of the model to locate the hydraulic jump in triangular channels knowing the upstream and downstream depths. We present a matrix of flows ranging Froude numbers from 3 to 8, initial depth from 0.035 m to 0.05 m and velocities from 1.3 m/s to 4.5 m/s. Results of locations, as expected are better similar to experimental conditions for low slopes, the changing of slope and Froude number has an effect on its prediction uncertainty that can be estimated by a relation provided in this work.*

Keywords: *Saint-Venant equations, hydraulic jump, triangular channels, MacCormack scheme, free surface flows*

1. INTRODUCTION

In irrigation systems several sills and gates are placed and measures of flow depth are fundamental to their management. Triangular channels allow the discharge prediction more accurately compared to rectangular channels, which are much more sensitive to water depth measurement.
A hydraulic jump is formed whenever flow changes from supercritical to subcritical flow. In this transition, water surface rises abruptly, surface rollers are formed, intense mixing occurs, air is entrained, and energy is dissipated (Gharangik and Chaudhry 1991). The dissipation capacity of a hydraulic jump evolving in a triangular channel is larger than that of a hydraulic jump evolving in a rectangular or trapezoidal channel, (Hager and Wanoschek 1987). Several researchers studied the hydraulic jump properties and location in recent years in horizontal rectangular channels (Hager and Bretz 1987; Hager 1992; Ead and Rajaratnam 2002; Carvalho et al. 2008; Chanson, 2009; Chanson and Carvalho 2015), in horizontal triangular channels (Hager and Wanoschek 1987; Achour and Debabeche 2003; and Debabeche and Achour 2007) and in a sloped triangular channel (Debabeche et al. 2009).
The hydraulic jump is formed at a location where the specific forces on both sides of the jump are equal. The hydraulic jump location and properties can be determined using continuity and momentum considerations. Chow (1959) computed the water surface profiles for supercritical flow in a channel, starting from the upstream end, and the subcritical flow starting from the downstream end. Mc-Corquodale and Khalifa (1983) used the strip-integral method to compute the jump length, water surface profile, and pressures at the bottom. To solve the Saint-Venant equation numerically, Abbott et al. (1969) used a finite-difference method and

Katopodes (1984) used the finite-element method (Gharangik and Chaudhry 1991). Garcia-Navarro et al. (1992) applied high-resolution MacCormack scheme TVD Saint-Venant equations to simulate unsteady flows in several applications. However the simulation of the hydraulic jump was always in low slopes or when there was a sudden decrease in the bottom slope.

The present study aims to analyse the location of a hydraulic jump predicted in a sloped triangular channel by the model based on 1D Saint-Venant equations for free surface flows. We used a high-resolution Mac Cormack scheme TVD to simulate hydraulic jumps location in channel up to slopes of 5 %. The work comprised more than 90 experimental hydraulic jumps in the laboratory which were reproduced with numerical simulations.

Every hydraulic jump in experimental conditions was formed on the apron by testing several different downstream water depths h_2, setting specified sill height S, and adjust flow *Q*. (Figure 1a) shows the characteristics of hydraulic jump; h_1 is the upstream water depth measured at the toe of hydraulic jump, h_2 is the downstream water depth measured at the maximum surface level, α is the angle of inclination of the channel relative to the horizontal, *Lj* is the length of the hydraulic jump measured from the toe of the hydraulic jump to the section where maximum surface level occurs. The hydraulic jump is located at the upstream of the channel for the channel downstream depth h_2. If the channel downstream depth h is less than h_2, the hydraulic jump moves downstream (Figure 1b). However, the jump is pushed back as shown in (Figure 1c) if the channel downstream depth is higher than h_2 (Chaudhry 2008). In experimental conditions position can be settled by adjusting flow.

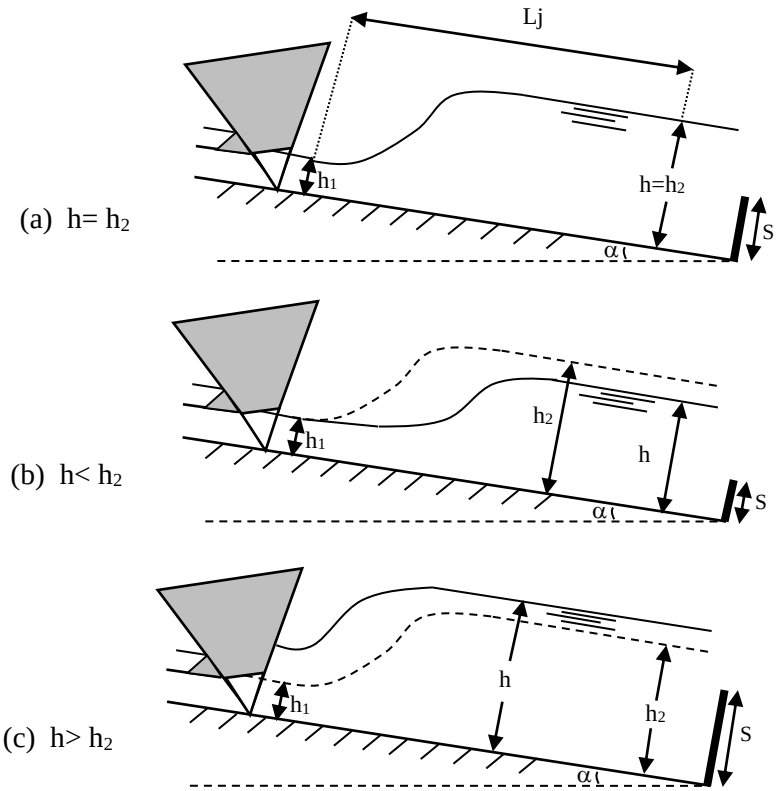

Figure 1. Location of hydraulic jump scheme

Next section presents the description of the experimental tests in the laboratory, the governing equations and numerical scheme used to simulate the hydraulic jumps. Section 3 presents and discusses the results of the numerical simulations in rectangular and triangular channels for different slopes as it was founded that numerical simulation doesn't predict accurately the hydraulic jump location for all hydraulic jump tests. The main conclusions are presented in Section 4.

2. METHODOLOGY

2.1. Description of the experimental model and tests

The experiments of hydraulic jump were made at the Research Laboratory in Subterranean and Surface Hydraulics (LARHYSS) of the Hydraulic Department of University of Biskra. The rectangular channel was 7 m long and 0.295 m wide (Debabeche 2003) and the triangular channel was symmetrical with 3 m long and a triangular cross section with the bottom angle of 90°. A circular pipe of 0.115 m diameter connected the channel with pressure box, on which was inserted a pressure convergent of triangular cross section opening directly into the channel. The role of the pressure convergent was to generate the flow at high velocity as shown in Figure 2. The Figure 3 shows a general view of the triangular channel and in Figure 4 an aspect of the hydraulic jump in the slopped triangular channel for (F_1= 6.32 ; s = 0.22 m ; Lj = 1.22 m ; h_2 = 0.1882 m, tang(α) = 0.05).

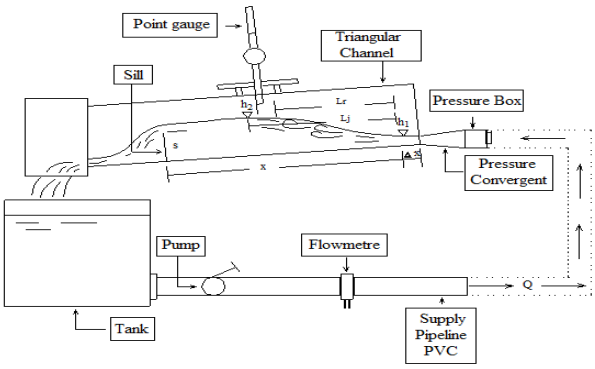

Figure 2. Experimental model

Figure 3. General view of the experimental channel

Figure 4. Hydraulic jump in a sloped triangular channel

The experimental study was conducted in three initial upstream water depth h_1 = 0.035, 0.04 and 0.05 m. For each chosen upstream water depth, h_1, there were six different slopes tested characterized by tang(α) = 0 %, 1 %, 2 %, 3 %, 4 % and 5 %. A large range of Froude number F_1 from 3 to 8 was tested.

The flow was measured by a rectangular weir, connected with the triangular channel with its downstream part described by the following equation: $Q = 0.3794B(2g)^{0.5}\,\beta(1+0.16496\beta^{2.0716})^{1.5}h^{1.5}$, obtained by Hachemi (2006) where B is the width of the channel and β is the form ratio coefficient. The water depth in the channel was measured by a level indicator (limnimeter). The water level measurement range can be set to ± 0.01 m. The Froude number is calculated from the following universal relation: $F_1^2 = 2Q^2(gm^2h_1^5)^{-1}$ valid for a symmetrical triangular channel, where m is the cotangent of the angle of inclination of the channel.

2.2. Governing Equations and Numerical Scheme

The Saint-Venant equations (1871) represented by the mass and the momentum conservation equations are used for modeling non-stationary flows in gradually and rapidly varied flow at free surface, (Maher 2009). The Saint-Venant equations for one-dimensional flow can be written as follows:

$$\frac{\partial A}{\partial t} + \frac{\partial Q}{\partial x} = 0 \tag{1}$$

$$\frac{\partial Q}{\partial t} + \frac{\partial}{\partial x}\left(\frac{Q^2}{A} + gI_1\right) = -gAs - gAJ + gI_2 \tag{2}$$

where x is the distance along the channel bed, t is the time, A is the flow area, Q is the flow in the x-direction, I_1 is the pressure force, I_2 is the pressure forces due to longitudinal width variations, g is the gravitational acceleration, s is the channel bed slope and J is the friction slope. They are valid for horizontal and low slope, as the pressure distribution is considered hydrostatic, the fluid is incompressible, and the velocity is assumed constant in the section.
The friction slope can be expressed using the Manning's equation as:

$$J = \frac{|Q|Q}{K_S^2 A^2 R^{4/3}} \tag{3}$$

where K_s is the Strickler's roughness coefficient; and R is the hydraulic radius. The MacCormack scheme is an explicit finite difference method which belongs to the class of methods called fractional step method. It resulted from changes in the methods of two steps based on the expansion of second order Taylor series, specifically in the method of Lax Wendroff, this scheme guarantees the approximation in second order in space and time (Carmo 2009). For the application of the MacCormack scheme, the Saint-Venant equations could be written as:

$$\frac{\partial U}{\partial t} + \frac{\partial F}{\partial x} = S \tag{4}$$

with

$$U = \begin{Bmatrix} A \\ Q \end{Bmatrix} \qquad F = \begin{Bmatrix} Q \\ \frac{Q^2}{A} + gI_1 \end{Bmatrix} \qquad S = \begin{Bmatrix} 0 \\ -gAs - gAJ + gI_2 \end{Bmatrix} \tag{5}$$

The MacCormack scheme is explicit and applied with two-step: initially a calculation based on the values of variables in the previous time (predictor) and then a correction step based on the predicted values (corrector). The accuracy of the second order is guaranteed by the discretization in two symmetrical steps.

Predictor:

$$U_i^{(1)} = U_i^n - \frac{\Delta t}{\Delta x}\left[F_{i+1}^n - F_i^n\right] + \Delta t S_i^n \tag{6}$$

Corrector:

$$U_i^{n+1} = \frac{1}{2}\left[U_i^n + U_i^{(1)} - \frac{\Delta t}{\Delta x}\left(F_i^{(1)} - F_{i-1}^{(1)}\right) + \Delta t S_i^{(1)}\right] \tag{7}$$

For the stability of The MacCormack scheme, as of other explicit methods, it is necessary to check the Courant-Friedrichs-Lewy (CFL) condition:

$$\Delta t = C_n \frac{\Delta x}{max(|U| + \sqrt{gy})} \tag{8}$$

where C_n is Courant number and y is hydraulic depth. The resolution of Saint-Venant equations using MacCormack scheme can generate numerical oscillations. To reduce these oscillations, an extension of high-resolution based on the theory of the Total Variation Diminishing TVD could be introduced into the MacCormack method, which leads to a more robust model. The TVD extension on the MacCormack method can be written as:

$$U_i^{n+1} = U_i^{(2)} + \left(\tilde{R}_{i+\frac{1}{2}}\tilde{D}_{i+\frac{1}{2}} - \tilde{R}_{i-\frac{1}{2}}\tilde{D}_{i-\frac{1}{2}}\right) \tag{9}$$

where $\tilde{R}$ is the right-eigenvector matrix corresponding to the approximated Jacobian, and $\tilde{D}$ is a scheme dependent vector function. Details could be founded in (Garcia-Navarro et al. 1992) work who studied the role of TVD-MacCormack scheme for the reduction of oscillations resulting from the classical method of

MacCormack. This study was done in rectangular and trapezoidal channels with slope and the presence of hydraulic jump, after a comparison between a classical scheme of MacCormack and extension TVD, the results showed an effectiveness to minimize the oscillations by TVD- MacCormack scheme.

2.3. Model validation and application to study hydraulic jump characteristics

MATLAB® Model was developed based on 1D Saint-Venant equations and the MacCormack finite difference scheme with TVD extension described above, was validated with literature data "benchmarkdata" (Mendes, 2001) and was used to simulate a large range of hydraulic jumps tested in the laboratory. Figure 5 shows the numerical results of the flow $Q = 0.18$ m^3/s in a rectangular channel of 25 m length with water depth $h_1 = 0.33$ m over an obstacle which induce a subcritical-supercritical-subcritical regime (t = 100 s and Δx = 0.1 m). The comparison of the analytical and numerical solutions shows that the results are similar. It is noticed an insignificant difference in the change of the super to sub-critical regime.

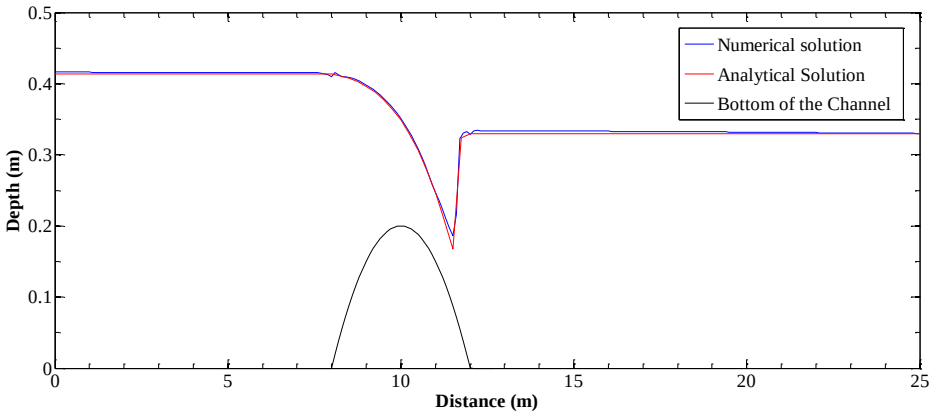

Figure 5. Numerical simulation of flow over an obstacle

The selected tested simulations are presented in Table1 for the rectangular channel and in Table 2 for the triangular channel. Tables 1 and 2 shows the main characteristics of the hydraulic jumps accordingly the experimental tests and the results of hydraulic jump location simulated with the presented model. The model allowed quantifying uncertainty of the simulation results reproducing hydraulic jumps. Courant number used in the simulations varied from 0.2 ($F_1 > 7$) and 0.5 ($F_1 = 3$).

Table 1: Hydraulic jump in rectangular channel simulations

Slope: s = 0.00; mesh: dx = 0. 1 m; time test: t = 60 s; Coefficient of roughness: $K_s = 100\ m^{1/3}s^{-1}$							
results from experimental tests						*results from numerical model*	
Experiment number	***Flow Q (m^3/s)***	***Froude number F_1***	***upstream water depth h_1 (m)***	***downstream water depth h_2 (m)***	***sequentdepths ratio $Y = h_2/h_1$***	***Location of h.jumpLc (m)***	***Lc/L***
1	0.02527	3.42	0.040	0.1859	4.65	0.1	0.014
2	0.02737	5.70	0.030	0.2390	7.97	0.1	0.014
3	0.01869	7.15	0.020	0.1914	9.57	0.1	0.014

Table 2: Hydraulic jump in triangular channel simulations

mesh : dx = 0.1 m; time test : t = 60 s; Coefficient of roughness: $K_s = 100\ m^{1/3}s^{-1}$								
results from experimental tests							*results from numerical model*	
Experiment number	***Slope s***	***Flow Q (m^3/s)***	***Froude number F_1***	***upstream water depth h_1 (m)***	***downstream water depth h_2 (m)***	***sequentdepth s ratio $Y = h_2/h_1$***	***Location of h. jump Lc (m)***	***Lc/L***
1	0.00	0.00278	3.92	0.040	0.1038	2.60	0.6	0.2069
2	0.00	0.00227	4.48	0.035	0.1013	2.89	0.3	0.1034
3	0.00	0.00327	6.44	0.035	0.1339	3.83	0.1	0.0345
4	0.00	0.00868	7.01	0.050	0.2013	4.03	0.1	0.0345
5	0.00	0.00991	8.00	0.050	0.2213	4.43	0.1	0.0345

6	0.02	0.00342	2.76	0.05	0.1537	3.07	0.3	0.1034
7	0.02	0.00457	3.69	0.05	0.1730	3.46	0.3	0.1034
8	0.02	0.00311	4.39	0.04	0.1502	3.76	0.7	0.2414
9	0.02	0.00390	5.50	0.04	0.1670	4.18	0.8	0.2759
10	0.02	0.00281	5.53	0.035	0.1403	4.01	1.1	0.3793
11	0.02	0.00378	7.45	0.035	0.1722	4.92	0.8	0.2759
12	0.05	0.00373	3.01	0.05	0.1451	2.90	2.1	0.7241
13	0.05	0.00469	3.78	0.05	0.1681	3.36	1.8	0.6207
14	0.05	0.00292	4.12	0.04	0.1458	3.65	1.9	0.6552
15	0.05	0.00581	4.69	0.05	0.2001	4.00	1.5	0.5172
16	0.05	0.00726	5.87	0.05	0.2404	4.81	1.3	0.4483
17	0.05	0.00424	5.98	0.04	0.1764	4.41	1.7	0.5862
18	0.05	0.00337	6.65	0.035	0.1757	5.02	1.5	0.5172
19	0.05	0.00581	8.20	0.04	0.2215	5.54	1.4	0.4828
20	0.05	0.00433	8.52	0.035	0.2042	5.83	1.4	0.4828

3. RESULTS AND DISCUSSION

3.1. Location of hydraulic jump predicted through numerical simulations

In this part the numerical simulation in rectangular and triangular horizontal channels is presented, and the location of the hydraulic jump in a triangular channel with different slopes is analyzed. Figures 6 and 7 illustrate the hydraulic jump profile obtained by the simulations of horizontal rectangular and triangular channels, respectively.

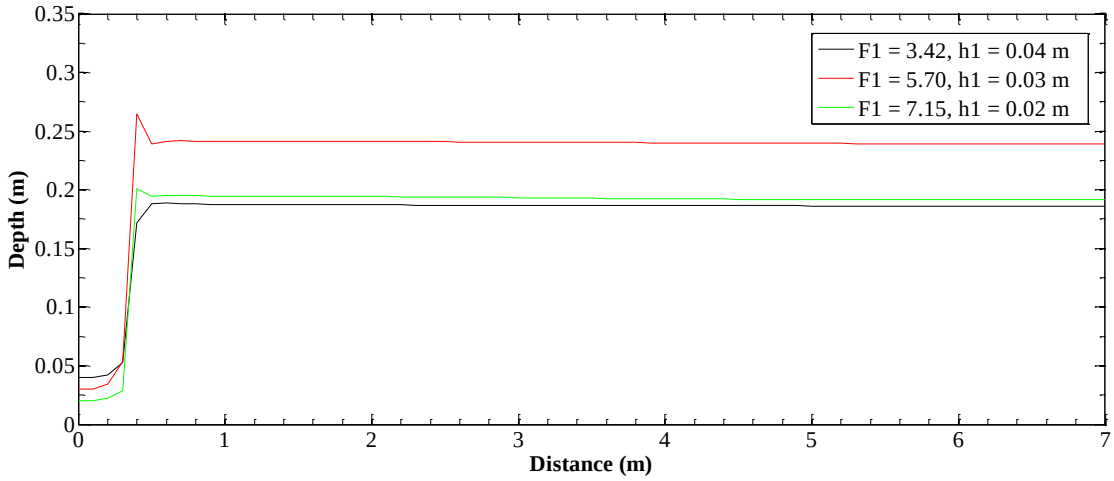

Figure 6. Hydraulic jump profile in a rectangular section channel predicted by numerical simulations (s = 0)

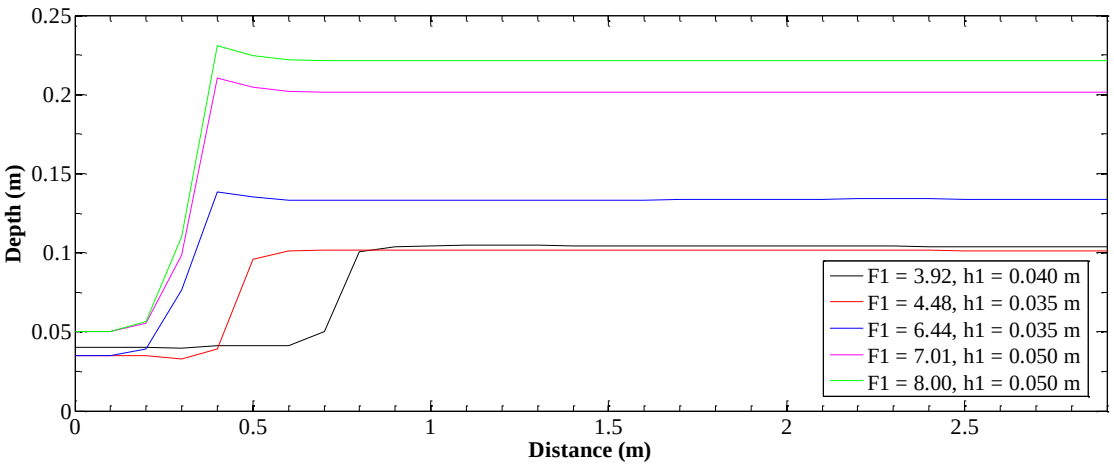

Figure 7. Hydraulic jump profile in a triangular section channel predicted by numerical simulations (s = 0)

Analysing these results, we can remark the following:

- For the rectangular section the location of hydraulic jump is placed upstream as was observed in experimental tests.
- For the triangular section and for high Froude number the location of the hydraulic jump is placed in upstream of channel; however for low Froude numbers, at the simulation 1 ($F_1 = 3.92$, $h_1 = 0.04$) and 2 ($F_1 = 4.48$, $h_1 = 0.035$), the location of hydraulic jump is previewed slightly downstream.

The prediction of the location of the hydraulic jump in a triangular channel with variable slope using Saint-Venant equation are illustrated in Figures 8 and 9. In our numerical simulations we chosed the slope 0.02 and 0.05. As initial conditions it was used the flow Q and the upstream water depth h_1, and we imposed the boundary condition downstream water depth equal to h_2. It was fixed two first points in the upstream and two last points in the downstream of the channel to give the model more rigidity, the time test t = 60 s and Δx = 0.1 m.

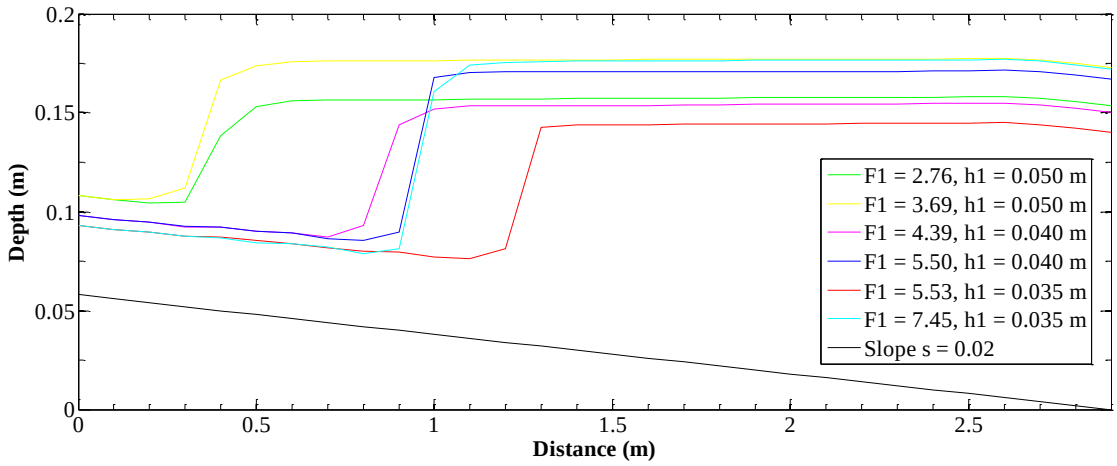

Figure 8. Hydraulic jump profile in triangular section channel predicted by numerical simulation (s = 0.02)

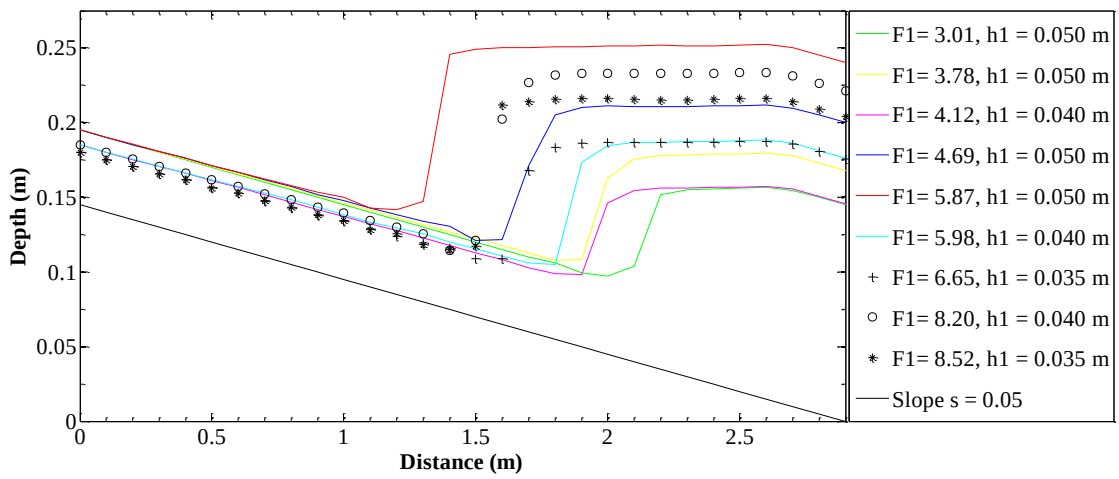

Figure 9. Hydraulic jump profile in triangular section channel predicted by numerical simulation (s = 0.05)

It is noticed that the hydraulic jump takes different locations in the channel. In the horizontal slope most the locations of the hydraulic jump are in the upstream of the channel as settled in experimental conditions, as well as, for hydraulic jump with small Froude numbers with slope equal to 0.02. However for larger Froude numbers the hydraulic jump moves downstream. Whenever the slope increases the hydraulic jump moves more downstream. This can be returned to the validity of the Saint-Venant equations for low slopes and also to the measurement of the downstream water depth h_2.

It was observed in the experimental tests, for larger slopes and large Froude numbers, that was difficult to measure the downstream water depth h_2 accurately, because the free surface flow is not constant and may increase slightly to downstream given underestimate downstream water depth, h_2 (h_2 measurements are ± 0.01 m accurately). We then increased downstream water depth h_2 to settle the hydraulic jump in the upstream of the channel, as verified in experimental conditions, and we studied the relation between the numerical simulation

imposed downstream water depth h_2 (h_2 simulated) which gives the hydraulic jump location in channel upstream extremity and other characteristics of the hydraulic jump.

3.2. Relation between h_2 and the location of hydraulic jump

Figure 10 shows the variation of the sequent depths ratio simulated and experimental depending to Froude number F_1 for slopes 0.02 and 0.05. Relations between the sequent depths ratio Y_{sim} and Y_{exp} with Froude number F_1 and slope s were founded. The relations obtained are shown in the Figure 11 are following: Eq. (10) variation of the sequent depths ratio Y_{sim} depending on Froude number F_1 and slope, Eq. (11) variation of the sequent depths ratio Y_{exp} depending on Froude number F_1 and slope.

$$\frac{h_{2\,sim}}{h_1} = a + bF_1 + cF_1{}^2 + \frac{d}{tg\alpha} \tag{10}$$

where a = 3.3622, b = 0.9703, c = –0.0582 and d = –0.0432; with r^2 = 0.97

$$\frac{h_{2\,exp}}{h_1} = a + bF_1 + cF_1{}^2 + \frac{d}{tg\alpha} \tag{11}$$

where a = 1.5254, b = 0.5869, c = –0.0078 and d = –0.0083; with r^2 = 0.93

These relations could give the difference between downstream water depth, the h_{2exp} (observed in the laboratory) and h_{2sim} (that lead to a hydraulic jump simulation located at upstream of the channel) in function on Froude and slope.

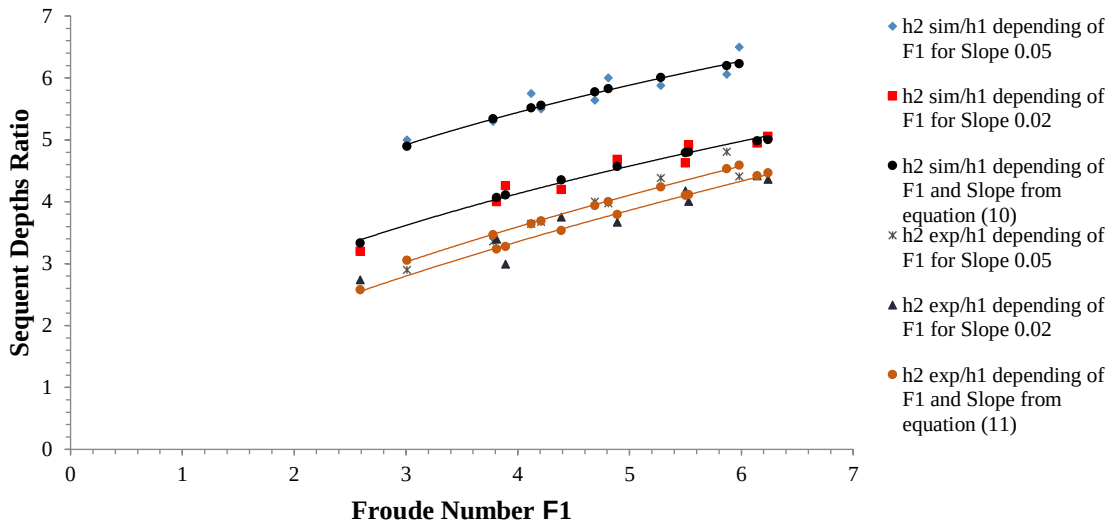

Figure 10. Variation of the sequent depths ratio simulated/experimental depending to Froude number and slope

Subtracting the equations (10) and (11), we reach to relation (12).

$$\frac{h_s}{h_1} = a + bF_1 + cF_1{}^2 + \frac{d}{tg\alpha} \tag{12}$$

where a= 1.8368, b = 0.3834, c = –0.0504and d = –0.0349; with r^2 = 0.93

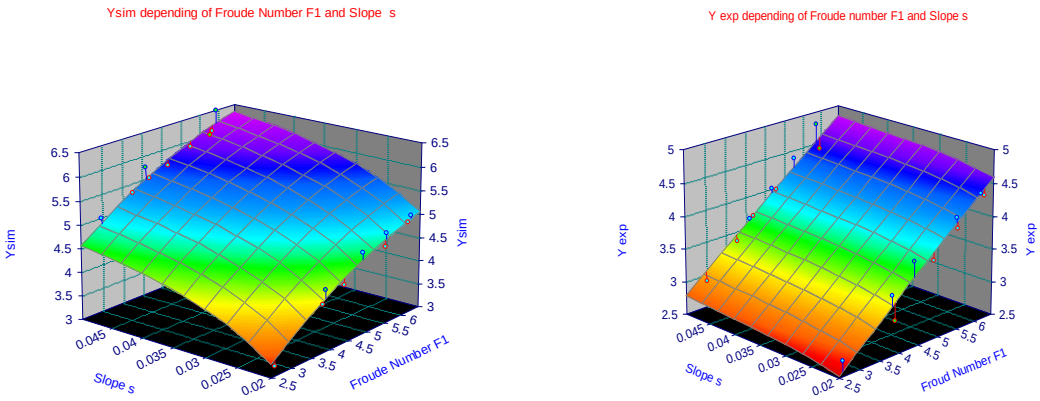

Figure 11. Relation between conjugate depths, Froude number and slope from the equations (10) and (11)

Through this last relation we can calculate the downstream water depth required to include in the downstream boundary condition in the simulation model for the hydraulic jump be located on upstream of the channel as verified in experimental conditions.

3.3. Location of hydraulic jump

In this part we study the relation between the location of the hydraulic jump and the difference between water depth $h_s = h_2\text{sim} - h_2\text{exp}$, Figure 12 represents relations between Lc/h_1, h_s/h_1 and slope s.

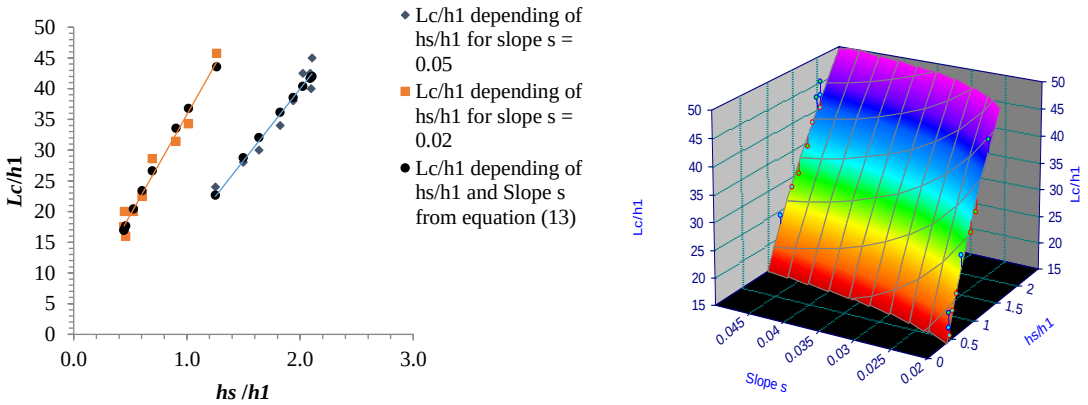

Figure 12. Relation between $Lc/h_1$and h_s/h_1: (left) $Lc/h_1$and h_s/h_1 and (right) Lc/h_1, h_s/h_1 and slope s

The results showed a linear relation between Lc/h_1 and h_s/h_1 for both slopes 0.02 and 0.05. The general equation obtained for the variation of Lc/h_1 depending with h_s/h_1 and slope s is:

$$\frac{L_c}{h_1} = a + b\frac{h_s}{h_1}^{0.5} + \frac{c}{(tg\alpha)^{1.5}} \tag{13}$$

where $a = -49.55$, $b = 58.28$ and $c = 0.08$; with $r^2 = 0.96$

4. CONCLUSION

In this work a MATLAB® model based on Saint-Venant equations and the TVD MacCormack explicit scheme for different sections was developed. It was applied to simulate a large range of hydraulic jumps tested in the laboratory with rectangular and triangular channels for Froude numbers ranging from 3 to 8. The location of a hydraulic jump was studied in a slopped triangular channel previewed by the model as some differences in the hydraulic jump location prediction compared with experimental tests were found. These differences with hydraulic jump characteristics which allows to quantify uncertainty in measured h_2 to reproduce hydraulic jumps location were related.

For using model based on Saint Venant equations to simulate flows on slopped triangular channels, care should be taken if a hydraulic jump forms in the channel as their location could be predicted slightly downstream if downstream water depth are not measured in a required distance from the jump. It is recommend to use (12) to predict location more accurately or using also (13) to know the uncertainty of *Lc*.

5. ACKNOWLEDGMENTS

The first author would like to acknowledge the support of mesrs (Ministry of Higher Education and Scientific Research, Algeria) through the scholarship PNE.
Second author would also like to acknowledge for the support of FCT (Portuguese Foundation for Science and Technology) through the Project UID/MAR/04292/2013 financed by MEC (Portuguese Ministry of Education and Science) and FSE (European Social Fund), under the program POCH (Human Capital Operational Programme).

6. REFERENCES

Abbott, M. B., Marshall, G., and Rodenhuis,G. S. (1969). Amplitude-Dissipative and Phase-Dissipative Scheme for Hydraulic Jump Simulation, *Proc.,13^{t} h Congress*, Inter. Assoc. Hyd. Research, Tokyo, pp.313-329.

Achour, B. (1989). Jump flow meter in a channel of triangular cross-section without weir: *Journal of Hydraulic Research.*, 27(2), 205-214.

Achour, B., and Debabeche, M. (2003). Control of hydraulic jump by sill in a triangular channel: *Journal of Hydraulic Research*, 41(3), 97-103.

Carmo, J.S. (2009). Modelação em Hidráulica Fluvial e Ambiente, imprensa da universidade de Coimbra.

Carvalho, R.F., Lemos, C.M., and Ramos, C.M. (2008). Numerical computation of the flow in hydraulic jump stilling basins:*Journal of Hydraulic Research.*, 46(6), 739–752.

Chanson, H., (2009) Current knowledge in hydraulic jumps and related phenomena. A survey of experimental results, European Journal of Mechanics B/Fluids 28.

Chanson, H., and Carvalho, R. F. (2015). Chapter 4, Hydraulic Jumps, in Energy Dissipation in Hydraulic Structures, IAHR Monograph, *CRC Press*, Taylor & Francis Group, Leiden, The Netherlands, 168 pages.

Chaudhry, M. H. (2008). Open-Channel Flow, University of South Carolina, Columbia, *Springer Science and Business Media, LLC.*

Chow, V. T., (1959), Open Channel Hydraulics, *McGraw-Hill Book Company*.

Debabeche, M., (2003). Le ressaut hydraulique dans les canaux prismatiques, université de Biskra, Algérie.

Debabeche, M., and Achour, B. (2007). Effect of sill in the hydraulic jump in a triangular channel: *Journal of Hydraulic Research.*, 45(1), 135–139.

Debabeche, M., Cherhabil, S., Hafnaoui, A., and Achour, B. (2009). Hydraulic Jump in a Sloped Triangular Channel: *Canadian Journal of Civil Engineering.*,36, 655-658.

Ead, S.A., and Rajaratnam, N. (2002).Hydraulic jump on corrugated beds: *Journal of Hydraulic Engineering.*,128(7), 656-663.

Gharangik, A. and Chaudhry, M. (1991). Numerical Simulation of Hydraulic Jump: *Journal of Hydraulic Engineering*, 9(1195), 1195-1211.

Garci'a-Navarro, P. ,Alcrudo, F., and Saviron, J. M. (1992).1-D Open-Channel Flow Simulation Using TVD-Mccormack Scheme: *Journal of Hydraulic Engineering.*,118, 1359-1372.

Hachemi, R.L. (2006). Analyse d'un écoulement au travers d'un contraction latérale, université de Biskra.Algérie.

Hager,W. H. (1992). Energy dissipators and hydraulic jump. *Kluwer Academic Publishers*, Dordrecht, The Netherlands. 288 pages.

Hager, W. H., and Bretz, N. V. (1987). Hydraulic jumps at positive and negative steps: *Journal of Hydraulic Research.*,24(4), 237-253.

Hager, W. H., and Wanoschek, R. (1987). Hydraulic jump in triangular channel: *Journal of Hydraulic Research.*, 25(5), 549-564.

Hubert, C. (2009). Current knowledge in hydraulic jumps and related phenomena.A survey of experimental results: *European Journal of Mechanics B/Fluids.*, 28 (2009), 191-210.

Katopodes, N. D. (1984). A Dissipative Galerkin Scheme for Open-Channel Flow: *Journal of Hydraulic Engineering*, 110(4), 450-466.

Maher, A. (2005). Sur les méthodes de discrétisation numérique de problèmes hyperboliques non linéaires appliquées aux équations de Barré de Saint-Venant pour la modélisation de l'hydraulique en réseau d'assainissement, Université Louis Pasteur de Strasbourg, École Nationale du Génie de l'Eau et de l'Environnement de Strasbourg.

McCorquodale, J. A. and Khalifa, A. (1983). Internal Flow in Hydraulic Jumps: *Journal of Hydraulic Engineering*, 109(5), 684-701.

Mendes, P.J. (2001). Contribuiçao para o Estudo da Modelação das Ondas de Cheia Provocadas pela Ruptura de Barragens, Universidade de Coimbra.

DOI:10.15142/T3W01S

Capacity of street inlets with partially severed grate openings

S. Kemper[1], A. Schlenkhoff[1]
[1]School of Architecture and Civil Engineering
University of Wuppertal
Wuppertal, Germany
E-mail: s.kemper@uni-wuppertal.de

ABSTRACT

Due to an increasing number of extreme rainfall events, the management of urban flooding requires new design approaches concerning the underground drainage system as well as the temporary surface water runoff. Latest developments on bidirectional coupled models, 1D-1D as well as 1D-2D models, are already employed in practice. Street inlets are the connecting elements between the surface and the underground system. Depending on the longitudinal and transversal slope of the street as well as the street inlet type, the hydraulic efficiency of grate inlets is hardly available. Thus, physical model test runs were done. With longitudinal slopes up to 10 % only supercritical flow conditions with flow depths up to 3 cm and flow velocities of approximately 1-2 m/s occur. In previous physical model test runs the overall grate capacity of selected grate inlets was measured. Depending on the street geometry up to 75 % of the approaching surface flow is captured by the inlet. The aim of the present paper is to investigate the inflow conditions in detail. By measuring the intercepted flow for defined parts of the grate openings separately the main inflow regions with their respective efficiency can be determined. A typical street inlet used in Germany is investigated exemplarily. The main inflow areas of the grate inlet are located in a typical triangular pattern on the curbside. The front half of the inlet intercepts nearly 70 % up to 95 % of the total captured flow. Physical model results are compared to numerical results in order to calibrate and validate the numerical model. Within both models nearly the same inflow zones can be identified qualitatively.

Keywords: *street inlets, inlet capacity, supercritical flow, urban flooding*

1. INTRODUCTION

According to the Synthesis Report of the Intergovernmental Panel on Climate Change (IPCC) the number of heavy rainfall events and their intensity will increase in the future (IPCC 2014). Therefore, urban flood risk management becomes more important and requires new design approaches in urban drainage engineering. Digman et al. (2014) define four key events regarding the management of urban flooding: (1) everyday rainfall, (2) drainage design rainfall, (3) exceedance rainfall and (4) extreme rainfall. Usually, urban drainage systems are designed for events one and two with return periods of 2-10 years (DIN EN 752 2008) and consist of underground infrastructures. Street inlets capture the surface runoff and the connecting pipes then carry the discharge to the underground-piped drainage system. It is not sustainable to enlarge the underground infrastructures when designing for exceedance (key event 3). Drainage systems above the ground need to be developed to manage surface flooding e.g. flood routes or temporary storage areas. Emergency plans must exist for the case of key event four (Digman et al. 2014). According to Fratini et al. (2012) a “dual drainage” or “major and minor systems” approach has not yet been prevailed in Europe whereas e.g. in Australia the runoff after heavy rainfall events may be discharged above ground already. With bidirectional coupled numerical models the interaction between the underground drainage system (minor system) as well as the surface runoff using topography and streets (major system) can be calculated. Even extreme flow conditions can be represented (Butler and Davies 2011). 1D-1D models (one-dimensional pipe flow model and one-dimensional surface flow model) are applicable as long as the surface flow stays within the road cross-section. 1D-2D models (one-dimensional pipe flow model and two-dimensional surface flow model) give results that are more realistic if the surface flow exceeds the capacity of the street profile. Inundation areas with flow depths and velocities are calculated. Most of the coupled numerical models use a weir or orifice equation to calculate the exchange between both systems. Djordjevic et al. 2013 pointed out that uncertainties regarding the parameters exist and the equations are not fully representative of the real flow conditions. More realistic information concerning the hydraulic efficiency and flow conditions of existing street inlets is necessary to build up the bidirectional coupled numerical models. Djordjevic et al. (2013) investigated the interaction between above and below ground drainage systems with full-scale physical and three-dimensional numerical models. The authors

identified the need for a better understanding of the interaction process between above and below ground drainage systems. The authors' CFD model was able to replicate qualitatively the observed complex flow conditions in the entire street inlet system.

Street inlets exist in four types: (a) grate inlets, (b) curb-opening inlets (c) combination inlets and (d) slotted drain inlets (Brown et al. 2009), see Figure 1. The hydraulic efficiency of grate inlets depends primarily on the street's geometry with longitudinal and transverse slope, the surface runoff (discharge) and the grate itself (type, geometry, opening area). Several investigations deal with the hydraulic efficiency of grate inlets, or more precisely, only with the grates efficiency neglecting the system below, e.g. Spaliviero et al. (2000), Despotovic et al. (2005), Gómez and Russo (2005) and Guo and MacKenzie (2012).

Gómez and Russo (2007) and Gómez and Russo (2009) studied different inlet types like continuous transverse grates and macro grate inlets. Russo et al. (2013) tested methods to estimate the efficiency of non-tested continuous transverse grates. Lopes et al. (2016) investigated the ability of a volume of fluid (VOF) model to reproduce the efficiency of a continuous transverse grate inlet by comparing the results with experimental data. The authors recommend the use of a numerical model as a useful alternative to experiments to predict efficiencies of different types of inlet structures with grates, since similar results were obtained.

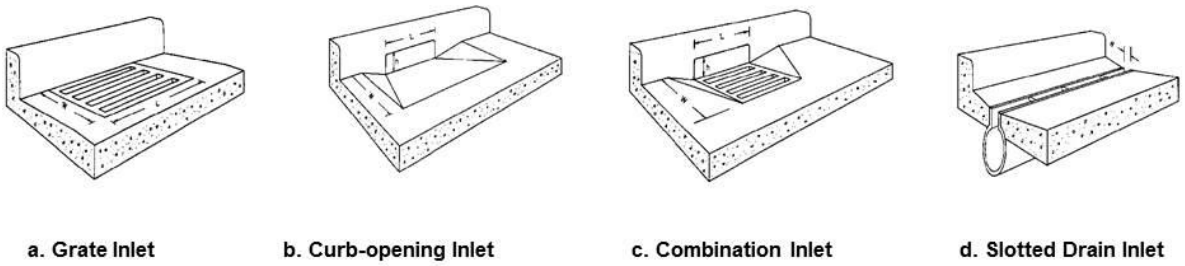

Figure 1. Street inlet types (Brown et al. 2009), modified.

There is only less information about the inflow conditions of grate inlets in detail. Detecting the discharge through defined parts of the grate openings enables for instance the prediction of a reduced efficiency due to clogging effects. Furthermore, the geometry of the grate may be improved to increase the efficiency in future research work. The present paper focuses on the main inflow areas of a grate typically used in Germany and their corresponding efficiencies.

In order to calibrate and validate a numerical model to calculate the capacity of grate inlets with an extended range of parameters, e.g. transverse slope or inlet geometry, the physical model results were compared to the numerical results.

2. MODEL SETUP

2.1. Physical Model

The physical model consists of a flume made of acrylic glass with L_{Flume} = 10.0 m in length and W_{Flume} = 1.5 m in width where the slope is adjustable in longitudinal and transverse direction. The bottom roughness is approximately k = 1.5 mm (roofing paper). In an opening area of 500 mm x 500 mm the grate of real street inlets can be integrated (scale: 1:1). All of the presented investigations were done with the standardized grate inlet mostly used in Germany and described in DIN 19583 (2012). Water depths were measured with ultrasonic sensors upstream of the inlet where steady as well as uniform flow conditions were already reached. The resolution of the ultrasonic sensors is 0.18 mm with a reproducibility of ± 0.15 % (General Acoustics e.K.). The surface flow velocities were measured with a radar measuring device with an accuracy of ± 0.5 % ± 0.03 m/s and a measuring range of 0.15 m/s up to 9 m/s (FLOW-TRONIC S.A./N.V.). Both measurements were done over the whole cross section 1 m upstream of the inlet with steps of Δy = 6 cm. Using platform load cells, the volume of the water intercepted by the grate, flowing beside the grate and flowing over the grate was measured over time. Backwater effects caused by the underground drainage system were not considered within the

presented investigations. Instead, a free outflow through the grate exists. Furthermore, only supercritical flow conditions occur for all investigated discharges and slopes and therefore no influence arises due to the physical outflow condition. In order to locate the main inflow areas of the grate, the grate was separated into eight parts (see Figure 2, right side). In addition to the described flows above, the discharge through each part was measured separately. The opening area of the grate in total is A_0 = 910.00 cm². Parts one, four, five and eight each have an opening area of $A_{1,4,5,8}$ = 97.50 cm² (10.71 % of A_0) and parts two, three, six and seven each have an opening area of $A_{2,3,6,7}$ = 130.00 cm² (14.3 % of A_0), see Table 1.

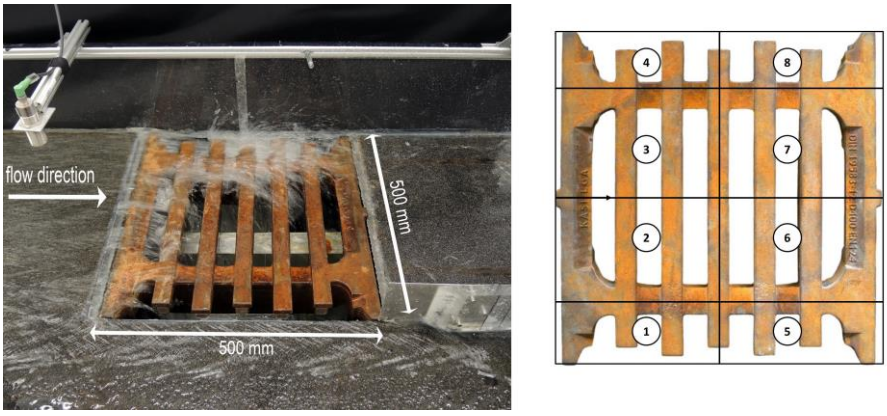

Figure 2. Detail of the physical model (left) and definition of the opening parts (right)

Table 1. Dimensions of the opening parts

Part No.	**Width b_i [cm]**	**Opening Area A_i [cm²]**	**Ratio A_i/ A_0**
1	9.8	97.50	0.1071
2	15.0	130.00	0.1429
3	15.0	130.00	0.1429
4	9.8	97.50	0.1071
5	9.8	97.50	0.1071
6	15.0	130.00	0.1429
7	15.0	130.00	0.1429
8	9.8	97.50	0.1071
Total	**-**	**A_0 = 910.00**	**-**

The German guideline for designing street inlets recommends a connected catchment area of 400 m² for one inlet each (FGSV 2005). Therefore, based on KOSTRA-DWD-2000 (2000), the surface runoff approaching one inlet can be determined assuming 100 % runoff on the street. Table 2 gives the surface runoff for Wuppertal, a city in the western part of Germany with different return periods T [a] and durations D [min] as an example.

Table 2. Surface runoff approaching one street inlet (FGSV (2005), KOSTRA-DWD-2000 (2000))

***T* [a]**	**0.5**	**1.0**	**2.0**	**5.0**	**10.0**	**20.0**	**50.0**	**100.0**
***D* [min]**	Q [l/s]	Q [l/s]	Q [l/s]	Q [l/s]	Q [l/s]	Q [l/s]	Q [l/s]	Q [l/s]
5	4.30	6.80	**9.29**	12.59	15.08	17.58	20.88	23.37
10	3.84	5.46	7.07	**9.21**	10.82	12.44	14.58	16.20
15	3.30	4.56	5.81	7.47	**8.72**	9.98	11.64	12.89

Usually, drainage structures are designed for rainfall events with T = 2 a to 10 a. In order to consider exceedance rainfall events with return periods of more than T = 10 a, the discharge for the model test runs was varied between Q = 3 l/s up to Q = 21 l/s, which corresponds to a rainfall event with T = 100 a (see Table 2). The transverse slope was fixed to S_T = 2.5 % and the longitudinal slope was varied between S_L = 2.5 % and S_L = 10.0 % with ΔS_L = 2.5 %. The present paper focuses on rainfall events with a resulting surface runoff of Q = 9 l/s (just reaching exceedance) and an intermediate longitudinal slope of S_L = 5.0 % and S_L = 7.5 %.

2.2. Numerical Model

The CFD Software FLOW-3D v.11.1 (Flow Science Inc.) was used for the numerical simulations. The model geometry was taken from the physical model, hence, no scaling effects occur. Surface tension is not calculated within the numerical model test runs. The grate inlet geometry is included using an STL (Stereo Lithography) file. The cross bar width of the grate is 32 mm and the opening width between two cross bars is 36 mm. Due to these small dimensions, the mesh size was set to $dx = dy = 4$ mm and $dz = 3$ mm in Mesh Block 2 (nested mesh block including the street inlet, see Figure 3). The mesh size of the basic mesh block 1 in z-direction corresponds to the respective parameter in mesh block 2 with $dz = 3$ mm. The mesh size in x-y direction lies between $dx = dy = 12 – 8$ mm. Previous investigations have proven the independence of the mesh. The mesh size was decreased as well as increased for *dx*, *dy* and *dz*. Convergence was reached with the resulting mesh size. The street inlet geometry was modeled precisely using the FAVOR™ method (Fractional Area-Volume Obstacle Representation, Flow Science Inc. (2015)). The numerical model consists of approximately 26 million cells in total. The RNG turbulence model was used (Renormalized group, based on the k-ε turbulence model). The inflow boundary condition was set to *Volume Flow Rate*, the *Outflow* condition was set for the lower boundary as well as for the outflow of the street inlet (*Zmin*). The surface roughness of the flume is $k = 1.5$ mm, the roughness of the inlet $k_I = 0.3$ mm. The discharge through each of the eight parts can be determined by defining eight plane *Baffles* as a flux surface (100 % porous, does not affect the flow) beneath the grate inlet. Furthermore *Baffles* were defined to measure the approaching flow as well as the water flowing beside and over the grate (see Figure 3).

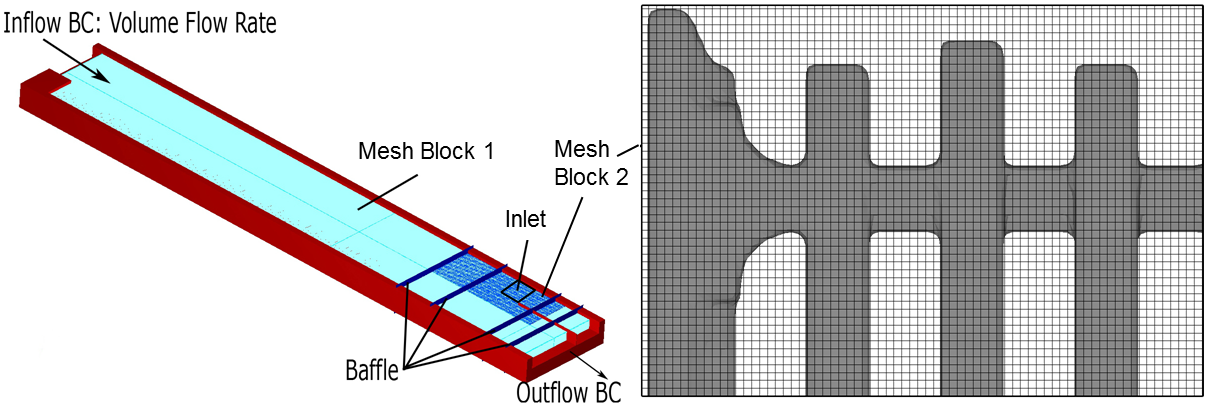

Figure 3. Numerical model

3. RESULTS AND DISCUSSION

The approaching flow is characterized by a uniform triangular cross section area with transverse slope S_T [m/m], water depth h [m] directly at the curb and water spread width W [m]. As investigated in previous test runs (Kemper and Schlenkhoff 2015) the discharge in a triangular channel can be calculated by a modified form of the Manning equation developed by Izzard (1946):

$$Q = 0.376/n\ S_T^{5/3}\ W^{8/3}\ S_L^{1/2} \tag{1}$$

where Q = street discharge [m³/s] (approaching flow), n = Manning's roughness coefficient of the street surface [s/m$^{1/3}$], S_L = street longitudinal slope [m/m] and W = water spread width W [m] with $W = h/S_T$. The measured water depths in the laboratory, the resulting water depths from the numerical model as well as the calculated water depths from Eq. (1) are compared in Figure 4 (left). The Manning's roughness coefficient in Eq. (1) is set to $n = 0.013$ s/m$^{1/3}$. With Eq. (1) the water depths h [m] can be calculated very well – a good approach is given. Also, the numerical model results fit to the physical model results with maximum deviations of ± 10 % (Figure 4, right).

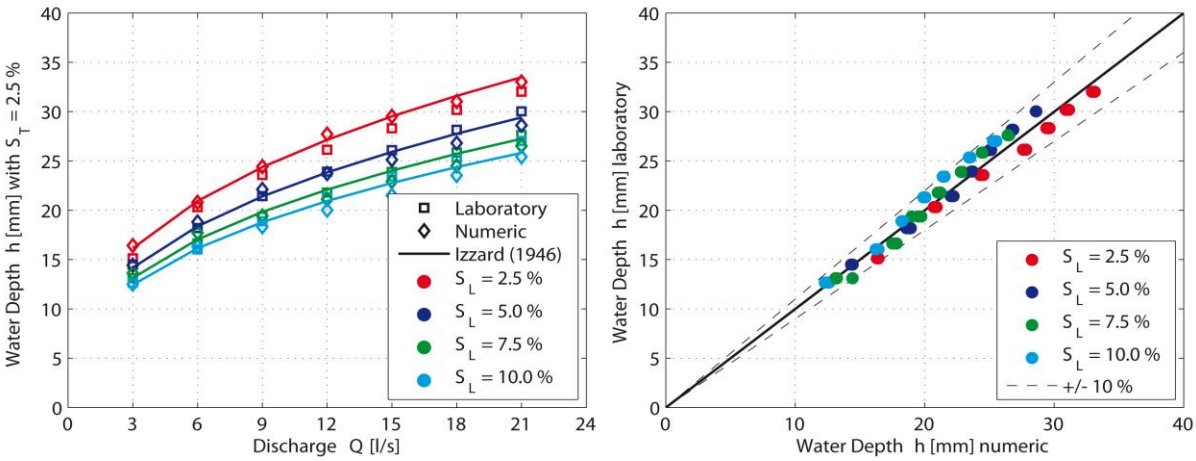

Figure 4. Water depths *h* (a) calculated with equation (1) compared to results from numerical model and laboratory and (b) corresponding comparison of water depths from numerical model and laboratory

The flow velocity upstream of the inlet measured at several points transverse to the flow direction is given for $S_L = 5.0$ % and $S_T = 2.5$ % and an exemplary approaching discharge of $Q = 9$ l/s in Figure 5. The velocities calculated with the numerical model differ from the physical model results with maximum deviations of ± 15 %. Uncertainties appear in the laboratory results at the transition between dry and wet areas where small velocities occur which cannot be measured with the used technique. For all test runs supercritical flow conditions appear with water depths up to 3 cm and flow velocities of approximately 1-2 m/s.

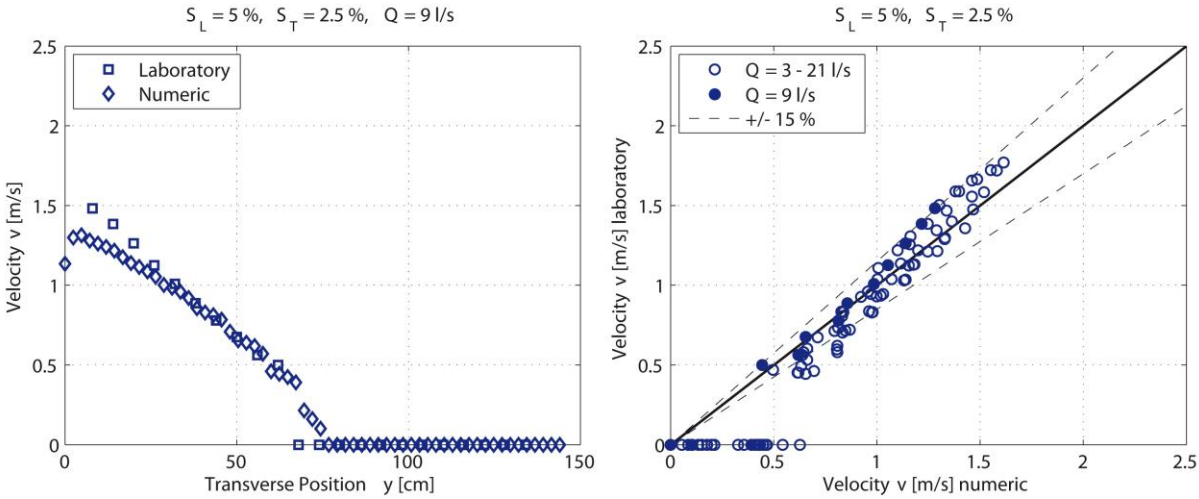

Figure 5. Flow velocities *v* (a) along cross section from numerical and physical model and (b) corresponding comparison of velocities from numerical model and laboratory

The grate capacity is defined as the quantity of the intercepted flow rate Q_I [l/s] whereas the hydraulic efficiency E of the grate inlet is described as a percentage of the approaching flow rate with:

$$E = Q_I / Q \tag{2}$$

where Q_I [l/s] is the intercepted flow rate and Q [l/s] the approaching flow. The remaining discharge $Q - Q_I$ is divided into the water flowing beside the inlet Q_B (bypass flow) and the water flowing over the inlet Q_O.

In Figure 6 the physical model results for the overall grate capacity are given with a resulting dependency curve. The total intercepted flow Q_I depends on the approaching surface flow Q. With a constant transverse slope of $S_T = 2.5$ % the intercepted flow rates vary between $Q_I \approx 2.95$ l/s and $Q_I \approx 16.00$ l/s for the investigated grate geometry, depending on the longitudinal slope and surface runoff. Therefore, the grate efficiency is minimum $E = 75$ %. It is expected that with increasing surface runoff the intercepted flow will converge to a maximum

value (not tested yet). The influence of the longitudinal slope is very low (Figure 6). High longitudinal slopes such as S_L = 10 % result in high flow velocities and small water spread widths on the street. The bypass flow Q_B decreases. However, the higher the flow velocities, the more water is flowing over the inlet, Q_o increases. Both effects nearly cancel each other out, then, the total amount of the intercepted flow is nearly unaffected by the longitudinal slope.

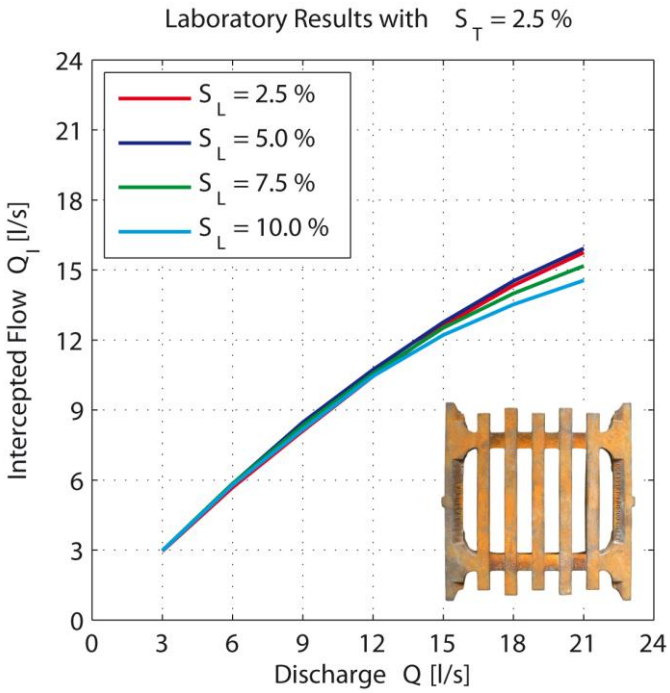

Figure 6. Intercepted flow depending on approaching flow rate (physical model results)

The efficiency of particular areas of the grate inlet can be calculated by:

$$E_i = Q_{Ii} / Q_I \tag{3}$$

Depending on the approaching flow, the front half of the inlet captures nearly 70 % up to 95 % of the intercepted water Q_I. Dividing the grate into two parts longitudinal to the flow direction, the curbside half has an efficiency of approximately 60 % up to 80 %. Referring to the division into eight parts (Figure 2, right side), the roadside back parts five and six are nearly useless. To get more detailed information about the efficiency of particular parts, the intercepted flow rate Q_I is divided into eight parts – Q_{Ii} [l/s] with i = 1, 2 … 8. Due to different opening areas $A_{0,i}$ of each part (Table 1), the specific discharge q_i is calculated with regard to the width of the part perpendicular to the flow direction b_i to achieve comparability:

$$q_i = Q_{Ii} / b_i \tag{4}$$

Two main capacity zones can be identified in Figure 7, exemplarily for longitudinal slopes of S_L = 5.0 % and S_L = 7.5 %. The front half parts of the inlet (except part one) show nearly the same capacity curve progression, as well as the remaining parts one, five, six, seven and eight. The specific discharge in the front half part can be approximated with a less than linear shape curve whereas the capacity curve progression for the back half part depends nearly linearly on the approaching flow.

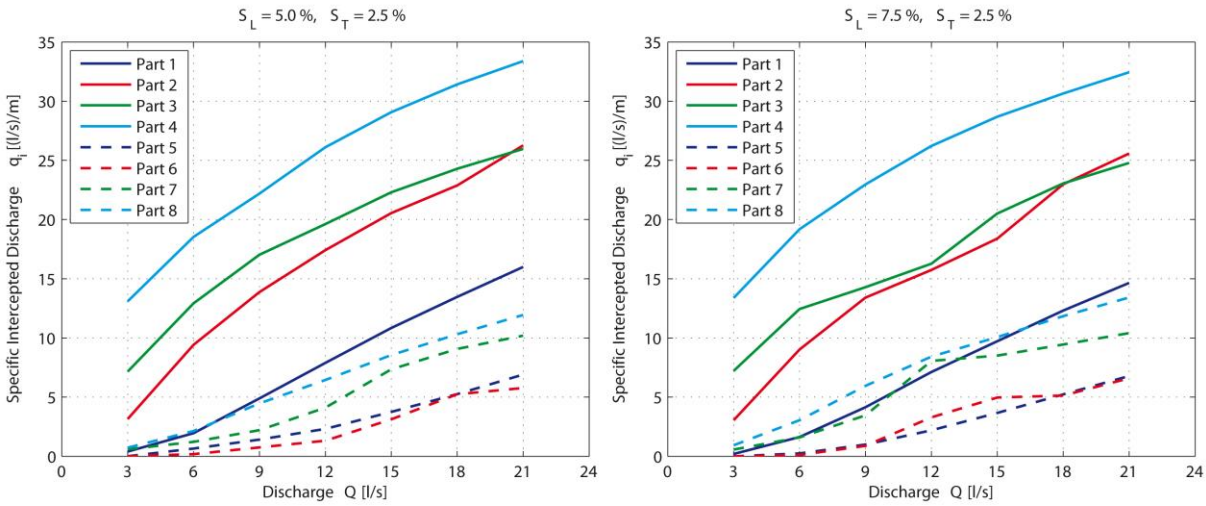

Figure 7. Specific inlet capacity (laboratory results)

Figure 8 gives interpolated specific discharges over the inlet area. The left side shows the laboratory results, the right the results from the numerical model. Flow direction is from left to right with the curbside on the upper edge.

In Table 3 the approaching flow $Q_{apr,i}$ for each transverse part is given, calculated with the measured water depths and flow velocities from both models. The corresponding intercepted flow through each part resulting from the model runs is presented in column 3. The influence of the transverse slope is recognizable since the discharge through the roadside parts is slightly higher than the approaching flow. This is caused by the additional lateral inflow from the street. Within both the laboratory and numerical model, nearly the same inflow zones can be identified qualitatively on the front curbside zone. However, the amount of the discharge still differs. Further research is necessary to investigate the ability of the used numerical model to calculate the intercepted flow rates.

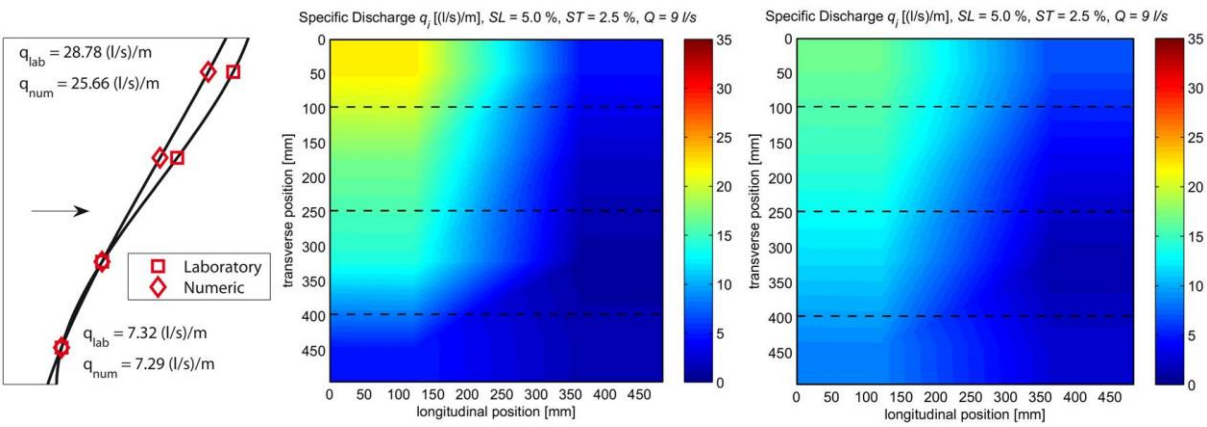

Figure 8. Specific inlet capacity – laboratory (left) vs. numeric (right), flow direction: left to right

Table 3. Approaching flow $Q_{apr,i}$ for each part with corresponding intercepted flow Q_{Ii}
(Q = 9 l/s, S_L = 5.0 %, S_T = 2.5 %)

Part	$Q_{apr,i}$ **[l/s]** (Lab / Num)	Q_{Ii} **[l/s]** (Lab / Num)
4+8	2.82 / 2.51	2.61 / 2.26
3+7	3.27 / 2.94	2.89 / 2.75
2+6	1.86 / 1.86	2.19 / 1.91
1+5	0.72 / 0.71	0.62 / 1.08

4. CONCLUSION

In order to develop new design approaches in urban drainage engineering several simulation runs were performed to improve planning tools, especially bidirectional coupled models which consider the interaction between the underground drainage system and the surface runoff. The connecting elements between both systems are street inlets which exist in different types and geometries. The present paper focuses on the hydraulic efficiency of a typical grate inlet used in Germany (500 mm x 500 mm) and its flow conditions in detail by locating and describing the main inflow areas of the grate and their corresponding efficiencies. In order to calibrate and validate a numerical model to calculate the efficiency of street inlets, physical model results were compared to three-dimensional numerical model results. With water depths up to 3 cm upstream of the inlet and flow velocities of 1-2 m/s only supercritical flow conditions occur due to steep longitudinal slopes up to S_L = 10 %. Depending on the investigated longitudinal and transverse slopes of the street, approximately 75 % of the approaching surface flow is captured by the inlet. The front half of the inlet intercepts nearly 70 % up to 95 % of the captured surface flow. The main inflow zone is on the front curbside zone which can be seen in both the physical and the numerical model. In order to validate the ability of the numerical model further research is necessary.

5. REFERENCES

Butler, D., Davies, J.W. (2011). Urban Drainage, Third Edition, Spon Press.

Brown, S.A., Schall, J.D., Morris, J.L., Doherty, C.L., Stein, S.M., and Warner, J.C. (2009). Urban Drainage Design Manual – Hydraulic Engineering Circular 22 (HEC-22), Third Edition, FHWA-NHI-10-009, U.S. Dept. of Transportation, Federal Highway Administration, Washington, D.C., National Highway Institute, Virginia.

Digman, C., Ashley, R., Hargreaves, P., and Gill, E. (2014). Managing urban flooding from heavy rainfall – encouraging the uptake of designing for exceedance. Recommendations and summary. CIRIA, London.

Despotovic, J., Plavsic, J., Stefanovic, N., and Pavlovic, D. (2005). Inefficiency of storm water inlets as a source of urban floods. *Water Science and Technology*, 51(2), 139-145.

DIN 19583 (2012). Gully tops 500 x 500 for road gullies, class C 250 and class D 400 – Part 2: Particulars. DIN Deutsches Institut für Normung e. V., Beuth Verlag GmbH, Berlin, Germany (in German).

DIN EN 752 (2008). Drain and sewer systems outside buildings; German version. DIN Deutsches Institut für Normung e. V., Beuth Verlag GmbH, Berlin, Germany (in German).

Djordjevic, S., Saul, A.J., Tabor, G.R., Blanksby, J., Galambos, I., Sabtu, N., and Sailor, G. (2013). Experimental and numerical investigation of interactions between above and below ground drainage systems. *Water Science and Technology*, 67(3), 535-542.

FGSV (2005). Richtlinie für die Anlage von Straßen – Teil Entwässerung (RAS-Ew). Ausgabe 2005. Forschungsgesellschaft für Straßen- und Verkehrswesen e. V., Cologne, Germany (in German).

Flow Science Inc. (editor) (2015). FLOW-3D User's manual. Version 11.1.

Fratini, C.F., Geldof, G.D., Kluck, J., and Mikkelsen, P.S. (2012). Three Points Approach (3PA) for urban flood risk management: A tool to support climate change adaption through transdisciplinarity and multifunctionality. *Urban Water Journal*, 9(5), 317-331.

Gómez, M., and Russo, B. (2005). Comparative study of methodologies to determine inlet efficiency from test data. HEC-12 methodology vs UPC method. Water Resource Management 2005, Algarve, Portugal.

Gómez, M., and Russo, B. (2007). Hydraulic efficiency of macro-inlets. *Proc. NOVATECH 2007*, 1157-1164

Gómez, M., and Russo, B. (2009). Hydraulic Efficiency of Continuous Transverse Grates for Paved Areas. *Journal of Irrigation and Drainage Engineering*. 135(2), 225-230.

Guo, J.C.Y., and MackKenzie, K. (2012). Hydraulic efficiency of grate and curb-opening inlets under clogging effect. Report No. CDOT-2012-3, Final Report. Colorado Department of Transportation, Denver.

IPCC (2014). Climate Change 2014: Synthesis Report. Contribution of Working Groups I, II and III to the Fifth Assessment Report of the Intergovernmental Panel on Climate Change [Core Writing Team, R.K. Pachauri and L.A. Meyer (eds)]. IPCC, Geneva, Switzerland.

Izzard, C.F. (1946). Hydraulics of runoff from developed surfaces. *Highway Res. Board Proc.* 26, 129-150.

Kemper, S. and Schlenkhoff, A. (2015). Determination of the hydraulic efficiency of intake structures like grate inlets and screens in supercritical flow. E-proceedings of the 36th IAHR World Congress, the Hague, the Netherlands.

KOSTRA-DWD-2000 (2000). Heavy precipitation totals in Germany (1951-2000). Deutscher Wetterdienst, Offenbach, Germany.

Lopes, P., Leandro, J., Carvalho, R.F., Russo, B., and Gómez, M. (2016). Assessment of the Ability of a Volume of fluid Model to Reproduce the Efficiency of a Continuous Transverse Gully with Grate. *Journal of Irrigation and Drainage Engineering*, 142(10).

Russo, B., Gómez, M., and Tellez, J. (2013). Methodology to Estimate the Hydraulic Efficiency of Nontested Continuous Transverse Grates. *Journal of Irrigation and Drainage Engineering*. 139(10), 864-871.

Spaliviero, F., May, R.W.P., and Excaramela, M. (2000). Spacing of Road Gullies – Hydraulic performance of BS EN 124 gully gratings and kerb inlets. Report SR 533, HR Wallingford.

DOI:10.15142/T3R599

Vertical Slot Fishway: Evaluation of numerical model quality

J. Klein[1] and M. Oertel[1]
[1]Hydraulic Engineering Section, Civil Engineering Department
Lübeck University of Applied Sciences
Lübeck, Germany
E-mail: jessica.klein@fh-luebeck.de

ABSTRACT

Numerical modeling is being used with increasing frequency to analyze and design complex hydraulic structures. Especially structures where a standard design or an analytic calculation isn't applicable, numerical investigations can provide important knowledge of flow parameters. During the past several decades, a number of research investigations have been conducted regarding fish passage structures. However, additional insights are still needed. Vertical Slot Fishways (VSF) have shown a range of applications that are well documented. In particular, these fish passage structures are well suited for slopes less than 5 %, which is needed for most fishes in Europe. Numerical modeling can provide a cost-effective tool to investigate flow on VSF. The present paper deals with an investigation on quality components of numerical 3D simulation of VSF. Four pools constructed as standard design are modeled and examined. A Large-eddy simulation, second order, with three various mesh resolutions was used. Comparison of flow depths showed that a mesh width of 4 cm is sufficient for practical use. The effect of mesh size on velocity distribution was more significant: with a mesh width of 2 cm no convergence could be reached.

Keywords: *Fish passage, vertical slot fishway, numerical modeling*

1. INTRODUCTION

Vertical slot fishways (VSF) are facilities to enable fish to migrate beyond (man built) obstructions such as dams or hydropower plants. VSF are rectangular channels separated into a sequence of pools by vertical walls. Vertical slots in these walls provide a migration corridor (Clay 1961; Rajaratnam et al. 1986). The sequence of pools subdivides the total hydraulic drop into a navigable series of smaller drops. Thereby, permissible velocities for fish species of interest are created.

Currently, there is a need to consider site-specific conditions and develop optimal designs for vertical slot fishways. In Europe, this is in part due to the European Water Framework Directive (WFD 2000), which states that all water bodies have to be restored into a good morphological and ecological condition. Therein, a fundamental part is providing ecological bridges at barriers via fishways. In some instances, the design of fishways is mostly conducted via one-dimensional analytical calculations. But it is known that only standard designs using said methodologies based upon robust hydraulic modeling are consistent with chosen simplifications. The lack of an adequate but simple design method for site-optimized VSF repeatedly causes the need of adjustments or modifications to existing constructions. The design of VSF is based not only on the calculation of discharge capacity but also the corresponding water depths and flow velocities. Minimum flow depths and minimum as well as maximum velocities are limiting values due to fish capability. Consequently, the discharge capacity has to be calculated by the means of providing fish capability with:

$$Q = C_d b_0 h_0 \sqrt{2g\Delta h} \tag{1}$$

where Q is the fishway discharge, C_d is the discharge coefficient, b_0 is the slot width, h_0 is the mean pool flow depth, g is the acceleration due to gravity, Δh is the head drop between two pools. Eq. 1 was first stated by Clay (1961) and was verified by e.g. Rajaratnam et al. (1986), Rajaratnam et al. (1992), Larinier (1992), Puertas et al. (2004), Wang et al. (2010). It gives a linear relationship between discharge and water depth, whereas the maximum velocity is solely dependent on the head drop:

$$v_{\max} = \sqrt{2g\Delta h} \tag{2}$$

where v_{max} is the maximum velocity in the fishway downstream the slot. Another calculation approach by Krüger et al. (2010) is applied in Germany, which is based on the Venturi principle (see also DWA-M 509 2014):

$$Q = \mu \cdot b_0 \cdot \sqrt{g} \cdot h_o^{1,5} \tag{3}$$

where $\mu = f(h_u/h_o)$ is the discharge coefficient, b_0 is slot width, h_o is depth upstream slot, h_u is depth downstream slot, g is acceleration due to gravity. Both, Eq. 1 and Eq. 2 were developed based on physical, hydraulic models and are applied to nowadays fishway design. Though, the empiric discharge coefficients were mostly developed using slopes of more than 5 % while in Europe slopes less than 5 % required. These circumstances generate the need of investigations of VSF with slopes less than 5 %. Till now physical models are common to analyze fishway structures. Particularly, where standard designs whereupon the design equation Eq. 1 and Eq. 2 are based cannot be applied physical models displays the design tool in such cases. Certain variations can be caused by site specific demands. Furthermore, optimization of internal geometry of VSF is ongoing. While the pool length and width were investigated extensively (Wang et al. 2010; Tarrade et al. 2008; Rajaratnam et al. 1992), inner installations such as baffles that have a flow guiding purpose, are analyzed rarely (e.g. in Rajaratnam et al. 1992, Puertas et al. 2004, Heimerl et al. 2008, Höger et al. 2014). Numerical investigations using computational fluid dynamics simulation (CFD) are being used more frequently by VSF design teams. CFD provides a cost- and time-effective way of analyzing diverse variations of VSF compared to physical models. One challenge is the number of models and solvers with limited well documented publications about model quality. A key step to developing a CFD model of quality is the influence of mesh size and simulation time properties. The present paper is a first approach on defining model qualities in respect to mesh size and simulation time properties. The aim is to find a reasonable mesh size to predict water depth and relevant velocities using CFD for design purposes as well as for further investigations concerning inner pool geometries.

2. NUMERICAL MODEL

2.1. General remarks

The presented simulation is carried out using the commercial CFD solver FLOW-3D (V. 11.1) by Flow Science, Inc.. The numerical code is based on the finite volume method (FVM) and includes the Volume-of-Fluid method (VOF) and the Fractional Area Volume Obstacle Representation (FAVOR) method (FlowScience Inc. 2016). The three-dimensional, one-fluid approach for free surface flows with second order accuracy was adopted in the current study.

2.2. Numerical conditions

The presence of turbulence in vertical slot fishways is widely known and of growing importance for design purposes (Puertas et al. 2004, Tarrade et al. 2008, Wang et al. 2010). Contemporary research attends to turbulence quantification in these hydraulic structures. In particular, the effect of turbulence on fishes corroborates the attempt to calculate and quantify turbulence in fishways. Numerous investigations deal with the effect of turbulence on fishes and confirm that highly turbulent zones are avoided by fish (e.g. Enders et al. 2003, Tarrade et al., 2008, Smith et al. 2014). Hence, some quantification of turbulent zones for site-specific designs is essential for a successful fishway. Within current analytical design approaches there is no detailed assessment of turbulence. New tools, like numerical simulation, have to be investigated to identify easy design processes and to expand knowledge of turbulences in VSF. Turbulent flow is characterized by a fluid velocity field that varies significantly and irregularly in both position and time, with turbulent motions at numerous size scales (Pope 2011; Ferziger and Perić 2002). Large Eddy Simulation (LES) is a three-dimensional and time dependent scheme to predict turbulent flows where motions and vortices of the grid's scale are computed directly while smaller scale motions are modelled (Ferziger and Perić 2002). For flows that involve unsteady separations and vortex shedding, LES provide important information about scales, kinematics and dynamics of turbulence yet represents a quite new tool to investigate small scale vortices in time and space (Adrian et al. 2000). Numerous numerical investigations state that LES reproduces the hydraulics of vertical slot fishways in good agreement with physical and full-scale models (e.g. Musall et al. 2012, Höger et al. 2014, Musall et al. 2015).

2.3. Geometry and mesh

VSF involve a large number of design parameters that each to some degree influence the flow structure. The present paper investigates a standard VSF design with geometry based on the German design guideline DWA-M 509 (2014) (see also Klein and Oertel 2015). The numerical model geometry includes five complete pools and an inlet transition zone as well as an outlet transition pool. Figure 1 shows the geometry and all relevant parameters of the investigated vertical slot fishway.

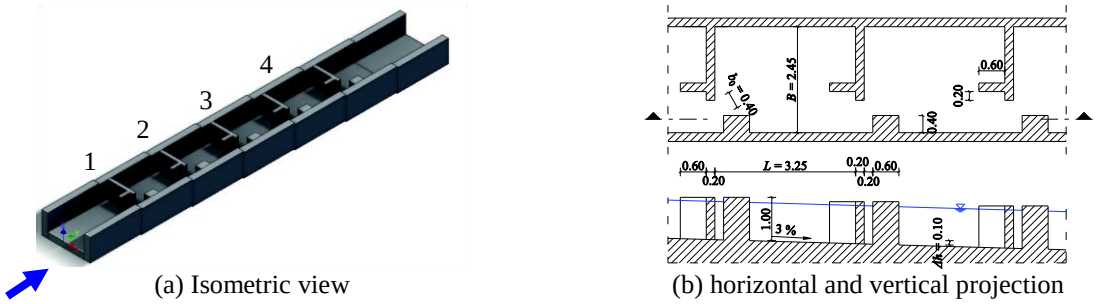

(a) Isometric view (b) horizontal and vertical projection

Figure 1. VSF Geometry of numerical model (flow direction left to right)

According to the simple design of a vertical slot pass, the discretized spatial domain consists of a rectangular channel with baffles. A structured mesh is applied to the model area. The advantage of a structured mesh can be found in a more accurate calculation than with unstructured mesh. Cubic meshes, as used herein, may yield a higher order of accuracy and can be computationally more efficient (Hirsch 2007). In Order to investigate the quality of simulation results in respect to numerical quality the mesh size is investigated in terms of a sensitivity analysis. The numerical CFD simulation is conducted using three mesh grids. Mesh cell sizes implied are: 8 cm, 6 cm and 4 cm for $\Delta x = \Delta y = \Delta z$. The refinement factor r (according to Celik 2008) is 1.33 and 1.50, exceeding the recommended value of 1.3. Furthermore, the total simulation time and the time step for result output are varied (see Table 1). The time step was increased with increasing total simulation time due to reduce the file size which corresponds to saved time steps. In total 6 model runs are presented.

Table 1. Description of simulation cases

Model run	Mesh-resolution Δm [cm]	Simulation time frame T [sec]	Time step Δt [sec]
L02a	4	5	0.02
L03a	6	5	0.02
L04a	8	5	0.02
L02b	4	30	0.05
L03b	6	30	0.05
L04b	8	30	0.05

2.4. Hydraulic boundary conditions

The hydraulic dimensioning followed the German design guideline DWA-M 509 (2014). The design process results in a discharge of Q = 0.46 m³/s which should yield to a mean pool flow depth of about h_0 = 0.9 m. The discharge was applied at the boundary of the transition pool as single inlet boundary condition. The outlet boundary condition was set to a forced fluid elevation which corresponds to the discharge. Within the present study the wall roughness has been neglected, because the general numerical behavior is of main interest. Further investigations will deal also with wall roughness effects. Generally, the development of flow characteristics takes place while the flow follows the structure's geometry. Result analysis will focus on pool No. 3 (see Figure 1a).

3. RESULTS

3.1. General

For each investigated numerical simulation the flow pattern as defined in Wu et al. (1999) can be allocated to FP 1 (see Figure 4 and Figure 2). However, the recirculation zone on the right side of the jet is really small. Figure 4 shows the time averaged velocity magnitude for all simulations at the middle of the vertical water column ($0.5h_o$). The time-averaging conducted herein can be formulated as:

$$v_{mean} = \frac{1}{n} \sum_{i=1}^{n} v_i \tag{4}$$

$$h_{mean} = \frac{1}{n} \sum_{i=1}^{n} h_t \tag{5}$$

where v_{mean} is the arithmetic mean velocity magnitude , v_i is the velocity magnitude at time step i, h_{mean} is the arithmetic mean flow depth, h_i is the flow depth at time step i, and $n = T/\Delta t$ as number of time steps calculated. In Figure 4 it seems that finer meshes produce the more curved flow structures. With increased mesh resolution also the eddy on the left side (also referred to as resting area) increases in size. Expectedly, with finer mesh grid resolutions the flow pattern can be described in more details. But the general flow structure can be reproduced for all investigated mesh resolutions. However, major differences can be observed for the absolute velocity magnitude (see Section 3.2). As a result differences in regard to the FAVOR-rendered geometry cannot be neglected. As it can be seen in Figure 4, the slot width and the width of baffles are dependent on the mesh resolution and can thereby majorly influence simulation results. In general, the calculated 0.9 m flow depth (specified by the design guideline) was not reached. The applied design approach could not be confirmed by the numerical results. The flow depth is non-uniform and raises from its minimum just downstream the slot towards the downstream baffle wall (see Figure 4). Contemporaneously, the largest velocities can be observed just downstream the slot. Figure 3 gives an exemplary flow depth distribution for model run L03a. Besides numerical errors, the rendered geometry might be responsible for errors. If the baffles are not rendered properly, the slot width, which influences the flow depth (see Eq. 1 and Eq. 2), will vary.

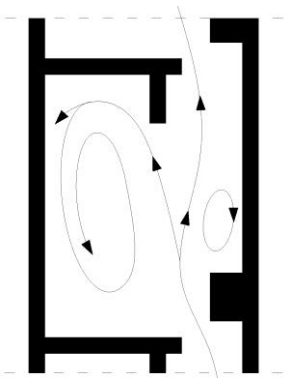

Figure 2. Sketch of flow pattern

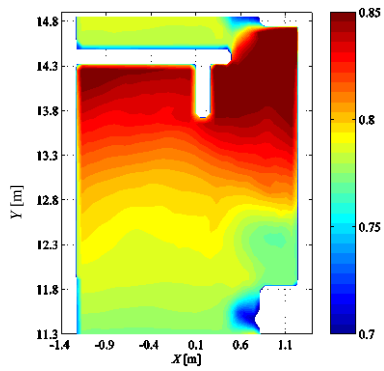

Figure 3. Time-averaged flow depth in [m], model run L03a (T = 5 sec, Δm = 6 cm)

3.2. Time dependency

Hydraulics in vertical slot fishways are majorly time depended (see exemplarily Figure 6). Recent findings lead to assume that some fish species use the time depended fluctuations in flow to save swimming capacity (Gebler 2015). Therefore, time dependence and frequencies are of main interest. On the other hand, engineers need parameters and values which guarantee a simple, yet practical application. Thus, mean values as stated above are still demanded. Therefore, it is fundamental to define a simulation time frame and a time step that generates reliable time averaged values. To evaluate which simulation time frame is needed to get reliable statements on velocities and flow depths standard deviations in each point are calculated. The standard deviation can provide information about fluctuations in the pool and indicate the grade of turbulence.

The standard deviation of flow depth does not vary majorly between all simulations. A dependence on time frame or time step cannot be identified. Figure 5 shows the standard deviation of the depth-averaged velocity for each model run at the middle of the vertical water column ($0.5h_o$). It can be seen that the highest deviation is located in the jet flowing from one slot to the next one. With decreasing mesh size detachment zones with high standard deviation can at the edges of the baffle wall and the right baffle be identified. This indicates high grade of turbulences in these zones. Within the resting area, the formed eddy shows standard deviations of less 0.08 m/s. Thus, turbulences in resting areas are, as expected, lower. Comparing model runs a (Figure 5a-c) and model runs b (Figure 5d-f), the results are clearly dependent on simulation time frame and time step. With an equal mesh width, areas of high standard deviation (above 0.15 m/s; red) increase as well as at most cells absolute standard deviation increases with longer simulation time frame or larger time steps. Figure 6 shows a velocity duration curve of two exemplary points in the fishway for each investigated simulation – one in the middle of the eddy (resting area) and one in the slot; both at $2/3h_o$. A fluctuating flow field can be obtained at different VSF in operation (Gebler 2015). The numerical simulation should reproduce the fluctuations because fishes, which use fluctuations to ascent the fishway, were observed (Gebler 2015). For model runs a (Figure 6a/c) no reoccurring frequency is obvious. This statement can be confirmed by a conducted Fast-Fourier-Transformation (FFT), which couldn't identify any frequency. Model runs b (Figure 6b/d) on the other hand enfolds a simulation time frame of 30 seconds but a time step of 0.05 seconds. The FFT showed a high amplitude at 0.5 Hz (2 s). However, to get reliable statements of the frequency more simulations, preferential with same time step and rising time frame, are needed.

Concluding, comparison of model runs a and model runs b results in a clear time dependency. Reason of the divergence can be found either in simulation time frame or time step. The variation of time interval might lead to the loss of extrema with consequence of error in time/averaged values. The simulation's time frames might be insufficient to identify fluctuations and frequencies. Besides, the stated time dependency the investigation of standard deviation reveals distinctions in the occurrence of turbulence due to mesh resolution. A trend of improvement with a decreasing mesh size cannot be found without defining a sufficient simulation time.

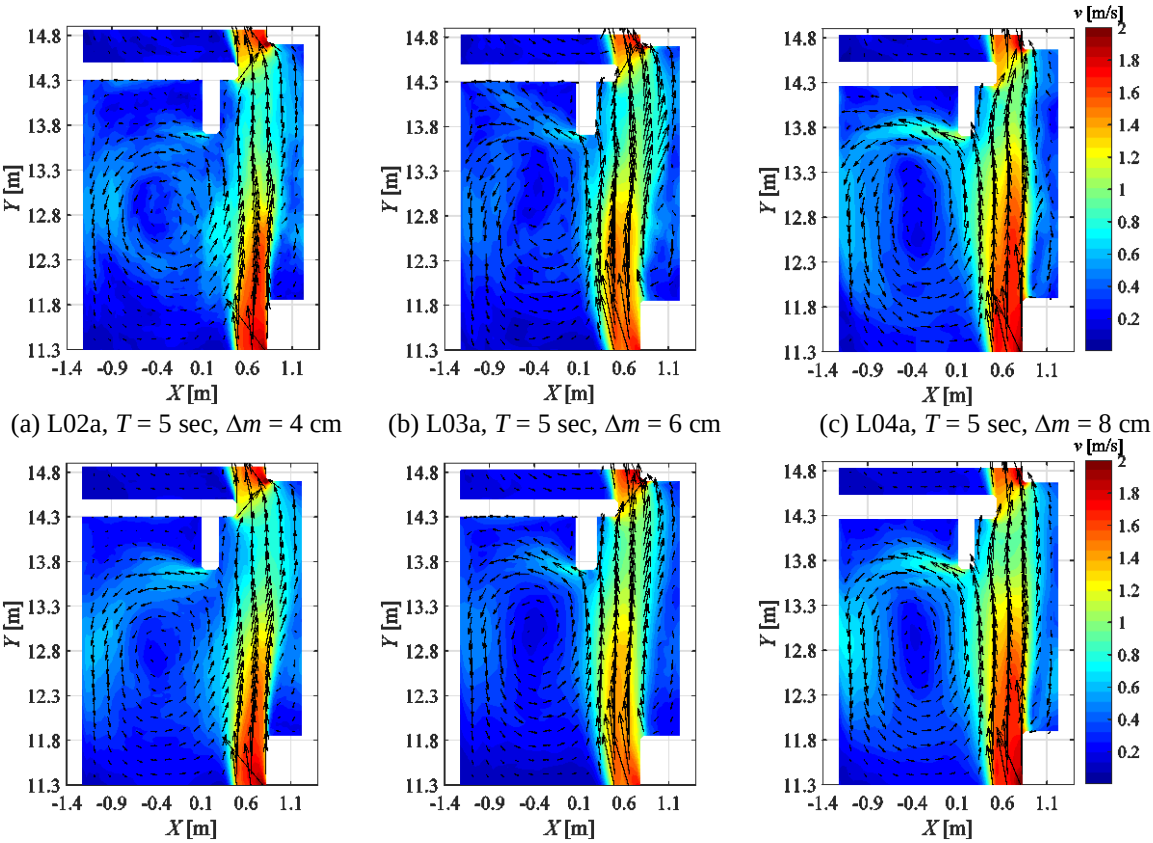

(a) L02a, T = 5 sec, Δm = 4 cm (b) L03a, T = 5 sec, Δm = 6 cm (c) L04a, T = 5 sec, Δm = 8 cm

(d) L02b, T = 30 sec, Δm = 4 cm (e) L03b, T = 30 sec, Δm = 6 cm (f) L04b, T = 30 sec, Δm = 8 cm

Figure 4. Time-averaged velocity magnitude for basin No. 3 at $0.5h_o$

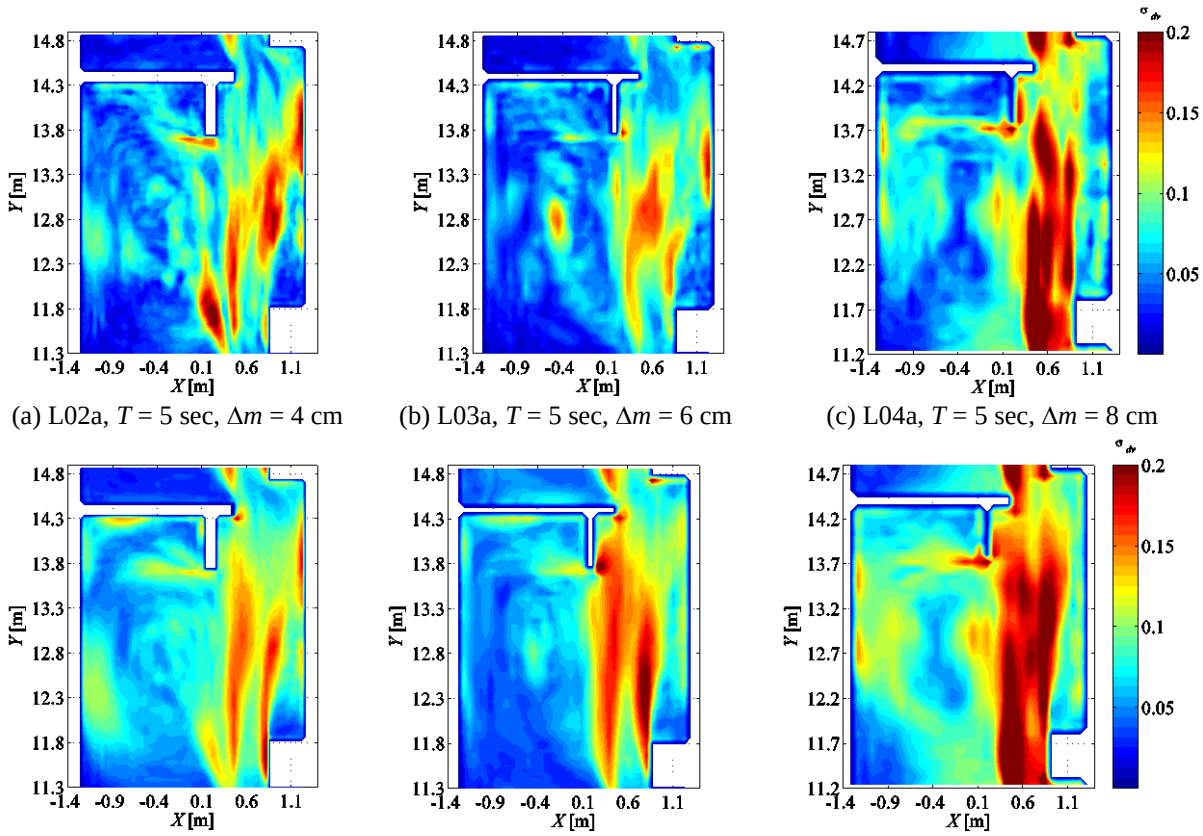

(a) L02a, T = 5 sec, Δm = 4 cm (b) L03a, T = 5 sec, Δm = 6 cm (c) L04a, T = 5 sec, Δm = 8 cm

(d) L02b, T = 30 sec, Δm = 4 cm (e) L03b, T = 30 sec, Δm = 6 cm (f) L04b, T = 30 sec, Δm = 8 cm

Figure 5. Standard deviation of depth averaged velocity at 0.5*ho*, top: T = 5 sec, bottom: T = 5 sec

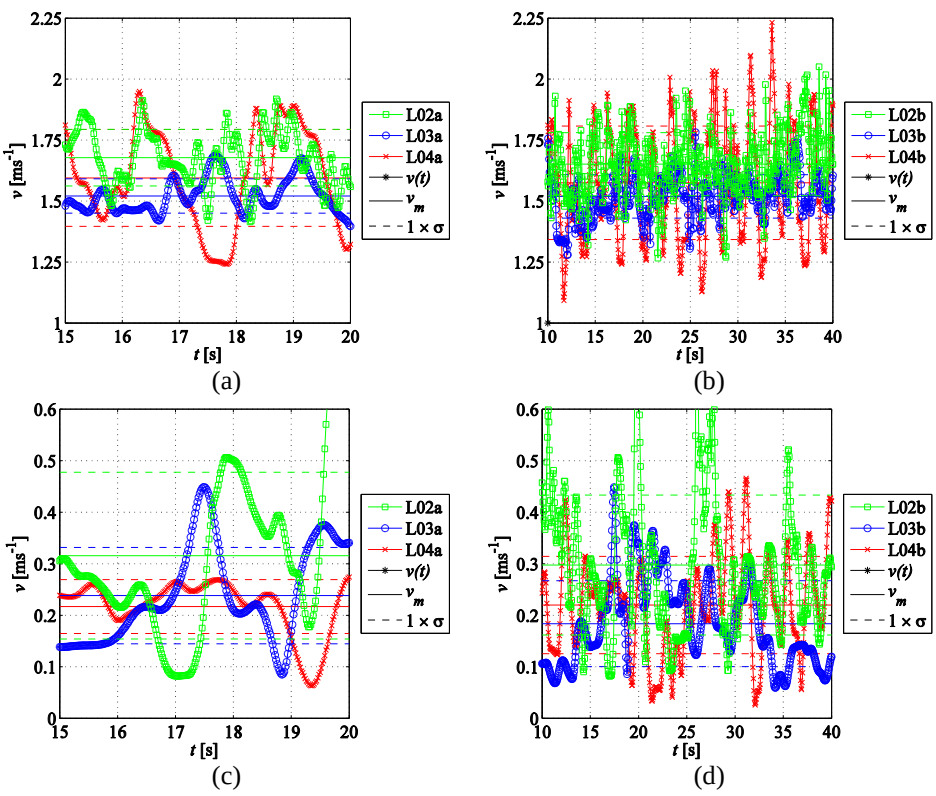

Figure 6. Velocity duration curve, (a) slot, T = 5 sec, Δt = 0.02 sec, (b) slot, T = 30 sec, Δt = 0.05 sec, (c) eddy, T = 5 sec, Δt = 0.02 sec, (d) eddy, T = 30 sec, Δt = 0.05 sec

3.3. Deviation of results concerning mesh resolution

To evaluate the influence of the mesh resolution, simulation results for all investigated mesh sizes were interpolated on the finest mesh resolution to fit an identical grid. This procedure provides a possibility to conduct a sensitivity analysis and calculate the deviation of two simulations at each point and to compare their results. Due to numerous time steps, a time-averaged value was used for comparison. As stated in Section 3.2, a clear time dependency of the results was identified. Thus, only simulation runs a (T = 5 sec, Δt = 0.02 sec) are examined. Simulation runs b show similar appearance. In the present investigation time-averaged flow depths and depth- and time-averaged velocities were proved, herein.

Figure 7 shows the time-averaged flow depth deviation for two simulations for pool No. 3. It can be shown that deviation in general will be increased with an increasing mesh width (compare Figure 7). Deviations in flow depths between L02a and L03a does not exceed 6 % overall (see Figure 7a). This value is located at wall domains and can be caused by calculation or numerical errors. Without wall domains the highest deviation is located just downstream the slot with a maximum of ±5 %. At the detachment areas downstream the right baffle the deviation does not exceed 2 %. Within the resting area deviation of 3 % can be observed. The highest deviation between L03a and L04a can be found with +14 % and is located close to the wall domain at the right baffle's detachment zone. Figure 7b clearly displays only a positive deviation. The maximum divergence in the resting area (pool middle) is +10 % compared to +6 % in the slot. Improvement between mesh resolutions of 6 cm to 4 cm is minute. Accordingly, the numerical simulation of vertical slot fishways with a mesh resolution of 6 cm in prototype scale provides sufficient results to calculate flow depths. Errors of less than 1 cm compared to a mesh resolution of 4 cm can be expected.

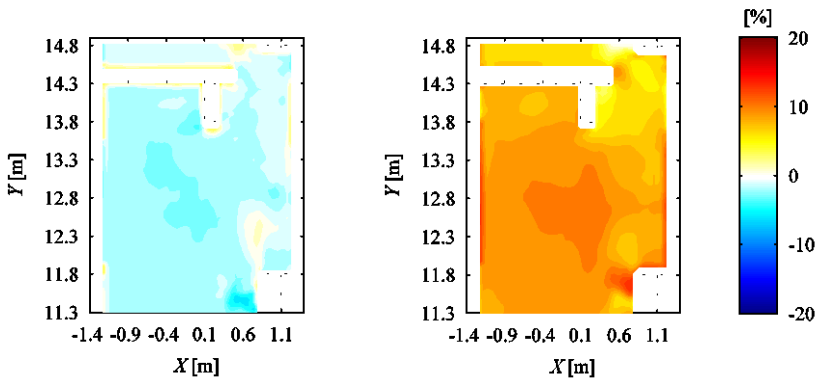

(a) L02a-L03a (b) L03a-L04a

Figure 7. Time-averaged flow depth deviation in [%] for pool No. 3

Subsequently, the deviation of two model run's depth-averaged velocities are examined (see Figure 8). Highest deviations of L02a and L03a are at the detachment zone downstream the baffle wall with values exceeding -100 %. Furthermore deviations of ±40 % are located downstream the right baffle (see Figure 8a). The deviation of the jet, guided from one slot to the next, is mostly +40 % (mean 15 %). Shear zones show a deviation close to 0 %, which generates a mean deviation of 13 % considering the absolute deviation. On the other hand, the deviation between L03a vs. L04b is reversed and shear zones are displayed less distinct. The location and value of the highest deviation corresponds to L02–L03: model runs a show a deviation of more than 100 %, whereas the deviation increases to approx. 45 % at the detachment zone downstream the wall baffle with rising time frame. The detachment area at the right baffle is less distinct than for L02 vs. L03 but shows deviation values of more than –100 %.

Comparing the deviations of depth-averaged velocities show that even with refining the mesh resolution from 6 cm to 4 cm the velocity distribution diversifies strongly in zones with low as well as high velocities. Exclusively in shedding zones, all simulation results show little (near 0 %) divergence in depth averaged velocity. Concluding, a mesh resolution of 4 cm for numerical simulation of vertical slot fishways can provide good convergence in respect to simulated flow depths in prototype scale with an error of maximum 2 cm. For design purposes concerning reaching flow depth a mesh size of 4 cm can be evaluated as sufficient. On the other hand, the velocity distribution varies hardly in respect to mesh resolution. Especially velocities at near slot zones are important for positive fish migration. These zones are not sufficient simulated having deviation of up to 100 %. Furthermore, decreasing cell sizes should be investigated in future research applications to verify an improvement of flow velocity deviation with increasing cell sizes.

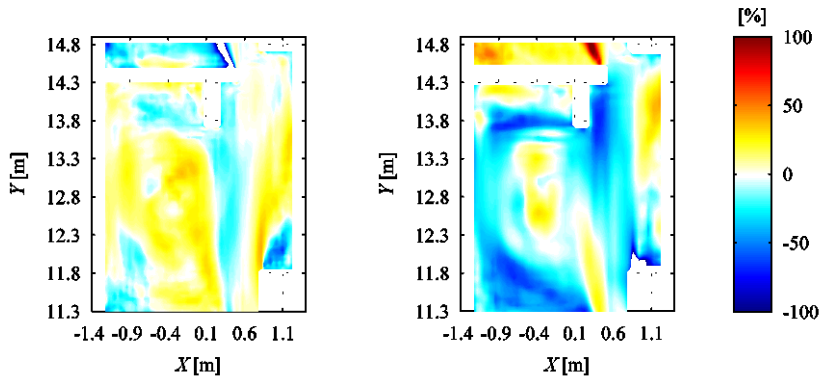

(a) L02a-L03a (b) L03a-L04a

Figure 8. Depth averaged velocity deviation in [%] for pool No. 3

3.4. Grid Convergence Index

Due to the lack of convergence concerning the velocity distribution a sensitivity analysis suggested by Celik et al. (2008) was performed calculating the Grind Convergence Index (GCI) for flow depths and flow velocity magnitude. Therefore, a seventh simulation with grid refinement to 2 cm quadratic cells at the pool of interest has been carried out (L01). The sensitivity analysis was performed using the simulation results of:

- L01: mesh resolution Δm = 2 cm, simulation time frame T = 5 sec, time step Δt = 0.02 sec
- L02: mesh resolution Δm = 4 cm, simulation time frame T = 5 sec, time step Δt = 0.02 sec
- L03: mesh resolution Δm = 6 cm, simulation time frame T = 5 sec, time step Δt = 0.02 sec

Figure 9a-c compares the results of the simulated water depth with (a) the calculated GCI of L01 and L02 $GCI_{21,depth}$ and (b) and (c) longitudinal profiles of the investigated simulation runs. The sensitivity analysis using GCI confirms previous findings: with a mesh size of 2 cm a good convergence is given except at points with high gradients. The overall mean $GCI_{21,depth}$ of the third pool is 3,9 %. 97 % of all points in the pool reach a $GCI_{21,depth}$ < 10 %. With $GCI_{21,depth}$ beneath 10 % it can be assumed that the dependency of numerical results on the mesh resolution has been reduced and the solution is reaching towards the grid independent solution. Compared to $GCI_{32,depth}$ (GCI of L02 and L03) a significant improvement can be found: 64 % of all points in the pool reach a to $GCI_{32,depth}$ < 10 %. $GCI_{21,depth}$ < 10 % can only be found at high gradients as seen in Figure 9b at $Y \approx$ 11.5 m and $Y \approx$ 11.9 m which is just upstream and downstream the slot. Though, the solution is reaching towards the grid independent solution.

Table 2. Results of grid convergence study via GCI

	depth averaged $GCI_{21,veloc}$ [%]	% of $GCI_{21,veloc}$ < 10% [%]
P1	77	29
P2	154	2
P3	10	74
P4	26	45
P5	16	58
P6	300	0

Calculating the GCI for the velocity magnitude of L01 and L02 ($GCI_{21,veloc}$) 41 % of the points in one pool reach a $GCI_{21,veloc}$ < 10 %. Compared to $GCI_{32,veloc}$ (L02 and L03) there is a significant improvement: $GCI_{32,veloc}$ < 10 % are reached in 27 % of all points in one pool. In Figure 9d-f the calculated GCI for the velocity magnitude at six points as well as two axial velocity profiles are shown to represent the whole pool. P3-P5 (see Table 2, Figure 9d) show in general low $GCI_{32,veloc}$, which indicates that the dependency of numerical results on the mesh resolution has been reduced and the solution is reaching towards the grid independent solution. High $GCI_{21,veloc}$ can be found near the water surface and near the bed which indicates that the grid convergence is highly important for shear zones. The axial velocity in Figure 9e is located in the middle of the slot. The differences in velocity are at maximum 0.1 m/s which can be evaluated as sufficient taking fish migration into account. On the other hand P1, P2 and P6 result in high $GCI_{21,veloc}$ of more than 77 % depth averaged and a little rate of values under 10 %. The axial velocity profile shown in Figure 9f is located at a near

wall domain. The possible error of 0.3 m/s is too high taking fish migration into account. As a possible reason it can be assumed that refinement of the mesh can result in shifting of the vortexes (as also seen in Figure 4) which can result in a high GCI. Also oscillating convergence can lead to high GCI.
In Figure 9d it can be seen that in general there is a good agreement with GCI < 10 % over most of the water column. High differences are located at the water surface and circa 0.3 m above ground, except for point 6 ($X = -0.9$ m; $Y = 11.51$ m, see also Figure 9f). This possible error is too high taking fish migration into account. The refinement of the mesh can result in shifting of the vortexes (as also seen in Figure 4) which can result in a high GCI.

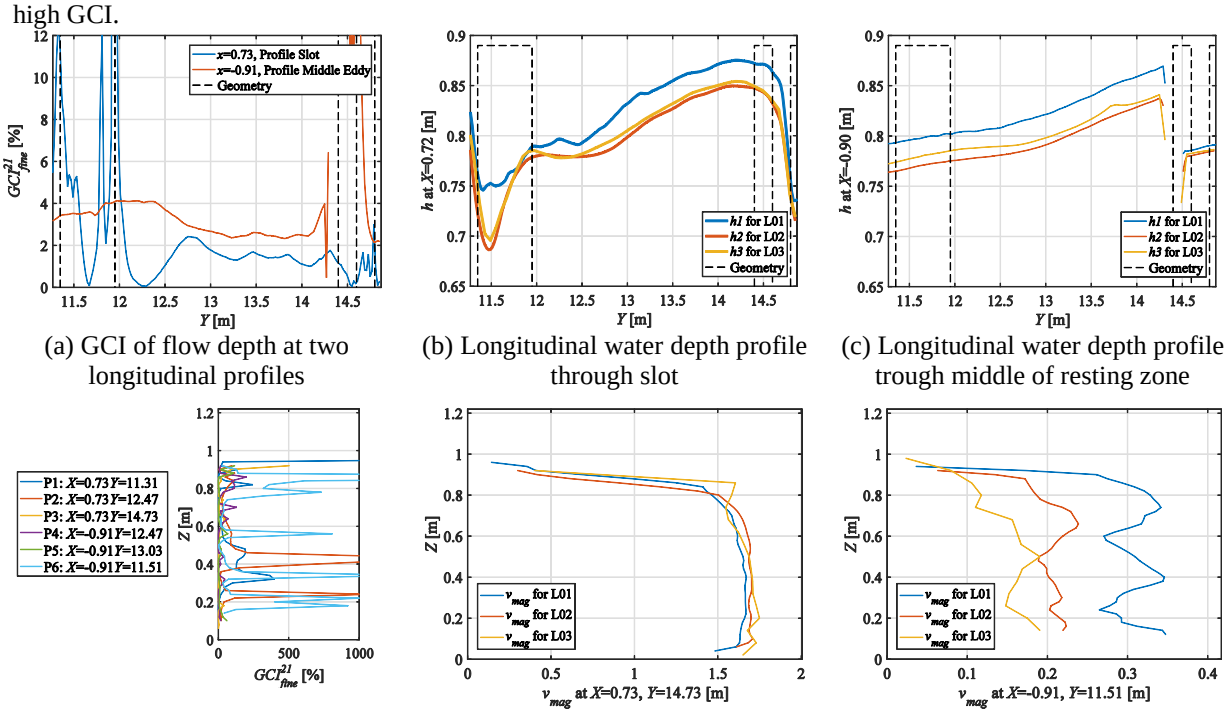

(a) GCI of flow depth at two longitudinal profiles

(b) Longitudinal water depth profile through slot

(c) Longitudinal water depth profile trough middle of resting zone

(d) GCI of axial velocity magnitude at six points

(e) Axial Velocity magnitude Profile at the slot

(f) Axial Velocity magnitude near wall domain

Figure 9. Results of flow depth (a-c) and velocity magnitude (d-f)

4. CONCLUSIONS

The present investigation on mesh quality parameters can be considered as a first step for mesh quality recommendations. Basic parameters like time properties and mesh sizes were evaluated. The findings presented herein show, as expected, that mesh size and grid convergence are essential to guarantee sufficient numerical quality and to produce reliable numerical results.

While general flow patterns can be reproduced sufficiently in large mesh resolutions like Δm = 8 cm, the absolute velocity magnitude require a finer mesh resolution to generate sufficient results. Comparing the depth-averaged velocities of different mesh resolutions high divergences can be identified. With deviations of locally more than 100 % between two mesh resolutions it can be concluded that a mesh size of 4 cm does not provide reliable flow velocities to evaluate fish capability. The sensitivity analysis using GCI shows still lacking convergence with mesh width Δm = 2 cm in respect to the velocity magnitude. The alteration of the position of vortexes contributes to the high velocity distribution comparing certain points. On the other hand a 2 cm mesh provides a sufficient simulated flow depth with deviations of less than 2 cm and is rarely dependent on simulation time properties.

Considering time dependency and turbulences analog assumptions due to mesh resolution can be made. The location of zones with high resp. low grade of turbulence can be identified using a coarse mesh resolution, short simulation time and large time step. Though, their dimension majorly depends on the mesh size as well as on simulation time properties. However, the present simulations couldn't provide a recommendation for simulation time properties since more varying simulation runs have to be performed. Furthermore, fluctuations of flow in VSF could be reproduced but are not yet reliable. More numerical simulations need to be conducted with differing simulation time frames, too.

Finally, the present paper discusses mesh quality aspects, but without comparing results with those from experimental hydraulic models. Consequently, also further experimental model runs are necessary to confirm numerical model results. Therefore, extensive hydraulic experiments are planned at the Luebeck University of Applied Sciences' Hydraulic Laboratory.

5. REFERENCES

Adrian, R. J., Christensen, K. T. and Liu, Z.-C. (2000). Analysis and interpretation of instantaneous turbulent velocity fields, *Experiments in Fluids* 29 (3), 275–290.

Celik, I. B. (2008). Procedure for Estimation and Reporting of Uncertainty Due to Discretization in CFD Applications, *J. Fluids Eng.* 130 (7), 1–4.

Clay, C. H. (1961). Design of Fishways and Other Fish Facilities, Ottawa.

DWA-M 509 (2014). Merkblatt DWA-M 509: Fischaufstiegsanlagen und Fischpassierbare Bauwerke – Gestaltung, Bemessung, Qualitätssicherung, Deutsche Vereinigung für Wasserwirtschaft, Abwasser und Abfall e.V. (DWA), Hennef [in German].

Enders, Eva C., Boisclair, D. and Roy, A. G. (2003). The effect of turbulence on the cost of swimming for juvenile Atlantic salmon (Salmo salar). *Canadian Journal of Fisheries and Aquatic Sciences* 60 (9), 1149–1160.

Ferziger, Joel H. and Perić, M. (2002). Computational methods for fluid dynamics. 3rd, rev. ed., Springer, New York.

FlowScience Inc. (2016). FLOW-3D 11.0.0 documentation, Santa Fe, USA.

Gebler, R.-J. (2015). Dimensionierung von Schlitzpässen Anforderungen der Fische und der Hydraulik, *WasserWirtschaft* 105 (7/8), 73–79 [in Gernan].

Heimerl, S., Hagmeyer, M. and Echteler, C. (2008). Numerical flow simulation of pool-type fishways: New ways with well-known tools. *Hydrobiologia* 609 (1), 189–196.

Hirsch, C. (2007). Numerical computation of internal and external flows, 2. ed., Elsevier Butterworth-Heinemann, Amsterdam, Heidelberg.

Höger, V., Musall, M. and Sokoray-Varga, B. (2014). Hydraulik von Fischaufstiegsanlagen in Schlitzpassbauweise: Physikalische und Numerische Untersuchungen zur Optimierung der Passierbarkeit. *Tagungsband zur Kolloquiumsreihe Herstellung der ökologischen Durchgängigkeit der Bundeswasserstraßen, 4. Kolloquium,* Bundesanstalt für Wasserbau (BAW), Koblenz, 2014 [in German].

Klein, J. and Oertel, M. (2015). Comparison between crossbar block ramp and vertical slot fish pass via numerical 3D CFD simulation. *E-Proceedings of the 36th IAHR World Congress,* IAHR, The Hague, NL.

Krüger, F., Heimerl, S., Seidel, F. and Lehmann, B. (2010). Ein Diskussionsbeitrag zur hydraulischen Berechnung von Schlitzpässen. *WasserWirtschaft* 100 (3), 30–36 [in German].

Larinier, M. (1992). Passes à bassins successifs, prébarrages et rivières artificielles. *Bull. Fr. Pêche Piscic.* (326-327), 45–72 [in French].

Musall, M., Oberle, P., Carbonell-Baeza, R., Fuentes-Pérez, J. F., Tuhtan, J. A. and Nestmann, F. (2015). Beitrag zu detaillierten Analysen der Hydraulik von Schlitzpässen. *WasserWirtschaft* 105 (7/8), 67–72 [in German].

Musall, M., Seidel, F., Riestereer, J., Läkwmäkwwe, K., Oberle, P., Lehmann, B. and Nestmann, F. (2012). Numerische und physikalische Modelluntersuchungen im Rahmen der Planung der Fischaufstiegsanlage Geesthacht an der Elbe. *Dresdner wasserbauliche Mitteilungen* 47, Dresden [in German].

Pope, S. B. (2011). Turbulent flows. 8. ed. Cambridge University Press.

Puertas, J., Pena, L. and Teijeiro, T. (2004). Experimental Approach to the Hydraulics of Vertical Slot Fishways. *Journal of Hydraulic Engineering* 130 (1), 10–23.

Rajaratnam, N., Katopodis, C. and Solanki, S. (1992). New designs for vertical slot fishways. *Canadian Journal of Civil Engineering* 19, 402–414.

Rajaratnam, N., Van der Vinne, G. and Katopodis, C. (1986). Hydraulics of Vertical Slot Fishways. *Journal of Hydraulic Engineering* 112, 909–927.

Smith, D. L., Goodwin, R. A. and Nestler, J. M. (2014). Relating Turbulence and Fish Habitat: A New Approach for Management and Research. *Reviews in Fisheries Science & Aquaculture* 22 (2), 123–130.

Tarrade, L., Texier, A., David, L. and Larinier, M. (2008). Topologies and measurements of turbulent flow in vertical slot fishways. *Hydrobiologia* Vol. 609 (No. 1), 177–188.

Wang, R. W., David, L. and Larinier, M. (2010). Contribution of experimental fluid mechanics to the design of vertical slot fish passes. *Knowledge and Management of Aquatic Ecosystems* (Vol. 396), 2.

WFD (2000). Directive 2000/60/EC of the European Parliament and of the Council establishing a framework for the Community action in the field of water policy on 22 December 2000.

Wu, S., Rajaratnam, N. and Katopodis, C. (1999). Structure of Flow in Vertical Slot Fishway. *Journal of Hydraulic Engineering* 125 (4), 351–360.

DOI:10.15142/T3MG61

Frequencies of Nappe Vibration for Free-overfall Structures

M. Lodomez[1], M. Pirotton[1], B. Dewals[1], P. Archambeau[1] and S. Erpicum[1]
[1]Argenco Dept. – Research group Hydraulics in Environmental and Civil Engineering
University of Liège
Liège, Belgium
E-mail: m.lodomez@ulg.ac.be

ABSTRACT

Under relatively low-head discharges, the occurrence of nappe oscillation, otherwise known as nappe vibration, may be observed on hydraulic structures with a free overfall, such as weirs, crest gates and fountains. This phenomenon, which has been early identified as undesirable and potentially dangerous on gates, is characterized by oscillations in the thin flow nappe cascading downstream of the crest. In addition, these oscillations produce a significant level of noise and acoustic pressure waves that increase the environmental and societal impacts of the structure. A review of the scientific literature shows a lack of consensus regarding the causes and source of the oscillations development. In this context of relatively poor understanding of the dominant processes, a detailed investigation has been undertaken to identify and quantify the nappe vibration mechanism. The research is being performed with a prototype-scale linear weir located at the Engineering Hydraulics laboratory of the University of Liège. The study employs high-speed cameras and audio equipment to characterize the nappe vibration. This paper presents first characteristics of the nappe vibrations gained from images and sound analysis, especially in terms of vibration frequency, for a quarter round and a half round weir crest. This study shows that frequencies measured by sound and image analyses are identical and depend on the crest shape, the fall height and the unit discharge.

Keywords: *Spillway, nappe vibration, nappe oscillations, physical modelling, flow characterization*

1. INTRODUCTION

When water falls in the form of thin sheet from a weir, a gate or a fountain, nappe vibration may occur (Casperson 1993; Naudascher and Rockwell 1994). These nappe vibrations are known to produce excessive noise that can be heard far away from the source and may cause problems such as vibrations in doors or windowpanes in buildings nearby such as reported in the case of Linville Land Harbor Dam rehabilitation (Crookston et al. 2014).

As regards to gates, the occurrence of nappe vibration has been attributed in part to the interaction between the flow and the air pocket between the gate and the nappe (Naudascher and Rockwell 1994). In fact, spoilers attached at the gate crest to divide the nappe and aerate the air pocket have proven to be an effective mitigation technique (Naudascher and Rockwell 1994; Sumi and Nakajima 1990; USBR 1964). However, vented nappe does not prevent the vibration occurrence in the case of free surface weir (Binnie 1972; Crookston et al. 2014; Crookston and Tullis 2012; Falvey 1980). Effective mitigation techniques have been proposed to prevent the development of nappe vibration on free surface weirs. Anderson (2014) and ("Investigation into spillway discharge noise at Avon Dam" 1980) reports the effectiveness of crest roughness modification. Lodomez et al. (2016) asses and optimizes practical geometric countermeasures (crest modifications) which do not modify the weir hydraulic efficiency.

Several studies have been conducted on nappe vibration mechanism. Schwartz (1966) investigated the influence of boundary layer conditions. Squire (1953) attributes nappe instabilities to shear forces that occur at the interface between the falling water and air, in a Kelvin-Helmholtz mechanism (Helmholtz (1868)). Casperson (1996) studied oscillation occurring on curved crest while Chanson (1996) suggested a pressure discontinuity at the weir crest as the cause of the phenomenon, with an origin of the vibrations at the crest. Casperson (1993) investigated the feedback mechanism played by the confined air chamber behind the nappe. Following the nappe vibration problems experienced after the rehabilitation of the Linville Land Harbor Dam, new investigations have been undertaken recently at the Utah Water Research Laboratory (Utah State University) (Anderson 2014; Crookston et al. 2014). They suggest that the nappe instability most likely arises at the weir crest. Indeed, the horizontal bandings on the nappe created by the oscillations are observed directly after the

flow separation from the weir crest. These recent observations with some conflicting results from previous analysis confirm the complexity of the studied hydraulic mechanism.

The present experimental study has been initiated on large-scale models to come up with generic scientific conclusions as well as a deeper systematic analysis of scale effects. This paper provides an overview of the preliminary results regarding the characterization of the nappe vibration.

2. EXPERIMENTAL SETUP

Figure 1 shows the experimental apparatus used and installed at the Engineering Hydraulics laboratory of the University de Liège. The prototype-scale linear weir is an elevated box divided in two identical weirs with a 3.50-m long crest. The air cavity behind the nappe can be confined or vented to the atmosphere. Indeed the weir located on the left bank is confined between two lateral walls and a back wall, one lateral confinement wall being transparent (Plexiglas) and others black multiplex panels. The other model is vented except on the shared lateral side. The models are used independently by obstructing with multiplex panels the unwanted crest. The fall is adaptable with a maximum value of 3.00-m.

Figure 1. Experimental apparatus.

Two weir crest geometries have been tested, a quarter round crest (15-cm radius and 15-cm long flat element) and a half round crest (15-cm radius), which are modelled with typical prototype dimensions of reinforced concrete weir (Figure 2).

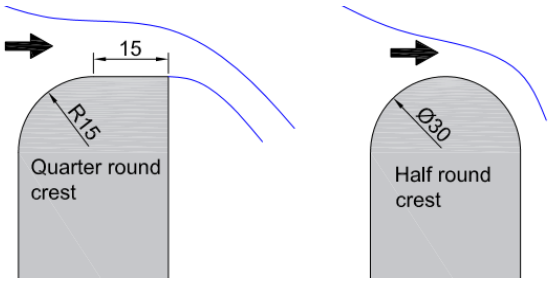

Figure 2. Crest shapes tested– dimensions in cm.

Water is supplied to the model by means of two pipes connected to two regulated pumps. Butterfly valves help in controlling very low discharges. Water enters the reservoir through perforated pipes parallel to the crest and located on the bottom of the reservoir. As illustrated in Figure 3, a baffle wall of synthetic membranes has been inserted in the reservoir to ensure uniform velocity conditions upstream of the crest. The discharge is measured

with an electromagnetic flow meter installed on the supply piping, with an accuracy of 0.5% FS. The maximum unit discharge is 7.22×10^{-2} m²/s (250 l/s in the model).

Figure 3. Upstream view of the facility: reservoir, water supply pipes and baffle wall upstream of the right side crest.

The first nappe vibration characterization has been achieved by means of a free-field microphone (MCE 212) with a frequency range between 6 Hz and 20 kHz placed in front of the falling nappe (2 m downstream of the crest and at 2 m high to avoid water projection). Based on acoustic measurements, audio spectra analysis, carried out by means of the SYMPHONIE software suite, provides the dominant sound frequencies and their associated intensity (Lodomez et al. 2016). A second mean of characterization is a high-speed video camera (Go-Pro Hero 4 - acquisition frequency of 240 Hz) to capture images of the falling water. Image analysis enables to quantify the nappe oscillation frequency by the detection of horizontal bands in the falling water, assuming that these horizontal bands arise from the lighting on the undulating surface. Indeed, the use of spotlights lighting up from downstream the falling nappe allow to visualize these bands on images shot from 2 m downstream of the crest.

In this paper, the characteristics of the nappe vibrations, especially of the phenomenon frequency gained from image and sound analysis, are presented and discussed for four model configurations with varied crest shape and fall height. The main parameters of these configurations are listed in Table 1.

Table 1. Main parameters of the discussed configurations.

Configurations	**A**	**B**	**C**	**D**
Crest length (m)	3.50			
Crest shape	Quarter round	Half round		
Fall (m)	3.00	3.00	1.00	0.50
Discharge range (m²/s)	0.015-0.07		0.01-0.06	
Confinement	Confined			

3. RESULTS AND DISCUSSION

3.1. Sound analysis

As already mentioned, the first quantitative results have been obtained by acoustic measurements. These measurements have been performed to characterize the flow rate range for which the nappe vibration phenomenon appears. For various flow rates between 0.01 m²/s and 0.07 m²/s, an audio recording of 4 minutes has been made and processed to highlight the dominant frequencies in the audio spectrum.
For a common range of unit discharges, audio spectra of sound recordings are illustrated in Figure 4 for the four configurations studied. They clearly show for configurations A and C a local frequency peak up to a unit discharge of 0.045 m²/s. For configuration D, the local peak is visible for unit discharge of 0.015 m²/s and 0.03

m²/s and disappears for higher discharges while for configuration B, no local frequency peak is visible in the discharge range.

In Figure 5 the maximum intensity of the spectrum and its corresponding frequency (illustrated in Figure 4 by red circles) are reported as a function of the unit discharge. If the frequency is a local frequency peak, this frequency may be considered as the frequency of nappe vibrations. Therefore, the detection of local frequency peak and the bell-shaped evolution of the maximum intensity with the discharge in Figure 5 allow defining the nappe vibration flow range.

For configuration A, it can be noticed that the frequency of vibrations varies between 30.75 Hz and 35.5 Hz, for unit discharges between 0.015 m²/s and 0.07 m²/s. For configuration B, no local peak being detected, for all unit discharge tested, the maximum sound level and it corresponding frequency are therefore meaningless regarding nappe vibration phenomenon. Indeed, nappe vibrations do not appear for this configuration. Sound measurements will be confirmed by the flow visualization. For configuration C, the nappe vibration can be detected between 0.015 m²/s and 0.045 m²/s when a local frequency peak exists. Indeed, in some periods of tests, despite a slight buzzing sound, no vibration was heard, while at other times the vibrations could be clearly heard and viewed. If vibrations exist, the frequency of the peak is however variable with the discharge. Between 0.015 m²/s and 0.03 m²/s, dominant frequency is between 44 Hz and 44.5 Hz although a frequency of 51 Hz has also been detected for 0.02 m²/s. For 0.04 m²/s and 0.045 m²/s dominant frequency is equal to 41.25 Hz. This value corresponds to the frequency of the maximum intensity of the spectrum when nappe slightly buzzes between 0.015 m²/s and 0.03 m²/s. This finding leads to the conclusion that the nappe may vibrate preferentially between 41.5 Hz and 44 Hz in the range of 0.015m²/s to 0.045 m²/s. Finally, Configuration D shows vibrations for unit discharge between 0.01m²/s and 0.04 m²/s. In this unit discharge range, there are three types of vibrations: a first one around 36.75 Hz between 0.01 m²/s and 0.02 m²/s, a second one around 40.75 Hz between 0.02m²/s and 0.03 m²/s and a third one around 34.5 Hz between 0.03 m²/s and 0.04 m²/s .

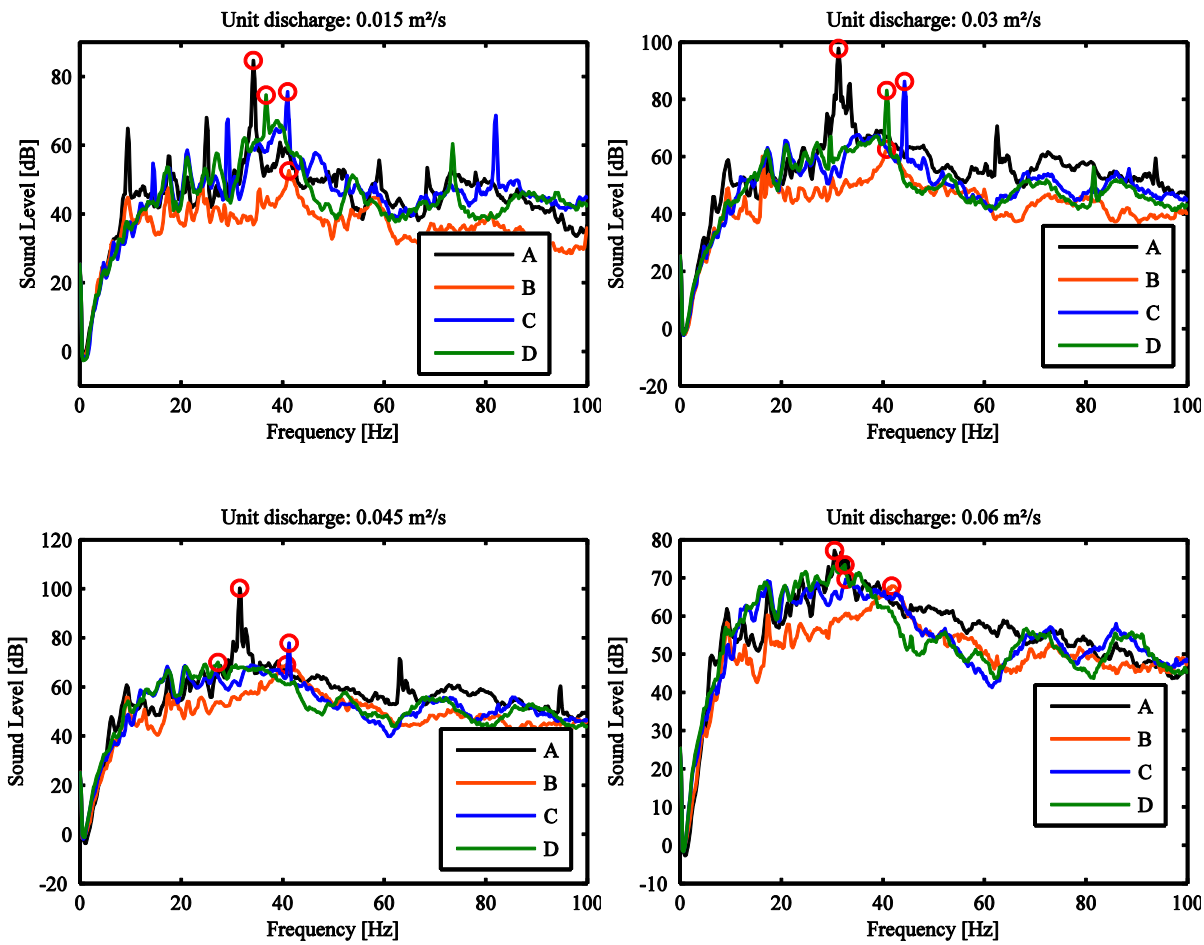

Figure 4. Audio spectrum of sound recording for A, B, C and D configurations, unit discharge between 0.015 m²/s and 0.06 m²/s.

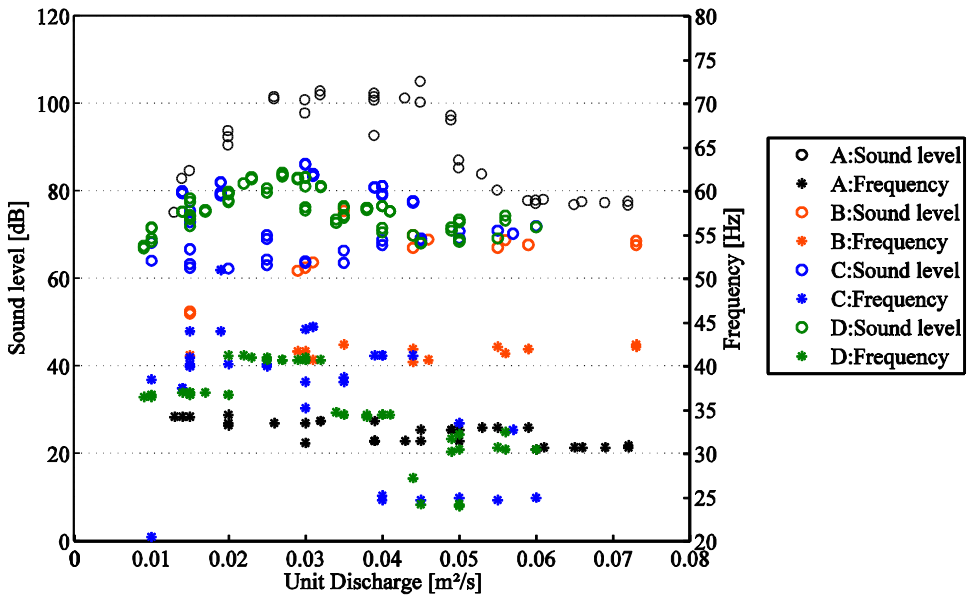

Figure 5. Summary of sound measurements for configuration A, B, C and D.

3.2. Image analysis

Horizontal bands are the visible characteristics of the nappe oscillation phenomenon. For various flow rates and all model configurations, flow visualization has been conducted. Figure 6 shows the images obtained for the configuration A and B. For the quarter round crest, horizontal bands are clearly visible for unit discharges lower than 0.06 m²/s, which is in agreement with sound measurements. In fact, the flow visualization shows nappe vibrations for the same flow ranges as those derived from the sound analysis. In contrast, for the configuration B no horizontal band is visible excepted for 0.015 m²/s. This is consistent with sound measurements as a dominant frequency peak could only be identified in configuration B for low unit discharge. However, in that configuration the nappe is impacting the back wall. For higher discharge, nappe breaks up. This creates small aerated nappes, which do not vibrate. In Configuration C and D with smaller chutes (1.00-m and 0.50-m, respectively), horizontal bands can be detected on the whole crest width (Figure 7(a)) or by zone, depending of the lighting (Figure 7(b)).

(a)

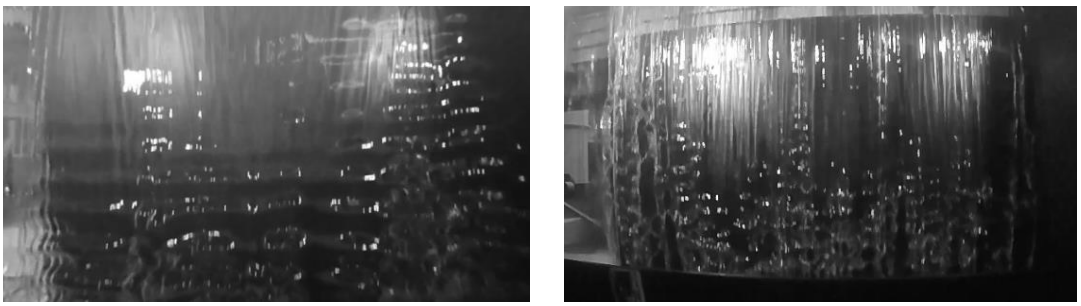

(b)

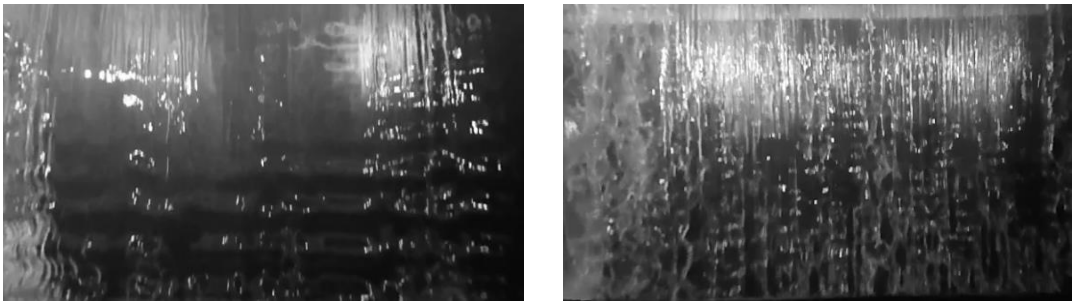

(c)

(d)

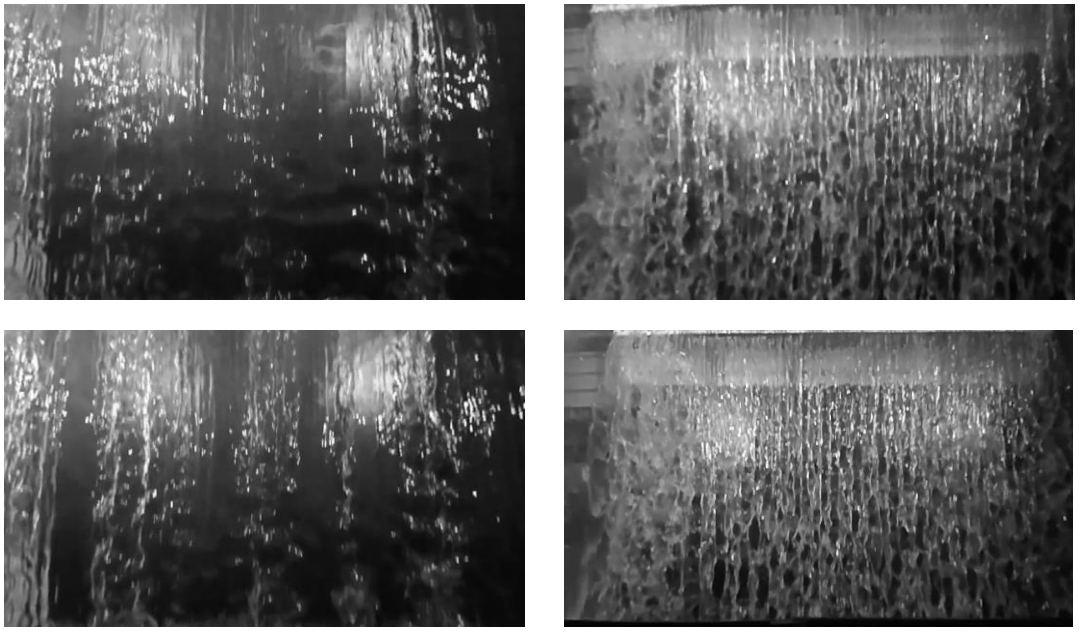

Figure 6. Nappe vibration visualization for (a) 0.015 m²/s, (b) 0.03 m²/s, (c) 0.045 m²/s and (d) 0.06 m²/s for the configuration A on the left column and the configuration B on the right column.

(a)

(b)

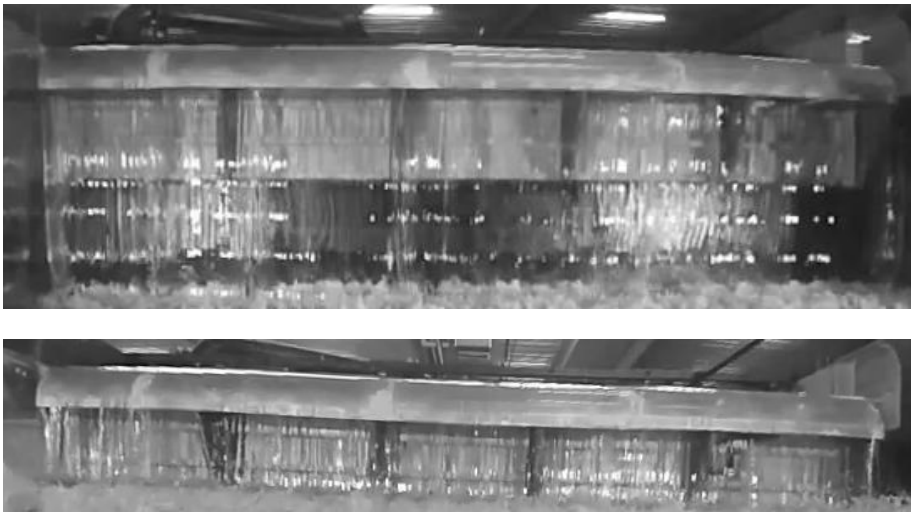

Figure 7. Nappe vibration visualization for (a) 0.01 m²/s - Configuration C and (b) 0.02 m²/s - Configuration D

Assuming that the horizontal bands are due to the lighting on the undulating surface, the frequency of the horizontal bands has been determined by the extraction of information carried by a fixed set of pixels on a succession of images. The method is conceptually sketched in Figure 8. The undulating nappe surface, represented at three successive time steps, shows horizontal bands (lit or unlit bands) that move according to the flow direction. Then, for a fixed image frame, a chosen line of pixel carries information which varies depending on whether the pixels are on the saturated zone of the oscillation or not. This information is translated on each pixel of the line into a numerical value between 0 and 255 (images encoded in 8 bits). Then, the vibration frequency is calculated by means a Fast Fourier Transform of the fluctuation of this mean value of the line of pixels. The image analysis on 100 images (recorded at 240 Hz) is illustrated for the configuration D and a unit discharge of 0.02 m²/s in Figure 9. This figure illustrates (1) the chosen line of pixel, (2) the mean value of this line and (3) the FFT of the fluctuation of this mean value. Repetitive bands are clearly visible even if for the instantaneous image (Figure 7(b)) these bands are hard to see. Moreover, this pattern corresponds to an oscillating mean value of the pixel line. And, the dominant frequency is 36 Hz, corresponding to 15 bands passing through 100 images recorded every 1/240 second.

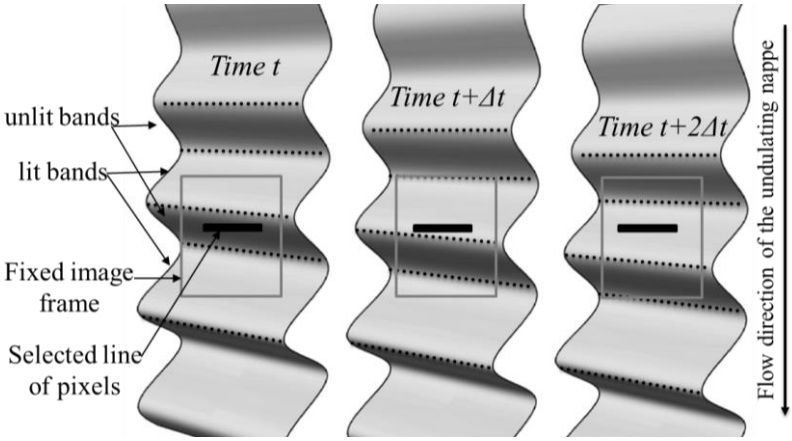

Figure 8. Conceptual representation of image analysis.

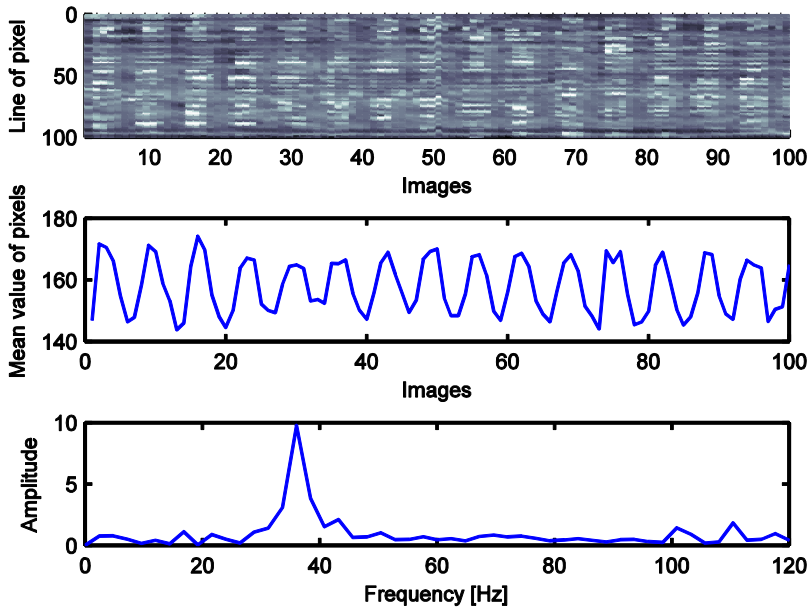

Figure 9. Image analysis on 100 images for Configuration D, a unit discharge of 0.02 m²/s.

The resolution of the image frequency calculation depends of the ratio between the acquisition frequency and the number of images frames. For an acquisition frequency of 240 Hz, a minimum of 480 frames have to be used to ensure a resolution of 0.5 Hz. For configuration A, C and D, the image analysis has been applied to unit discharges for which horizontal stripes can be observed. Indeed, for configuration B and a unit discharge of 0.03 m²/s and for configuration D and a unit discharge of 0.05 m²/s, the image analysis respectively in Figure 10 and Figure 11 provides no information regarding the nappe vibration phenomenon. Potential peaks are very low amplitudes and represent the noise of the signal. The number of chosen pixels lines (100 pixels per line) is at least 3 for each set of images. The number of sets of analyzed images is between 3 and 5 per unit discharge. The results are shown in Figure 12 and compared to relevant dominant frequencies detected by sound measurements. The frequencies derived from image analysis are identical to those resulting from sound measurements and do not depend on the considered pixels and images sets, excepted for configuration C, unit discharge of 0.01m²/s. The vibrations for the Configuration C do not appear systematically. Image analysis is thus reducing to few unit discharges. However, the derived frequency corresponds to the sound frequency measured at the same time.

As a consequence of this finding, it appears that the noise is linked to the oscillations in the falling nappe but, it cannot be explained by the impact of the nappe on the ground. Indeed assuming that the cause of noise is due to the impact, the sound frequency should be twice the visual frequency since the impact varies between two opposite particle of the cyclical nappe waves. Finally, the various behaviors observed for the 4 configurations suggest that the vibrations depend on the crest shape, the fall height and the unit discharge.

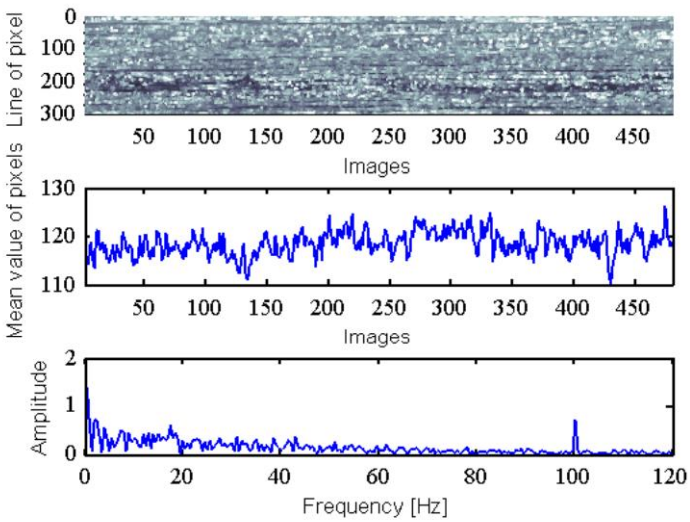

Figure 10. Image analysis on 480 images for Configuration B, a unit discharge of 0.03 m²/s.

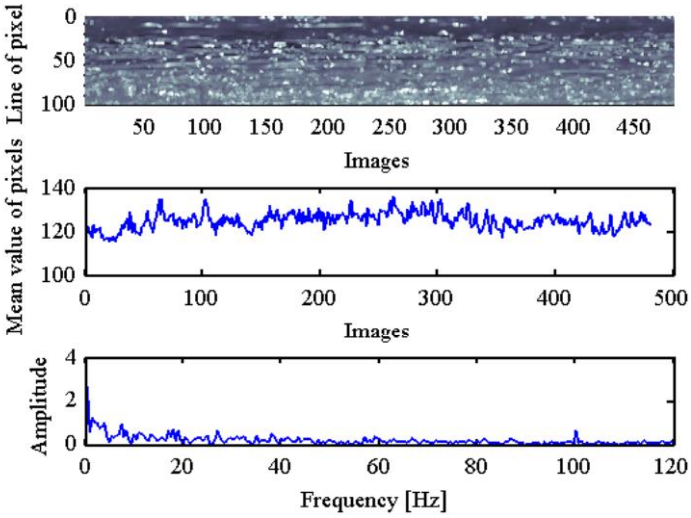

Figure 11. Image analysis on 480 images for Configuration D, a unit discharge of 0.045 m²/s.

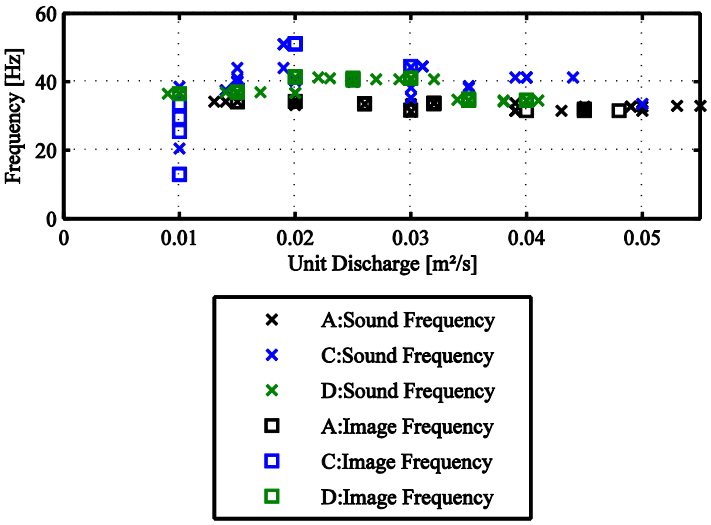

Figure 12. Results of sound and image analysis in terms of frequencies.

4. CONCLUSIONS

The research conducted on a prototype-scale linear weir model enables to describe the nappe vibration phenomenon, especially in terms of frequencies, by means of image and sound analysis. The main result is the obvious link between the frequency of the sound and the frequency of horizontal stripes in the thin flow nappes. For a prototype-scale linear weir with a 3.46-m long crest, a 3.04-m high chute and a quarter round crest, theses frequencies are in the range of 31 Hz to 37 Hz. In contrast, for a vibrating half round crest configuration and a limited fall, the dominant frequencies vary with the unit discharge, in the range of 34.5 Hz to 44.5 Hz.

The tests made on half round crest clearly show that this type of crest shape is less likely to induce nappe vibrations. A possible explanation could be the variability of the detachment point of the nappe along the crest length which disrupts the oscillations alignment. The study is still ongoing with additional tests to determine potential parameters that characterize the initiation of nappe vibration.

5. REFERENCES

Anderson, A. A. (2014). “Master thesis : causes and countermesures for nappe oscillation.” Utah State University.

Binnie, A. (1972). “The stability of a falling sheet of water.” *Proceedings of the Royal Society of London A: Mathematical, Physical and Engineering Sciences*, The Royal Society, 149–163.

Casperson, L. W. (1993). “Fluttering fountains.” *Journal of Sound and Vibration*, 162(2), 251–262.

Casperson, L. W. (1996). “Fluttering fountains: Annular geometry.” *Journal of Applied Physics*, 79(3), 1275–1278.

Chanson, H. (1996). *Some hydraulic aspects during overflow above inflatable flexible membrane dam*. The University of Queensland.

Crookston, B. M., Anderson, A., Shearin-Feimster, L., and Tullis, B. P. (2014). “Mitigation investigation of flow-induced vibrations at a rehabilitated spillway.” *Proceedings of the 5th IAHR International Symposium on Hydraulic Structures*.

Crookston, B., and Tullis, B. (2012). “Hydraulic design and analysis of labyrinth weirs. II: Nappe aeration, instability, and vibration.” *Journal of Irrigation and Drainage Engineering*, American Society of Civil Engineers.

Falvey, H. (1980). “Bureau of reclamation experience with flow-induced vibrations.” *Practical Experiences with Flow-induced Vibrations (ed. E. Naudascher & D. Rockwell). Springer*.

Helmholtz, H. von. (1868). “Ueber die Thatsachen, die der Geometrie zum Grunde liegen.” *Nachrichten von der Königl. Gesellschaft der Wissenschaften und der Georg-Augusts-Universität zu Göttingen*, 1868, 193–221.

“Investigation into spillway discharge noise at Avon Dam.” (1980). *Metropolitan water, sewerage and drainage board*, 57, 31–36.

Lodomez, M., Crookston, B. M., Tullis, B. P., Pirotton, M., and Erpicum, S. (2016). “Nappe Vibration Mitigation Techniques for Free-overfall Structures.” *ISHS 2016 - Hydraulic Structures and Society - Engineering Challenges and Extremes: Proceedings of the 6th IAHR International Symposium on Hydraulic Structures*.

Naudascher, E., and Rockwell, D. (1994). *Flow-induced vibrations: an engineering guide*. Balkema.

Schwartz, H. I. (1966). “Edgetones and nappe oscillation.” *Journal of the Acoustical Society of America*, 39(3), 579.

Squire, H. (1953). “Investigation of the instability of a moving liquid film.” *British Journal of Applied Physics*, IOP Publishing, 4(6), 167.

Sumi, T., and Nakajima, Y. (1990). “Three-dimensional characteristic of nappe oscillation and the estimation of sound pressure levels.” *Journal of Hydroscience and Hydraulic Engineering*, 8(1), 89–99.

USBR. (1964). *Experience of the Bureau of Reclamation with flow-induced vibrations*. Hydraulics branch.

DOI:10.15142/T3GP43

Water wave measurements at Bellsund in the western Spitsbergen

D. Majewski[1], W. Sulisz[1], M. Paprota[1], M. Szmytkiewicz[1]
[1]Institute of Hydro-Engineering
Polish Academy of Sciences
Gdansk, Poland
E-mail: d.majewski@ibwpan.gda.pl

ABSTRACT

The Arctic region has experienced rapid changes in the last few decades. The Arctic coasts in times of progressing global warming are exceptionally vulnerable to erosion. Arctic sea-ice extent is decreasing dramatically leaving coasts exposed to destructive action of waves. The lack of sea ice causes a dramatic increase of wave energy reaching coastline. In order to provide insight into coastal changes in Arctic areas, field measurements were carried out in the area of Calypsobyen, Bellsund, west Spitsbergen. Data of free-surface elevation, wave orbital velocities, water currents and bathymetry were collected during expedition in the western Spitsbergen. In the frame of this study a detailed analysis of wave field were performed. The collected database constitute unique and valuable source of information on Arctic wave climate.

Keywords: *Field measurements, Arctic, water waves, database.*

1. INTRODUCTION

The Arctic region is very intensively explored in the last few decades and coastal settlements are exposed to great risk. Coastal changes in the Arctic are affected by many environmental factors such as sea-level and sea-ice extend variations, wind, waves and storminess. Also the geology and morphometry of the coastline, permafrost concentration and its ground-ice content have an impact on coastal changes (Zagórski 2011). As a result of costal processes such as sediment transport due to waves and currents and degradation of permafrost, the erosion or accretion occurs affecting biological and human systems (Rachold et al. 2005). The Arctic coasts in times of progressing global warming are exceptionally vulnerable to erosion. The Arctic sea-ice extent is decreasing dramatically. According to the newest studies, sea ice extent in Arctic is decreasing 3.8% i.e. about 400,000 km^2 per decade. The situation is more dramatic when we consider the average winter ice thickness, which decreases about 16 % per decade (Comiso and Hall 2014). Disappearing of natural barrier in the form of sea ice, leaves the coasts exposed to destructive action of waves (Reda et al. 2015, Paprota et al. 2016, Sulisz et al. 2015).

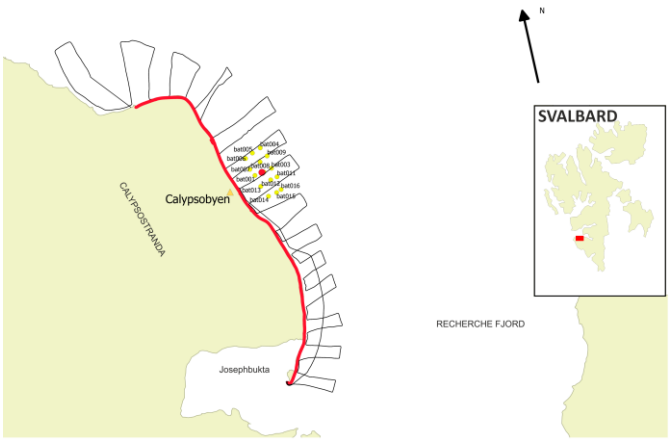

Figure 1. Measurements site at the southern part of Bellsund, Spitsbergen. Red line – coastline position, black line – bathymetry survey tracks, yellow dots – bathymetry survey with CTD probe.

The main objective of this study is to create a database of wave field characteristics in Arctic regions which will be constantly updated. The database will include other parameters useful in the estimation of coastal erosion rates such as bathymetry of nearshore zone, coastline position, and topographic profiles of the beach. This database is going to be used to verify numerical model of marine scour in Arctic conditions. Further work includes the estimation of Arctic coasts vulnerability to wave-induced erosion. In order to estimate wave energy reaching the shoreline, water wave measurements were carried out in the area of Calypsobyen, Bellsund, West Spitsbergen. Field campaign was conducted by the team of researchers from the Institute of Hydro-Engineering and Maria Curie-Skłodowska University (UMCS) during the summer season of 2015 in the vicinity of Polish Polar Station in Calypsobyen (Figure 1). Although measurements of currents, salinity, etc. were conducted in Svalbard archipelago, very little attention has been given to surface waves in that area (Mędrek et al. 2015). The database will also contribute to other fields of science. To provide full insight in the process of coastal erosion, wave measurements were supported by complementary bathymetry surveys and shoreline position tracking. Authors are going to perform second expedition to the Calypsobyen in the summer season of 2016 and supplement the database with new measurements. It will allow to estimate seasonal change of coastal erosion rate in Bellsund. This paper presents analysis of raw measurement of wind waves, currents and bathymetry.

2. FIELD MEASUREMENTS

In the Arctic conditions, a higher possibility of drifting ice and iceberg appearance, makes the use of conventional methods of surface wave measurements impossible. The floating buoy such as WaveRider is likely to be carried away or completely damaged by floating ice. Therefore, the Acoustic Wave and Current (AWAC) measuring system was chosen to be deployed. The advantage of the AWAC system is its sea floor deployment, which makes the system less vulnerable to weather conditions. The system also offers the possibility of current velocity and direction measurements. Taking into account the logistic issues regarding the expedition and morphological characteristic of the Svalbard archipelago (Zagórski 2011), authors decided to choose Calypsobyen, Bellsund, west Spitsbergen as the study area. Desirable place had to be an intermediate or shallow water area, i.e. the ratio of water depth to wavelength is less than 0.5 and the waves are already refracted and tend to propagate perpendicularly to the shoreline. The measurements were conducted from 10.06.2016 to 03.09.2016. The area of planned deployment of AWAC system was initially probed with YSI 600XL-B-M CTD device equipped with the pressure sensor. These measurements are presented as yellow dots in Figure 1. As a result, the position of the system was determined by the distance of 1 km from the coastline and is marked by a red dot in Figure 1. The water depth ranged from 8 to 10 m depending on the tide level. The device was fixed at the bottom on a tripod stand with the head of the device 0.8 m above the bottom. The AWAC was programmed to record free-surface oscillations with the highest available frequency of 4 Hz. One wave record lasted for 1,200 seconds which resulted in 4,800 points per wave record. The interval between wave records was 1,320 s. The gap between wave records lasted only 120 s and was used to register water current profile. The profiles were recorded in 18 vertical cells, every 1,320 seconds for 55 seconds and then the results were averaged. The cell vertical size was 0.5 m and the number of cells was chosen to reach the surface at the highest water level.

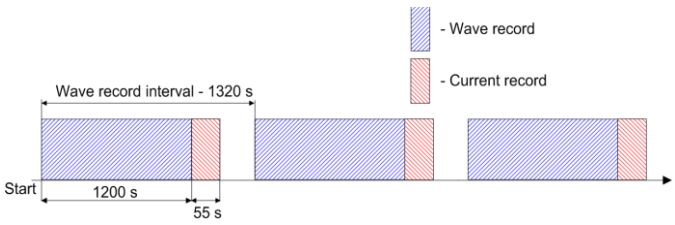

Figure 2. Time schedule of AWAC measurements.

Wave measurements were supported by bathymetry surveys and coastline position tracking. Bathymetry measurements were made from a boat by applying Garmin echoMAP DV50 echo sounder. The black line in fig. 1 depicts the path of depth measurements. The speed of the boat was kept constant to avoid the noise appearance in the bathymetry record. Moreover, archival digital bathymetry that consists of interpolated point data in the array of 10 m by 10 m was available. The position of the shoreline was measured with the Leica GPS System 500 at a known sea level. The track of coastline position is marked by red line in Figure 1. The second record of the coastline position is planned to be performed in the frame of the next expedition and will allow to determine interannual variability. Additionally, meteorological parameters such as temperature, atmospheric pressure, wind speed and wind direction were recorded by four automatic weather stations located in the western Spitsbergen.

3. RESULTS AND DISCUSSION

3.1. Waves

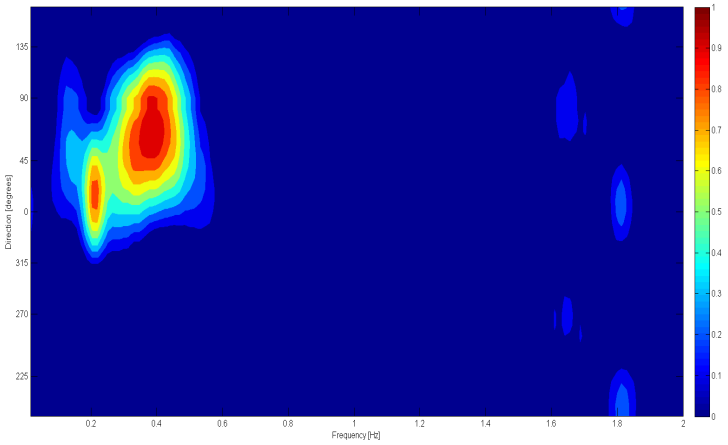

Figure 3. Normalized directional wave energy density spectrum.

Wave measurements collected using AWAC system resulted in more than 5300 wave records. The directional wave energy spectrum $S(\theta, f)$, where θ is a wave direction and f is a wave frequency, were calculated for each 20 minutes wave record. The directional spectra were calculated by applying a directional Fourier series approach which is commonly used in a wave field analysis (Boukhanovsky et al. 2007). The method was originally developed by Longuet-Higgins et al. (1963) and consists of counting first five coefficients of the directional Fourier series expansion a_0, a_1, a_2, b_1, b_2 of the directional wave spectrum $S(\theta, f)$. The spectrum is given by:

$$S(\theta, f) = \frac{a_0}{2} + a_1 \cos(\theta) + b_1 \sin(\theta) + a_2 \cos(2\theta) + b_2 \sin(2\theta) \tag{1}$$

The detailed procedure can be found in Longuet-Higgins et al. (1963) or in Earle et al. (1999). The directional spectrum for the whole period of measurements is shown in fig. 3. It can be seen that the majority of wave energy is focused around 0.2 to 0.4 Hz. The significant wave height H_s was derived with the zero up-crossing method and was compared to its spectral counterpart H_{m_0} to check the results. Differences were less than 2 %. H_{m_0} is the wave height derived on the basis of zeroth-order spectral moment from the following formula:

$$H_s = 4\sqrt{m_0} \tag{2}$$

The significant wave height H_s is plotted in Figure 4. One can distinguish some periods of stormy weather when the significant wave height grew rapidly. The most spectacular storm occurred around 28th of July when the significant wave height grew to over 1 m. The growth in H_s can be also seen on days 06/12, 07/15, 08/18, 08/25. The topography of Bellsund area enforce less wave energy which causes that the significant wave height is lower than in open waters of North-East Atlantic (Vikebø et al. 2003). Peak periods, and dominant wave directions were calculated on the basis of spectral parameters and are also plotted in Figure 4. The distributions of peak periods and wave directions are uneven when the water surface is relatively calm. With increasing H_s, when the storm is developing, the peak periods and dominant wave directions are more stable in time. The directional distribution of dominant wave directions is shown in Figure 5. The dominant wave direction coincides with North-East direction, which is with some deviation, perpendicular to the shoreline in the vicinity of Calypsostranda. Wave directions are in reasonable agreement with wind directions (Figure 6). Wavelengths were calculated according to the linear dispersion relation. Wavelengths corresponding to significant wave height are presented in Figure 7.

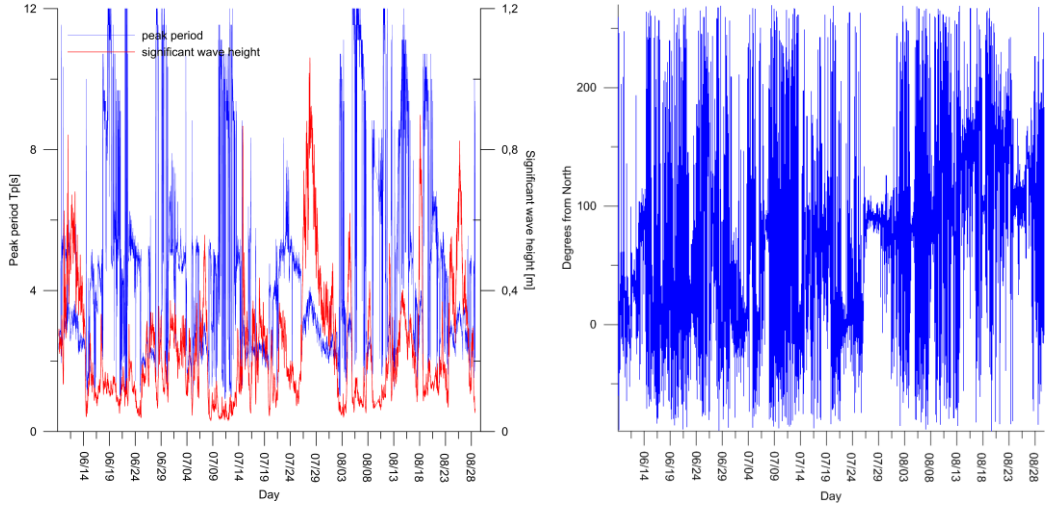

Figure 4. Time distribution of peak period, significant wave heights and dominant wave direction.

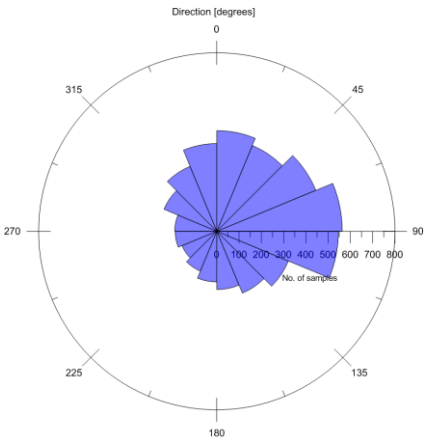

Figure 5. Wave peak directions. Zero degree is N.

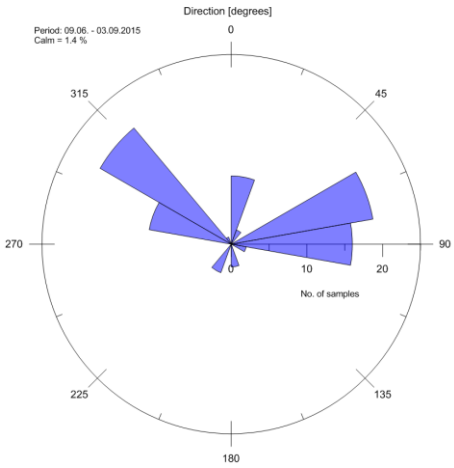

Figure 6. Wind Directions. Zero degree is N.

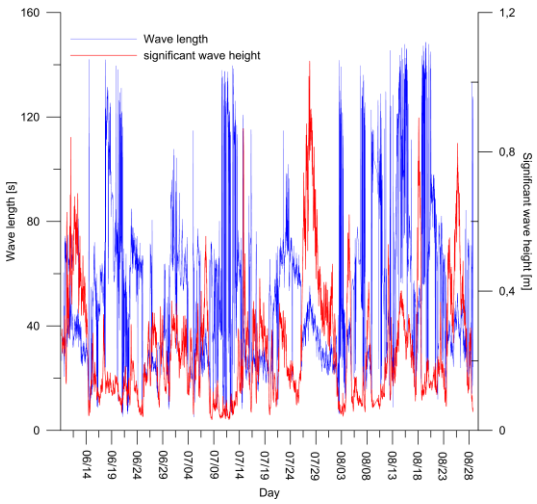

Figure 7. Time distribution of wavelengths and significant wave heights.

3.2. Currents

The current speeds and directions recorded during expedition are shown in Figure 8. Angels on right plot correspond to the real north shown in Figure 1. The plots show that during strong storms, when significant wave height is increased, the current becomes more homogenous over depth and its magnitude increases, as expected. This is especially seen on day 07/28 on both plots in Figure 8. Similar situation can be observed also around days 06/12, 06/28, 08/10, 08/18, 08/25. When the significant wave height decrease and the storms become weak, the upper and bottom layers of the water column move southward, which is consistent with wave directions. The middle layer of water column moves northward, creating a certain circulation pattern. For weak storms the current usually decreases with water depth.

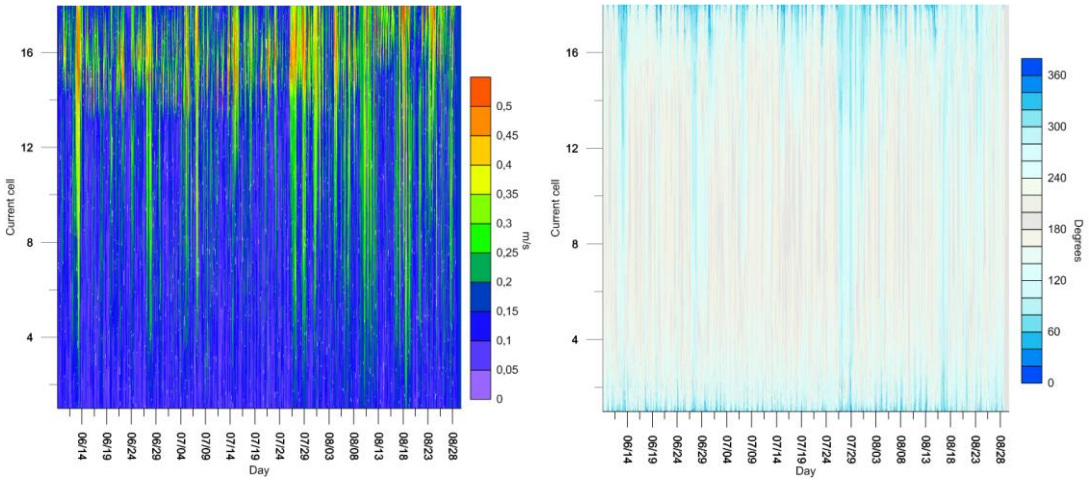

Figure 8. Current speed and current direction profiles.

3.3. Bathymetry

The bathymetry measured during the expedition and the archive data are presented in Figure 9. The archive data were collected by Norwegian Hydrographic Service (NHS) and consist of interpolated data in the grid of 10 m by 10 meters. The comparison of the historical data with the bathymetry recorded in the course of this study showed that the NHS bathymetry is very general and misses many details related to underwater land forms. This can be seen on the chosen profiles taken from both databases (Figure 10). In Figure 10, the profiles were set to be perpendicular to the shoreline and to pass through the AWAC position. Due to large uncertainty in historical bathymetry data, the analysis of changes in depth over time led to unreliable results. Nevertheless, archival bathymetry can be useful as a supplement data collected in the course of this study. Analysis of the bathymetry showed that the coastal zone of Recherche Fjord is composed of two steep slopes and the 1.5 km long relatively flat section between the slopes. The toe of the first steep slope is located at the depth of 10 m, while the second one is located at the depth of 80 m.

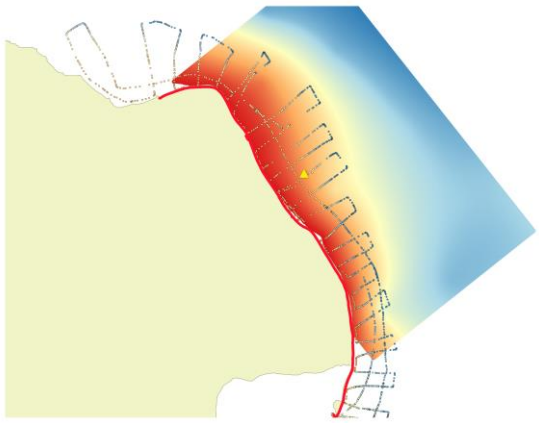

Figure 9. Bathymetry surveys and archival bathymetry data.

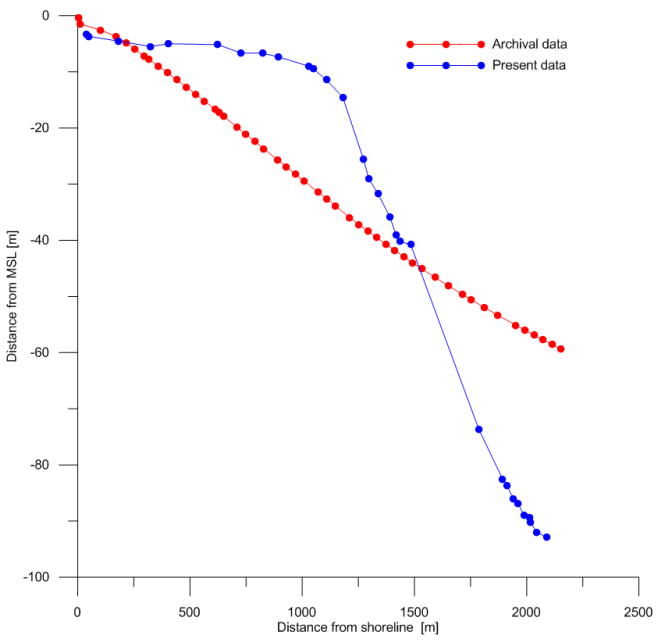

Figure 10. Depth profiles from bathymetry data.

4. CONCLUSIONS

The results of the present work constitute a unique and valuable database of Arctic wave climate parameters. Particularly, wave records of frequency 4 Hz are very rare. Data of free-surface oscillations and wave peak direction are in good correlation with wind directions and show the maximum variance of 50 degrees. Significant wave height is lower than in open waters of North-East Atlantic, which limits wave-induced erosion. Current directions are parallel to the shoreline with some discrepancies during storms. The authors were unable to estimate time dependent bathymetry changes due to inaccuracy of archival data. A detailed analysis will be performed on the basis of measurements collected during presented and future expedition, which is planned to be carried out in the summer season of 2016. Accordingly, an estimation of coast vulnerability to wave-induced erosion will be performed when the data of seasonal changes of the coastline position will be available.

5. ACKNOWLEDGMENTS

The research leading to these results has received funding from the Polish-Norwegian Research Program operated by the National Centre for Research and Development under the Norwegian Financial Mechanism 2009-2014 in the frame of Project Contract No. POL-NOR/200336/95/2014.

6. REFERENCES

Boukhanovsky A. V., Lopatoukhin L. J., Soares C. G. (2007). Spectral wave climate of the North Sea, *Applied Ocean Research*, 29(3).

Comiso JC, Hall DK. (2014). Climate trends in the Arctic as observed from space. *Wiley Interdisciplinary Reviews Climate Change*, 5(3).

Longuet-Higgins, M.S., Cartwright, D.E., Smith, N.D. (1963). Observations of the directional spectrum of sea waves using the motions of a floating buoy, Ocean Wave Spectra, *Prentice-Hall, Englewood Cliffs, NJ*.

Earle, M. D., Steele, K. E., & Wang, D. W. C. (1999). Use of advanced directional wave spectra analysis methods. *Ocean engineering*, 26(12).

Mędrek K., Herman A., Moskalik M., Rodzik J., Zagórski P. (2015). Impact of wave action on the structure of material on the beach in Calypsobyen (Spitsbergen). *European Geosciences Union General Assembly*, Vienna.

Paprota M., Majewski D., Sulisz W., Szmytkiewicz M., Reda A. (2016). Effects of climate changes on coastal erosion in Svalbard. *Proc. of the 7th International Short Conference on Applied Coastal Research*. (in press)

Rachold, V. , Are, F. E. , Atkinson, D. E. , Cherkashov, G. and Solomon, S. M., (2005). Arctic Coastal Dynamics - An Introduction, *Geo-marine letters*, 25.

Reda, A., Sulisz, W., Majewski, D., Paprota, M., Szmytkiewicz, M. (2015). Application of a new approach for modeling of coastal erosion in Arctic areas. *Proc. 2nd International Workshop on Hydraulic Structures: Data Validation*, Coimbra, 217-221

Sulisz W., Szmytkiewicz M., Majewski D., Paprota M., Reda A. (2015). A new approach for the prediction of coastal erosion in Arctic areas. *Proc. of the 9th Symposium on River, Coastal and Estuarine Morphodynamics*, Iquitos, 1-4.

Vikebø F., Furevik T., Furnes G., Kvamstø N. G., Reistad M., (2003). Wave height variations in the North Sea and on the Norwegian Continental Shelf, 1881–1999, *Continental Shelf Research*, 23(3–4).

Zagórski, P., (2011). Shoreline dynamics of Calypsostranda (NW Wedel Jarlsberg Land, Svalbard) during the last century. *Polish Polar Research*, 32(1).

DOI:10.15142/T3C014

Large Eddy Simulation of the water flow around a cylindrical pier mounted in a flat and fixed bed

P. X. Ramos[1,2], R. Maia[1], L. Schindfessel[2], T. De Mulder[2] and J. P. Pêgo[1]
[1]Dep. Civil Engineering
University of Porto – Faculty of Engineering
Porto, Portugal
[2]Hydraulics Laboratory
Dep. Civil Engineering – Ghent University
Ghent, Belgium
E-mail: pedro.ramos@ugent.be

ABSTRACT

In the present work, a numerical model based upon the Large Eddy Simulation approach has been set up for predicting the three-dimensional flow around a cylindrical pier, mounted on a flat and fixed bed, a generic case that is relevant for the study of flow and scour around bridge piers. This turbulent flow configuration was studied experimentally by Nogueira et al. (2008) with Particle Image Velocimetry (PIV). The main goal of this paper is a first validation of the numerical model, based upon the available data. The numerical tool is capable to qualitatively reproduce the characteristic flow features around the pier, like e.g. the horseshoe vortex system and the vortex shedding in the wake. The predicted extent of the initial scour hole, based upon the bed shear stress magnitudes, agrees well with the observations at the onset of the souring process during the lab experiments. Further quantitative validation of the numerical model will benefit from additional measurement efforts in the experiments.

Keywords: *CFD, LES, Ansys Fluent, cylindrical pier*

1. INTRODUCTION

The flow past a circular cylinder is of practical relevance for many engineering fields, with regards to the flow around e.g. towers, chimneys, cables or bridge piers, with the latter being the subject of this work.
The flow disturbance caused by piers on riverbeds usually induces scour around those structures. The principal features of the corresponding flow pattern are shown in Figure 1. As the flow approaches the pier, its velocity decreases down to the point where the flow is halted at the upstream face of the obstacle. As a consequence of the change of the pressure field, an increment on the level of the free surface on the upstream side of the pier occurs, forming the so-called surface roller. Accordingly, the approach velocity is higher near the water surface than near the bed, as well as the pressure. Therefore, this pressure gradient results in a downflow that impinges on the bed and it is partially deflected upstream. Simultaneously, the boundary layer of the approaching flow undergoes a three-dimensional separation due to the adverse pressure gradient induced by the pier. The resulting horseshoe vortex is subsequently advected along both sides of the pier base. The aforementioned phenomena tend to scour the pier's foundation, both upstream and at the sides of the pier.
Scour around obstacles in rivers occurs after the formation of a scour cavity of sufficiently large dimensions to stabilize the large-scale oscillations of the horseshoe vortex (Kirkil and Constantinescu 2010). The latter dissipates itself downstream the pier, having an important role in the bed scour due to the bed material trailing (Melville and Coleman 2000).
At the lee side of the pier, the shedding of wake vortices can be seen. While the horseshoe vortex causes essentially the entrainment of the bed material, the wake vortices pluck the particles with a suction effect, transporting them then in suspension (Melville and Coleman 2000).
In summary, turbulent structures over a wide range of scales are present around the cylinder, controlling the entrainment and transport of sediment from the scour hole. Hence, to understand how the flow induces scour on the bed, it is necessary to properly account for the structure of the large-scale eddies around the cylinder.

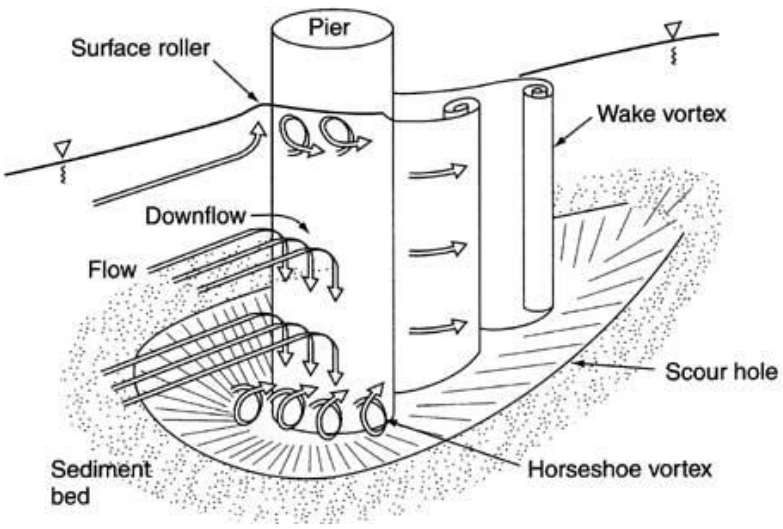

Figure 1. Flow pattern around a circular pier (Hammil 1999)

The flow around a circular cylinder has been extensively studied in fluid mechanics. For many years, due to the complexity of the flow structures involved, the study of this issue has been mostly experimental. Nevertheless, in the last decades, the numerical modeling of the flow around piers has been a growing field.

Thwaites (1960) reviewed the previous aerodynamic experimental studies about the flow around cylindrical structures. One of the earliest computational studies about flow around circular cylinders was conducted by Beaudan and Moin (1994). Nakamura et al. (1996) studied the vortex shedding from a rectangular pier both numerically and experimentally. Yulistiyanto et al. (1998) focused on the modeling of the flow over cylinder on shallow-water. Large Eddy Simulation (LES) was initially introduced for simulating atmospheric flows in the 1960s (Smagorinsky 1963) and has become one of the most successful methodologies for eddy-resolved modeling of turbulent flows (Zhiyin 2014). Researchers' attention has turned to the application of this model to flow around bluff bodies (e.g. Sakamoto et al. 1993, Yang et al. 1993, Murakami and Mochida 1995, Rodi et al. 1997, Franke and Frank 2002, Lisenko et al. 2012). Breuer (1998) studied the numerical and modeling influences on Large Eddy simulations for the flow past a circular cylinder. Catalano (2003) performed LES simulations of the flow around a circular cylinder at high *Reynolds* numbers. Kuroda et al. (2007) studied the flow around a rectangular cylinder (applying LES) and then compared the results with particle image velocimetry (PIV) data. Zhao and Huhe (2006) presented a 3D LES of the flow around a cylindrical pier.

Reviews of advances in the use of LES to study flow around bodies can be found in Zhiyn (2014), Majeed et al. (2015) and Schanderl and Manhart (2016), with the latter focused on the bed shear stress around a cylinder.

The hydrodynamic studies are important to understand and minimize the result of the deflection of the flow caused by the obstacle: scour. To understand scour around piers quantitative and qualitative data of the flow field are required. Although this subject has been extensively studied, some features of the flow are not fully understood. The body geometry is quite simple, but the flow structures around the body can be very complex, including separation with no fixed separation point, transition to turbulence in the thin shear layers, which are separating, and shedding of large scale vortices (Zdravkovich 1997). Nogueira et al. (2008) studied the flow around a cylindrical pier by means of PIV, showing the presence of the downflow and horseshoe vortex system upstream the cylindrical pier (schematized in Figure 1).

Although the main interest of the authors is scour around bridge piers, the primary goal of this paper is to assess the quality of an eddy-resolving numerical model based upon the LES approach for the flow field around a cylindrical pier in a flat fixed bed, representative for the initial phase of the scour process. More specifically, the objective is to simulate the flat bed lab experiments of Nogueira et al. (2008), allowing a partial validation of the numerical predictions. Additionally, validation data from literature will be used. This validation exercise is a first step towards numerical simulation of the scouring process and countermeasures (of cylindrical and even more complex bridge pier geometries).

Note that the use of the LES approach allows to reveal the dynamics of large-scale eddies in the flow around a circular pier, enabling the study of the influence of the flow structures on the bed shear stresses (which are difficult to measure in laboratory experiments) and on the cylinder itself. The bed shear stress values are useful to identify where and how scour will start to occur.

The outline of the paper is as follows. In section 2, the characteristics of the studied flow configuration will be described. Section 3 presents the numerical model set-up and verification criteria. Results on the instantaneous velocity fields, drag coefficient and bed shear stress are presented and discussed in section 4. Conclusions are drawn in section 5.

2. FLOW CONFIGURATION

As stated before, the reference case used for the numerical simulation is the experimental work of Nogueira et al. (2008), namely the configuration with a flat and fixed bed (Figure 2 and Table 1). The laboratory work was performed in a long water flume with 0.7 m width (*B*) and 8 m length. A PVC cylinder with 0.048 m diameter (*D*) was positioned and founded in the channel bed. The bed material consisted of quartz sand with a median diameter (d_{50}) equal to 0.837 mm with a coefficient of gradation (σ_D) equal to 1.48.

Figure 2. Experimental installation (from Nogueira et al. 2008)

Nogueira et al. (2008) also aimed at the study of the scour around the pier, measuring the scour cavity after 5 minutes (corresponding to 45 % of the equilibrium scour depth). The maximum depth of local scour is obtained for flow conditions near the critical condition ($U \approx U_c$), i.e. the mean flow velocity corresponds to the initiation of the particles' motion (Melville and Coleman 2000). Thus, the flow rate supplied (*Q*) was 20 l/s and the flow depth (*h*) equal to 0.10 m, resulting in a mean flow velocity of 0.286 m/s, a value which lies between the critical velocities suggested by Goncharov and Neil equations (Nogueira et al. 2008). The water temperature was kept around 20°C. Taking in consideration the features provided, the Reynolds number of the flow calculated based on the pier diameter is given by $\mathrm{Re}_D = 1.37\times10^4$. The contraction and wall effects were negligible to the scouring process, since ratios of $B/D \geq 10$ and $B/h \geq 5$ (Moreno et al. 2012, Ramos et al. 2015) were guaranteed (see Table 1).

In accordance with the Shields diagram (Shields 1936), the critical shear stress of the bed particles is approximately 0.48 Pa. This parameter will be useful to compare with the bed shear stress values obtained in the numerical simulations.

Table 1. Characteristic parameters of experiment by Nogueira et al. 2008

d_{50} (mm)	B (m)	D (m)	B/D (-)	h (m)	B/h (-)	Q (m^3/s)	U (m/s)	Re_D (-)
0.837	0.7	0.048	14.58	0.10	7.00	0.20	0.286	1.37×10^4

No measured data for the drag force on the pier are available in the data set of Nogueira et al. (2008). Therefore, use is made of information in the literature. The drag force on the pier depends on the *Reynolds* number. If the approaching flow were to be uniform over the flow depth, which is not the case in the experiment, the drag coefficient, C_D, is expected to oscillate around the mean value of 0.683 for $\mathrm{Re}_D = 1.37\times10^4$ (Figure 5.3 of White 2006).

The oscillations of the drag force may (in principle) also be important to the pier's structural design, but this is beyond the scope of this paper. To quantify the shedding frequency of the wake vortices, no use can be made of measured velocities in the lee side of the pier, since they are absent in the data set of Nogueira et al. (2008). Therefore, again information in the literature will be relied upon. For a given main frequency, *f*, of the vortex shedding, the corresponding dimensionless *Strouhal* number, *St* (White 2006) is:

$$St = \frac{f.D}{U} \tag{1}$$

where *D* is the diameter of the pier. For the present case, the *Strouhal* number according to literature (Figure 3) assumes a value of about 0.20. This yields a vortex shedding frequency of 1.19 Hz, hence a period (*T*) of 0.84 s.

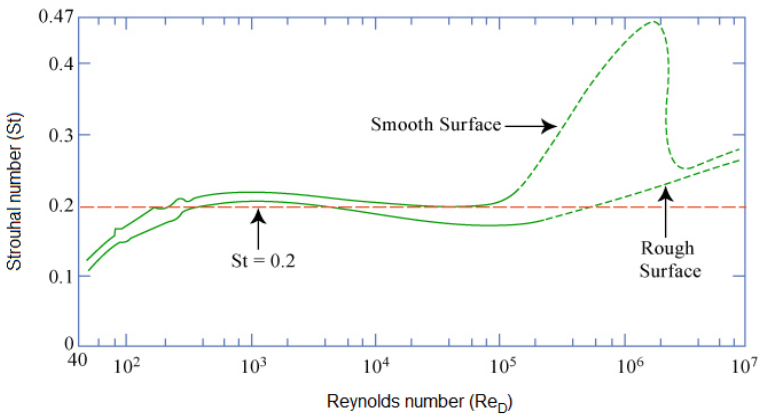

Figure 3. Relationship between *Strouhal* number and *Reynolds* number for circular cylinders, after Techet (2005), data from Lienhard (1966) and from Roshko (1955)

3. NUMERICAL MODEL

3.1. Computational mesh

A 3-D finite-volume incompressible Navier-Stokes model, applying the Large Eddy Simulation approach, is set up and run by means of the *Ansys Fluent* software. The mesh used for the simulations is a parallelepiped (0.7 m wide and 0.1 m high), representing the fluid domain, with a cylindrical cavity, with a diameter of 0.048 m, representing the pier (Figure 4). The geometric model is not very complex, allowing the adoption of a block-structured mesh with an O-grid mesh with a radius of 6*D* around the cylinder. The pier's zone was subjected to a further refinement (Figure 5 and Figure 6), as well as the cells next to the walls and bed. Note however, that the wall boundary layers are not fully resolved. In order to limit the computational time, a so-called wall model will be relied upon. In Figure 4, the sub-zones of the mesh are indicated. The grey arrows indicate the cell size gradient direction (from the smallest to the biggest cell). Note the smaller cells are next to the cylindrical pier and walls (Table 2). Also, a size cell gradient in the *z*-direction was applied (with the finer cells near the bed). Note that the presented mesh is the final result of some (iterative) mesh optimization efforts, aiming at mesh independency of the solution as well as respecting some quality criteria (see also 3.5).

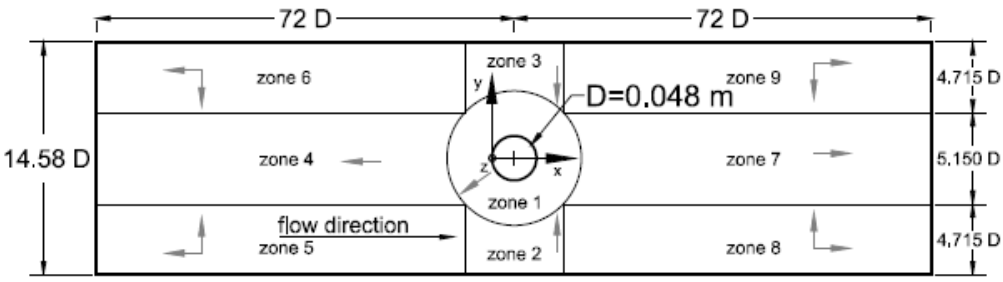

Figure 4. Computational domain with indication of the zones of the mesh and direction of the cell size grading (not to scale)

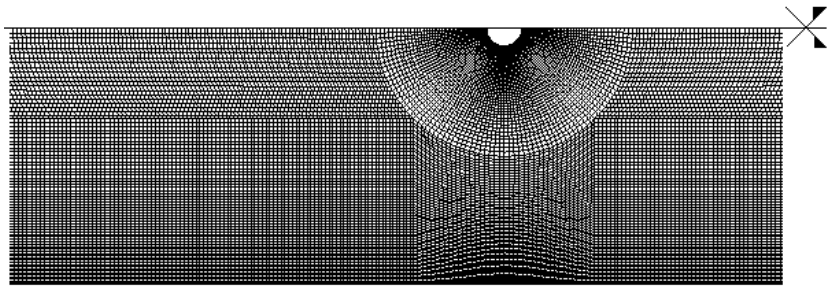

Figure 5. Partial plan view of the mesh (mesh is symmetric with respect to the x axis shown in Figure 4)

Table 2. Number of cells in each zone of the mesh

Zone of the mesh	*x*-direction		*y*-direction		*z*-direction	
	Size of first cell (mm)	Number of Cells	Size of first cell (mm)	Number of Cells	Size of first cell (mm)	Number of Cells
1	0.005	200	0.0025	100	0.015	80
2, 3	0.010	30	0.010	50	0.015	80
4	3.000	400	3.000	80	0.015	80
5, 6	0.010	400	0.010	60	0.015	80
7	3.000	300	3.000	80	0.015	80
8, 9	0.010	300	0.010	30	0.015	80

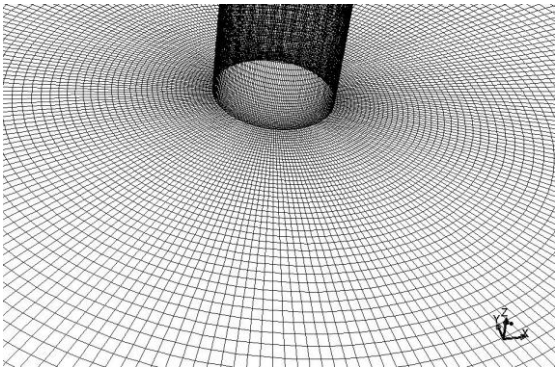

Figure 6. Detailed view of the mesh next to the pier

3.2. Boundary conditions

Taking advantage of the available PIV data regarding the approaching flow, the inlet boundary condition was defined by three velocity profiles at y = 0.175 m, y = 0 m (symmetry axis) and y = –0.086 m, respectively (i.e. points A, B and C of Figure 7), corresponding to the total discharge (Q = 20 l/s). According to the literature, the inlet distance from the pier (72D) is sufficient for the turbulence to be developed (Ferziger and Peric 2002). The standard wall model from *Fluent* (Launder and Spalding 1974) was used to model the flow near the walls, bed and pier. In the outlet, the outflow condition from *Fluent* was applied, meaning a zero diffusion flux for all flow variables (the conditions of the outflow plane are extrapolated from within the domain and have no impact on the upstream flow) and an overall mass balance correction.

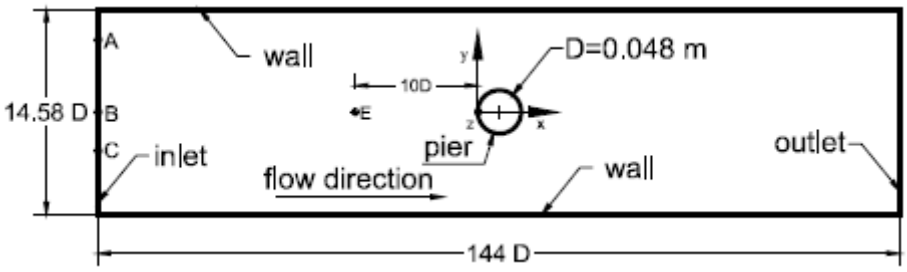

Figure 7. Schematic description of the domain (plan view) and its boundary-conditions (not to scale).

The upper boundary condition (water surface) was modelled by means of a rigid lid without any friction. As mentioned before (Section 1) and shown in Figure 8, in reality an elevation of the water level occurs upstream of the pier, a phenomenon which is accompanied by a surface roller.

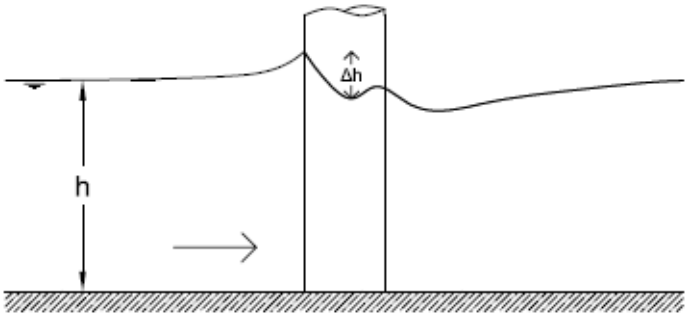

Figure 8. Schematic description of free-surface upstream the pier (Roulound et al. 2005).

The free surface elevation upstream the pier is a phenomenon mostly influenced by the *Froude* number of the flow (Roulund et al. 2005). The higher the *Froude* number, the bigger is the described effect. For relatively small *Froude* numbers, Δh (i.e. the difference between the water level immediately upstream the pier and the lowest point of the water surface close to the pier) is given by Equation 2 (Roulund et al. 2005).

$$\frac{\Delta h}{h} = \frac{Fr^2}{2} \tag{2}$$

In the present case, the *Froude* number is 0.29. Thus, Δh is expected to be about 4.2 mm, i.e. about 4 % of the flow depth. Since this value is relatively small (Roulund et al. 2005), the rigid lid approximation seems to be acceptable.

3.3. Sub-grid scale model

When using LES, the time-dependent, three-dimensional, spatially-averaged Navier-Stokes equations are solved. In this method, the largest scales are resolved numerically on the mesh, while the unresolved scales must be modeled with a sub-grid scale model. This study adopts the most widely used sub-grid scale model, being the standard Smagorinsky model with a Smagorinsky constant C_s=0.1 (Smagorinsky, 1963).

3.4. Numerical solution

The PISO solver was used, since it is the most suitable one for turbulent flows of incompressible fluids (Singh 2004). Both skewness and neighbor correction values were set to 1. Discretization in space and time are second order accurate. A constant time step $\Delta t = 1\times10^{-3}$ s was chosen (regarding $\Delta t/T << 1$ and after conducting several sensitive analysis). The maximum number of iterations per time-step was 20.
Simulations were carried out on the supercomputer platform of Ghent University. The residual values were controlled and kept below the recommended values for convergence (Kulkarni and Moeykens 2005). After a period of 100*T*, a quasi-steady vortex shedding was established.

3.5. Model verification

During the simulations, the residuals value were recorded and kept under the values recommended by Ansys Fluent Theory Guide. After trying several meshes and model parameters, the model described above was found to (largely) fulfill two important criteria. The first criterion is related to the use of the standard wall function and requires the dimensionless wall distance y+ of the first cells near solid walls to be within the range of $30 \leq y+ \leq 500$ (Keylock et al. 2012). This condition was verified in several locations of the computation domain, with a special look to the cells near the pier and the bed.
The second criterion requires a LES simulation to have at least 80 % of the turbulent kinetic energy being resolved by the mesh (Pope 2004). Not all parts of the mesh meet this criterion (see Figure 9, obtained by the approach described in Coussement et al. 2012). In the region around the pier, however, the second criterion is largely met.

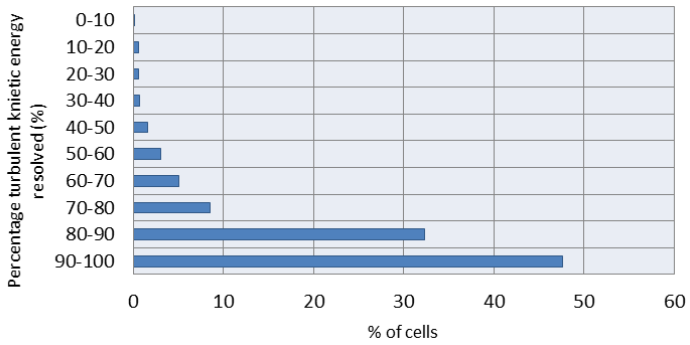

Figure 9. Percentage of turbulent kinetic energy resolved on the mesh

4. RESULTS AND DISCUSSION

4.1. Drag force on the pier

Figure **10** presents the variation in time of the drag coefficient for the entire pier during a period of 60*T*. Note that the drag coefficient is calculated automatically by *Fluent* by integrating the instantaneous pressures and shear stresses on the entire pier surface. The drag coefficient is found to oscillate around a mean value (0.602). The irregularities observed in the behavior of the drag coefficient, and thus the drag force, might be explained by the unstable three-dimensional breakup of the vortices, as other studies report (Lysenko et al. 2012). Note that the time-averaged value of the drag coefficient (0.602) is somewhat lower than the value according to the literature (0.683), which was derived in Section 2. The latter value, however, assumes an infinitely long cylinder (with a uniform approaching flow over the depth).

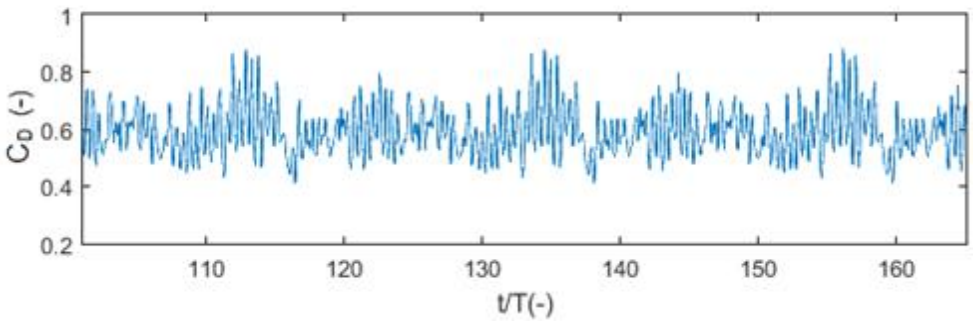

Figure 10. Time evolution of numerically predicted drag coefficient for the entire pier

To quantify the vortex shedding frequency – which is half the value of the drag coefficient oscillations (Blevins 1999) – a Fourier analysis was carried out, resulting in a main frequency of approximately 2.20 Hz (Figure 11). Therefore, the vortices detach themselves from the pier at a frequency of 1.10 Hz. This corresponds to a *Strouhal* number (Equation 1) of 0.19, a value relatively close to the one expected from the literature (0.20, see Section 2).

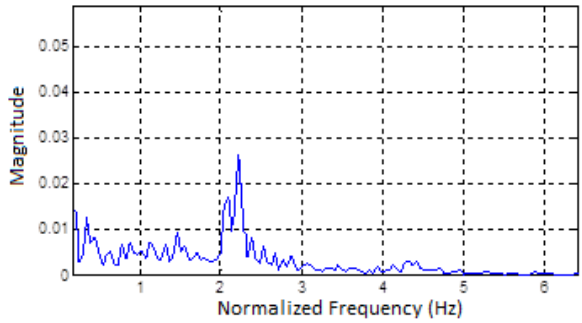

Figure 11. Spectrum of frequencies of the numerically predicted drag coefficient of the entire pier (FFT analysis)

4.2. Velocity fields around the cylindrical pier

The turbulent flow features around a cylinder are vastly documented in the literature. To validate the numerical model results, however, first the available experimental data for this particular flow configuration, will be used. In Figure 12, the velocity profiles 10*D* upstream of the cylindrical pier in the symmetry plane (i.e. point E in Figure 7) are compared (R^2=0.89).

Note that the PIV data of the approaching flow are used as inlet boundary condition. Around 3 meters (62*D*) downstream of the inlet, i.e. at point E, the numerical and experimental profiles still match reasonably well, with some discrepancies near the bed (specifying inlet boundary conditions in a LES model is particularly difficult (Zhiyin 2014). Moreover, it seems that the rigid lid approach does not affect the velocity profile too much, near the upper boundary.

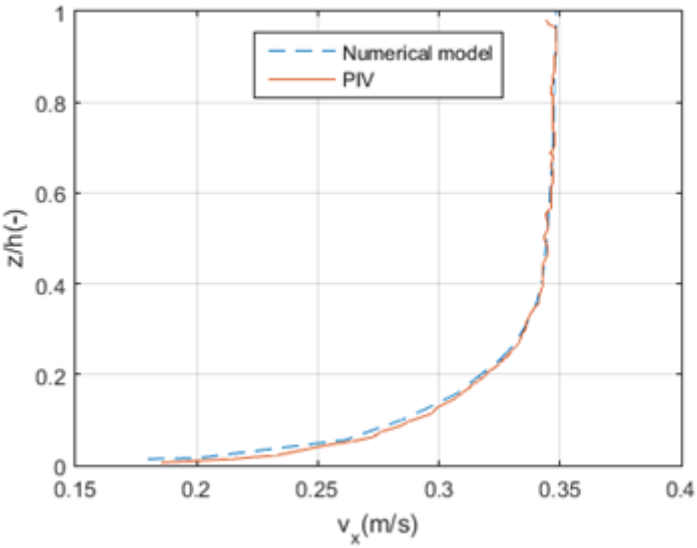

Figure 12. Comparison of measured and numerically predicted approaching velocity profiles in point E of Figure 7 (10*D* upstream of the cylinder in symmetry plane)

A map of an instantaneous velocity field is presented in Figure 13, for the zone near the bed, upstream of the cylinder. The presence of the horseshoe vortex system and the downflow is evident and the qualitative comparison with the PIV results is satisfactory (see Figure 11 of Nogueira et al. 2008).

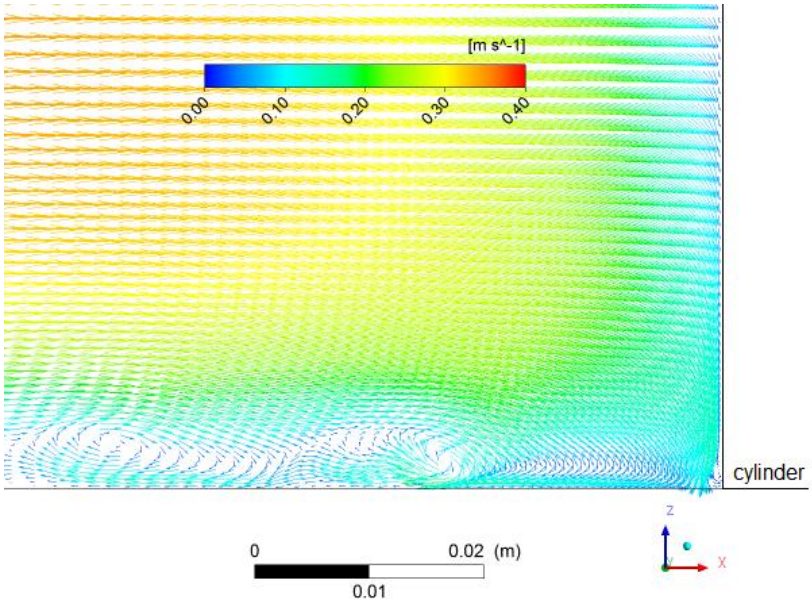

Figure 13. Numerically predicted instantaneous velocity field (near the bed, upstream of the pier) with vectors with colours according to the magnitude (m/s)

In plan view, numerically predicted instantaneous velocity magnitudes around the pier are shown in Figure 14 (at z/h = 0.5) and in Figure 15 (at z/h = 0.01). In both figures there is a clear influence of the vortex shedding, since the velocities occur asymmetrically in the two distinct instants in time and the individual vortices are perceptible.

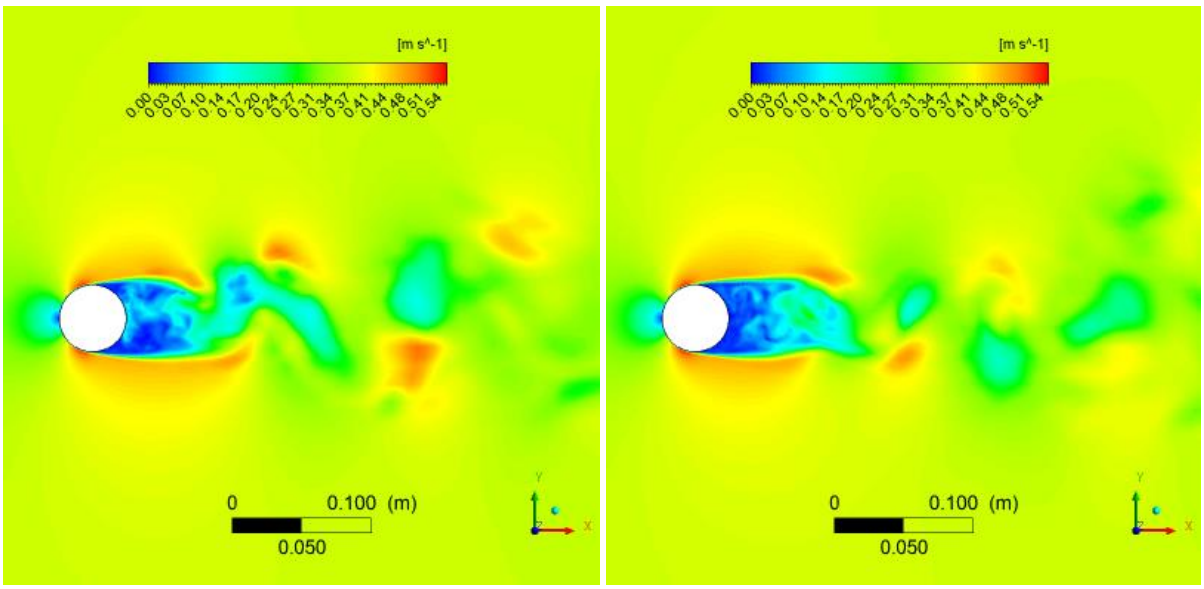

Figure 14. Numerically predicted instantaneous velocity magnitudes in plane z/h = 0.5 at two instances in time: t/T = 150 (left panel) and t/T = 155 (right panel)

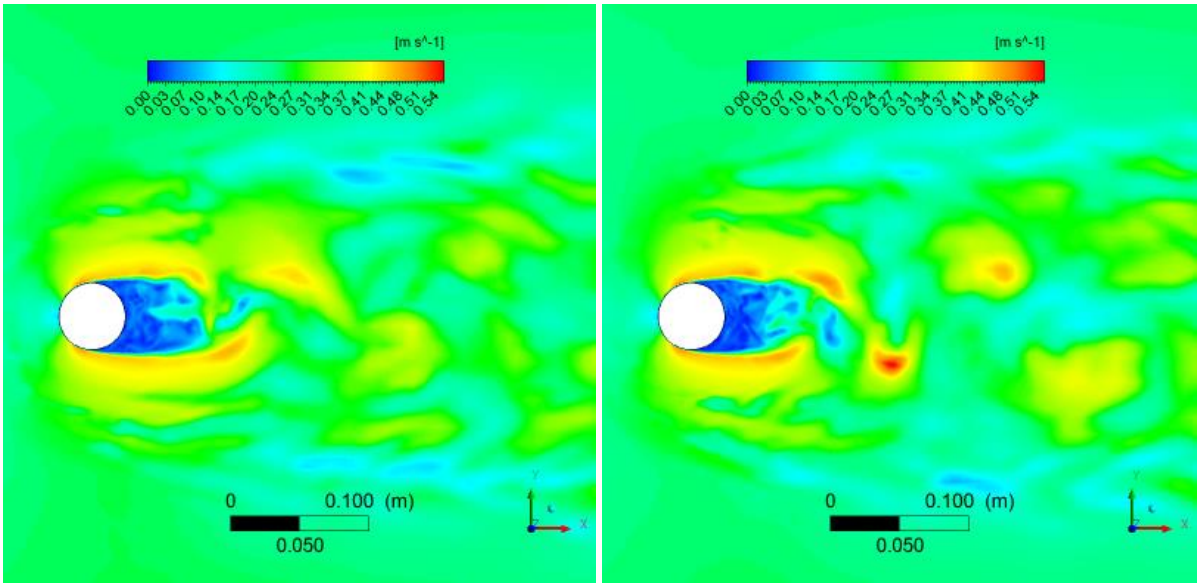

Figure 15. Numerically predicted instantaneous velocity magnitudes in plane $z/h = 0$.
at two instances in time: $t/T = 150$ (left panel) and $t/T = 155$ (right panel)

In Figure 16 the velocity in point 1 is presented for a duration of $2T$. The chosen (small) window of time is intended to be able to illustrate the effect of alternating vortices (higher amplitudes) as well as the effect of the smaller turbulence scales (minor variations). However, there is no clear dominant frequency, perhaps due to the location of the chosen point.

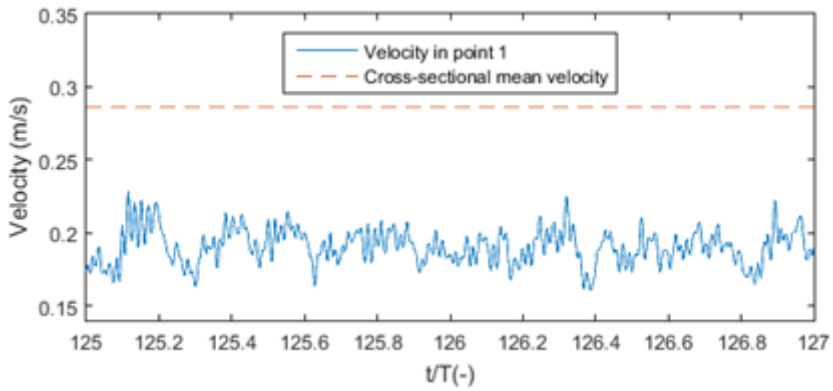

Figure 16. Numerically predicted velocity magnitude at half-height in point 1 (marked in Figure 17)

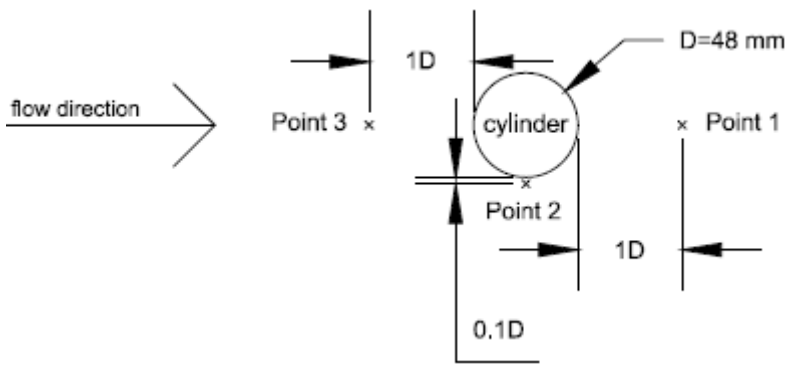

Figure 17. Schematic description (plan view) of the discrete points used to investigate time series of velocity magnitude and bed shear stress. Points 1, 2 and 3 are at $z/h = 0.5$ (half-height), $z/h = 0$ (bed) and $z/h = 0.1$ (near bed), respectively.

Analysis of the velocity magnitude time series in a near-bed point upstream of the pier (point 3 of Figure 17) does not reveal a distinct dominant frequency, suggesting that the horseshoe vortex system has a complex dynamic behaviour.

4.3. Bed shear stress

The flow deflected by the pier induces increased bed shear stresses, capable of moving bed particles, with the higher values in the side close to the pier. Figure 18 shows the temporal evolution of the bed shear stress in point 2 (at the side of the pier, see Figure 17), demonstrating that the critical shear stress for the median diameter of the bed material in the experiments (0.48 Pa, based on the Shields diagram) is often exceeded.

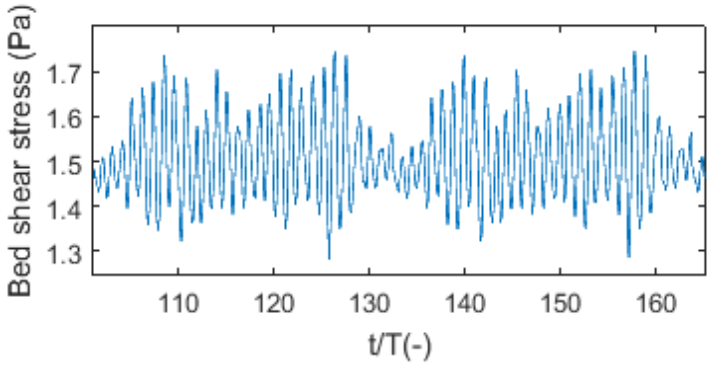

Figure 18. Numerically predicted bed shear stress in point 2 (marked in Figure 17)

Figure 19 shows the shear stress distribution in the vicinity of the pier, highlighting the fact that the highest values are localized on the sides (such as point 2) and in the wake of the pier, possibly associated with the inception of scour.

Nogueira et al. (2008) did not only study the flow around a pier mounted on a flat, non-movable bed (i.e. the flow configuration that is simulated in the present paper), but they also studied the scour around the pier mounted in a movable bed. In Figure 20, the bed after 5 minutes of scour is presented. Note the similarities between the bed shear stress as predicted by the present numerical model and the scour pattern found in the lab experiments.

As literature suggests (Majeed et al. 2015; Guney and Turkben 2015; Ramos et al. 2015), the maximum scour depth during the initial scouring phase in a flume test of this type is not upstream of the pier (i.e. where the equilibrium scour depth is located), but rather at the lateral sides of the cylinder. Note that the bed shear stress patterns predicted in the simulation (which is representative for the initial phase of the scouring process) indeed are in accordance with the observations reported in literature.

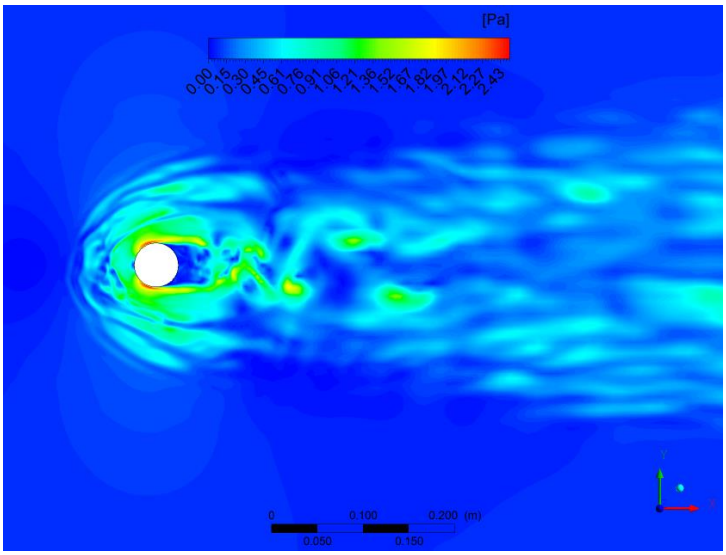

Figure 19. Numerically predicted instantaneous bed shear stress (Pa) around the cylindrical pier

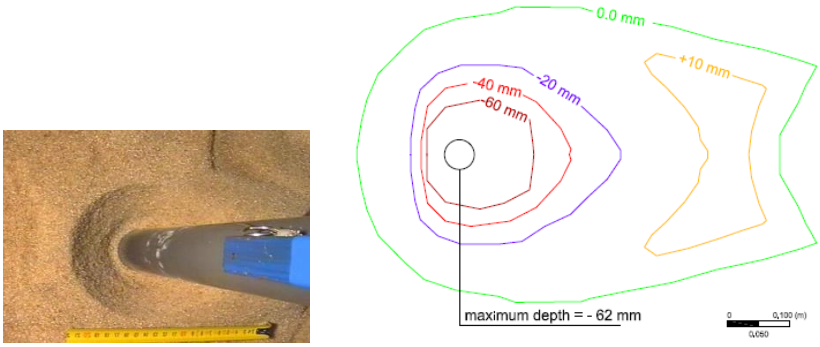

Figure 20. Scoured bed after 5 minutes of flow in movable bed experiments (Nogueira et al. 2008) and contour lines of the corresponding bed level (obtained by P.X. Ramos by means of photogrammetry)

5. CONCLUSIONS

In the present work, an eddy-resolving numerical model based upon the Large Eddy Simulation approach has been set up for predicting the three-dimensional flow around a cylindrical pier, mounted on a flat and fixed bed. This turbulent flow (Re_D = 1.37×10^4) configuration was studied earlier experimentally by Nogueira et al. (2008), allowing a partial validation of the numerical results. Since no PIV data are available in the lee side of the cylinder, other validation data from the literature were used as well.

The numerical simulation has confirmed the presence and complex dynamics of the horseshoe vortex system at the upstream side of the cylinder, as was measured by Nogueira et al. (2008). Similarly, the numerical model predicted the vortex shedding in the wake of the cylinder, with a main frequency (and corresponding Strouhal number 0.19) that is very close to value (0.20) in the literature. The mean drag coefficient for the entire pier (0.602) is somewhat lower than the value (0.683) derived from the literature on infinitely long cylinders (i.e. flow configurations with an approaching flow that is uniform over the flow depth). The numerical model confirms the instantaneous drag coefficient (of the entire pier) to oscillate around the mean value, as was reported in the literature.

Since no PIV data are available close to the downstream half of the pier surface, neither in the wake of the pier, no further direct validation of the numerically predictions is possible based upon the data set of Nogueira et al. (2008). An indirect validation of the numerical model is, however, possible based upon the predicted bed shear stresses around the pier. The latter turn out to be higher than the critical value according to the Shields diagram for the bed material used in the experiments, in agreement with the fact that scour was initiated in the experiments. Moreover, the predicted extent of the zone in which the bed shear stress exceeds the critical value, agrees well with the extent of the scour hole observed in the initial phase of the scouring process during the experiments.

Based on this first validation exercise, which is constrained by the limitations of the available data set, it can be concluded that the numerical model is capable of predicting the flow structures well, at least in a qualitative way. However, to enable a further (quantitative) validation of the numerical model, it is advocated to extend the experimental data set. These efforts are needed before the numerical tool is adapted to study the further phases of the scouring process around a cylindrical (or even a geometrically more complex) bridge pier. Currently, both in Ghent University and University of Porto, research on this topic is being carried out, namely regarding complex piers (structure with group of cylinders, a cap and a column) and efforts are being made to implement VoF (Volum of Fluid) in the present numerical model, enabling the study of the phenomena at higher Froude numbers.

6. ACKNOWLEDGEMENTS

The work in this paper has been supported by the European Regional Development Fund (FEDER) through the funds of Competitiveness Factors Operational Programme (COMPETE), the Portuguese Foundation for Science and Technology (FCT) under the project ‘Numerical and experimental study of the flow around complex bridge piers’ (Ref. FCT EXPL/ECM-HID/1663/2013) and by the Hydraulics Laboratory (Dep. of Civil Engineering) of Ghent University. The authors would like to gratefully mention the contributions of Helena Nogueira and Stéphan Creëlle.

7. REFERENCES

Beaudan, P. and Moin, P. (1994). Numerical experiments on the flow past a circular cylinder at sub-critical Reynolds number. Technical Report, CTR Annual Research Briefs, NASA Ames/Stanford University.

Blevins, R. (1990). Flow Induced Vibrations, Krieger Publishing Co., Florida.

Breuer, A. (1998). Numerical and modeling influences on large eddy simulations for the flow past a circular cylinder. International. *J. Heat and Fluid Flow*, 19, 512-521.

Catalano, P. Wang, M., Iaccarino, G. and Moin, P. (2003). Numerical simulation of the flow around a circular cylinder at high Reynolds numbers. *Int. J. Heat and Fluid Flow*, 24, 463–469.

Coussement, A., Gicquel, O. and Degrez, G. (2012). Large eddy simulation of a pulsed jet in cross-flow. *J. Fluid Mech.*, 695, 1–34.

Ferziger, J.H. and Peric, M. (2002). Computational Methods for Fluid Dynamics, 3rd Edition. Springer, Berlin.

Fluent theory guide, version 15 (2013), ANSYS, Inc., PA, USA.

Franke, J. and Frank, W. (2002) Large eddy simulation of the flow past a circular cylinder at Re_D=3900. *J. Wind Eng. and Ind. Aerodyn.*, 90: 1191–1206.

Guney, M.S. and Turkben, A. B. (2015) Experimental Study of Local Scour around Circular Pier under Hydrographs Succeeding Steady Flow. *E-proceedings of the 36th IAHR World Congress 28 June – 3 July, 2015, The Hague, The Netherlands.*

Hammil, L. (1999). Bridge Hydraulics, E and F Spon, London and New York.

Keilock, C. Constantinescu, G. and Hardy, R. (2012). The application of computational fluid dynamics to natural river channels: eddy resolving versus mean flow approaches. *Geomorphology*, 179,1-20.

Kirkil, G. and Constantinescu, G. (2010). Flow and turbulence structure around an in-stream rectangular cylinder with scour hole. *Water Resources Research*, Vol. 46, W11549.

Kulkarni, A. & Moeykens, S. (2005). *Flow over a cylinder*. FlowLab 1.2 User's Guide, Fluent Inc. New Hampshire, USA.

Kuroda M., Tamura T. and Suzukim M. (2007). Applicability of LES to the turbulent wake of a rectangular cylinder-comparison with PIV data. *J. Wind Eng. Ind. Aerodyn.*, 95(9):1242–1258

Launder, B.E. and Spalding, D.B. (1974). The Numerical Computation of Turbulent Flows. *Computer Methods in Applied Mechanics and Engineering*, 3:269-289.

Lienhard, J.H. (1966). Synopsis of lift, drag and vortex frequency data for rigid circular cylinders. Technical Extension Service, Washington.

Lisenko, D. A., Ertervag, I. S. and Rian, K. E. (2012). Large-eddy Simulation of the Flow around a Cicular Cylinder at Reynolds Number 3900 using the OpenFOAM toolbox. *Flow Turbulence Combust.*, 89:491-518.

Majeed, H., Wright, N. and Sleigh, A. (2015). Large eddy simulations and analysis for bridge scour development. *E-proceedings of the 36th IAHR World Congress 28 June – 3 July, 2015, The Hague, The Netherlands.*

Melville, B. and Coleman, S. (2000). Bridge Scour. Water Resources Publications LLC, Colorado, USA.

Moreno M, Maia R, Couto L, Cardoso H. 2012. Evaluation of local scour depth around complex bridge piers. *River Flow – International Conference on Fluvial Hydraulics; San Jose, Costa Rica*.

Murakami, S. and Mochida, A. (1995). On Turbulent Vortex Shedding Flow Past 2D Square Cylinder Predicted by CFD. *J. Wind Eng. Ind. Aerodyn.*, 54: 191.

Nakamura Y., Ohya Y., Ozono S. and Nakayama R. (1996). Experimental and numerical analysis of vortex shedding from elongated rectangular cylinders at low Reynolds numbers 200-103. *J. Wind Eng. Ind. Aerodyn.*, 65(1–3):301–308.

Nogueira, H., Franca, M., Adduce, C. and Ferreira, R. (2008). Bridge piers in mobile beds: visualization and characterization of the surrounding and approaching flows. *Proc. River Flow 2008*, Turkey, 2397-2406.

Pope, S. B. (2004). Ten questions concerning the large-eddy simulation of turbulent flow. *New J. Phys*., 6.

Ramos, P. X., Bento, A. M., Maia, R. and Pêgo, J. P. (2015). Characterization of the scour cavity evolution around a complex bridge pier. *J. Applied Water Eng. and Research*, DOI: 10.1080/23249676.2015.1090353

Rodi, W., Ferziger, J., Breuer, M. and Pourquie, M. (1997). Status of Large Eddy Simulations: Results of a Workshop. *ASME J. Fluids Eng.*, 119: 248–262.

Roshko, A. (1955). On the wake and drag of bluff bodies. *J. Aero. Sci*. 22, 124-32.

Roulund, A., Sumer, M., Fredsøe, J. and Michelsen, J. (2005). Numerical and experimental investigation of flow and scour around a circular pile. *J. Fluid Mech.*, 534: 351- 401.

Sakamoto, S., Murakami, S., and Mochida, A. (1993). Numerical Study on Flow Past 2D Square Cylinder by Large Eddy Simulation. *J. Wind Eng. Ind. Aerodyn*., 50, pp. 61–68.

Schanderl, W. and Manhart, M. (2016). Reliability of wall shear stress estimations of the flow around a wall-mounted cylinder. *Computers and Fluids* 128

Shields, A. (1936). Anwendung der Ähnlichkeitsmechanik und der Turbulenzforschung auf die Geschiebebewegung; In Mitteilungen der Preussischen Versuchsanstalt für Wasserbau und Schiffbau, 26.

Smagorinsky, J. (1963). General Circulation Experiments with the Primitive Equations. *Mon. Weather Rev*., 91, 99–165.

Techet, A. H. (2005). Vortex Induced Vibrations. *MIT OCW*: <http://ocw.mit.edu/courses/mechanical-engineering/2-22-design-principles-for-ocean-vehicles-13-42-spring-2005/readings/lec20_viv1.pdf> (April 25, 2016).

Thwaites, B. (1960). Incompressible aerodynamics, University Press, Oxford.

White, F. (2006). Fluid Mechanics. 6th edition. McGraw-Hill Companies. South Kingstown, UK.

Yang, K.S., and Ferziger, J. (1993). Large-Eddy Simulation of Turbulent Obstacle Flow Using a Dynamic Subgrid-Scale Model. *AIAA J*., 31, 1406–1413.

Yulistiyanto, B. Zech, Y. and Graf, W. H. (1998). Flow around a Cylinder: Shallow-Water Modeling with Diffusion-Dispersion. *J. Hydr. Eng.*, 124(4): 419-429.

Zdravkovich, M.M. (1997). Flow around circular cylinders, Vol 1: fundamentals, Oxford University Press, Oxford, New York.

Zhao, W. and Huhe, A. (2006). Large-Eddy simulation of three-dimensional turbulent flow around a circular pier. *J. Hydrodynamics*. 218(6):765-772.

Zhiyin, Y. (2014). Large-eddy simulation: past, present and the future. *Chinese J. Aeronautic*. 28(1):11-24.

DOI:10.15142/T3759N

Coupling Process for 1D-2D Numerical Flash Flood Simulation: A Parameter Study of Involved Variables for Gullies and Manholes

S. Schlauß[1] and M. Grottker[1]
[1]Laboratory for Urban Water Management
Civil Engineering Department
Lübeck University of Applied Sciences
Lübeck, Germany
E-mail: sebastian.schlauss@fh-luebeck.de

ABSTRACT

Urban flash floods and their hydronumerical coupled modelling are influenced by various parameters and assumptions for model setup and implementation. Hence, the present paper deals with coupling details of 1D-sewer and 2D-surface models. Considered hydraulic parameters will be analyzed concerning their impact on computed results for flood levels and the discharge rate (bi-directional) between both, 1D and 2D, model approaches. Additionally, flood durations will be investigated. Considered parameters are the inlet area, the limitation of the discharge capacity according to standards of the legislation and the discharge coefficient, which has only minor impacts on the discharge rates in this configuration. Comparisons of limited and unlimited numerical computation for discharge capacity at the coupled nodes show that the flood duration will be influenced more than flood levels. The quantitative exchange at each node is calculated by applying the Torricelli approach and by including variable parameters. Analyzing flash floods with coupled numerical models allows the implementation of measures and their evaluation regarding flooding depth and thus provides security against flooding. Exemplary improvements will be shown. Additionally, the model is primarily evaluated by comparing its results with measurements in the sewer system.

Keywords: *gullies, flash flood, coupled numerical modeling, parameter study, discharge coefficient, inlet capacity.*

1. INTRODUCTION

The present investigation is part of the "RainAhead" project, which is funded by the Federal Ministry for the Environment, Nature Conservation, Building and Nuclear Safety (BMUB). The main aim of the project is to develop an integrated planning and warning tool for heavy rain events and their resulting flash flood in urban areas. Heavy rain events and possible resulting flash floods occur locally or regionally as a result of convective precipitation of high intensity (e.g. Maniak 2010). These events can mostly be observed during the summer period (Hatzfeld et al. 2008). The analysis of an event data-base regarding flash floods (within the project URBAS) shows that flash floods arise with an occurrence of 72 % between March and September (Oertel 2012). Intensities of heavy rains can vary considerably regarding their precipitation quantity as well as their duration. Consequently, the German Meteorological Service defines three warning intensities (GDV 2015). DIN-4049-3 (1994) also describes heavy rain events by comparing their duration and intensity. IPCC (2014) expects an increase of intensive rain events and with it an increase of urban flash floods. The number of extreme events has increased significantly since 1980 according to MunichRE (2015). Additionally, with an increase of surface sealing, negative effects can be assumed regarding heavy rainfalls. Infiltration (g), evapo-transpiration (v) and runoff will change the water cycle in urbanized regions compared to natural conditions (Figure 1).

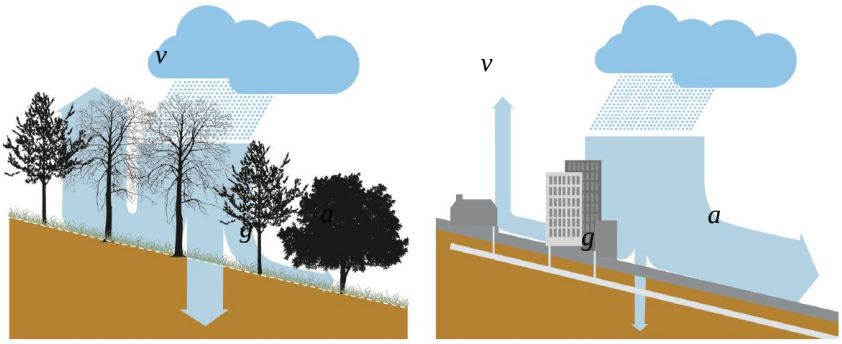

Figure 1. Increase of runoff (*a*) due to surface sealing and decrease of infiltration (*g)* and evapo-transpiration (*v)* in urban areas (Kruse et al. 2014)

Urban drainage systems are designed for defined water amounts and rainfall return periods within a particular catchment area. Hatzfeld et al. (2008) mentioned a variation of design boundary conditions for various catchment areas. Generally, the design return period for urban drainage facilities is defined in DWA-A 118 (2006). With residential areas, as an example, the typical design frequency (or return period) is n = 0.2 to 0.5 (or T = 5a to 2a respectively). DIN EN 752 requests a proof of the return period for the investigated catchment area depending on the usage (DIN EN 752 2008).

Numerical flash flood analyses usually use 2D surface runoff simulations to describe resulting flood situations. Other methods are based on Geographic Information Systems (GIS) with integrated flow-path analyses (e.g. Koch et al. 2015 and Chen et al. 2009) or coupled 1D-1D models (Maksimovic et al. 2009). Additionally, experimental models are used to describe detail processes like inlet capacities of gullies and to compare these with in-situ measurements (Kemper et al. 2015) as well as with 3D numerical models only for gullies or other details of the drainage system (Djordjevic et al. 2013). Results can also be used for validating and calibrating numerical models. The present paper focuses on coupling processes of drainage systems with surface runoff by means of analyzing the coupling process of independent numerical hydrodynamic models. Thereby, the parameters considered within applied analytical solutions are in the main focus of interest. In contrast to other research projects and national handling rules for urban flash floods, a coupled hydrodynamic numerical 1D-2D model allows a more detailed analysis of occurring flow paths and pipe capacity utilization. It represents an expensive method regarding time consumption (Ghostine et al. 2015), data input, data accuracy, simulation duration and expert knowledge (see Henonin et al. 2013 and DWA-T1 2013). Nevertheless, coupled 1D-2D models are often used in urban areas (Hunter at al. 2008; Vojinovic and Tutulic 2009; Leandro et al. 2009). Additionally, measures to avoid flash flood damage (e.g. retention areas or barrier removal, see e.g. Hoppe et al. 2011) can be adopted and investigated accurately. Forecasting of storm events can also be used to manage flash floods (Einfalt et al. 2009).

2. INVESTIGATOIN AREA AND HYDRODYNAMIC NUMERICAL MODEL

The investigation area is located in the northern part of Germany within the city of Lübeck. The district St. Lorenz Süd is located close to the city center at the river Trave (Figure 2). The catchment area is A = 2.4 km². Within the current investigation the commercial numerical models DHI MIKE21 (2D) and MOUSE (1D) are used. The 1D model allows a time-dependent simulation of the sewage system. The 2D model is a surface runoff model with a mesh resolution of 1 m in x- and y-direction and 5.1 Mio. cells in total (Table 1). Both models are coupled via connecting nodes. These nodes represent gullies and manholes in the sewage system, allowing a bi-directional mass transfer. The governing equations are the Saint-Venant-Equations complying with the principles of the conservation of mass and momentum. A detailed description can be found in DHI (2015). Details of the coupling process, as implemented here, are shown in Figure 3.

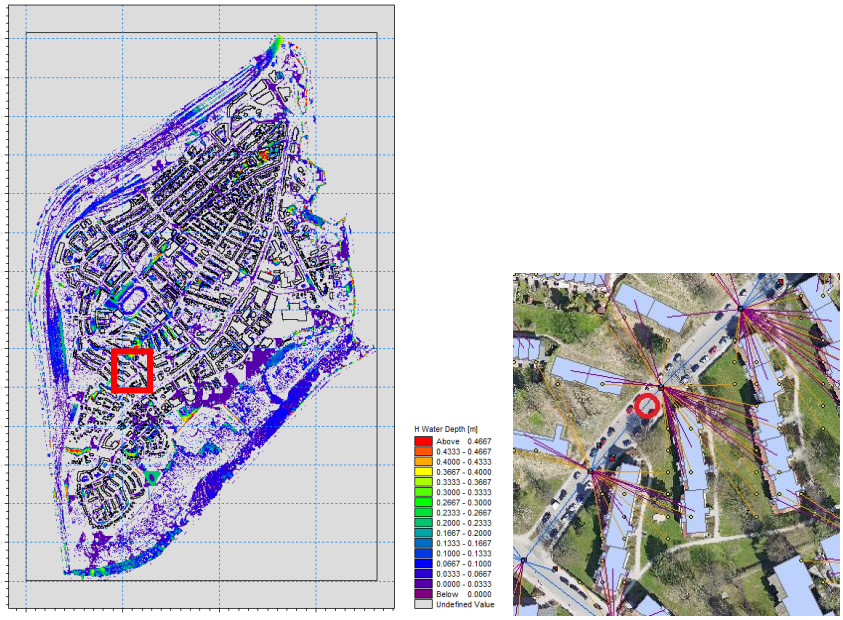

Figure 2. Overview of the investigation area (St. Lorenz Süd), left: exemplary flooding results for a once in 100 years rain event, right: exemplary investigation point within the catchment area

Table 1. List of control points within the catchment area, coordinates and nearest manhole ID in Mike Urban

Point no.	Location	Type	*x* [m]	*y* [m]	Manhole [MUID]
1	Stettinerstr.	low point	281	602	7480001
2	Hansestr.	elevated point	392	1004	7170014
3	Moislinger Allee	elevated point	501	501	7370309
4	Lachswehr Allee	close to low point	729	729	7280101
5	Lindenstr.	low point	613	1145	7310022

Table 2. Types and number of the 1D sewer model MOUSE of nodes, links and catchments, and 2D overland model

Type	*Amount / length*
Catchments (roofs)	4216
Nodes (total)	2572
Manholes	1031
Gullies	1513
Basin	1
Inlets	3
Outlets	24
Coupled nodes	2549
Links (pipes)	2580
total length of links	73.9 km
Weirs	6
Area 2D	2.4 km²
Number of cells 2D (1m)	5.1 Mio
Number of cells 2D (2m)	2.8 Mio

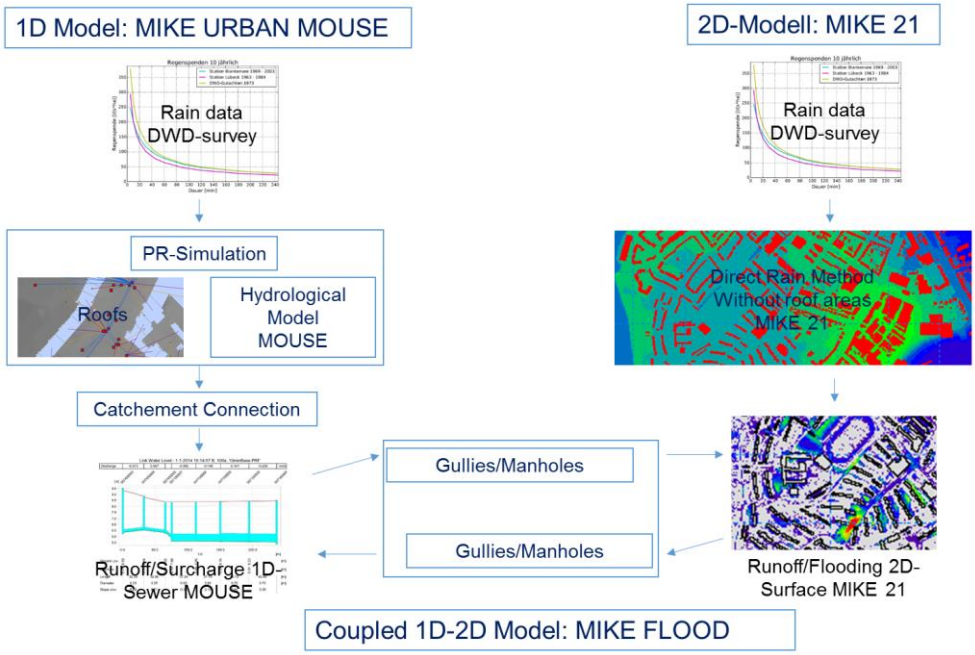

Figure 3. Schematic overview of coupling process for 1D and 2D numerical model (according to Kühnel 2015)

The input data is rainfall data provided by the German Meteorological Service (DWD), which is also used by local authorities to calculate drainage facilities. A precipitation runoff model computes the runoff from the house's roof areas; these areas are directly connected to the 1D sewage model. The same precipitation data set is used for the 2D surface runoff computation. Both models are connected via nodes so that an exchange of water can be calculated by an implemented analytical approach. Details of the coupling process are shown in Figure 4. Table 2 gives additional information about the models used in the present investigation.

Other connective configurations of the catchment areas with the 1D-sewer model are described and applied during different investigations. Runoff computation without a separate precipitation runoff model can be applied. The rainfall boundary is thus applied to the bathymetry (2D) only. Therefore, the roughness values for the buildings should be lowered allowing the flow time towards the coupled nodes to be shortened (Babister and Barton 2012). The direct connection of runoff into the sewer system is not possible in this way.

Figure 4 illustrates two varying flow directions for the coupled nodes: (1) surcharge and (2) inflow. The mathematical description is implemented in the numerical model via the analytical Torricelli approach (DHI 2015):

$$Q = A \cdot C_D \cdot \sqrt{2 \cdot g \cdot h} \tag{1}$$

where Q is the total gully discharge, A is the inlet area, C_D is the discharge coefficient, g is the acceleration due to gravity and h is the flow depth above the coupled node. The principle is the exchange of energy between the potential energy at the surface and the kinetic energy at the opening. Q is also defined as the inlet capacity, which can be limited to a maximum allowed value within the numerical model according to standards like Ras-Ew (see e.g. Kemper et al. 2015) out of FGSV (2005).

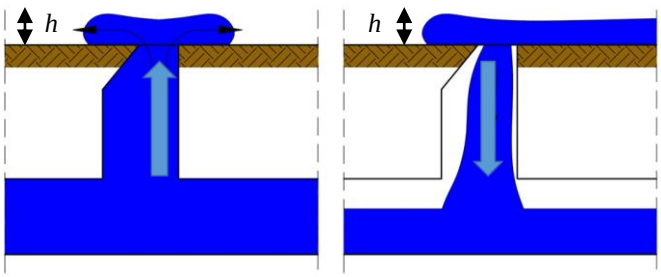

Figure 4. Schematic plot of coupled nodes (manholes and gullies) with bi-directional exchange of water between 1D-2D model, left (1): surcharge, right (2): inflow from 2D overland (DHI, 2015)

Default values for maximum gully discharges and their discharge coefficients within the numerical software are $Q = 0.1$ m^3/s and $C_D = 0.98$. The gully's flow area A is computed with geometric specification of each node (the same is valid for manholes), g is constant and the flow or flooding depth h is computed during the simulation process because of the time-dependent flow development.

Within the present paper above mentioned parameters will be studied concerning their influence on resulting sewage and surface discharges. Therefore, particular DIN regulations or maximum inlet capacities for gullies and manholes are used. As an example, Figure 5 shows two established gully dimensions in Germany especially chosen, as they are located in the analyzed catchment area. Within the investigated numerical model, various pre-defined inlet areas will be set as a constant.

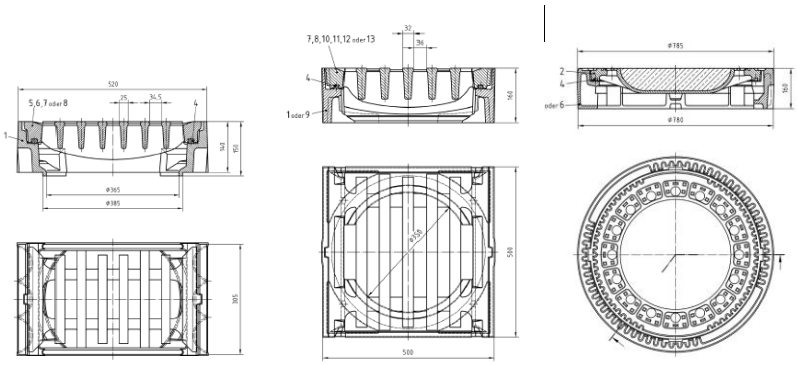

Figure 5. Exemplary gully geometries, left: 300 mm x 500 mm, $A = 0.0515$ m², middle: 500 mm x 500 mm, $A = 0.0815$ m², right: example of a manhole with an inlet area $A = 0.025$ m² (DIN-19583-1, DIN-19594-1, DIN-19584-1)

The conducted simulation runs with different set- ups and different variations of applied parameters of the coupling process are listed below. The boundary condition for the rainfall intensity is the once in 100 years storm event with a rainfall duration of $D = 10$ min. for each model run. For variations of the inlet area a duration of $D = 30$ min. was chosen with the same return period of once in 100 years and its correlating intensity of rainfall.

3. RESULT ANALYSIS

3.1. General remarks

Results will be analyzed concerning the influence of parameter variation within the analytical coupling approach (see Eq. 1) on flooding processes, like e.g. flooding depth, flood duration and exchange rate between both models. This exchange rate is called discharge MOUSE to MIKE21. Therefore, it is positive for a surcharge flowing from the 1D-sewage model into the 2D surface model. Furthermore, it is negative for an inflow running from the 2D model into the 1D model. Generally, a surcharge can be observed with early time steps, which is characteristic for the investigated catchment area. After a defined time, the exchange turns into an inflow discharge into the gully. (The boundary condition of the rainfall time series starts after 10 min. of the simulation period for both models).

Following model variations will be investigated:

(1) Influence of implemented measures (simulation period 2 h, grid resolution 2 m, 2D and 1D-2D)
(2) Comparison between 2D and 1D-2D model (simulation period 2 h, grid resolution 1 m)
(3) Influence of inlet area and inlet capacity variation (simulation period 2 h, grid resolution 2 m
(4) Influence of discharge coefficient variation (simulation period 2 h, grid resolution 2 m)
(5) Comparison of 1D sewage model with in-situ measurements (simulation period 8 h)

For all parameter variations, a once in 100 years rainfall event is used, with an intensity of rainfall of $r_{(15,1)} = 106$ l/(s ha)[1] which corresponds with an investigation of the DWD of rainfall data analysis of Lübeck

[1] In this case $D = 15$ [min]. and $n = [1/a]$ with D: duration and n: frequency of rain event per year and $T = [a]$ annuity

from 1973. For data analysis, an exemplary control node was selected (point nr. 1) to identify flooding variations and changing exchange rates. The chosen node is a low point with a nearby manhole (see Figure 2 and Table 1). In this case, only point 1 is referred to in the results. It is located on the street and is a low point where flooding depth usually increases significantly during storm events (See Figure 2).

The coupling process will be analyzed by investigating both the separated 2D surface model and the coupled 1D-2D sewage-surface model. Figure 6 gives exemplary results. It shows that the flooding depth and its time-dependent development vary significantly. With the 2D surface model, a continuous increase of resulting flow depths can be observed. As opposed to this, the coupled model shows a major increase just after the beginning of the rainfall event for the first 25 min. until a peak flow depth is reached. Finally, the sewage system will be involved in the discharge process and subsequently a decrease of inundation can be observed. It should be noted that the flooding process occurs with greater intensity within a shorter time period due to the effects of involved underground pipe systems. In this regard, Johnson (2013) refers to the Direct Rainfall Method (DRM), which cuts the flood peak due to losses especially in cases of low intensities with separated 2D overland computation (trough losses due to the bathymetry). This phenomenon is presented in Figure 6. The DRM takes only trough and depression losses of the bathymetry into account, but no evaporation and infiltration.

The influence of the 1D sewage system can be claimed to contribute to defined and fast flood levels on the one hand and to drain the surface floods on the other hand. Whereas the 2D computation results in an accumulation of flood level during the simulation as there is no drainage capacity available and no infiltration or evaporation implemented in the model. The results show reasonable differences between the two model configurations and leads to the statement that the coupling is implemented correctly, because the peak of the flooding depth is not shifted towards the end of the simulation period as in the 2D computation. Correctness can also be verified according to the above-mentioned correlations.

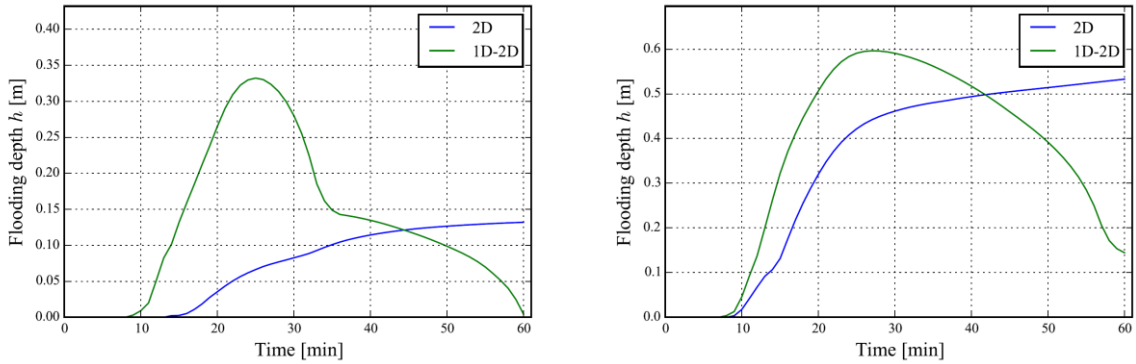

Figure 6. Comparison of exemplary model results (flooding depth) for the simple 2D surface model (2D) and the coupled sewage-surface model (1D-2D), left: T= 5a, right: (b) T = 100a of D = 30 min. (according to Kühnel 2015)

3.2. Inlet area and inlet capacity

The inlet area was varied for manholes only between the aerated area and the completely open manhole without the lid. With gullies the areas are bound to the known values according to their dimensions (see Figure 5) Investigated gullies have their particular area as described previously. The inlet area has a direct impact on the exchange rate between the two models (discharge MOUSE to MIKE21). The effect is comparable to a limitation of the inlet capacity itself (Figure 7 and Figure 8).

It can be found that the discharge for the fully opened manhole is Q = 280 l/s. In comparison with resulting gully discharges, which are mainly responsible for surface drainage, these values are much too high compared to those of gullies defined in Ras-Ew corresponding with Thiele (1983). Consequently, a limitation of the area is recommended to be set as A = 0.025 m² (see Figure 7).
When limiting the capacity to a certain threshold value, the resulting influence on exchange discharges is comparable to an area limitation. Since limiting values for manholes are not established, they have been set as default values within the numerical model (Figure 8) which means to Q = 100 l/s for the manholes, as they are not defined in Ras-Ew.

The gullies' inlet capacity has been limited due to their area and according to Ras-Ew FGSV (2005) to Q = 2.5 l/s and 5.0 l/s respectively (according to their area shown in Figure 5) for a longitudinal slope of 2.5 % and a lateral slope of 1 % to 2 %, according to Ras-Ew FGSV (2005).

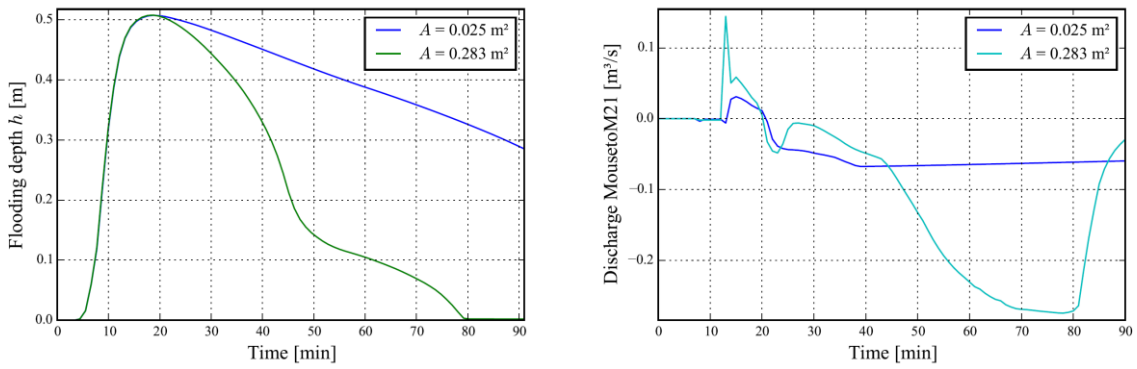

Figure 7. Comparison of manhole inlet area variation (A = 0.025 m² = aerated area and A = 0.283 m² = manhole fully opened), left: influence on flooding depth and flood duration, right: influence on exchange rate (discharge MOUSE to MIKE21) T = 100a and D = 30 min.

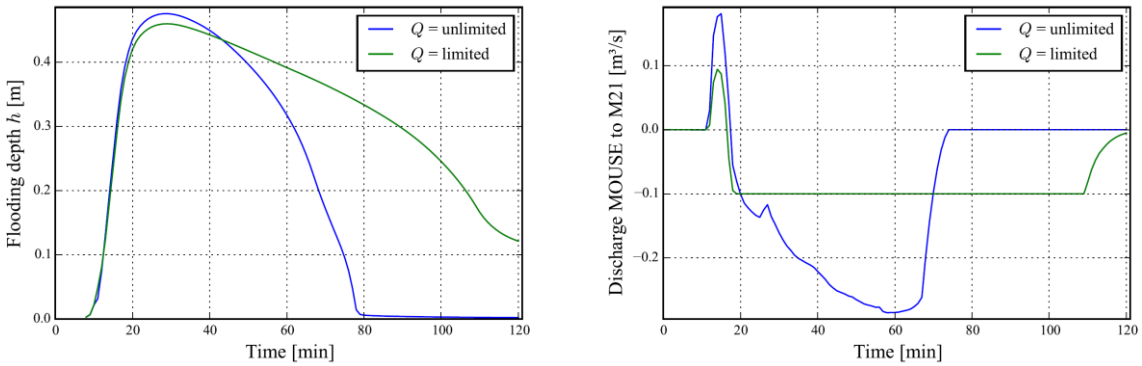

Figure 8. Comparison of limited and unlimited inlet capacity of gullies, left: influence on flooding depth and flood duration, right: influence on exchange rate (discharge MOUSE to MIKE21), T = 100a and D = 10 min.

3.3. Discharge coefficient

Another investigated parameter is the discharge coefficient C_D. Therefore, default values of C_D = 0.98 will be decreased in steps of 1/3 and 2/3 of the default value (C_D = 0.98; 0.65; 0.32). It can be found, that there is only a minor influence on resulting flooding depths and exchange discharges compared to the variations of the area (A = 0.283 m² and 0.025 m²) and the inlet capacity (Figure 9), limited according to the geometry of gullies (Q = 5 l/s or 2.5 l/s) or unlimited capacity. The variation of C_D seems to have minor influence on the flooding depth and the discharge. Similar behavior was observed when changing the area for the manholes. For small variations, no changes were observed. Only for changes of a factor of 10, the different discharges are visible, as shown in Figure 7. Thus, C_D could well be lowered further in order to see a clear impact on the discharge. The implementation of the coefficient is not well documented in the software and needs to be investigated further as the results are not reasonable.

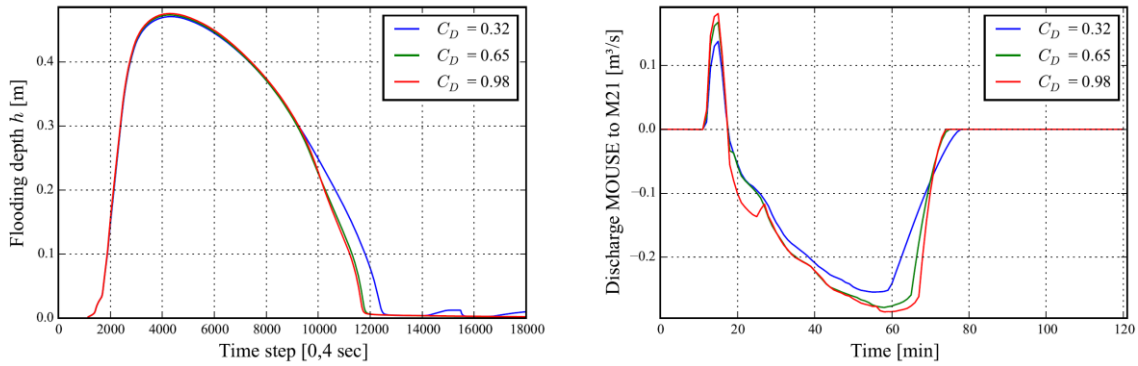

Figure 9. Comparison of discharge coefficient variation, left: influence on flooding depth and flood duration, right: influence on exchange rate (discharge MOUSE to MIKE21), T = 100a and D = 10 min

A reduction of C_D of 1/3 or 2/3 should also result in a reduction for Q in the same order of magnitude. Instead, a change of Q is observed only by appr. 15 to 20%.

3.4. Model verification

The model results have been compared to measured data so far in one spot that drains an area with a separated sewer system. The parameters compared are the water depth in the sewer pipes and the flow velocity respectively. The precipitation data gathered and defined as boundary condition in the model was radar data from the HydroNet-SCOUT portal of hydro & meteo GmbH. The rain intensity was relatively low (6 mm/6h) and did not cause a surcharge given off by the sewer system. Nevertheless, the hydrographs measured and simulated correspond to each other and are in the same order of magnitude (see Figure 10).

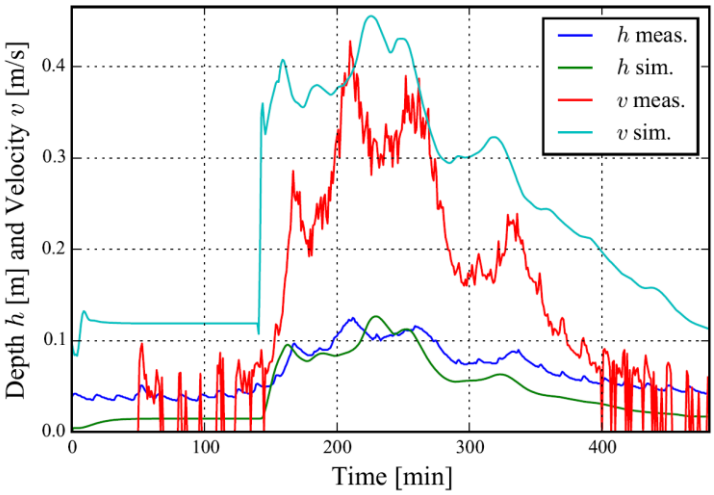

Figure 10. Comparison of measured water depth and flow velocity and simulated results for these parameters with the 1D model, duration from 8 a.m. until 4 p.m. at the 15th of April 2016

Velocity is simulated to a greater extent than it is measured. This can rely on the fact that ground water was infiltrated into the pipes and this caused an algae layer on the surface, which increased the roughness compared to the roughness implemented in the model matching the material of the specific pipe. If no measured data are available, recorded damages and fire brigade data can be used to validate the model (Velasco et al., 2016) by comparing these data with the results of the inundation computation. Both methods where applied here and helped to trust the results.

The model can be used for implementing possible measures at the flooded areas. The comparison of the change of the flood levels can lead to a judgement about the efficiency of different measures.

Figure 11gives an exemplary result of the comparison of implemented measures in the coupled model and of the comparison with a simple 2D model approach.

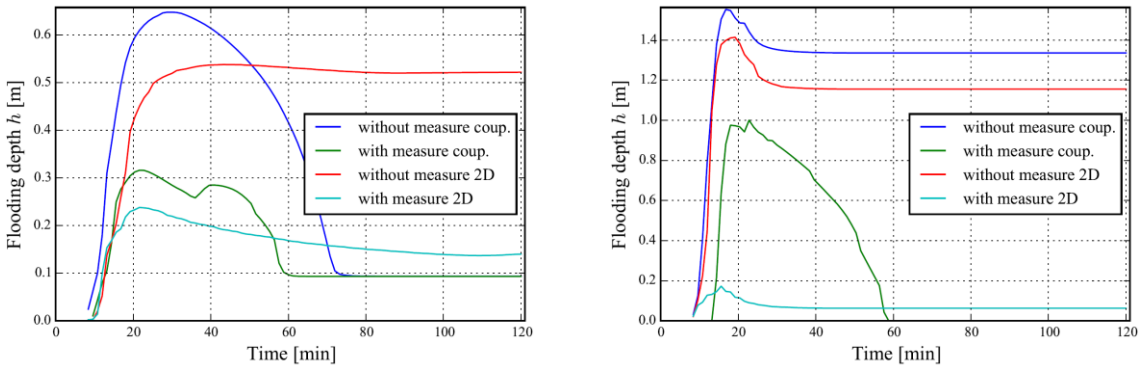

Figure 11. Exemplary results for the comparison of implemented measures at two points within the modelled catchment area for a simple 2D surface model and 1D-2D coupled model, left: a low point on the street, without and with retention basin as measure, right: a low point in front of a house without and with gully as measure, T = 100a and D = 10 min

3.5. Parameter value choice and recommendations for coupled numerical 1D-2D simulations

According to the parameter analysis, the variables can be adopted and changed different from their default state. In terms of manholes the area is set to the aerated area A = 0.025 m². The areas gullies require are set to (A = 0.0515 and 0.0815 m²) the inlet capacity is limited for the gullies in reference to the Ras-Ew (Q = 2.5 and 5.0 l/s). The discharge coefficient with a value of C_D = 0,6 is defined due to sharp-edged openings found in literature (Schneider et al. 2010). The limitation for the inlet capacity of manholes cannot be defined, nevertheless the limitation is implemented by the aerated area because the capacity of manholes is not defined in any regulation or standard as they are no drainage facilities like gullies. Despite of this, manholes do influence the situation in case of completely flooded streets by draining the water.

4. CONCLUSIONS

The different parameter variations have a relatively minor impact on the flooding depth concerning its maximum. The flood duration is clearly influenced. The limitation of the inlet capacity has the greatest impact on the exchange rate between the two models apart from the area limitation of manholes. The default values in the model are not adopted to the situation in urban sewer systems. The values computed due to the default settings do not relate to the values found in the Ras-Ew (FGSV, 2005).

The differences between Ras-Ew and the computed values as well as in in respect to other surveys might be bound to the fact that there is a certain safety factor implemented and that gullies are usually blocked by leaves and sand and are not maintained or cleaned regularly.

Concluding it can be stated that hydro numerical coupled modelling for urban flash flood analysis is an appropriate tool for the identification of areas susceptible of flooding and to implement appropriate measures. The model shows reasonable changes of the flooding depth and duration as well as the exchange rate by the parameters that were varied. The comparison between the results of the only use of a 2D overland computation and the coupled results can also be explained and show that the coupled method is the most accurate analysis in urban areas.

Further events need to be captured, different spots need to be measured and their results need to be compared to the simulated results. Especially storm events with high intensities need to be surveyed in order to prove the parameter settings for the coupling details. For the discharge coefficient, more variations need to be conducted and the implementation needs to be investigated.

To analyze suitable measures and to evaluate the improvement of flooding depth the coupled numerical model is an appropriate tool and should be preferred to the 2D overland modelling as these results show only limited validity.

5. ACKNOWLEDGMENTS

The authors would like to thank the Ministry of Env. Protection (BMUB), the project partners, the Hanseatic City of Luebeck Dept. 3, hydro & meteo GmbH and Co KG and the project affiliates (EBL amongst others) for data support and the project executing organization Juelich (PtJ) as well as Prof. Mario Oertel for his support on this paper.

6. REFERENCES

Babister, M. and Barton, C. (2012). Australian Rainfall & Runoff Revision Projects Project 15: Two Dimensional Modelling in Urban and Rural Floodplains. Engineers Australia - Water Engineering.

Chen, J., Hill, A.A. and Urbano, L.D. (2009). A GIS-based model for urban flood inundation. *Journal of Hydrology, 673(1-2), 184-192.*

DHI (2015). MIKE Zero – User Manual, The common DHI user interface for project oriented water modelling. DHI, Hörsholm, Denmark.

DIN 19583-1 (2012). Aufsätze 500 × 500 für Straßenabläufe, Klasse C 250 und Klasse D 400 – Teil 1: Zusammenstellung. Berlin: Beuth-Verlag GmbH [in German].

DIN 19584-1 (2012). Schachtabdeckungen für Einstiegsschächte, Klasse D 400 – Teil 1: Zusammenstellung. Berlin: Beuth-Verlag GmbH [in German].

DIN 19594-1 (2012). Aufsätze 300 × 500 für Straßenabläufe, Klasse C 250 – Teil 1: Zusammenstellung. Berlin: Beuth-Verlag GmbH [in German].

DIN-4049-3 (1994). Hydrologie, Teil 3: Begriffe zur quantitativen Hydrologie. Berlin: Beuth-Verlag GmbH [in German].

DIN EN 752 (2008): Entwässerungssysteme ausserhalb von Gebäuden. Berlin: Beuth-Verlag GmbH [in German].

Djordjevic, S., Saul, A.J., Tabor, G.R., Blanksby, J., Galambos, I., Sabtu, N. and Sailor G. (2013). Experimental and numerical investigation of interactions between above and below ground drainage systems. *Water Science & Technology*, 67(3), 535-542.

DWA-A 118 (2006). Hydraulische Bemessung und Nachweis von Entwässerungssystemen. Deutsche Vereinigung für Wasserwirtschaft, Abwasser und Abfall e. V. (DWA). Hennef: Fraunhofer IRB Verlag [in German].

DWA-T1 (2013). DWA-Themen Starkregen und urbane Sturzfluten-Praxisleitfaden zur Überflutungsvorsorge. Deutsche Vereinigung für Wasserwirtschaft, Abwasser und Abfall e. V. (DWA). Hennef: Fraunhofer IRB Verlag [in German].

Einfalt, T, Hatzfeld, F., Wagner, A., Seltmann, J., Castro, D., and Frerichs, S. (2009). URBAS: forecasting and management of flash floods in urban areas. *Urban Water Journal*, 6(5), 369-374.

FGSV (2005). Richtlinien für die Anlage von Straßen (RAS), Teil: Entwässerung (RAS-Ew), Forschungsgesellschaft für Straßen- und Verkehrswesen (FGSV), Köln [in German].

GDV (2015). Naturgefahrenreport 2015 – Die Schaden-Chronik der deutschen Versicherer in Zahlen, Stimmen und Ereignissen. Gesamtverband der Deutschen Versicherungswirtschaft e.V. [in German].

Ghostine, R., Hoteit, I., Vazquez J., Terfous A., Ghenaim A., and Mose R. (2015). Comparison between a coupled 1D-2D model and a fully 2D model for supercritical flow simulation in crossroads. *Journal of Hydraulic Research*, 53(2), 274-281.

Hatzfeld, F., Castro, D., Einfalt, T., Frerichs, S., Friedeheim, K., Kubik, A., Mittelstädt, R., Müller, M., Seltmann, J. and Wagner, A. (2008). Vorhersage und Management von urbanen Sturzflutereignissen (URBAS). Final Project Report des vom BMBF geförderten Vorhabens. hydrotec, Aachen [in German].

Henonin, J., Russo, B., Mark, O. and Gourbesville, P. (2013). Real-time urban flood forecasting and model – a state of the art. *Journal of Hydroinformatics*, 15(3), 717– 736.

Hoppe, H. and Einfalt, T. (2011). Klimawandel in Stadtentwässerung und Stadtentwicklung – Methoden und Konzepte – KISS, Projekt des Klima-Innovationsfonds IF-37, TU Kaiserslautern, Dr. pecher AG und hydro & meteo GmbH & CO KG für das Landesamt für Natur, Umwelt und Verbraucherschutz NRW [in German].

Hunter, N.M., Bates, P.D., Neelz, S., Pender, G., Villanueva, I., Wright, N.G., Liang, D., Falconer, R.A., Lin, B., Waller, S., Crossley, A.J. and Mason, D. (2008). Benchmarking 2D hydraulic models for urban flood simulations. *Proc. of the Institution of Civil Engineers, Water Management* 161(1) 13-30.

IPCC (2014). Synthesis Report. Contribution of Working Groups I, II and III to the Fifth Assessment Report of the Intergovernmental Panel on Climate Change, Eds. R. K. Pachauri and L. A. Meyer, IPCC, Geneva, Switzerland.

Johnson, P. (2013). Comparison of direct rainfall and lumped-conceptual rainfall runoff routing methods in tropical North Queensland – a case study of Low Drain, Mount Low, Townsville. Diss. University of Southern Queensland, Faculty of Health, Engineering & Sciences, Australia.

Kemper, S., Mayer, A. and Schlenkhoff, A. (2015). Modellversuche zur Untersuchung der Leistungsfähigkeit von Straßeneinläufen bei Starkregenereignissen. KW Korrespondenz Wasserwirtschaft 2/2015 [in German].

Koch, M., Behnken, K., Schneider, B., Gatke, D., Thielking, K., Wurthmann, J., Hoppe, H., Kirschner, N., Benden, J. and Gerdes, D. (2015). KlimaAnpassungsStrategie extreme Regenereignisse (KLAS), Final Project Report "Umgang mit Starkregenereignissen in der Stadtgemeinde Bremen", Stadt Bremen (SUBV) [in German].

Kruse, E., Zimmerman, T., Kittel, A., Dickhaut, W. and Knieling, J. (2014). Stadtentwicklung und Klimaanpassung – Klimafolgen, Anpassungskonzepte und Bewusstseinsbildung beispielhaft dargestellt am Einzugsgebiet der Wandse, HCU Hamburg, Germany [in German].

Kühnel, J. (2015). Entwicklung eines hydrodynamischen 2D-Oberflächenmodells mit Kopplung an ein 1D-Kanalnetzmodell für das Einzugsgebiet Lübeck St. Lorenz Süd. Master Thesis. Lübeck University of Applied Sciences, Germany [in German].

Leandro, J., Chen, A. S., Djordjevic, S. and Savic, D. A. (2009). Comparison of 1D/1D and 1D/2D coupled (Sewer/Surface) Hydraulic Models for Urban Flood Simulation. *Journal of Hydraulic Engineering*, 135(6), 495-504.

Maksimovic, C., Prodanovic, D., Boonya-Aroonet, S., Leitao, J. P., Djordjevic, S. and Allit R. (2009) Overland flow and pathway analysis for modelling of urban pluvial flooding. *Journal of Hydraulic Research* 47(4), 512-523.

Maniak, U. (2010). Hydrologie und Wasserwirtschaft. Berlin und Heidelberg: Springer [in German].

MunichRE (2015). NatCatSERVICE – Schadensereignisee Weltweit 1980-2014. Münchener Rückversicherungs-Gesellschaft, Geo Risks Research, NatCatSERVICE – Munich [in German].

Oertel, M. (2012). Starkregenereignisse und resultierende Sturzflutereignisse. Habilitationsvortrag, Bergische University of Wuppertal, Germany [in German].

Schneider, K., J.; Goris, A., Albert, A. (Hg.) (2010). Bautabellen für Ingenieure. Mit Berechnungshinweisen und Beispielen. 19. Aufl. Neuwied, Köln: Werner; Wolters Kluwer [in German].

Thiele, F. (1983). Fahrbahnlängsentwässerung im Strassengerinne mit kontinuierlichen oder diskreten partiellen Entnahmen und ein Entwurf für zukünftige Richtlinien zur Bemessung. Dissertation. Technical University Darmstadt [in German].

Velasco, M., Cabello, A. and Russo B. (2016). Flood damage assessment in urban areas. Application to the Raval district of Barcelona using synthetic depth damage curves. *Urban Water Journal*, 13(4), 426-440.

Vojinovic, Z. and Tutulic, D. (2009). On the use of 1D and coupled 1D-2D modelling approaches for assessment of flood damage in urban areas. *Urban Water Journal*, 6(3), 183-199.

DOI:10.15142/T33G6C

Analysis of clearance gap losses on the hydraulic pressure machine

O. Schwyzer[1] and N. Saenger[1]
[1] Institute of Hydraulic Engineering
Darmstadt University of Applied Sciences
Darmstadt, Germany
E-mail: olivier.schwyzer@h-da.de

ABSTRACT

The Hydraulic Pressure Machine (HPM) is an energy converter to exploit head differences between 0.5 and 2.5 m in small streams and irrigation canals. The HPM looks similar to a classic breast shot water wheel but has a smaller number of blades, a relatively large central hub and the wheel runs at variable speeds (2 to 12 min^{-1}). Preliminary results show that the HPM is an economically and ecologically viable technology for small hydropower generation. The clearance gap between the blade tip and the shroud at the bottom of the wheel is very important regarding power losses. A theoretical approach has been developed which considers a stationary wheel to quantify the leakage losses. However, no validation of this theory has been done. The goals of this research are to quantify the leakage at operating condition and to improve the HPM blade design to further reduce gap losses. Thus a large scale physical model is tested at laboratory conditions. The HPM model is 1.1 m in diameter, 0.8 m wide and has 12 flat blades. Variable blade tips machined from steel and EPDM rubber are investigated with gap sizes of 1, 5 and 10 mm. The physical model results show that the flow rate passing the wheel during operation is approximately one third of the flow rate calculated by the theoretical approach. The variation of gap sizes reveal the importance of small clearance gaps to reach high efficiencies.

Keywords: *Small Hydropower, Gap Loss, Hydraulic Pressure Machine*

1. INTRODUCTION

The history of water wheels goes back to antiquity. Scoop wheels are known for irrigation purpose at the Euphrates in Mesopotamia since 1200 B.C. (Wölfel 1987). Also at the Huáng Hé in China and Nile in Egypt, large wheels were used for water conveyance and to grind grain (Mosonyi 1963). Subsequently, water wheels were distributed widely and were optimized for a variety of purposes (e.g. mills, mines, metal working). The 19th century was the time of prosperity for the technology and it was significantly improved by several technological enhancements.

During this time the Swiss engineer Walter Zuppinger developed two types of water wheels: The well-known *Zuppinger wheel*, which is a special type of an undershot water wheel, and a different wheel with a closed hub (Delabar and Dingler 1867). To the authors' knowledge Figure 1 from the 1860s is the first illustration showing a water wheel with a closed hub. In the following text, these kinds of wheels are called Hydraulic Pressure Machines (HPM).

The HPM looks similar to a typical breast shot water wheel but has some significant differences. Special features of the technology are the fewer number of blades (around 12 to 24 – unlike traditional water wheels with around 36 to 48 blades) and a relatively large central and closed hub (measuring 1/3 of the outer diameter) to dam the upstream water level (see Figure 1 and Figure 2). For optimal power extraction the upstream water level is kept at the top of the hub. Therefore, the wheel runs at variable speeds in response to naturally changing flow.

The technology developed by Zuppinger was ignored completely during industrialization and was never applied for a real installation. But the technology was rediscovered in the beginning of the 21st century and investigated in detail by the University of Southampton (UK), the Darmstadt University of Technology (DE) and the University of Architecture, Civil Engineering and Geodesy in Sofia (BG) (Brinnich 2001, Senior et al. 2010, Bozhinova et al. 2012, Müller et al. 2012).

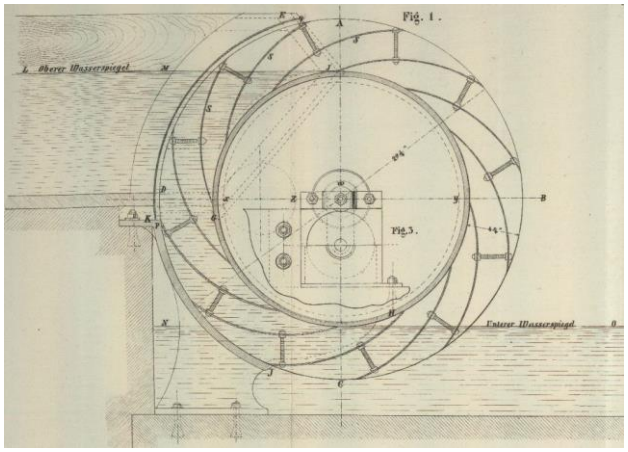

Figure 1. Hydraulic Pressure Machine (Delabar and Dingler 1867)

The HPM is run by the hydraulic pressure difference between upstream and downstream water levels (Senior 2009). Experimental results indicate that the technology is suitable for power extraction in sites with small head differences (0.5 to 2.5 m) (Senior et al. 2007). Furthermore, it was found that one of the main benefits of the HPM compared to other hydraulic machines like traditional water wheels and turbines, is that the wheel allows for good continuity for aquatic life (e.g. fish) and bed load (Senior et al. 2010). This advantage is due to the slow rotational speed (2 to 12min^{-1}) and the small number of blades, which creates a relatively large space between two blades. Efficiency rates from 60 to up to 80 % were achieved (Delabar and Dingler 1867, Senior et al. 2010, Müller et al. 2012, Paudel et al. 2013).

The research conducted to date revealed that gap losses are of high importance for the HPM technology due to the large proportion of the total energy losses within the converter (Linton 2013). Gap losses can be described as the flow rate passing the wheel between the side of blade and the housing or the blade tip and the shroud (see Figure 2). In literature, gap losses are given from 2 to 12 % of the total flow rate (Brinnich 2001, Müller et al. 2012). To further investigate the quantity of gap losses, a theory was developed and different bottom clearance gap sizes are investigated within a physical model in this study. The main goal is to compare measured data from a physical model with results from the previously developed theory.

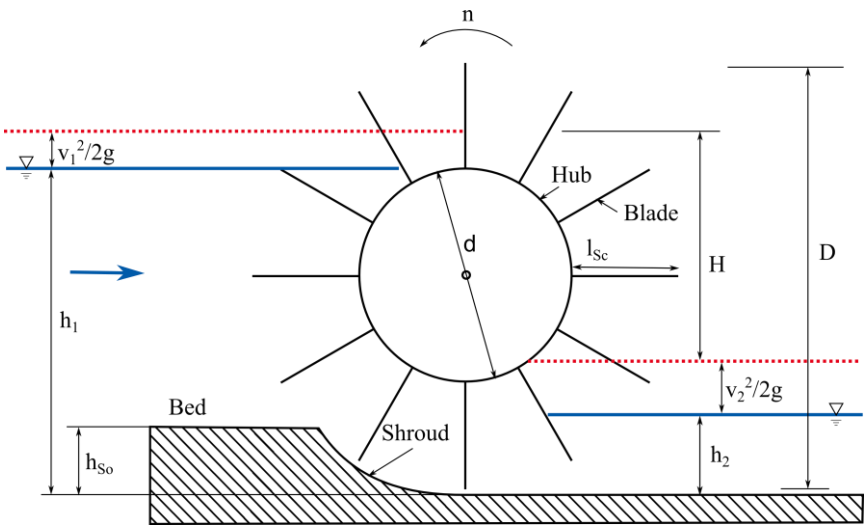

Figure 2. Functional principle of a Hydraulic Pressure Machine

2. THEORETICAL APPROACH

To quantify the gap loss flow rate (Q_L) a theoretical approach was developed (Senior 2009). The theory considers the pressure difference or rather the velocity by reason of the pressure difference at the gap, the

corresponding flow area of the gap (width of the gap and length or height of the blade) and an empirically determined flow coefficient (μ) that depends on the geometry of the blade tip or the blade tip material.

$$Q_L = \textit{flow velocity in the gap x gap area x flow coefficient} \tag{1}$$

To simplify calculations of the gap losses the surrounding gaps of the blade are divided into three characteristic sections as follows (see also Figure 3):

- Q_{L1}: Leakage loss between blade tip and shroud with the bottom gap size g_b and the blade width W
- Q_{L2}: Leakage loss between blade side and housing below h_2 with gap size on the side g_s
- Q_{L3}: Leakage loss between blade side and housing above h_2 with gap size on the side g_s

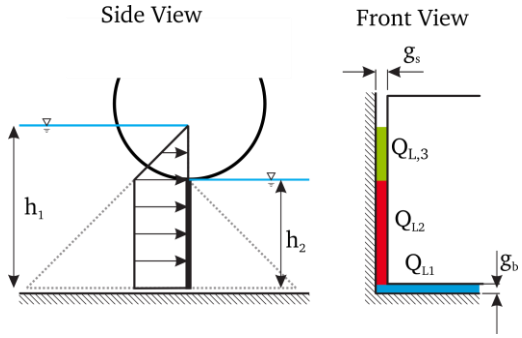

Figure 3. Gap losses sections

Based on Eq. (1) for the three sections three simplified calculation formulas can be derived as follows:

$$Q_{L1} = \sqrt{2\,g\,(h_1 - h_2)}\; g_b W \mu_b \tag{2}$$

$$Q_{L2} = \sqrt{2\,g\,(h_1 - h_2)}\; g_s\, h_2\, \mu_s \tag{3}$$

$$Q_{L3} = \frac{2}{3}\sqrt{2g}\,(h_1 - h_2)^{\frac{3}{2}}\, g_s\, \mu_s \tag{4}$$

The total gap losses can be described as follows:

$$Q_L = Q_{L1} + 2\left(Q_{L2} + Q_{L3}\right) \tag{5}$$

This theoretical approach to calculate the gap losses was initially developed for middle shot water wheels and was transferred to HPM technology (Senior 2009). Regarding the applicable flow coefficient (μ_b, μ_s) the literature on HPM quotes values ranged between 0.6 to 1.0 (Schneider 2016, Senior 2009).

Eq. 2 to Eq. 5 employed to calculate the gap losses are based on basic hydromechanics. The theory takes into consideration flow through a small orifice. The validation of this theory was done to date by measuring the flow rate passing the wheel while the wheel is standing still (Linton 2013). A validation of the previously developed theory on an operating wheel has, to the authors' knowledge, not been conducted.

3. EXPERIMENTAL PROGRAM

The objective of the experimental program is (1) to evaluate the efficiency and power output of the wheel and (2) to measure the flow rate passing the wheel without doing any work under operating conditions. A large scale physical model of a HPM was built and tested under laboratory condition to investigate these two main questions. The model scale corresponds roughly 1:2.5 to a real installation in Bulgaria (Bozhinova et al. 2012).

3.1. Test rig

The model of the HPM wheel was installed in a 20 m long and 3 m wide concrete flume in the hydraulic laboratory of the University of Applied Sciences Darmstadt (D). Figure 4 shows the flume with the tested HPM on the right and parts of a slot fish pass on the left.

The wheel itself has an outer diameter (D) of 1.1 m, a hub diameter (d) of 0.4 m and a width (W) of 0.8 m. 12 flat, 2 mm thick blades from stainless steel are diagonally mounted at the circumference of the hub. The blades are set at an angel of 15° to the shaft of the wheel. The hub is machined from polyethylene. The shaft and load bearing disks (mounted on the shaft) are made of stainless steel. The blades are bolted to the three load bearing disks at the sides and middle of the hub. The wheel is placed over a curved concrete shroud following the outer diameter of the wheel. The inlet and outlet channels are 1.2 m wide (W_1, W_2). Table 1 summarizes the main geometrical details of the tested wheel while Figure 5 shows the wheel in detail. The model itself is designed for maximum flexibility in order to allow further modification of blade geometry, blade number etc. The blade border at the tip and the sides of the blade are exchangeable. This enables tests of different blade tip versions and the variation of the clearance gap (up to 20 mm).

Table 1 Model parameter summary

Parameter		Dimension
Outer Diameter	D	1.1 m
Hub Diameter	d	0.4 m
Machine Width	W	0.8 m
Width In- and Outlet	W_1, W_2	1.2 m
Number of blades	N	12
Blade angle (to shaft)	β	15°

Figure 4. Photo of test rig from down- to upstream

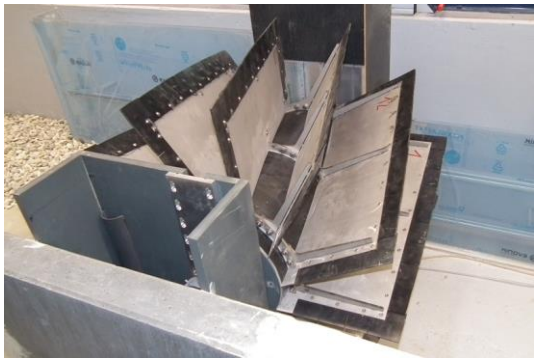

Figure 5. Wheel in detailed view

3.2. Measurement technique

To determine the power output and efficiency of the converter values for water levels up- and downstream (h_1, h_2), flow rate (Q), torque (M) and speed of the wheel (n) were measured. It is important for the operational characteristics of a HPM to keep the upstream water level constant. Thus, a control system is mandatory.

The HPM test setup is electronically braked by a coupled magnetic powder brake FRAT 2002 from Mobac Gmbh. The torque (M) is logged by torquemeter TRS 200 by Liedtke, the rotation (n) by shaft encoder ITD 01 A 4 1024 H NX KR1 S6 by Thalheim and the water levels up and downstream of the wheel (h_1, h_2) by ultrasonic sensor BUS R06K1-XA-12/070-S75G by Balluff. The water levels are measured from above to the water surface. A V notch weir is used for flow rate (Q) measurement (see Figure 4 left, background). Table 2 summarizes the measuring devices used for data acquisition and the corresponding accuracy. The head over the weir is measured via ultrasonic sensor (same make as for the water levels). As a control system for the brake and for data acquisition purpose, a LabVIEW based software in combination with a CompactRIO-9074 from National Instruments is used. A measurement period of 30 s and sampling rate of 30 Hz applies for all collected data.

Table 2 Data acquisition system

Parameter		Make	Model	Accuracy
Water level	h_1, h_2	Balluff	BUS R06K1-XA-12/070-S75G	±0.15 %
Flow rate	Q	Unknown	V notch weir	±0.8 %
Speed	n	Thalheim	ITD 01 A 4 1024 H NX KR1 S6	±0.23 %*
Torque	M	Liedtke	TRS 200	±1 Nm
* speed dependent (example for 8 min^{-1})				

3.3. Analysis

Data analysis is done in accordance with IEC 60193 *Hydraulic turbines, storage pumps and pump-turbines -- Model acceptance tests*. The most important parameter for comparison with other converters is the hydraulic efficiency (η_{Hy}). It is the quotient of the measured mechanical power (P_{Me}) at the output shaft of the wheel and the energy in the flowing water called hydraulic power (P_{Hy}).

The energy in the flowing water can be described by the product of the total energy head difference (H) in m, the flow rate (Q) in m^3s^{-1}, the density of the water ($\rho = 1000\ kgm^{-3}$) and the acceleration of gravity ($g = 9.81\ ms^{-2}$).

$$P_{Hy}=H\,Q\,\rho\,g \tag{6}$$

with

$$H= h_1+\frac{v_1^2}{2g}-\left(h_2+\frac{v_2^2}{2g}\right)=\frac{v_1^2-v_2^2}{2g}+h_1-h_2 \tag{7}$$

The flow velocity up- and downstream of the wheel (v_1, v_2) in ms^{-2} is calculated according to the law of continuity and not measured. The values therefore represent the mean velocity, with bed elevation upstream (h_{So}) and channel width (W_1, W_2) upstream and downstream of the wheel (see Figure 2).

$$v_1=\frac{Q}{W_1\,(h_1-h_{So})} \qquad v_2=\frac{Q}{W_2\,h_2} \tag{8}$$

The mechanical power measured at the shaft of the wheel is described as the product of torque (M) in Nm and the speed of the wheel (n) in s^{-1}.

$$P_{Me}=2\,\pi\,M\,n \tag{9}$$

The hydraulic efficiency is the quotient of mechanical power and hydraulic power.

$$\eta_{Hy}=\frac{P_{Me}}{P_{Hy}}=\frac{2\,\pi\,M\,n}{H\,Q\,\rho\,g} \tag{10}$$

The uncertainty involved in the derived quantities is calculated according to the constant odd combination method (Moffat 1988). Experimental data contains random (statistical) and bias (systematic or fixed) error. Random error is calculated based on standard deviation of the mean of multiple measurements taken at the same condition (IEC 1999). Fixed error is calculated based on the specification given by the producer of the used measurement equipment. Table 2 summarizes the accuracy of all measurement equipment used. The overall uncertainty for each measured value is calculated as the root sum square of the fixed error and random error (IEC 1999). To calculate the uncertainty of computed values, namely mechanical power output (P_{Me}) and hydraulic efficiency (η_{Hy}), the method of uncertainty propagation is used (Moffat 1988). The overall uncertainty for power output is summarized in Eq. (11) and for the hydraulic efficiency in Eq. (12).

$$\frac{\delta P_{Me}}{P_{Me}} = \pm\sqrt{\left(\frac{\delta M}{M}\right)^2 + \left(\frac{\delta n}{n}\right)^2} \tag{11}$$

$$\frac{\delta \eta_{Hy}}{\eta_{Hy}} = \pm\sqrt{\left(\frac{\sqrt{\delta h_1{}^2 - \delta h_2{}^2}}{h_1 - h_2}\right)^2 + \left(\frac{\delta Q}{Q}\right)^2 + \left(\frac{\delta M}{M}\right)^2 + \left(\frac{\delta n}{n}\right)^2} \tag{12}$$

3.4. Test procedure

Two different blade tip materials were chosen for comparison. The interchangeable blade tip spans the entire width of the blade and is approx. 60 mm long. First, a steel blade tip (2 mm thick), representing a conventional blade design as a reference case is analyzed (see Figure 6). Secondly, a combination of EPDM rubber (EPDM/SBR Shore hardness of 80 ±5°, 2 mm thick) and steel (stainless steel, 0.8 mm thick) is tested (see Figure 7). The two materials are layered (rubber, steel, rubber) and glued with adhesive. The blade tip itself is divided into 10 cm wide sections which are partly flexible. Each individual section is reinforced by a middle steel sheet and therefore is sufficiently rigid to resist the hydraulic forces that arise during regular operation. Three sides of each section are flexible enough to allow the blade edge to be flexible against a foreign object (e.g. fish). The main goal of this alternative blade design is to reduce damage to fish passing through the wheel.

To assess the influence of the size of the bottom clearance gap (between blade and shroud) on the efficiency and mechanical power output, three different bottom gap sizes (1, 5 and 10 mm) were investigated. Gap sizes for the two different blade tips, in order to register possible interdependency between blade material and gap size were analyzed.

For all tests the water level upstream is kept at the top of the hub (h_1 = 750 mm) and the downstream water level is kept at the bottom of the hub (h_2 = 350 mm). Earlier research showed that this water level combination (h_1 at the top of the hub and h_2 at the bottom of the hub) results in optimal energy extraction of these machines (Senior 2009). All experiments are conducted with a side gap size of 1 mm and flow rates between 30 and 180 ls^{-1} in 5 and 10 ls^{-1} increments. The variation of flow is done to evaluate whether the properties of these blades and especially of the EPDM blade tip remain constant over the whole band of operation.

Figure 6. Steel blade tip

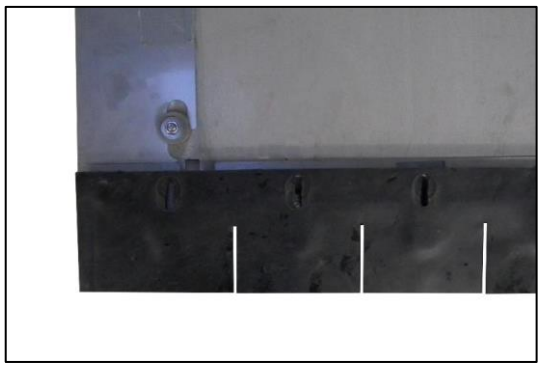

Figure 7. EPDM blade tip

4. RESULTS

4.1. Power output and efficiency

Figure 8 shows the power output of two different blade tips and bottom gap sizes of 1 and 10 mm in comparison. For better clarity, values for 5 mm gap size and error bars are suppressed in the diagram. The

curves indicate that there is no significant difference in mechanical power output between the two blade tip versions. It can be concluded that no disadvantages regarding power extraction can be noticed by using alternative EPDM blade tips.

The diagram further demonstrates that with larger gaps the curve shifts on the x axis into higher flow rates. Detailed analysis of the efficiency shows that the efficiency for 1 mm clearance gap with Steel and EPDM blade tips reaches 57.8±1.7% and 57.2±1.6% respectively and for 10 mm clearance gap 49.7±1.4% and 50.6±1.4% respectively. This supports the above made conclusion that there are no disadvantages for EPDM in comparison to metal blade tips regarding power extraction. However these results clearly show that the efficiency of the wheel decreases with larger gap sizes. This is due to the higher gap losses.

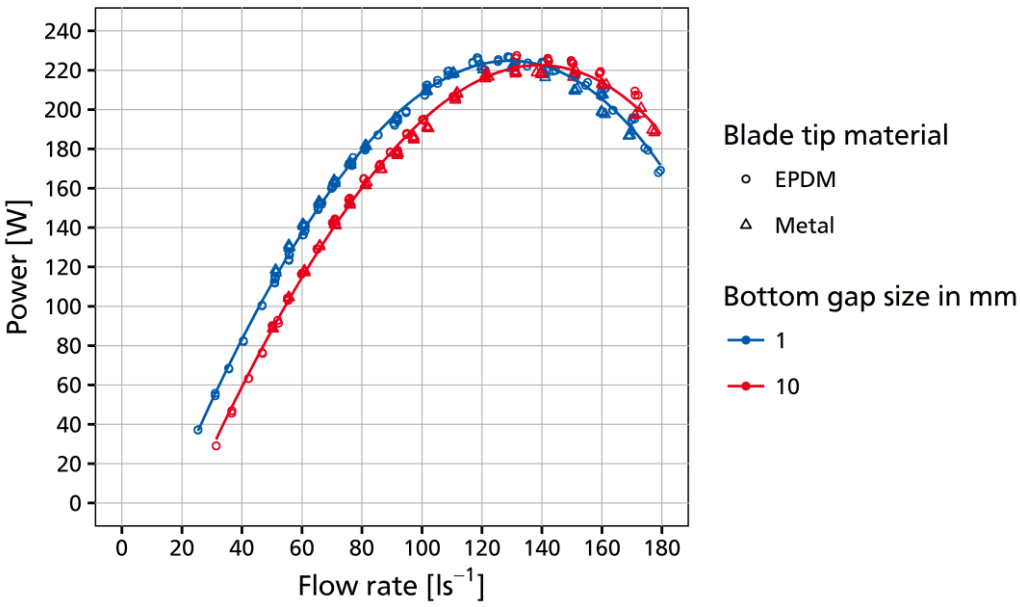

Figure 8. Results of different gap sizes and different blade tip materials on power output

4.2. Gap losses

To determine the gap losses under operation conditions, the values for the speed of the wheel (n) and the flow rate (Q) taken for 1 and 10 mm are displayed in one diagram (see Figure 9). The difference in y-axis intercept of the two displayed linear regression lines represents the difference in bottom gap losses between 1 and 10 mm bottom gap. This approach is only valid due to the fact that at the HPM, the cells between two blades are, in contrast to e.g. water wheels, completely filled up with water during operation.

Based on the parallelism of the two regression lines it can be confirmed that the gap losses are mainly dependent on the gap size (g_b, g_s) and the water levels up- and downstream (h_1, h_2) and independent on the speed of the wheel (n) as described in theory (see Eq. 2 to Eq. 5).

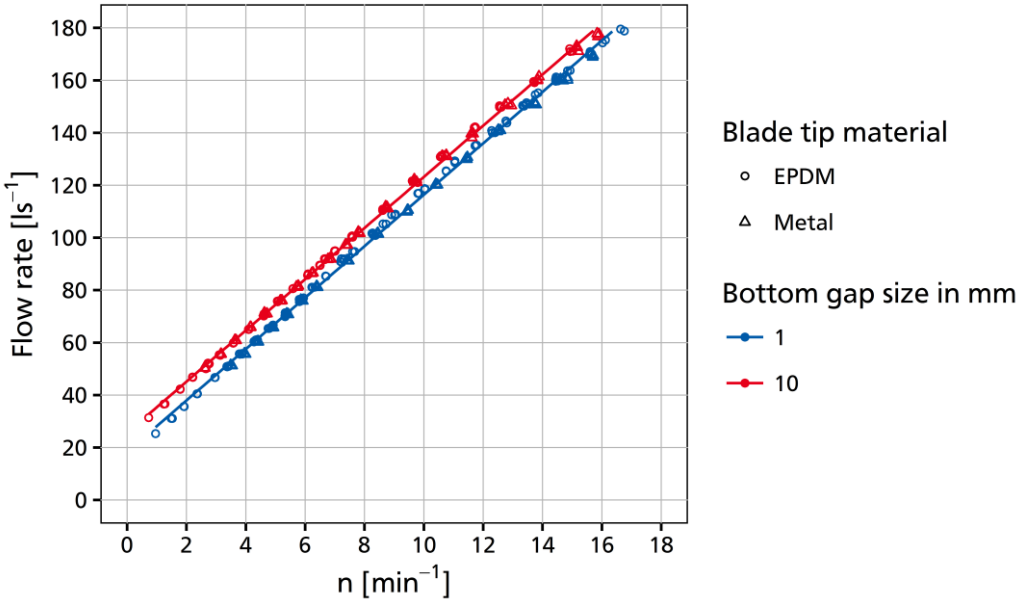

Figure 9. Results of different gap sizes on flow rate and speed of the wheel

Based on the difference in *y*-axis intercept between the two lines, a difference in gap losses of 7.0 ls^{-1} can be determined. Based on this value, Eq. 2 to Eq. 5 and the geometric details of the wheel, the coefficient for the bottom gap (μ_b) can be calculated by rearranging the equations or the use of a goal seek function. For the specific wheel tested the flow coefficient for the bottom gap is approx. $\mu_b = 0.33$. This value is far below the anticipation based on the literature quoting values between 0.6 and 1.0. The physical model results show that the flow rate passing the wheel during operation is approx. one third to half of the flow rate calculated by the theoretical approach taking a standstill wheel into account. This leads to the conclusion that gap losses are responsible for a much smaller proportion of the total energy losses within the converter than expected. That means other effects (inflow, turbulences etc.) have a bigger proportion than expected to date.

5. CONCLUSION

To determine the gap losses between the blade tip and the shroud of a HPM under operating condition, different gap sizes have been investigated in this study. Therefore, a conventional blade design (steel edge) and EPDM rubber as a sandwich construction were investigated. For analysis and comparison, a large scale physical model was built. Both materials reached with 1 mm gap size approx. 58 % hydraulic efficiency and a maximum mechanical power of approx. 220 W. Regarding power extraction and machine behaviour in general, no differences between the two analyzed blade tip materials were found. Results regarding the variation of the bottom gap size showed differences in efficiency of approx. 8 % between 1 and 10 mm. This underlines the importance of minimal gap sizes for high efficiency rates and optimal power extraction. To determine the gap losses (flow rate passing the wheel) a theory based on basic hydromechanics was developed in the past. This theory takes the flow through an orifice into account. The analysis of the results taken from the described physical model showed that the measured gap losses are approx. one third to a half of the flow rate calculated by the theory. This means gap losses have been overestimated and other losses (e.g. inflow, turbulences) underestimated in the past.

6. ACKNOWLEDGMENTS

This research was supported by German Federal Ministry for Economic Affairs and Energy (FZK 0325531A).

7. REFERENCES

Bozhinova, S., Petkova, S., Kisliakow, D., Andreev, I. (2012). Forschungskraftwerk mit einer Wasserdruckmaschine am Fluss Iskar (Bulgarien) im Rahmen des EU-Projektes HYLOW. In *Wasser - Energie, global denken - lokal handeln: [Tagungsband]*. G. Zenz, ed. Verl. der Techn. Univ, Graz, 329–336, in German.

Brinnich, A. (2001). Wasserkraft-Staudruckmaschine - Neues, konkurrenzlos wirtschaftliches Kraftwerkskonzept. *Wasserwirtschaft* 91(2), 70–74, in German.

Delabar, G., Dingler, J.G. (1867). Zuppinger'schen Wasserrades. *Polytechnisches Journal* 185(LXX), 249–253, in German.

IEC (1999). Hydraulic turbines, storage pumps and pump-turbines – Model acceptance tests. *International Electrotechnical Commission*. Geneva.

Linton, N.P. (2013). Field Trials and Development of a Hydrostatic Pressure Machine. *PhD Thesis*. University of Southampton, Southampton.

Moffat, R.J. (1988). Describing the uncertainties in experimental results. *Experimental Thermal and Fluid Science* 1(1), 3–17.

Mosonyi, E. (1963). Water Power Development: Low-Head Power Plants. Akadémiai Kiadó, Budapest.

Müller, G., Linton, N., Schneider, S. (2012). Das Projekt Hylow: Die Wasserdruckmaschine: Feldversuche mit einem Prototypen. *Korrespondenz Wasserwirtschaft* 102(1), 30–36, in German.

Paudel, S., Linton, N., Zanke, U.C., Saenger, N. (2013). Experimental investigation on the effect of channel width on flexible rubber blade water wheel performance. *Renewable Energy* 52, 1–7, doi:10.1016/j.renene.2012.10.014.

Schneider, S. (2016). Funktionsanalyse und Wirkungsoptimierung einer Wasserdruckmaschine. *PhD Thesis.* Technische Universität Darmstadt, Darmstadt. http://tuprints.ulb.tu-darmstadt.de/id/eprint/5443. in German.

Senior, J.A. (2009). Hydrostatic Pressure Converters for the Exploitation of Very Low Head Hydropower Potential. *PhD Thesis*. University of Southampton, Southampton.

Senior, J.A., Müller, G., Wiemann, P. (2007). The development of the rotary hydraulic pressure machine. In *32nd congress of IAHR, the International Association of Hydraulic Engineering & Research: Abstracts; July 1 - 6, 2007, Venice, Italy*. CORILA, Venezia.

Senior, J.A., Saenger, N., Müller, G. (2010). New hydropower converters for very low-head differences. *Journal of Hydraulic Research* 48(6), 703–714.

Wölfel, W. (1987). Das Wasserrad: Technik und Kulturgeschichte. U. Pfriemer, Wiesbaden, in German.

DOI:10.15142/T3ZP4F

An investigation of the velocity field over rippled sand bottom

B. Stachurska[1], R. Staroszczyk[1]
[1] Institute of Hydro-Engineering, Polish Academy of Sciences,
Gdansk, Poland
E-mail: b.stachurska@ibwpan.gda.pl

ABSTRACT

Ripples at a sandy seabed are the consequence of the oscillatory movement of water particles. The ripples are the reason for the increase of the bed roughness of the bottom becoming an important factor in the sediment transport process. Better understanding of the processes taking place in the near-bottom flow field will allow an accurate description of the mechanism of the sediment transport. An experimental investigation of the velocity field over rippled sand bottom has been carried out in a wave flume of the Institute of Hydro-Engineering of the Polish Academy of Sciences in Gdansk. Measurements were performed using the technique of Particle Image Velocimetry. The velocity fields of the sandy sediment were measured in the region immediately over the flume bottom coated by sand ripples. The results obtained describe the instantaneous velocity fields of sediment particles along vertical and horizontal profiles at different spatial locations and at different phases of the oscillatory flow induced by free-surface water wave propagation. It has been demonstrated that the Particle Image Velocimetry technique of measuring the movement of sediment particles at the bottom proximity has proven as a reliable and sufficiently accurate method. The experimental data obtained will enable the validation of a numerical model which is currently developed.

Keywords: *Sediment movement, sand ripples, velocity field, PIV method*

1. INTRODUCTION

The study of the velocity field over rippled sand bed is fundamentally important for understanding sediment transport processes. The roughness of the bed increases as the ripples develop, which affects the near-bed water flows. Near-bed velocities of water particles depend on various factors, such a surface wave height, wave period or wave length. Consequently, the morphology of the seabed depends on the hydrodynamics of both water and sediment. The velocity fields can be calculated from theory or by numerical modelling, but obviously these methods should be based on the results from experiments and in situ observations.

In the literature on the subject there are descriptions of many experiments that have been carried out on water wave-generated sand ripples. One of the first was that conducted by Bagnold (1946), in which trays of sediment were oscillated in still water. Bagnold studied the variability of the geometry of sand ripples, and observed that the length of the ripples depends on the magnitude of the oscillation amplitude of water particles in close proximity to the bottom. The first important field research concerning ripples geometry was presented by Inman and Bowen (1962). Further extensive research on ripples geometry was conducted by Mogridge and Kamphuis (1972), Sleath (1975), Pruszak (1978) and Miller and Komar (1980). Boundary roughness of sandy beds was studied by Grant and Madsen (1982). These authors found that the bed roughness parameter is a function of the shear stress at the boundary. Sato, Mimura and Watanabe (1984) investigated experimentally the characteristics of the oscillatory boundary layer flow above rippled beds. These authors concluded that the velocity of the oscillatory boundary layer above the rippled bed is strongly influenced by vortices formed near the slopes of ripples. A very thorough experimental investigation of the mechanism of vortex generation and ejection from the ripple surfaces was carried out by van der Werf et al. (2007). They made detailed measurements of sediment particle velocities near bottom ripples in a series of experiments carried out in an oscillatory flow tunnel. Their results showed that the geometry of sand ripples gives rise to the formation of convective cells in the near-bed flows, resulting in a significant increase in the sediment particle velocities compared to those in free stream flows over flat beds. These authors also gave detailed insights into the mechanism of sand particle pick-up and the process of sediment transport in oscillatory flows.

The above experimental results by van der Werf et al. (2007) have been obtained by making use of a PIV (Particle Image Velocimetry) technique. This technique is based on the analysis of images of tracer particles seeded in water and observed within a thin sheet of fluid lit by laser light (Willert and Gharib 1991). The PIV

method, commonly used for over two decades for making measurements in one-phase fluid flows, can still be treated as a relatively new experimental tool for two-phase fluid flows, such as the flows of sediments suspended in water. This situation is due to some technical difficulties encountered in the implementation of the PIV technique in the case of two-phase flows, and due to problems with proper interpretation of measurement results. One of the first successful attempts to use the PIV method in experiments involving the motion of sandy sediments caused by water wave propagation belongs to Ahmed and Sato (2001). These authors investigated the dynamics of the bottom boundary layer and used the PIV technique to measure the volume flux of sand transported in sheet flow under asymmetric oscillations. Based on the measured velocity and sand concentration, the net volume flux was calculated. In another paper by Van der Werf et al. (2008) two different sediment models were tested and validated against the PIV velocity and sediment concentration measurements above full scale-ripples in regular oscillatory flow. Yang, Wang and Liu (2011) presented a method which enables simultaneous determination of the velocity fields of both phases in sediment transport problems by using the PIV with fluorescent tracer particles. Umeyama (2012), in turn, focused on surface waves propagating in water of finite depth and used the PIV technique to measure the water particle velocities and trajectories.

From among the above papers reporting the use of the PIV method for measuring sediment particle motion in water, only two (Ahmed and Sato 2001 and Umeyama 2012) were concerned with flows induced by free-surface gravitational waves propagating over a sandy bed. Hence, there is a need of further experimental investigation of the sediment transport phenomena in water due to surface wave propagation in order to enhance our understanding of fundamental mechanisms involved. The present work is an attempt in this direction. Another motivation of this work was to gather detailed experimental data sets that could be used to validate a numerical model (based on the Smoothed Particle Hydrodynamics method) which is currently developed by the authors.
The paper focuses on the measurements of instantaneous velocity fields of both sandy sediment particles near a rippled bed, and of water particles higher above the bed. In Section 2 experiments conducted in a wave flume with the use of the PIV technique are described. In Section 3 the results obtained and the data analysis are presented. Section 4 is devoted to the calculations of the thickness of the bottom boundary layer, based on the PIV data. Finally, in Section 5 some conclusions are presented.

2. EXPERIMENTAL SETUP AND DATA POST-PROCESSING

Experiments were carried out in a wave flume of the Institute of Hydro-Engineering of the Polish Academy of Sciences (IBW PAN) in Gdansk, Poland. The wave flume is 64 m long, 0.6 m wide and 1.4 m deep. Water waves were generated by a programmable piston-type wave maker. For the purpose of the experiments described here, part of the wave flume (of a length 6.07 m) was isolated from the rest of the flume. In this selected flume section, a container (cuvette) with sand was placed at 2 m downstream of the wave paddle (see Fig. 1).The sand was taken from a beach at a village of Sobieszewo (part of the Gdansk agglomeration). The median diameter of the sand grains was determined during a sieve analysis and was established to be equal to d_{50} = 0.257 mm.

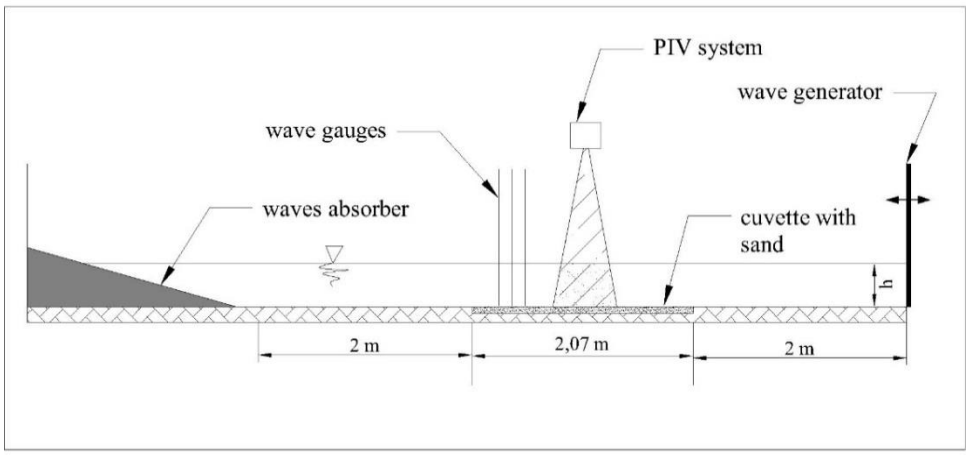

Fig. 1. Experimental setup.

The average water depth during the measurements was h = 0.3 m. Changes in the water free surface elevation were measured by a system of three wave gauges placed in the middle of the measurement area. The measurements were recorded with a sampling frequency of 100 Hz. In order to measure sand and water particle

velocities, a PIV system was applied. The PIV technique evaluates the instantaneous velocities through recording and analysing, at successive instances of time, positions of small tracer particles that are suspended in the fluid.

The main objective of the experiments was to determine the instantaneous velocity field in the near-bottom region. The main point of interest was to identify the velocity and direction of sand particles moving over rippled sandy bottom. During the PIV measurements, the laser light sheet was emitted from above the free surface of water in the flume. For recording successive images of sediment particle distributions, a high-definition digital video camera was used. The PIV system was supplied by *Dantec Dynamic*, and a *FlowSense EO 4M* camera was used during the measurements. In this system, the inter-frame time is 200 ns, and the sensor resolution is 2048 px × 2048 px. In our first experiments the water in the flume was seeded with glass hollow spheres. However, it turned out that the suspended sand grains in near-bed region acted as the seeding agent. The PIV post-processing was carried out by using the PIVlab1.4 software (Thielicke and Stamhuis 2014).

In the measurements, surface waves with a period of $T = 1.5$ s and a height of $H = 0.1$ m were used. Before starting the PIV measurements, water waves were generated for approximately 30 min, so as to achieve a state of equilibrium of bed forms. The resulting ripples had a height of approximately 1.7 cm and a length of approximately 7 cm.

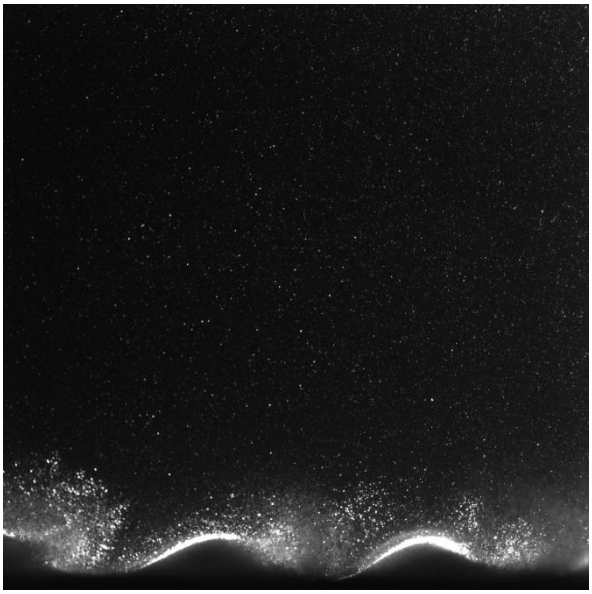

Fig. 2. Typical PIV image.

By analysing images (Fig. 2) recorded by the PIV camera, plots showing the instantaneous velocity field of sand particles were generated. The analysis of these data allowed the determination of the vertical and horizontal velocity profiles of the sand particles in the near-bed region.

3. VERTICAL AND HORIZONTAL VELOCITY PROFILES ABOVE THE RIPPLES

From the PIV experimental data, both the vertical and horizontal instantaneous velocity profiles were determined. Vertical velocity profiles were measured above the crest and trough of the representative bed form (Fig. 3a). A horizontal velocity profile was measured at a location just above the ripple crests (Fig. 3b), with the x-axis origin at the left border of the image and its direction to the right. The analysis of the vertical velocity distributions has been carried out for two cases: under the free-surface water wave crest, or under the water wave trough; that is, for two extreme cases of the water velocity magnitudes near the bed.

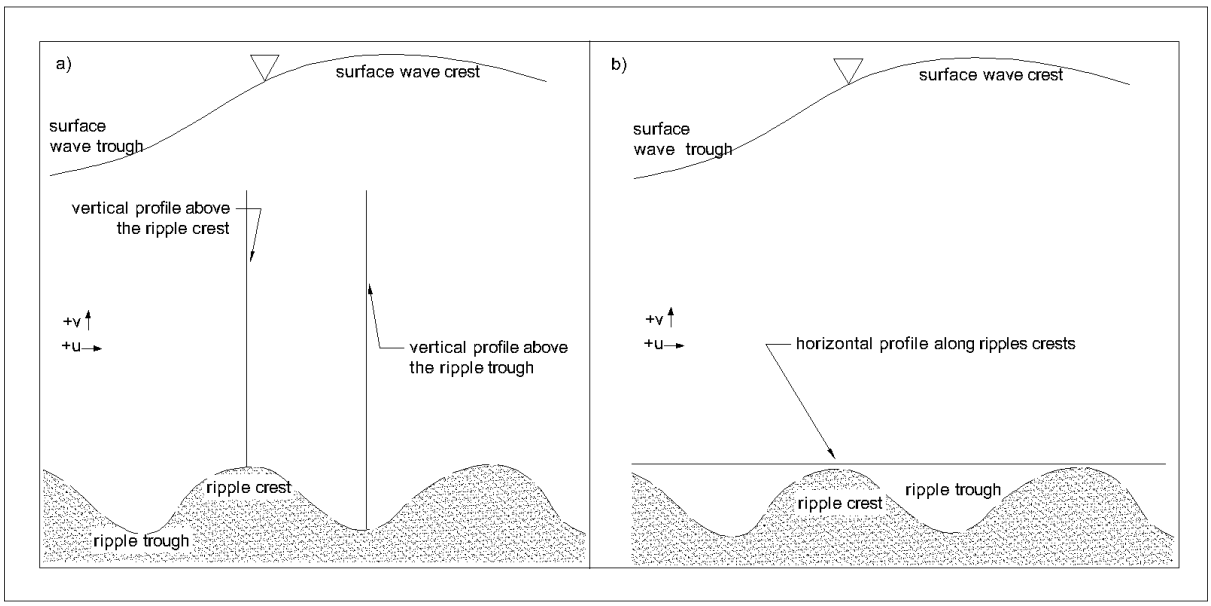

Fig. 3. Vertical (a) and horizontal (b) profiles above the rippled bed.

Figure 4 present the horizontal (*u*) component of the particle velocity. Fig 4a shows the vertical profile located in the ripple crest, and Fig 4b the vertical profile located in the ripple trough. The left plot in each figure shows the *u*-velocity profile measured with a surface wave crest directly overhead; the *u*-velocities profile on the right corresponds to surface wave trough directly overhead of the profile location.

Figure 4a shows that the near-bed extremum horizontal velocities are similar in magnitude in both situations and their maximum values vary within the range ±0.24÷0.23 m/s. Slightly higher are the velocities occurring during the transition of the wave trough. Above the region of the sediment moving layer, in a region of the free stream velocity, the horizontal velocity component is significantly smaller and has a value of approximately 0.16 m/s under the wave trough, and 0.12 m/s under the wave crest. Moreover, it was found that the sediment moving layer located in the near-bed region has a thickness 0.01 m at the time of the surface water wave trough transition, and 0.008 m at the time of the water wave crest transition.

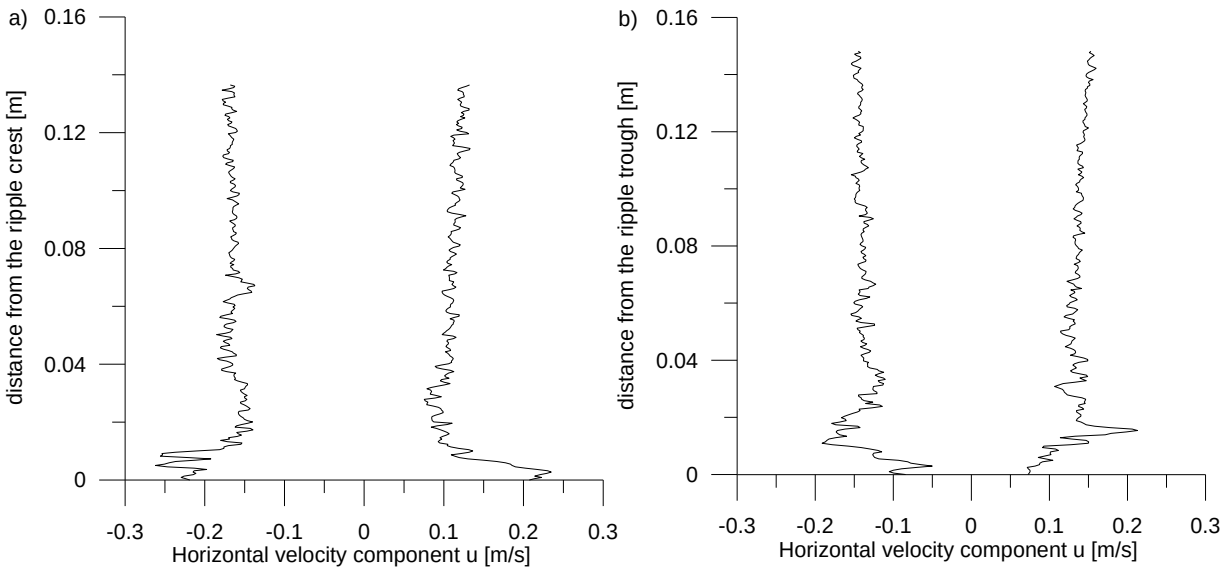

Fig. 4. Instantaneous horizontal velocity component distributions along the vertical profiles above the ripple crest (a) and above the ripple trough (b). For both locations shown are the velocity profiles under the surface water wave trough (left plot in each figure) and under the water wave crest (right plot).

Similarly, Figure 4b shows the vertical velocity profiles of the horizontal velocity component (*u*), but this time located at the ripple trough. Such a way of presenting the vertical profiles helps to determine the elevation above

the ripple trough at which the sediment movement under the action of surface wave begins. It was estimated that the thickness of this layer was 0.01m in case of the surface wave trough transition, and was 0.005 m in case of the wave crest transition. This finding is consistent with the results discussed above for the profile situated at the ripple crest (Fig. 4a). The wave-bottom boundary layer started at 0.01 m above the ripple trough surface at the time of the water wave crest transition, and at about 0.014 m at the time of the water wave trough transition. Moreover, it is seen that the near-bed extremum horizontal velocities, for the situation under the surface water wave trough, reach about 0.19 m/s (the left plot in Fig. 4b), and in the situation under the wave crest (the right plot in Fig. 4b) they are equal to about 0.2 m/s. It may seem a little surprising that the near-bed velocities are higher than those in the free flow field. This phenomenon, though, was already observed earlier by van der Werf et al. (2007), and results from the mechanism of the vortex generation and shedding off the sand ripple slopes, which considerably influences the flow within a region of about 1.5 ripple heights over the line of ripple crests.

The next step was to determine the vertical profiles of the vertical component (*v*) of the near-bed velocity. For this purpose, the same vertical profiles (Fig. 3a) as those described above were used. Figure 5 presents the vertical velocity distribution along a vertical profile located above the ripple crest. What is most characteristic for the two situations considered (the water wave crest and the wave trough transition) is the distinctive increase of the vertical velocity component in a near-bed region compared to the velocities occurring at higher locations in the free stream flow region. Under the water wave trough (Fig. 5a), the maximum vertical velocities in the near-bed layer of the moving sediment are 0.045 m/s, whereas under the wave crest (Fig. 5b) these velocities reach 0.05 m/s. The thickness of this wave-bottom layer was estimated as 0.008 m in the situation in the Fig. 5a, and 0.01 m in the situation in the Fig. 5b.

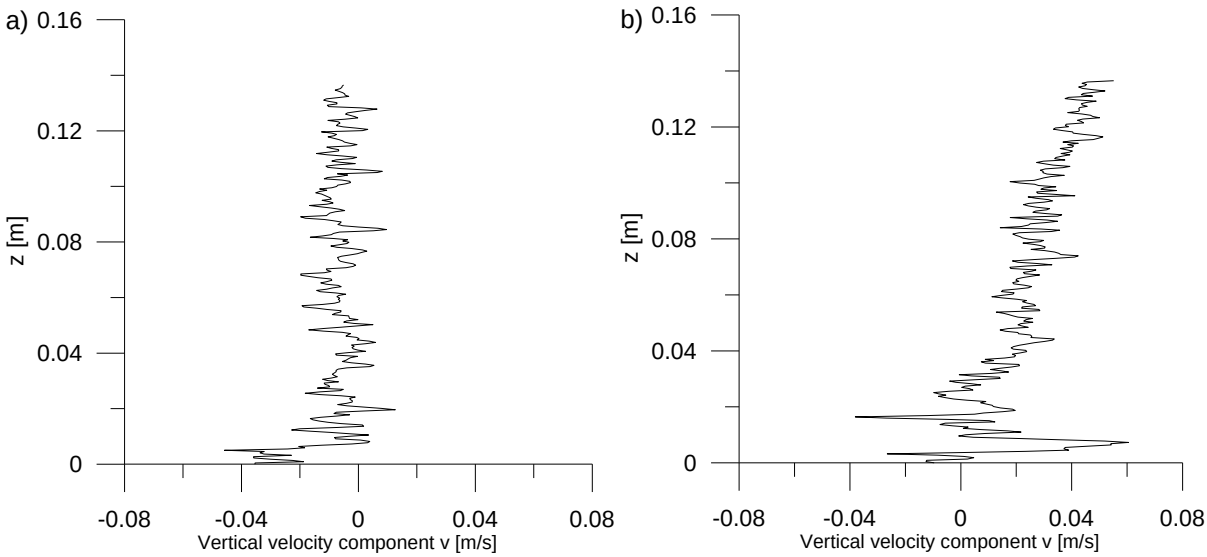

Fig. 5. Instantaneous vertical velocity component distributions along the vertical profile above the sand ripple crest: (a) under the water wave trough, (b) under the water wave crest.

From the vertical profiles located at the sand ripple trough (Fig. 6) some additional information about the vertical velocities of sand particles in the sediment moving layer was inferred. The thickness of the wave-bottom boundary layer under the surface wave trough (Fig. 6a) is about 0.03 m, and under the wave crest (Fig. 6b) it is about 0.02 m. The magnitudes of the vertical velocities in the moving sediment layer in both situations (under the surface wave trough and the wave crest) were similar and equal to about 0.05 m/s, which is compatible with the results plotted in Fig 5.

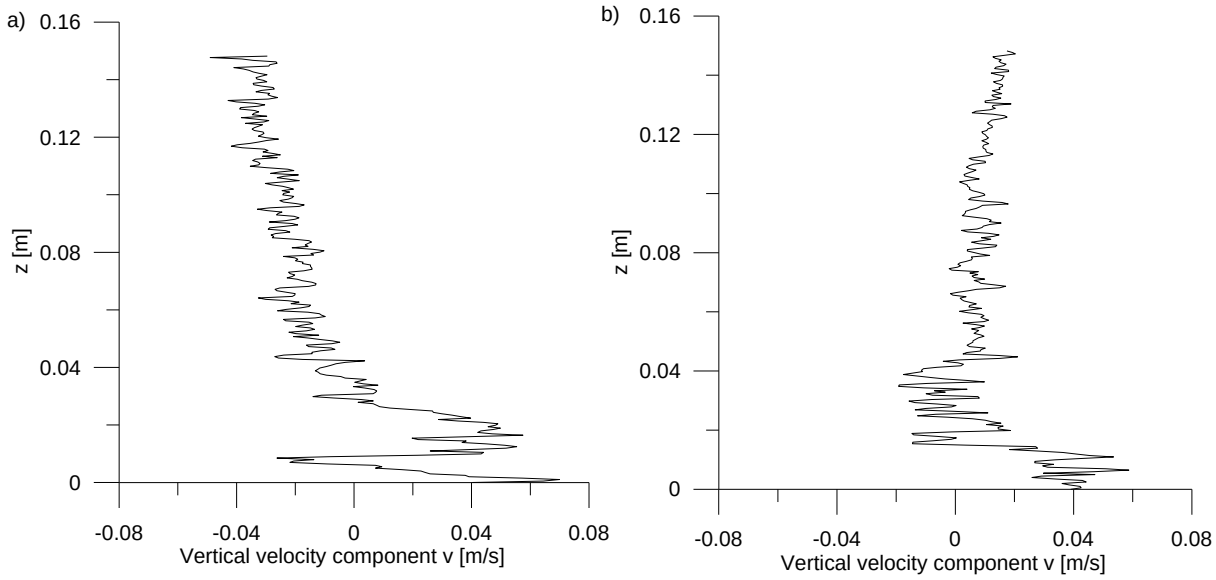

Fig. 6. Instantaneous vertical velocity component distributions along the vertical profile above the sand ripple trough: (a) under the water wave trough, (b) under the water wave crest.

Fig. 7 presents the vertical distributions of both sediment velocity components. Fig. 7a shows the distributions of the horizontal components (*u*), and Fig. 7b of the vertical components (*v*), at four different phases of a single free-surface water wave period *T* (*t* = 0 corresponds to the beginning of the flow period).

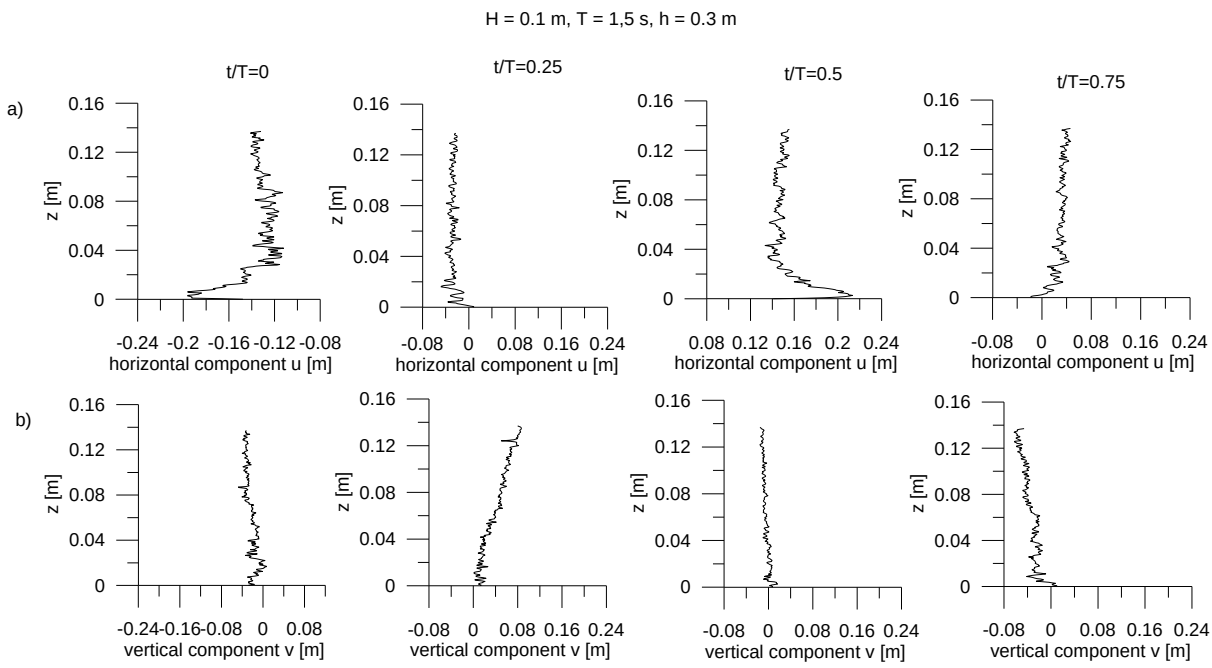

Fig. 7. Vertical profiles of instantaneous velocity distributions: (a) horizontal component (*u*), (b) vertical component (*v*), at four characteristic phases of a single free-surface water wave period.

The next stage of the PIV results analysis concerns the horizontal profile, which was located directly over the ripple crests (see Fig. 3b). The distribution of the horizontal velocity component (*u*) along that profile is presented in Fig. 8. It can be noted that the velocities *u* are clearly larger above the sand ripple crests than those over the ripple troughs. For instance, the mean values of *u* are 0.23 m/s over the ripple crests, compared to 0.08 m/s over the troughs. Moreover, both at the wave trough transition (Fig. 8a) and the crest transition (Fig. 8b), the values of the velocity components are comparable in magnitude along the horizontal profile.

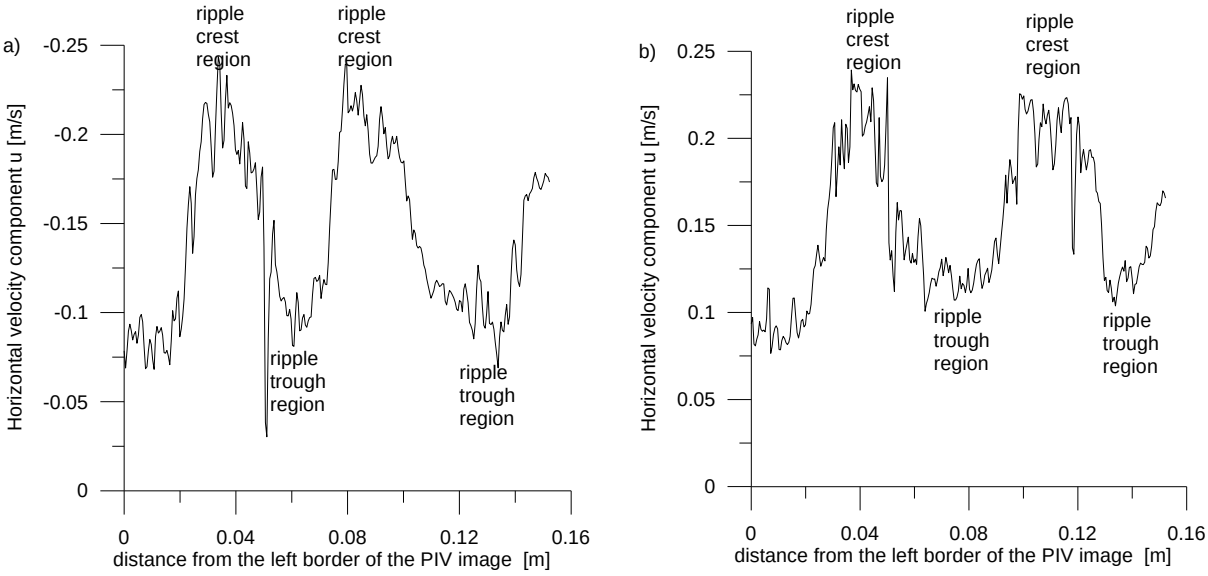

Fig. 8. Horizontal velocity component distributions along the horizontal profile: (a) under the water wave trough, (b) under the water wave crest.

Finally, the horizontal profiles of the vertical (*v*) velocity components are presented in Fig. 9. Also in this case, both during the free-surface water wave trough and the water wave crest transitions, the extremal measured values are quite similar in magnitude. Above the ripple troughs the vertical velocities are positive and vary from about 0.04 m/s to about 0.08 m/s. For comparison, over the ripple crests, the corresponding values are negative and change from –0.04 m/s to almost –0.08 m/s.

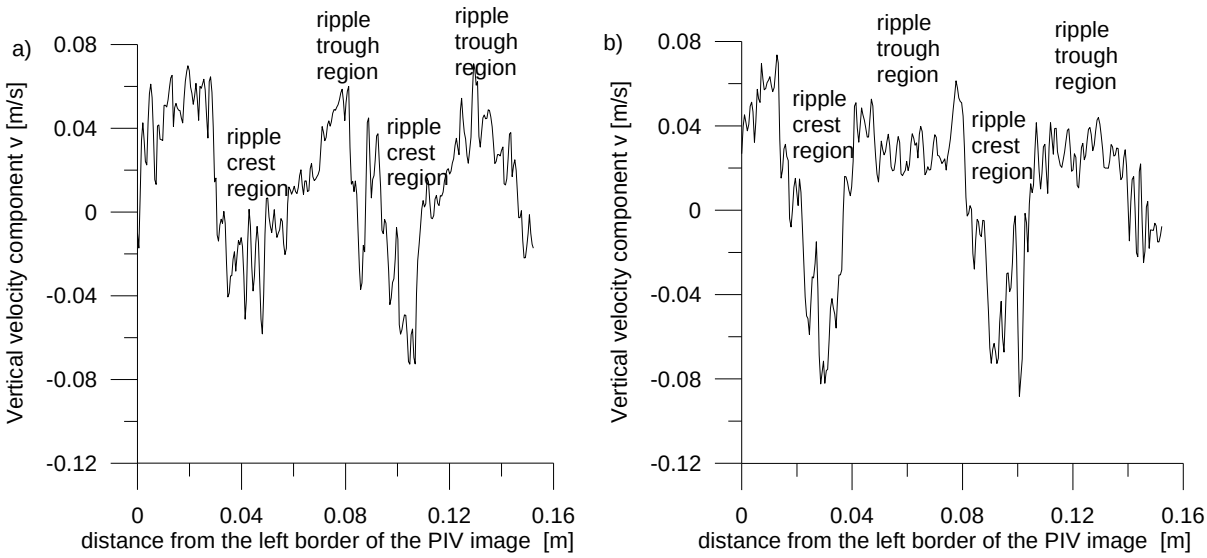

Fig. 9. Vertical velocity component distributions along the horizontal profile: (a) under the water wave trough, (b) under the water wave crest.

4. THICKNESS OF THE WAVE-BOTTOM BOUNDARY LAYER

The important part of the flow is the bottom boundary layer. The latter is meant as the layer inside which the flow is significantly influenced by the bed. The thinner the bottom boundary layer is, the larger shear stress is at a given flow velocity (Nielsen 1992). In this study, laboratory observations of the near-bed velocity are used to evaluate the thickness of the wave-bottom boundary layer (Fig. 10). As already noted, in a layer immediately above a rippled bed, the sand dynamics is dominated by the mechanism of vortex formation and shedding above the ripple slopes (van der Werf et al. 2007).

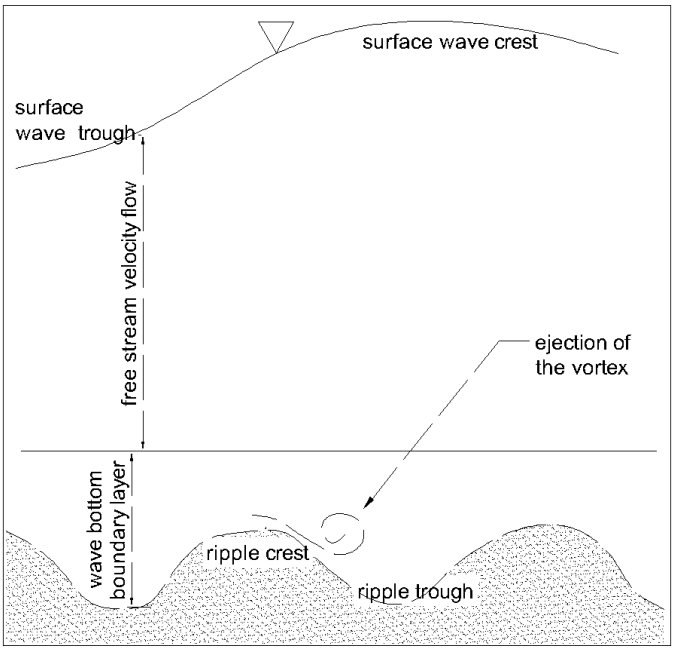

Fig. 10. Near-bed region with wave-bottom boundary layer.

In order to determine the thickness of the wave-bottom boundary layer, a formula proposed by Nielsen (1992) is used, which is exact for the case of simple time-harmonic flows:

$$\delta = \frac{1}{2}\frac{u}{\omega} f_w \tag{1}$$

where δ denotes the layer thickness, u is the horizontal velocity amplitude of the fluid occurring just above the boundary layer, ω is a wave angular frequency, and f_w is a so-called wave friction factor. The latter can be estimated by a method described in detail by Doering and Baryla (2002), based on formulae proposed by Nielsen (1992).

The first step to calculate the thickness of the wave-bottom boundary layer is to evaluate a grain roughness friction factor. This can be calculated by employing a formula by Swart (1974), which is expressed as:

$$f_{2.5} = \exp[5.213\left(\frac{2.5d_{50}}{u}\right)^{0.194} - 5.977] \tag{2}$$

where d_{50} is the median grain diameter of the sediment.

To measure the force exerted by fluid on a sediment particle during the surface wave transition, a dimensionless quantity is used, known as the mobility number, Ψ. The total disturbing force acting on a sand particle at the bed is approximately proportional to the square of the horizontal velocity amplitude u and the ratio between this disturbing force and the stabilising force due to gravity (Nielsen 1992). Hence, the number Ψ is defined by the equation:

$$\Psi = \frac{(u)^2}{(s-1)gd_{50}} \tag{3}$$

where s is the density of the sediment, and g is the acceleration due to gravity.

The sediment mobility number and the grain roughness friction factor define the grain roughness Shields parameter $\theta_{2.5}$ (Nielsen, 1992), expressed by the formula:

$$\theta_{2,5} = \frac{1}{2} f_{2.5}\Psi \tag{4}$$

The parameter $\theta_{2.5}$ is a dimensionless measure of the bottom shear stress, occurring in the flow over a sandy bed. When a bottom is covered by ripples, then $\theta_{2,5} < 0.25$, and it should be assumed that the hydraulic roughness of the bed is a function of the ripple height, its length and the grain roughness. To take into account the effect of the roughness due to the mechanisms of sand particles moving over ripples, a formula for the hydraulic roughness can be used:

$$r = \frac{8\eta^2}{\lambda} + 170 d_{50}\sqrt{\theta_{2.5} - 0.05} \tag{5}$$

in which η and λ are the ripple height and length, respectively.

The water under the surface wave interacts with the sandy bottom mainly due to shearing, which is measured by a shear stress τ. For this reason, the determination of the shear stress is an essential element in the calculation of the sediment transport. Generally, the friction factor of the wave is a function of the Reynolds number and the hydraulic roughness (r) of the bottom. Under certain conditions, the wave friction factor can be expressed in a simple way. For instance, if the bed is hydraulically smooth, than the friction factor f_w is a function of only the Reynolds number. If, in turn, the bottom is hydraulically rough, then f_w is a function of the bed roughness. It is assumed here that the bottom is hydraulically rough, which means that the boundary layer conditions are turbulent. In this case, the wave friction parameter is defined by:

$$f_w = \exp\left[5.5\left(\frac{r\omega}{u}\right)^{0.2} - 6.3\right] \tag{6}$$

where r denotes the hydraulic roughness of the bed, ω is the angular frequency. The wave friction factor, obtained from Eq. (6), can then be used to calculate the thickness of the boundary layer, as described by Eq. (1).

For the experiments described in this work, the ripple geometry was found to remain fairly constant, and could be described by the parameters η = 1.7 cm and λ = 7 cm. The median grain diameter d_{50}, as mentioned earlier, was 0.257 mm. For this case, the near-bed velocities in wave-bottom boundary layer were measured by the PIV technique, and the value adopted in the calculations was u = 0.24 m/s. With this information, the grain roughness Shields parameter ($\theta_{2.5}$), hydraulic roughness of the bed (r), and the friction factor (f_w) were found to be 0.16, 0.047, and 0.36, respectively. With these latter values, the thickness of the wave-bottom boundary layer, assuming rough turbulent conditions, was calculated to be equal to 1.04 cm. This result is consistent with that determined from the PIV measurements, wherein the thickness of the moving sediment layer in a wave-bottom boundary region, r, was approximately 1 cm, see the previous section.

5. CONCLUSIONS

The following conclusions can be drawn from the experimental observations presented in this paper:

(i) In the wave-bottom boundary layer, the maximum velocities near the ripple crest can be up to two times higher than the maximum free stream velocity. This is the result of the flow acceleration over the crest and the jet flow associated with the ejection of vortices on the slopes of the sand ripples (the mean velocity value in the near-bed region is 0.24 m/s, compared to 0.14 m/s in free stream flow).

(ii) The vertical velocities in the near-bed region vary from about 0.04 to about 0.06 m/s, and are strongly influenced by the presence of underlying sand ripples.

(iii) Bed forms significantly affect the near-bed sediment vertical velocities, leading to strong downward and upward local flows, depending on the local morphology of the ripples.

(iv) The thickness of the wave-bottom boundary layer (the sand active layer) was measured with a good accuracy, and its value was in accordance with the results of theoretical calculations.

6. ACKNOWLEDGEMENTS

Financial support for this research has been provided by the National Science Centre, Poland, under the contract no. UMO-2013/11/B/ST8/03818, and by the Institute of Hydro-Engineering of the Polish Academy of Sciences in Gdansk, Poland.

7. REFERENCES

Ahmed A.S.M. and Sato S. (2001). Investigation of bottom boundary layer dynamics of movable bed by using enhanced PIV technique. *Coastal Engineering*, 43 (4), 239-258.

Bagnold R. A., (1946). Motion of waves in shallow water, interaction between waves and sand bottom. *Proc. Royal Soc. London*, Series A, vol. 187, 1-15.

Doering J.C. and Baryla A.J. (2002). An investigation of the velocity field under regular and irregular waves over a sand beach, *Coastal Engineering*, 44, 275-300.

Grant W. D. and Madsen O. S. (1982). Movable bed roughness in unsteady oscillatory flow. *J. Geophys. Res*., 87, 469–481.

Inman D. and Bowen A.J. (1962). Flume experiments on sand transport by waves and currents, *Coastal Engineering Proceedings*, 8, 137-150.

Miller M.C. and Komar P.D. (1980). A field investigation of the relationship between oscillation ripples spacing and the near-bottom water orbital motions. *J. Sediment. Petrol*., 50, 183-191.

Mogridge G. R. and Kamphuis J. W. (1972). Experiments on ripple formation under wave action. *Proc. 13th Int. Conf. Coastal Engineering*, Vancouver, Canada, ASCE, 1123-1142.

Nielsen P. (1992). *Coastal Bottom Boundary Layers and Sediment Transport, Advanced Series on Ocean Engineering*, (4), World Scientific.

Pruszak Z. (1978). Procesy formowania się, rozwoju oraz zanikania małych form dennych w oscylacyjnym ruchu cieczy, *Rozprawy Hydrotechniczne*, 39, IBW PAN Publishing House (in Polish).

Sato S., Mimura N. and Watanabe A. (1984). Oscillatory boundary layer flow over rippled beds, *Proc. 19th Conf. on Coastal Engng.*, Houston, 2293-2309.

Sleath J.F. (1975). A contribution to the study of vortex ripples, *J. Hydraul. Res*., (13), 315-328.
Swart D.H. (1974). Offshore sediment transport and equilibrium beach profile, *Delft Hydr. Lab. Publ*., (131).

Thielicke W. and Stamhuis E.J., (2014). PIVlab – Towards User-friendly, Affordable and Accurate Digital Particle Image Velocimetry in MATLAB. *Journal of Open Research Software*.

Umeyama T. (2012). Eulerian–Lagrangian analysis for particle velocities and trajectories in a pure wave motion using particle image velocimetry. *Phil. Trans. R. Soc.* A 370, 1687–1702.

Van der Werf J.J., Doucette J.S., O'Donoghue T., and Ribberink J.S., (2007). Detailed measurements of velocities and suspended sand concentrations over full-scale ripples in regular oscillatory flow. *J. Geophys. Res.*, 112, F02012.

Van der Werf, Magar V. Malarkey J., Guizien K. and O'Donoghue (2008). 2DV modelling of sediment transport processes over full-scale ripples in regular asymmetric oscillatory flow. *Continental Shelf Research*, 28, 1040-1056.

Willert C. E. and Gharib M. (1991). Digital particle image velocimetry, *Original Experiments in Fluids*, 10, 181-193.

Yang B., Wang Y., Liu J. (2011). PIV measurements of two phase velocity fields in aeolian sediment transport using fluorescent tracer particles. *Measurement*, 44, 708-716.

DOI:10.15142/T3V01G

Feasibility Study and Optimization of the Structural Design of Locks made out of Plain Concrete

A. Tahir[1], C. Kunz[1] and K. Terheiden[2]
[1]Federal Waterways Engineering and Research Institute (BAW), Germany
[2]Institute for Modelling Hydraulic and Environmental Systems,
University of Stuttgart, Germany,
Email: arslan.tahir@baw.de

ABSTRACT

Modern ship locks are made of steel reinforced concrete. A crucial issue, similar to other hydraulic structures, is the intensive exposure to water and therefore consequently the contact to a highly varying physical and chemical environment. This may cause rapid deterioration of the concrete cover due to the ingress of chloride, oxygen and moisture leading to excessive corrosion of the embedded reinforcement. Consequently, a strong decrease in structural strength is inevitable. Against this background a study was conducted in which only a plain concrete structure was considered. This construction method had been used successfully in former times and was then replaced by reinforced concrete constructions in the 1960s. The study considered a typical concrete ship lock structure without any reinforcement, with length of 190 m, width of 12.5 and a fall of 10 m. The structural analyses are focused on the lock chamber walls as they are the most labor and cost intensive components rather than on the lock head and gates. The structural and geotechnical verifications were conducted in accordance to latest Eurocodes and German standards along with Finite Element Analysis using ANSYS. The structure was designed for three extreme operating conditions depending on different water level inside the chamber. Furthermore dimensional optimizations are preformed using linear programming and sensitivity analysis is conducted by variation of input parameters. Whereas this paper would only focus on effects due to variation in groundwater level, concrete and soil type. The findings suggest that the most critical loading condition is when there is no water in the chamber. In this case a gravity wall base length of 13.28m is required to reach sufficient stability. However, the bearing capacity of soil and the tensile strength of the concrete are the most critical safety checks for this type of structure.

Keywords: *Ship-Lock Structures, Plain Concrete, Static Structural Analysis, ANSYS, Feasibility, Optimization*

1. INTRODUCTION

Steel reinforced concrete can withstand high stresses in slender constructions which make it the obvious choice for hydraulic structures in general and modern ship locks in specific. However, these structures are permanently in contact with water and therefore subjected to highly variable physical and chemical environments depending on their location and usage. Processes like carbonation, freezing-thawing cycles and acid attack progressively reduce the durability of the concrete structure Rapid deterioration of concrete cover leads to an increasing ingress of chloride, oxygen and moisture causing excessive corrosion of the embedded steel reinforcement and a strong decrease in material durability and service life (Westendarp et al. 2014). In addition, "Navigation structures are subjected to significant weathering and deterioration that can result in spalling, scaling, and increased surface roughness along with scour and erosion in underwater locations." (USACE 2016).

It had been observed by the experts at German Federal Waterways Engineering and Research Institute (Bundesanstalt für Wasserbau, BAW) that the maintenance requirement for reviving the structural integrity of young reinforced concrete structure is comparatively higher when compared with older plain concrete structures. Similar problems are reported in United States navigation infrastructure, "Steel and other metallic materials may be damaged by corrosion, fatigue, mechanical overloading, stress-assisted corrosion and embrittlement" (USACE 2016).
In addition to high susceptibility of reinforcement to damage, it was found that the most dominant failure mode in existing hydraulic infrastructure under the BAW and Waterways & Shipping Board (WSV) was cracking, which was experienced in almost 25 % of inspected structures (Kunz and Bödefeld 2001). The crack allows the

penetration of water and air which additionally aids corrosion and exponential decrease of stress bearing capacity of structure.
The construction method employing only plain concrete in hydraulic structures had been extensively used in former times until in 1960s when the reinforced concrete design was introduced. It is estimated by BAW that about 65 % of the existing structures in the waterway's infrastructure are made out of plain concrete or light reinforced concrete. Most of the old unreinforced infrastructure still fulfills its functional requirements with little required maintenance. In view of this advantage a study was initiated by BAW in cooperation with Department of Hydraulic Engineering and Water Resources Management, University of Stuttgart with the research target of optimized structural and dimensional requirements of a modern ship lock structure. The research employed the concepts of using plain concrete under consideration of the current standards and design philosophies of Eurocodes and German standards. Similar concepts have been used in the past and reported in (PIANC 1986) and (Partenscky 1984) but the ship size and functional requirement of that time were lesser than present times. Therefore, a typical modern ship lock was chosen with a length of 190 m, width of 12.5 m with a fall of 10 m was selected.

The main focus of the initial design is on the lock chamber walls due to two reasons. Firstly, because it is well-known that concrete cannot withstand high tensile forces, therefore using plain concrete in head structures is not possible. Secondly, the lock chambers are the most labor and cost intensive component, hence its design and optimization would have a major impact on the feasibility of building such a structure. In order to assure the stability and safety of the structure, compliance with all current codes and standards is mandatory. The static structural and geotechnical verifications are made and additional verification for internal stresses was conducted using Finite Element Analysis of ANSYS. This study is conducted in accordance with the standards and design philosophies of Eurocodes (EN 1990, 1991, 1992, 1997) and German standards (i.e. DIN 19702). The structure was designed for three operating conditions, when the water level is at maximum, minimum operation water level and when there is no water in the lock chamber (maintenance condition). The last part of the research included the optimization of structural dimensions for each of loading conditions and varied input parameters. A literature review was conducted for selection of appropriate optimization algorithm. Several algorithms have been used for various objective functions for hydraulic structures, PSO (Particle Swarm Optimization Algorithm) was employed for hydraulic structural optimization field (Xinmiao et al. 2008), Genetic Algorithm (GA) was used in optimization model for optimum dimensions of the dam section under dynamic loadings due to seismic excitation (Ahmed et al. 2014), computation and comparison was conducted for optimized dimensions of a concrete gravity dam structure using gravitational search algorithm; particle swarm optimization; weighted least squares support vector machine (Salajegheh and Khosravi 2011). But all these advanced methods are requires high computational power and input data. Therefore a more generalized method "Linear programming" was used, considering the advantage that it requires no generation of new data points and its functioning could be understood intuitively. Consequently for this study the dimensional optimizations was performed by using linear programming for deign loading cases (water level in chamber) as well as for assessment of most sensitive parameters by varying the groundwater level, concrete type and soil type.

2. METHODOLOGY

2.1. Codes and Standards

In the last few decades Europe has seen a major shift in engineering design methodology with the inclusion of limit states design in its standards. This study considers both the European codes (EN) as well as German codes (DIN). The standards that were considered in the study are enlisted below.

European Standard (Eurocodes) with German Annexes

- DIN EN 1990 Eurocode 0 - Basis of structural design
- DIN EN 1991-1-1 Eurocode 1: Actions on structures - Part 1-1:
- DIN EN 1992-1-1 Eurocode 2: Design of concrete structures - Part 1-1
- DIN EN 1997-1 Eurocode 7: Geotechnical design - Part 1: General rules

DIN - Deutsches Institut für Normung (German Institute for Standards)

- DIN 19702 Solid structures in hydraulic engineering–Bearing capacity, serviceability and durability

- DIN 19703 Locks for waterways for inland navigation –Principles for dimensioning and equipment
- DIN 1054 Subsoil –Verification of the safety of earthworks and foundations –Supplementary rules to DIN EN 1997-1

Since the Eurocodes were used, the structure was designed and analyzed against ultimate and serviceability limit state using the corresponding partial safety factor for different actions and materials. This ensures that the design resistance (R_d) should not be less than the deign effects of actions (E_d). Furthermore a "safety ratio" was calculated which is the ratio between design resistance and design effect of actions. The key purpose of safety ratio is to translate all calculation of each limit state to a single value which later on assisted in simplification of the optimization process. The limit states considered in the research include limit state for failure by hydraulic uplift (UPL), by loss of static equilibrium (EQU), by failure of structure (STR) and geotechnical (GEO) failure.

2.2. Design load conditions and materials

Ship lock structures experience diverse environments; hence several loading conditions, corresponding shapes and sizes are possible. One of the investigated shapes consists of three disjoint structures, two concrete gravity retaining walls and an unreinforced concrete base slab. The preliminary shape and dimensions of the structure is shown in Figure1. The applied loads include hydro-static pressures, effective earth pressures, ground water forces, surcharge loads, up-lift pressures, self-weight of structures, weight of overburden soil. The application of these forces is indicated in Figure 2.

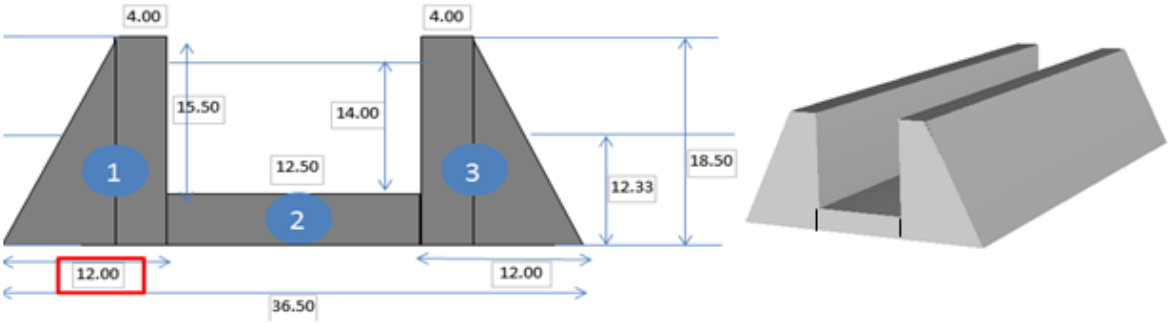

Figure 1. Shape and initial dimensions of the locks structure

Pressures/ Forces	Forces on the figure
Hydro-static Pressure	Fo
Ground water Table Force	F4
Effective Earth Pressure	F1,F2,F3
Self Weight of Structure	F8,F9
Surcharge Load	F5
Weight of overburden Soil	F10
Up-lift Pressure	F6,F7

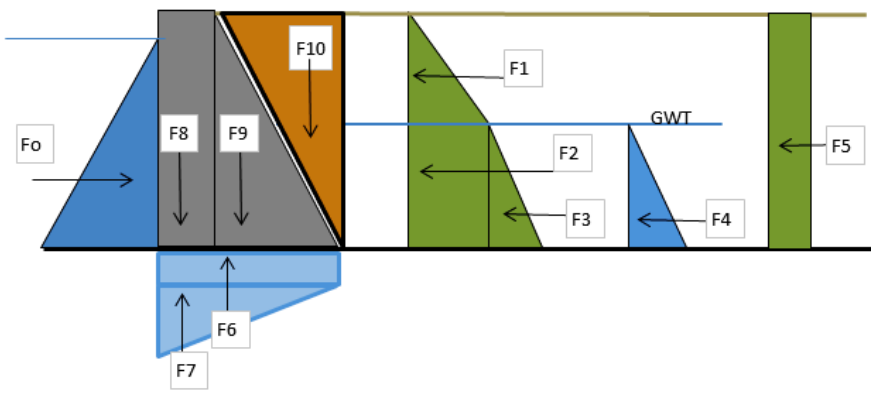

Figure 2. Forces and pressures applied on walls of the lock

The combinations of these forces lead to three design loading conditions. The material considered for the study was concrete class C 20/25, C 25/30 and C 30/35. The material strength and partial safety factor for the design compressive and tensile strength were taken from EN 1992(2014). For the design conditions concrete class C 20/25 was considered with design compressive strength (f_{cd}) of 9.33 MPa and design tensile strength ($f_{ctd,0.05}$) of 0.70 MPa. The properties of the earthen material for design conditions include the specific weight of the unsaturated soil with 20 KN/m^3 and of the saturated soil with 10 KN/m^3, the angle of internal friction was set to $\varphi = 30°$. For initial conditions, the earth pressure is 50 % active earth pressure and 50 % passive earth pressure resulting in an effective earth pressure coefficient of $K_{eff} = 0.39$.

Nine other conditions were evaluated in the sensitivity analysis by parameter variation. The following Table1 indicates the conditions and its respective changes.

Table 1. Parameters changed for Design conditions

Group No	Parameter	Situation	Case
1	Water level in the chamber	Highest operational water level in the chamber (w.l +14.0 m)	Design conditions
		Lowest operational water level (w.l + 4.0 m)	
		No water in chamber/maintenance case (w.l + 0.0 m)	
2	Water level in the ground	Water at 2/3 of total height of structure	Sensitivity analysis 1
		Water at the ground surface level	
		Water at lowest level of structure	
3	Different concrete strengths	Concrete class C 20/25	Sensitivity analysis 2
		Concrete class C 25/30	
		Concrete class C 30/35	
4	Soil type	Fine sand γ = 20 KN/m^3 γ' = 10 KN/m^3 , φ = 30°	Sensitivity analysis 3
		Clay γ = 19.5 KN/m^3 , γ' = 9.5 KN/m^3 ,φ = 22.5^o	
		Gravel γ = 21 KN/m^3 , γ' = 12 KN/m^3 , φ = 37.5^o	

2.3. Static verifications & Finite Element Analysis

For each limit state function corresponding actions, materials and partial safety factors were selected from the Eurocodes and DIN as mentioned in the section earlier. In total seven static verifications were made, which include safety against uplift, overturning, sliding, eccentricity, bearing capacity failure, shear forces and compressive strength check. The respective resistances and actions were calculated and a safety ratio was evaluated for each case. The details are given in the Table 2.

Table 2. Limit state function for verifications

Static verifications	Limit State condition			Remark	Reference literature
Failure by hydraulic uplift	Vertical design destabilizing force	<	Vertical design stabilizing force		EN 1997-1, DIN 1054
Overturning stability	Factored overturning moments	<	Factored reacting moments	For both pivot points, heel & toe	EN 1997-1, DIN 1054
Sliding resistance	Total horizontal sliding forces	<	Resisting forces	No cohesion between concrete & soil	EN 1997-1, DIN 1054
Load eccentricity	Factored load eccentricity	<	Allowable eccentricity	for both conditions Only permanent force & with variable force	DIN 1054
Bearing capacity check	Stress on soil	<	Allowable ultimate bearing capacity of soil	For both about heel & toe	DIN 1054
Shear forces check	Shear stress (design load)	<	Concrete design strength(shear & compression)	Shear stress in the concrete from axial load	EN 1992-1-1
Compressive strength check	Compressive stresses	<	Concrete design compressive strength	With & without pore water pressure	DIN 19702, EN 1992-1-1

In order to evaluate the internal stresses and possible failure of the material, Finite Element Analyses (FEA) was conducted. ANSYS Mechanical was used for the FEA for the proposed structure. For the current study a traditional approach was adapted for the static analysis of the subject structure, whereas the future work could

possible include dynamic analysis. The approach included selection of element type as "Solid 185" with eight nodes and homogenous isotropic structural solid elements. The concrete material properties for FEM modelling considered material as isotropic linear elastic concrete with a young's modulus of 30 GPa, Poisson's ratio $\nu = 0.2$ and unit density of 24000 kg/m^3 with a typical concrete material failure stress strain curve. For generation of the computational mesh the triangular element shape was selected along with Ansys automatic meshing option. The boundary conditions, displacements $U_{x,y,z}$ and rotation $R_{x,y,z}$ were selected in accordance to the structural systems considered in the codes and standards, where the chamber retaining wall was considered a cantilever with fixation at the base only. In the current feasibility study the variation in the soil adjacent to the chamber was not considered and earth pressure was considered as a fixed load. The consideration and modelling of soil-structure interaction in the FEM model might be a part of the subsequent future studies. The pressures and forces systems considered are shown in the Figure 2. The overall handling of the FEA from element selection to post processing of results was automated by developing a code in ANSYS-APDL (Ansys Parametric Design Language).

In post processing both nodal and parametric solutions were extracted. These solutions include tensile stresses, compressive stresses, maximum horizontal shear stresses (T_{xy}) and maximum horizontal normal stresses on vertical planes (compressive, σ_y) for assessment of ultimate limit state. For evaluation of the serviceability limit state, the nodal solution of maximum displacement in x-direction was evaluated and compared with the permissible values of the standards. For validation of the FEA results, the solutions from Ansys and results of static verifications with regards to compressive stress in principle axis, horizontal planes and vertical planes are compared with those computed by ANSYS using FEA. Once an approximation is found between the analytical calculations and FEA results, the boundary conditions, mesh size, shape and force system are fixed for other loading conditions and cases.

2.4. Optimization and Sensitivity Analysis

Upon completion of static verification and FEA in accordance to respective limit states, each case is condensed to one value, "the safety ratio". The ratio is evaluated by comparing calculated value of limit state (static/FEM) and values allowed by the standards. Table 2 enlists some of static verification and limit states. In general this ratio indicates the order of sufficiency of the proposed structure in context to verifications enforced by standardization, a value smaller than one means that the proposed structural dimensions are insufficient and need to be revised. Whereas, a safety ratio more than one indicates more than code required sufficiency and a need of optimization for reduction of dimensions.

As discussed before as well, there are several optimization schemes and algorithms used for structural optimization which include but not limited to Particle Swarm Optimization Algorithm PSO (Xinmiao et al. 2008), Genetic Algorithm GA (Ahmed et al. 2014), gravitational search algorithm; particle swarm optimization; weighted least squares support vector machine (Salajegheh and Khosravi 2011). Since the orientation and requirement of the subject study was limited to assess feasibility, therefore selection of method was based on ease of application and less computational power requirement. Considering this, linear programming optimization scheme was selected. A linear programming model was constructed based on the objective of minimizing the base length. The constraints of the model were that all safety ratios must be at least equal to 1.0. For acceptance of the optimal design, the performance function was the most critical verification whose safety ratio must be equal to 1.0. The optimization process did not only give the optimal dimensions of the proposed geometry but also indicated the critical parameters and limit states for various loading scenarios. Similarly each design case was optimized and dimensions corresponding to the worst case scenario were selected. Subsequently a sensitivity analysis was conducted by changing the input parameters. The influences of three parameters were analyzed, which include change in ground water level, concrete type and soil type. Each input change was applied to the dimensions finalized from design conditions and then static verification and FEA was done to assess sufficiency. For each change, safety ratios were computed to determine the most critical safety aspect and then optimization was performed to evaluate the dimensional requirements.

3. RESULTS

Three design situations depending on the water level in the lock chamber, respectively water level at +14.00 m, +4.00m and no water in the chamber, were selected for this study. The initial base length of gravity wall was considered to be 12.0 m. The results of the analysis for design case 1 show that the structural dimensions are sufficient, while the eccentricity is the most critical parameter. For optimization the eccentricity check was set

as performance function and base length as parameter. The optimized length was found out to be 9.78 m. The same procedure was carried out in case of the water level at +4.00 m, which indicated the bearing capacity as critical safety check; the optimized length was 11.65 m. Also case 3 representing no water in the chamber showed that the eccentricity was the critical safety check where the safety ratio was decreased to 0.92. The corresponding optimized base length was calculated to 13.28 m and was set as design value for all further analysis. The analysis of the design conditions show that bearing capacity, eccentricity and sliding resistance are among the most critical checks. In the Finite Element Analysis, the lowest safety ratios were found for the safety check of tensile stresses, where the safety ratio decreased from 2.89 to 1.53 for the decrease of the water level in the chamber as shown in Table 3. The location of the maximum tensile stresses is at the toe shown in Figure 3. The safety ratios for shear stresses decrease from 4.12 to 1.96 with the decrease in water level. The structure is abundantly safe against compressive stresses. The safety ratios increase as the stresses inside the structure increase due to the bigger size and higher weight. This is validated from the results in static verifications. The maximum compressive stress is 1.79 MPa whereas the allowed compressive stresses are 9.33 MPa giving a safety ratio of at least 5.21. The location of the maximum compressive stress (least safety ratio) is at the heel of the structure in design case 2 as shown in Figure 3. Concluding that the optimized base length of 13.28 m is sufficient to fulfill all limit states under design conditions and loadings.

Table 3. Results of safety ratios in design conditions and optimization

Group 1 (Design Conditions)		Design 1		Design 2		Design 3	
Std = Standard, Opti = Optimized		Std	Opti	Std	Opti	Std	Opti
	Optimizing parameter Base length →	12	9.78	12	11.65	12	13.28
Static Calculations	Uplift stability	2.02	2.03	3.25	3.25	4.97	4.96
	Overturning stability	1.65	1.20	1.27	1.23	1.43	1.61
	Sliding resistance	1.69	1.39	1.22	1.19	1.35	1.49
	Eccentricity limit	1.42	1.00	1.42	1.35	1.13	1.34
	Bearing capacity	1.87	1.70	1.02	1.00	0.92	1.00
	Shear strength	2.57	2.10	2.67	2.59	2.60	2.88
	Compressive strength	10.40	8.72	8.21	7.98	7.74	8.55
FEM using ANSYS	Principle tensile stress	2.89	2.04	1.33	1.32	1.53	1.90
	Principle compressive stress	10.02	8.79	5.21	5.17	6.31	6.69
	Max shear stress Txy	4.12	3.69	1.96	1.77	2.76	2.94
	Max normal tensile stress σy	6.72	3.61	1.72	1.67	2.43	3.33
	Max displacement-x	7.98	5.68	4.53	4.32	4.43	5.27

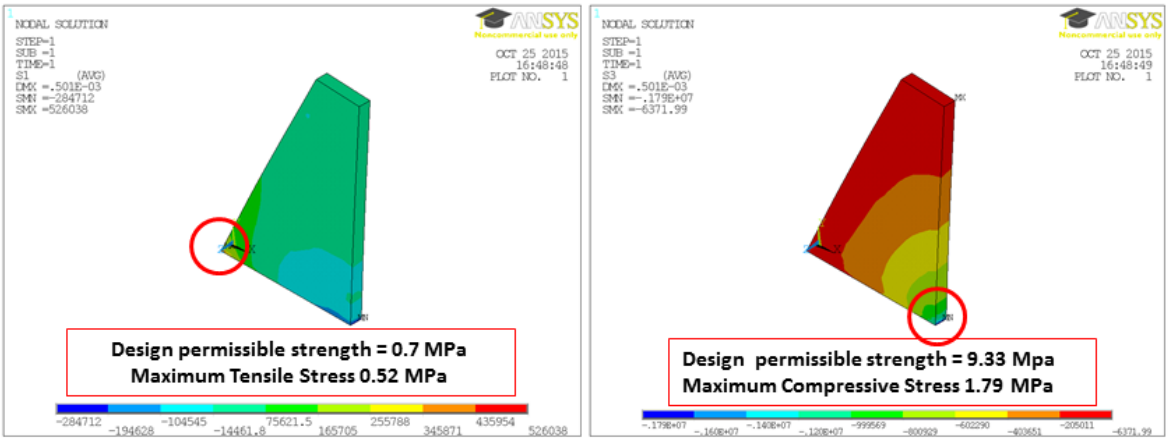

Figure 3. Tensile and compressive stress distribution through Ansys-APDL

Another auxiliary structure considered for design was the base slab of the lock structures. Two types of construction possibilities were considered in the initial part of the research. Firstly a U frame monolithic construction where all components of the structure are connected and secondly a construction considering three disjoint sub-structures which is indicated in Figure 1. The U frame monolithic construction with plain concrete was analyzed and it was found as an unfeasible shape as the tensile stress at the connection of base slab and chamber walls exceeded the concrete design tensile strength of 0.7 MPa. The details of this design and analysis

are not a part of this paper. Whereas the plain concrete base slab design and consideration for a disjoint system would be discussed briefly here. Similar to the chamber wall structure, the base slab was also considered for three design cases, two of which meaning the critical. Firstly, when the water level in the chamber is at maximum operational level and secondly when no water is within the chamber and only the self-weight of the structure could resists the forces. The following figure indicates equivalent factored loading system for the both critical design cases. Considering the beam theory, respective applicable standards and the evaluated bending moment the appropriate depth of the slab was calculated to be 3.0 meters.

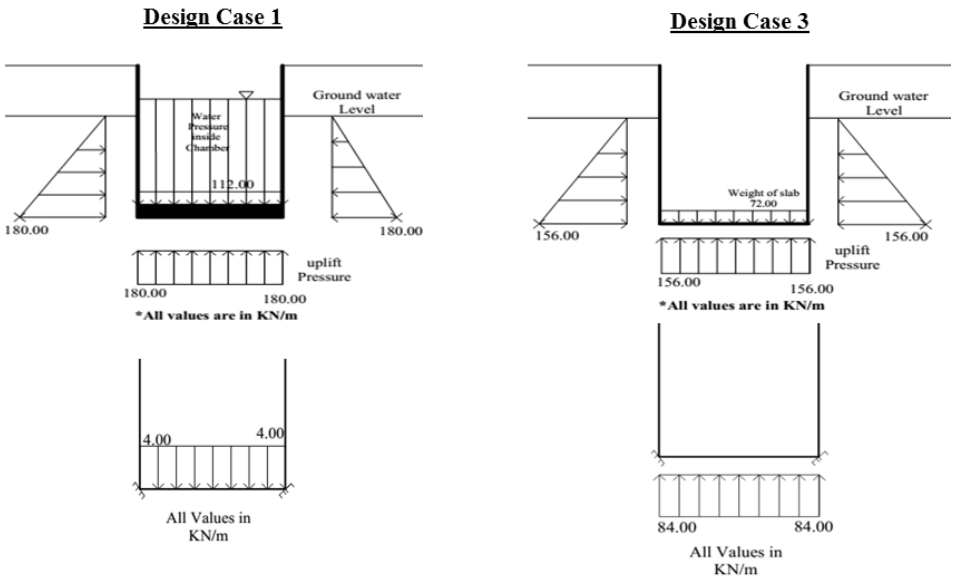

Figure 4. Equivalent force systems on base slab for design cases

All design cases considered a groundwater level up to two third of the height of the structure. The ground water level is now altered to evaluate the sensitivity of this parameter on the safety of the lock structure.

To assess the variation in safety ratios due to change in ground water level, three loading conditions were assessed. First being that the ground water level equals to structure height (maximum level), it was witnessed that a rise in uplift pressure improves the bearing capacity but reduces all other stabilities making the eccentricity limits and sliding safety to be the most critical. However, the results show that a base length of 13.28 m is still sufficient for all stabilities. Although the safety ratios for eccentricity limits (1.03) and sliding resistance (1.05) with base length 13.28 m are marginally higher than 1.0 as indicated in the graph figure below. Nevertheless the optimization was conducted and an optimized base length is found to be 13.05 m. The change in ground water level was reduced to a minimum level. In this case the original base length of 13.28 m failed to fulfill required bearing capacity check and the safety ratio reduced to 0.93, this is shown in the figure with comparison to other ground water level. To fulfill this requirement the dimensions were increased and the respective optimized length was 14.0m. The following figure indicates the various static and FEM verifications for the respective structure with the variation in the ground water level where the aspects of interest are those with safety ratio around 1.

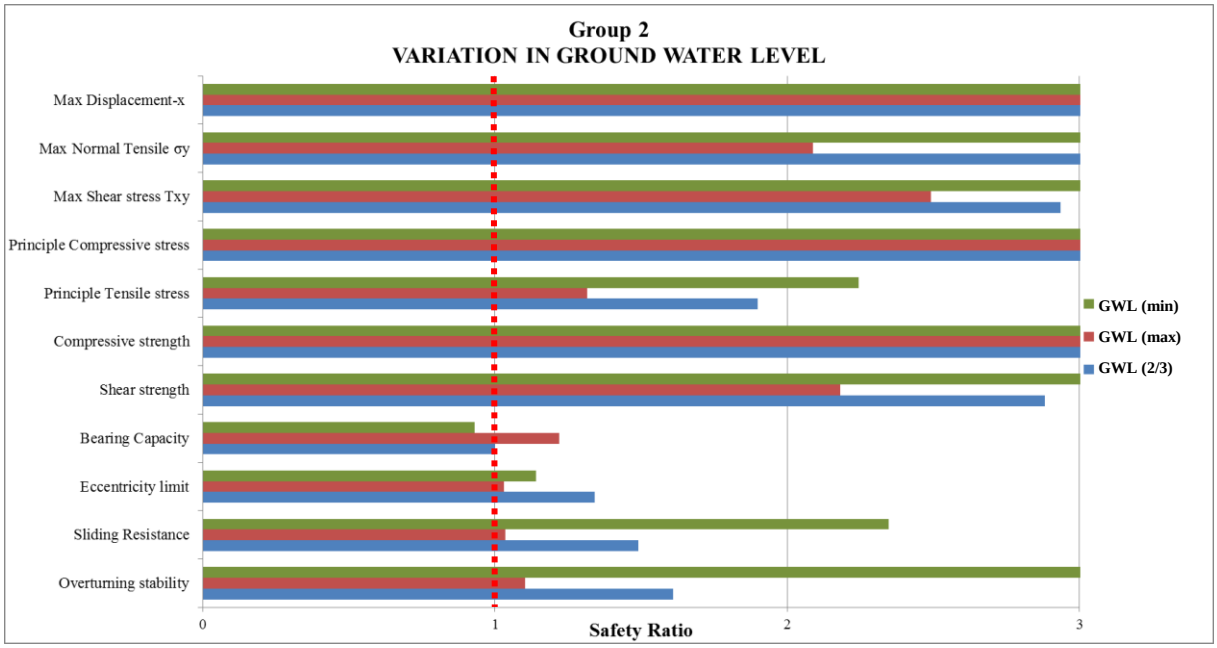

Figure 5. Sensitivity analysis for change in ground water level with base length of 13.28 m

The next sensitivity analysis is conducted considering the change in concrete quality. The stability related to structure geometry and geotechnical properties are not sensitive to any small change in concrete properties. Since the changes of the strength class will keep the weight and density almost at the same value. For C20/25, C25/30 and C30/35, only the safety ratios related to the material strength i.e tensile, compressive and shear strength are improved slightly. But none of these stabilities are critical and the bearing capacity has the least a safety ratio of 1.00. Therefore the optimized base length remains at 13.28 m, regardless of an improved concrete class. This is indicated in the figure below with identical safety ratios for critical aspects.

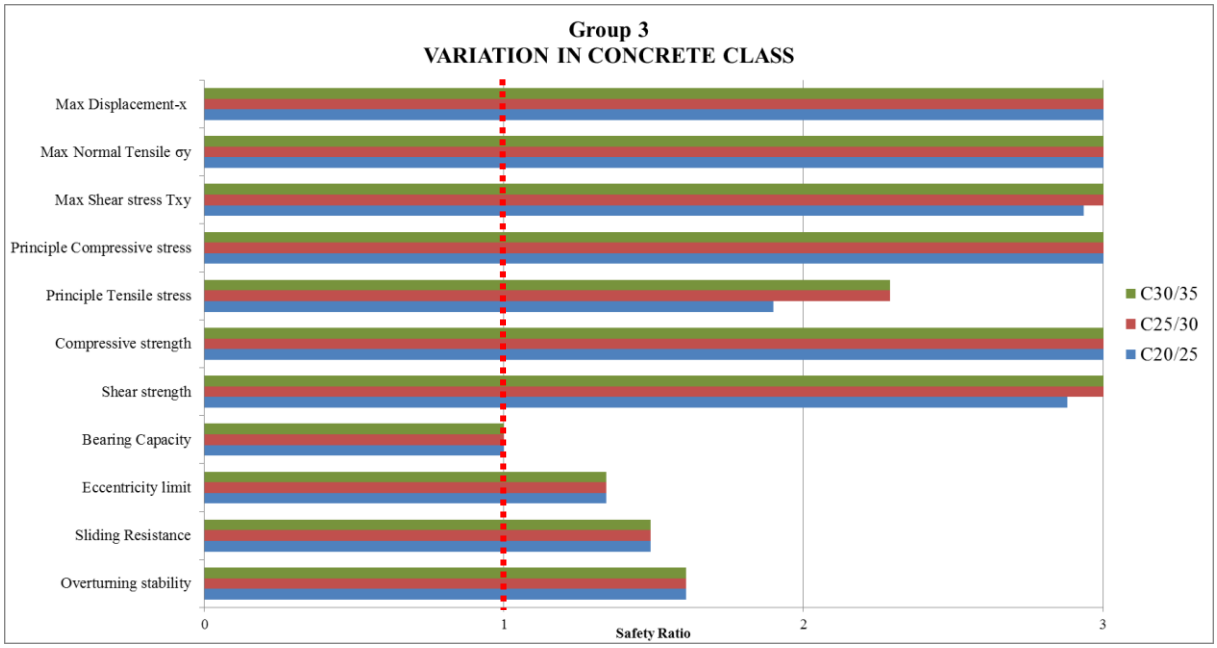

Figure 6. Sensitivity analysis for change in concrete type with base length of 13.28 m

Sand was considered as design soil, the sensitivity of a change in soil type was evaluated. The soil type was varied choosing clay and gravel with basic properties written in table 1. The results indicate that clayey soil reduces the stabilities, hence decreasing the bearing capacity ratio to 0.95. Therefore, the required base length

was computed to be 14.11 m. Gravel soil provided more stability and a higher bearing capacity resulting in a reduced optimized base length of 12.58 m.

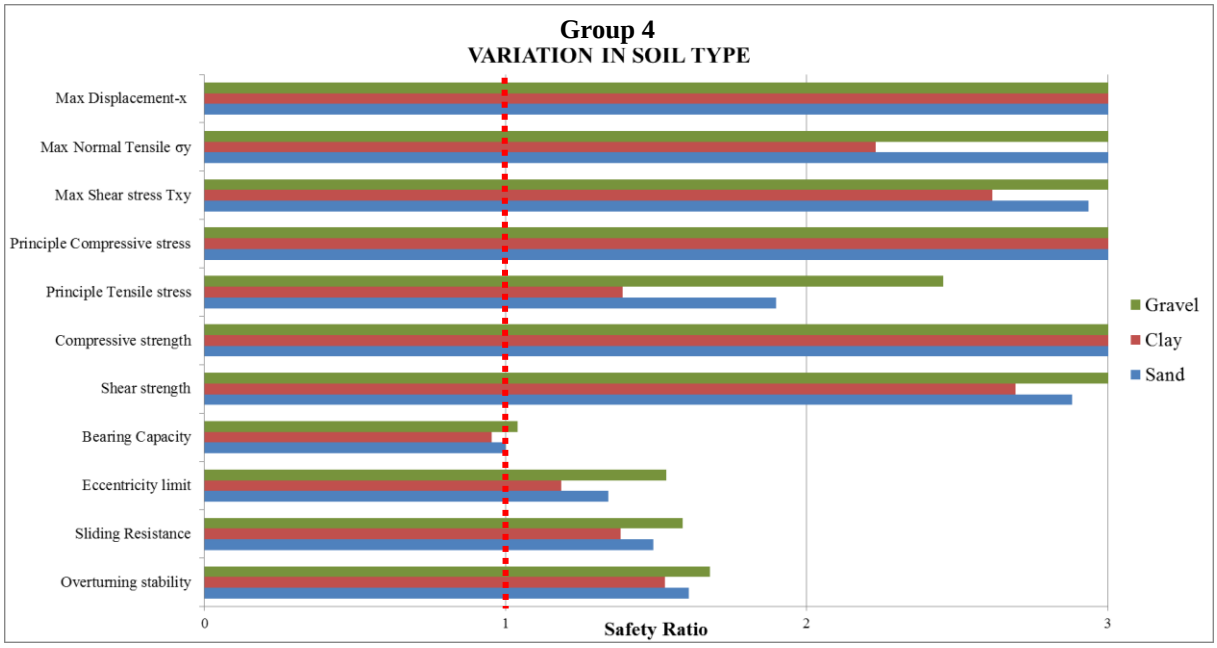

Figure 7. Sensitivity analysis for changes of the soil type with base length of 13.28 m

A general perspective of the sensitivity analysis carried out in this study shows that for retaining gravity walls made out of plain concrete, the stability is most critically restricted by the bearing capacity of soil and eccentricity limits. However, the safety against internal stresses (tensile stresses) is the most critical aspect which needs to be corroborated.

4. CONCLUSIONS

When considering latest standards and concrete without reinforcement, for design of a modern ship lock structure, the construction arrangement consisting of three disjoint sub-structures was found more feasible, in contrast to the currently employed typical reinforced concrete U frame structure which has rapid reinforcement deterioration and maintenance issues. The suggested arrangement consists of two identical concrete gravity retaining chamber walls and a plain concrete base slab. The static verification and finite element analysis in accordance with Eurocodes and German standards was conducted for a lock with a length of 190 m, width of 12.5 m and a fall of 10 m. From the three design conditions considered it is found that critical loading conditions occur when no water is inside the chamber. The most critical verifications were the eccentricity check and bearing capacity of the soil. A linear programming optimization scheme was employed. This provided the optimized base dimension of 13.28 m. The critical loading conditions were applied to the base slab resulting into a final thickness 3.00 m, which was determined using beam theory.

Upon completion of verification of the design conditions, a sensitivity analysis was conducted to investigate the impact of the change in input parameters on the dimensional requirements and stabilities. The conducted analyses determine that stabilities are sensitive to changes in the ground water level. The increase of the ground water results into a decreased stability and lowered safety ratios for all verifications with exception to the bearing capacity verification, where the safety ratio increased. The reason for the observed reduction is the increase in vertical forces due to uplift. The second sensitivity analysis determined the influence of change in concrete type. The analysis revealed that such change will have no impact on the structure's critical verifications i.e. eccentricity and bearing capacity which depend on the weight of the structure rather than on the strength of concrete. The third change in the input parameters was the change in soil type. The analysis showed that coarse soils provide a better environment and higher stabilities, thus reducing the dimensions of the structure. Soils having finer material or smaller angles of friction require a longer base length to guarantee the stability.

It can be concluded that bearing capacity verification is most critical, whereas eccentricities check can be ranked second for this type of concrete structure. Since the base length is a function of base pressure and eccentricity, it is recommended to elongate the base of the structure and gradually reduce the other dimensions along with the height for an optimal shape. As established before the change in concrete class does not have an impact on the optimal dimensions of the structures. The bearing capacity remains the most critical verification, which is independent of concrete strength.

The sensitivity analyses indicate that coarse soils will improve the bearing capacity and reduce the earth pressures on the walls, the proposed structural arrangements would be more feasible and stable in regions with gravel and rock foundations. Soil replacement could be an option in cases where the soil is clayey. In conditions where foundation soils have a very low bearing capacity, a pile foundation could be employed.

An increased ground water level has an impact on the sliding resistance of the structure, hence recommendations are presented. Firstly, providing a key at the bottom of the structure would improve the stability. Secondly, the application of a ground water drainage system along the earthen side of the structure is suggested. Furthermore a drainage system along the chamber walls is of vital importance when the structure is undergoing maintenance conditions (no water in the chamber). Since this loading condition is critical but at the same time temporary, the reduction of the natural ground water level in the vicinity of the structure is suggested, however this short duration will not have any major impact on the regional ground water system.

The same methodology could be adapted for the assessment of stabilities for existing hydraulic structures made out of plain concrete which consists of about 60 % of navigation infrastructure of Germany. Further studies regarding fracture mechanism and location of potential failure planes within the structure due to tensile stresses are recommended. This would ensure the safety of the overall structure especially foundations against progressive development of uplift pressures leading to hydraulic fracturing and deterioration. A better understanding of the soil-structure interaction and fluid-structure interaction considering dynamic loadings and soil variation would be highly beneficial for additional optimization on the structure in terms of shapes and dimensions. Other structural configurations involving decrease in height of retaining wall by cascading smaller lock structures in series could further improve the scheme which needs to be investigated. However, an economic and life-cycle cost analysis would be pivotal in making the final decision concerning selection and usage of lock structures made out of plain concrete.

5. REFERENCES

ANSYS Inc. (2013). ANSYS Mechanical APDL Structural Analysis, 15.0 ed. *Canonsburg*, USA.

Chen, S.H. (2015). Hydraulic Structures, 1st ed. *Heidelberg: Springer-Verlag* Berlin. (in German).

Kunz, C., and Bödefeld , J. (2001). "Von der Bauwerksinspektion zum Bauwerksmanagement." *Mitteilungsblatt der Bundesanstalt für Wasserbau Nr. 83*, 39–49. (in German)

DIN-19703. (2014). Schleusen der Binnenschifffahrtsstraßen – Grundsätze für Abmessungen und Ausrüstung. *Beuth-Verlag*, Berlin, 2014. (in German)

DIN-19700-11.(2004), Stauanlagen –Teil 11: Talsperren, *Beuth-Verlag*, Berlin, 2004. (in German)

DIN-1054. (2010). Baugrund – Sicherheitsnachweise im Erd und Grundbau – Ergnzende Regelungen, *Beuth-Verlag*, Berlin, 2010. (in German)

DIN-19702. (2013). Massivbauwerke im Wasserbau – Tragfähigkeit, Gebrauchstauglichkeit und Dauerhaftigkeit, *Beuth-Verlag*, Berlin, 2013. (in German)

Eurocode 1990. (2013). Basis of structural design, *CEN*, Brussels.

Eurocode 1991(2013). Actions on structures - Part 1-1: General actions, *CEN*, Brussels.

Eurocode 1992 (2013). Design of concrete structures. General rules and rules for buildings, *CEN*, Brussels.

Eurocode EN 1997. (2013). Geotechnical design - Part 1: General Rules, *CEN*, Brussels.

Ghodousi, H. and Oskouhi, M. (2015). Determination of Optimal Dimensions of Concrete Gravity Dams Using LINGO11 Nonlinear Modeling. *Journal of Civil Engineering and Urbanism*, 05(02), 47-52.

Harris, (2008). Decoding Eurocode 7, First ed. Abingdon, Oxon, *Taylor & Francis*, UK

Salajegheh, J. and Khosravi, S. (2011). "Optimal shape design of gravity dams based on a hybrid meta-heruristic method and weighted least squares support vector machine." *International Journal of Optimization in Civil Engineering*, 4, 609–632.

Partenscky, H. (1984). *Binnenverkehrswasserbau: Schleusenanlagen*, Springer, Berlin.(In German)

PIANC Permanent International Association of Navigation Congresses (1986). *Final report of the International Commission for the Study of Locks*, Brussels.

Ahmed, Al-Suhaili, Behaya (2014). "A Genetic Algorithm Optimization Model for the Gravity Dam under Seismic Excitation with Reservoir-Dam- Foundation Interactions." *American Journal of Engineering Research (AJER)*, 03(06), 143–153.

US Army Corps of Engineers (USACE) (2016). "Technologies to Extend the Life of Existing Infrastructure." *Navigation Infrastructure*, 1–16.

US Army Corps of Engineers (USACE) (2016). “Forensic Investigations of Infrastructure Deterioration and Failure." *Navigation Infrastructure*, D-2.

Westendarp, A., Becker, H., Bödefeld, J., Fleischer, H., Kunz, C., Maisner, M., Müller, H., Rahimi, A., Reschke, T., & Spörel, F. (2014). "Erhaltung und Instandsetzung von massiven Verkehrswasserbauwerken." *BetonKalender* 2015, E. K. Bergmeister, F. Fingerloos, and J.-D. Wörner, eds., *Wiley-VCH Verlag GmbH*, Weinheim, Germany, 185–246. (in German)

Working Group 140 (2015). Report no 140 Semi-Probabilistic Design Concepts For Inland Hydraulic Structures, *PIANC*, Brussels.

Wu, X., Qie, Z., Zhou, Z., and Zhang, H. (*2008)*"Application of improved PSO to optimization of gravity dam and sluice gate," *Intelligent Control and Automation. WCICA 2008. 7th World Congress*, Chongqing, 2008, pp. 6178-6182.

DOI:10.15142/T3Q590

Interfacial velocity estimation in highly aerated stepped spillway flows with a single tip fibre optical probe and Artificial Neural Networks

D. Valero[1, 2] and D. B. Bung[1]
[1]Hydraulic Engineering Section (HES)
FH Aachen University of Applied Sciences
Aachen, Germany
[2]Dept. of ArGEnCo, Research Group of Hydraulics in Environmental and Civil Engineering (HECE)
University of Liege (ULg)
Liège, Belgium
E-mail: valero@fh-aachen.de

ABSTRACT

Air-water flows can be found in different engineering applications: from nuclear engineering to huge hydraulic structures. In this paper, a single tip fibre optical probe has been used to record high frequency (over 1 MHz) phase functions at different locations of a stepped spillway. These phase functions have been related to the interfacial velocities by means of Artificial Neural Networks (ANN) and the measurements of a classical double tip conductivity probe. Special attention has been put to the input selection and the ANN dimensions. Finally, ANN have shown to be able to link the signal rising times and plateau shapes to the air-water interfacial velocity.

Keywords: *air-water flows, Artificial Neural Networks, air-water interfacial velocity, stepped spillways*

1. INTRODUCTION

Air-water flows can be easily found in large hydraulic structures, where self-aeration occurs as a complex and turbulent air-water compatibility phenomenon (Valero and Bung 2016). In spillway flows, researchers' efforts have focused both in the aerated regions (Zhang and Chanson 2016a, Bung 2011, Felder and Chanson 2011, Boes and Hager 2003, Chanson and Toombes, 2002) and non-aerated regions (Valero and Bung 2016, Zhang and Chanson 2016b, Meireles et al. 2014, Meireles et al. 2012, Amador et al. 2006); while some unresolved key challenges still exist (Matos and Meireles 2014, Chanson 2013). Hydraulic jumps have been also a common case of air-water flow studies as the impingement induced aeration plays a main role (Murzyn et al. 2005, Wang and Murzyn 2016, Wang and Chanson 2015, Wang et al. 2014, Chanson and Brattberg 2002).

Although some new non-intrusive techniques are available (Bung and Valero 2016, Bung and Valero 2015, Felder and Chanson 2014, Nóbrega et al. 2014, Leandro et al. 2014, Bung 2013, Chachereau and Chanson 2011, Kucukali and Chanson 2008, Misra et al. 2006), intrusive techniques have been more widely used (Wang et al. 2014, Boes and Hager 2003, Chanson and Brattberg 2002). When the air fraction C, or water fraction $(1 - C)$ exceeds 1 to 3 %, accuracy of common instrumentations for single phase flow measurements is typically affected and conductivity/optical probes become the best option (Felder and Chanson 2015). However, when using intrusive measurement techniques, some drawbacks and limitations can arise (Borges et al. 2010). In order to save some difficulties involved in air-water flow velocity measurements, Artificial Intelligence (AI) techniques have recently been used (Bung and Valero 2016a). Optical fibre probes work based upon the difference on light refraction at air/water interfaces. Usually, when velocity measurement is required, these probes comprise two conical tips. First and second tip are intended to record two signals based on the same bubbly events. Then, by cross-correlating the signals the most probable lag time can be obtained. Altogether with the known distance between both probes, a velocity may be computed. Nonetheless, a second option is available based on a single tip configuration.

In this study, raw signals are recorded in a highly aerated flow on a moderately sloped stepped spillway; similar to the setups described in Bung and Valero (2015) and Bung (2011). These signals, altogether with the previously obtained information, are later processed and used to train different Artificial Neural Networks (ANN) configurations by using PyBrain open-source package (Schaul et al. 2010).

2. EXPERIMENTAL SETUP

2.1. Stepped spillway

All measurements have been conducted in a moderately sloped stepped spillway (1V:2H, ϕ = 26.56º) with step height s = 6 cm for three different flow rates q = 0.07, 0.09 and 0.11 m^2/s. Total drop height is 1.74 m with a width of 0.50 m. Water was pumped from a lower basin into an open head tank from where it was conveyed into the stepped chute via an approaching channel of 1 m length. In order to complete a wider range of air concentrations, measurements have been conducted at steps (E) 13, 14, 18, 19 and 21; being the flow fully developed at step 21 for the highest discharge (see Fig. 1).

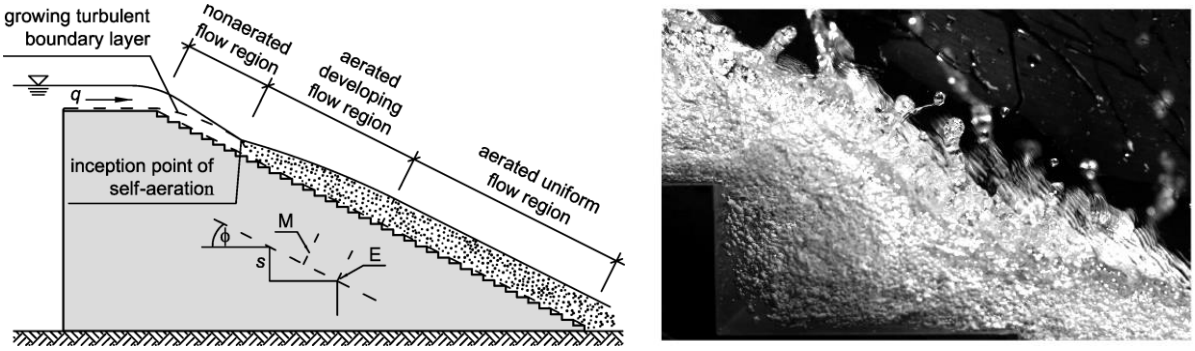

Figure 1. Sketch of flow regions over a spillway (left) and aerated flow at step 21 for q = 0.07 m^2/s (right).

2.2. Single tip optical probe description and settings

Since the early study of Neal and Bankoff (1963), phase detection probes have become a common measuring technique in multiphase flows disciplines. In this study, a single tip optical probe is employed (Fig. 2). This probe (also known as mono-optical probe) has been placed in the centreline of the spillway, over the step edges. As shown in Fig. 2, the probe is moved by a CNC controlling system (isel) with an accuracy of ~0.1 mm. The probe is manufactured and distributed by A2 Photonic Sensors, including a signal recording and analyser software and an optoelectronic module.

Vertical interfacial velocity profiles (raw signals) have been recorded perpendicularly to the pseudo-bottom with 2 mm spacing, at steps 13, 14, 18, 19 and 21, resulting in 646 measurements.

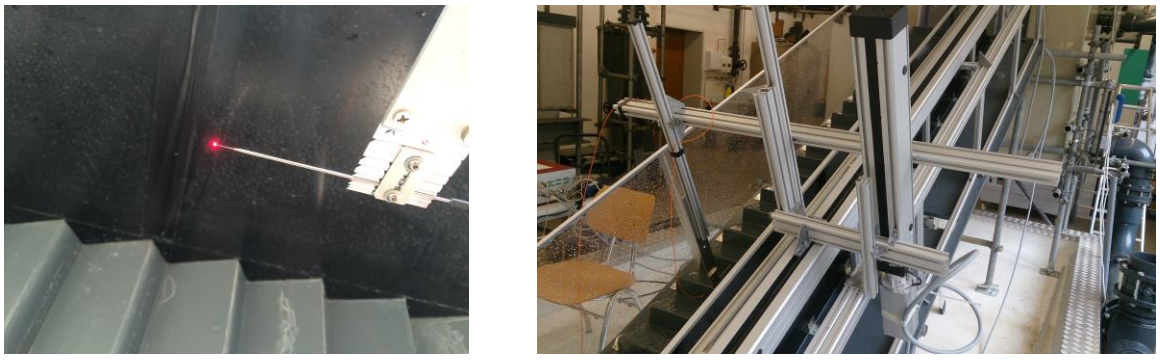

Figure 2. Monofibre optical probe location (left) and 2D controlling system configuration (right).

Single optical phase detection probes are able to measure gas velocities provided that their sensitive length (or latency length, L) is accurately known (Cartellier 1998, Cartellier and Barrau 1998a, b). To avoid a certain level of sensitivity to uncontrollable parameters (i.e.: angle of the impact on the bubble interface), probes geometry can differ from the commonly used dual tip optical fibres. Thus, more complex geometries can be used

(Cartellier and Barrau 1998b), e.g.: a cone + cylinder + cone geometry where the tip reduces its inner diameter through an intermediate cone. However, the employed probe corresponds to a simple cone geometry, which is more sensitive to uncontrolled parameters.

Air-water interface velocity can be approximated by using:

$$v = L \cdot {t_r}^b \tag{1}$$

where t_r is called the rising time, which represents the time it takes the signal to pass from level 10% to 90% of the air level, b is a dimensionless parameter taking a value close to –1 to correct the estimation and L depends on the probe's tip length. For the employed probe, b = –1.02 and L takes the value of 45.3 μm when the rising times are taken in microseconds to obtain the velocity in meters per second. Threshold levels 10% and 90% are based on the provider's experience and directly affect the values taking the other parameters.

Cartellier (1998) reports a relative error of around 10 % both for air fraction and gas flux, while the provider points out that an error of 15 % can be expected for the used probe. Further discussion on the probe/bubble interaction and the effect upon the air fraction measurement accuracy can be found in Vejražka et al. (2010). Errors are globally comparable for the monofibre and the bi-probe techniques, but these techniques are not equally sensitive to the flow regime. For finely dispersed flows, monofibre optical probes are better suited while double tip probes seem better adapted whenever large gas inclusions are present (Cartellier 1998). This makes a challenge for monofibre probes to measure in highly turbulent aerated spillway flows. Also, their actual response is sensitive to small geometrical defects occurring at their tips as pointed out by Cartellier and Barrau (1998a, b). This fact underlines the benefit of using more complex techniques than the rise time/velocity correlation provided by Eq. 1.

In order to obtain an accurate estimation of t_r, the sampling rate has been set to 1 MHz, being around 50 times larger than the minimum recommended sampling rate for dual tip probes for similar types of flows, where only small discrepancies can be observed in the turbulence estimations at a higher sampling frequency of 20 to 40 KHz (Felder and Chanson 2015). The sampling duration is recommended to be over 45 s, however in the study of Felder and Chanson (2015) only small differences can be observed over 20 s for similar flows. André et al. (2005) investigated the effects of sampling duration upon the interfacial velocity and the cross-correlation coefficient and suggested a sampling duration of more than 30 s. Consequently, the sampling duration has been set to 30 seconds, yielding over 30 million data points per recorded signal and nearly 20,000 million data points considering the entire set of recorded signals.

3. SIGNAL ANALYSIS

As described above, 646 million raw signals have been recorded, obtaining 30 million data points at each location to be later analyzed and used to train and test the artificial neural network employed in this study. Each signal displays a signature every time that a bubble impacts the monofibre probe tip (see Fig. 3 for an exemplary bubble event), which may provide a large amount of information.

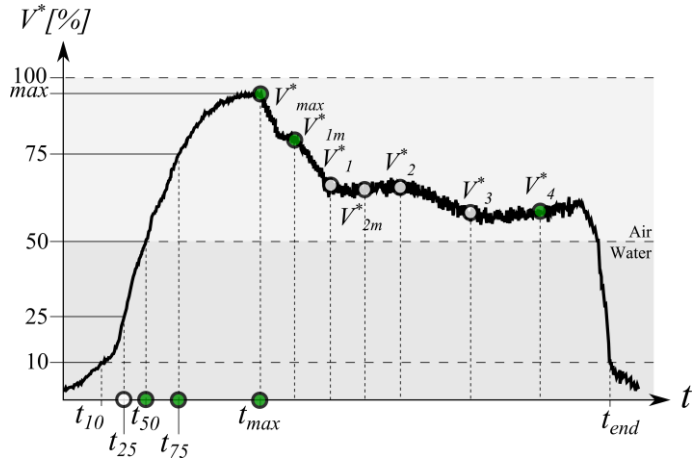

Figure 3. Exemplary signal of a bubble-tip impact extracted from the phase function recorded by the single tip probe, main features and ANN input definition (variables marked in green).

High frequency small amplitude oscillations can be observed in the data files which may affect the analysis of the phase indicator function. To remove these small oscillations, a central moving average filter with a moving window of 10 time steps (at a time resolution of 1 MHz produces a 1 μs signal delay) has been applied. By removing sampled frequencies above a certain cutoff frequency, the moving average creates a smoothing effect which has shown to remove effectively the noise. Further information on application of similar and more complex filtering techniques to air-water measurements can be found in the study of Bung and Valero (2015).

In order to make the signal independent from the used voltage range, water and air levels defined with the providers' software, all the signals have been scaled to be comprised between 0 and 100 %; thus a normalized voltage (V^*) results, but an air-water voltage range over 5 Volts was always ensured in the original recordings. Every recording included thousands of events (i.e. phase changes from water to air or bubble/droplet impacts). To make the ANN independent of the number of events and the bubble size, a median signature (or median phase indicator function) has been extracted from each recording. Different parameters defining this median phase indicator function have been selected, which may be separated in (a) rising time parameters and (b) phase indicator shape parameters. As defined in Fig. 3, rising time related variables are:

- t_{10-25}, which is the difference between the time the dimensionless voltage V^* reaches the 25 % value (t_{25}) and the time it reached the 10 % value (t_{10}).
- t_{25-50}, which is the difference between the time the dimensionless voltage V^* reaches the 50 % value (t_{50}) and the time it reached the 25 % value (t_{25}).
- t_{50-75}, which is the difference between the time the dimensionless voltage V^* reaches the 75 % value (t_{75}) and the time it reached the 50 % value (t_{50}).
- t_{75-max}, which is the difference between the time the dimensionless voltage V^* reaches the maximum value ($V^*{}_{max}$) at the time t_{max} and the time it reached the 75 % value (t_{75}).

The phase indicators shape variables (also defined in Fig. 3) are:

- $V^*{}_{max}$ is the dimensionless maximum value reached by the signature at each event, close to 100 %.
- $V^*{}_1$, $V^*{}_2$, $V^*{}_3$ and $V^*{}_4$ split the signal from t_{max} to t_{end} (where the signal crosses the 10% value again) in five equal portions.
- $V^*{}_{1m}$ and $V^*{}_{2m}$ are the normalized voltages measurements between $V^*{}_{max}$ and $V^*{}_1$, $V^*{}_1$ and $V^*{}_2$ respectively. These extra voltages where selected to better describe the exponentially decreasing tail which can be usually observed after the $V^*{}_{max}$ takes place.

All these time and phase parameters have been chosen arbitrarily based on a better representation of the overall phase function.

4. ARTIFICIAL NEURAL NETWORK FOR INTERFACIAL VELOCITY ESTIMATION

4.1. Introduction

Artificial Neural Networks (ANN), one of the earliest techniques of Artificial Intelligence, have become a powerful tool for prediction and forecasting of water resources, being a large number of studies published recently addressing mainly hydrological (Maier et al. 2010) and sediment problems. However, when it comes to hydraulic instrumentation prediction improvement, only a few attempts are documented. Carosone et al. (1995) and Chen et al. (1998) employed neural networks altogether with Particle Tracking Velocimetry (PTV) and Particle Image Velocimetry (PIV) techniques. Recently, Bung and Valero (2016a) and Bung and Valero (2016b) have applied Artificial Intelligence techniques obtaining, at least, as accurate velocity fields as classical cross-correlation based techniques for bubbly and swirling flows.

All ANN models take the form:

$$Y = f(X, W) + \varepsilon \tag{2}$$

Where Y is the vector of model outputs, X is the vector of model input, W the vector of model parameters (or connection weights), $f(\cdot)$ is a functional relationship between model outputs, inputs and parameters; and ε is the

vector of model errors. The functional relationship depends strongly on the ANN architecture (e.g.: the number of hidden layers and number of neurons). In this study, the model output is a single scalar (velocity, v), the vector of model input is discussed in Section 4.2 on the basis of the event-driven description of the recorded signal; the number of neurons is discussed in Section 4.3 and the vector of model errors is the result of the ANN training, discussed in Section 4.4. All the described operations have been carried out by using Python 2.7, altogether with PyBrain 0.3 for the ANN setup (Schaul et al. 2010) and Matplotlib 1.5 (Hunter 2007) for scientific plotting.

4.2. Input selection

One of the most important steps in the ANN model development process is the determination of an appropriate set of inputs (X). However, this task is generally given little attention in ANN modelling and most inputs are determined on an ad-hoc basis or using a priori system knowledge (Maier et al. 2010).

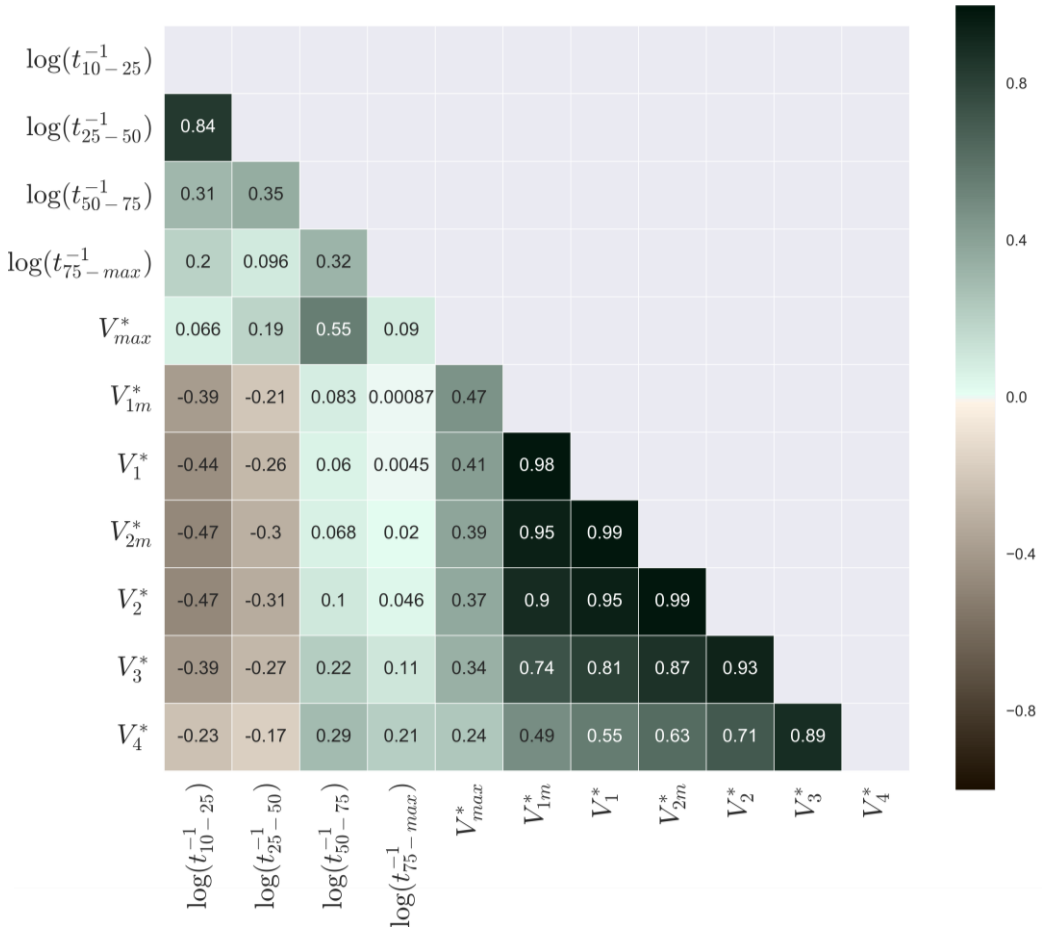

Figure 4. Correlation matrix for the signal descriptors marked in Fig. 3.

All the variables marked in Fig. 3 are obtained for each event of the 646 measurements. This yields thousands of values for each measurement. In order to get only one value per signal, the median value is computed. Temporal variables are inverted (t^{-1}) which physically represents a velocity – instead of a time – and the shape parameters are selected based on the observed fact that the bubble impacting the tip produces a characteristic signature (Cartellier 1998, Cartellier and Barrau 1998a, b). In order to make the shape parameters independent from the event duration (and consequently from the bubble size), they have been selected by splitting the plateau of each event in equal parts. For the temporal variables, a logarithmic distribution has been noticed. Consequently, logarithm of t^{-1} is used to obtain a more homogeneous distribution.

Given a fixed number of training samples, the addition of redundant model inputs increases the ratio of the number of connection weights to the number of training samples, thus increasing the likelihood of overfitting, while not providing any additional information to the model. Secondly, the inclusion of redundant model inputs introduces additional local minima in the error surface in weight space (Maier et al. 2010). To detect redundancy between the described variables, correlation among them has been computed (see Fig. 4).

A strong correlation between the shape variables has been observed in the tail of the signal while $V^*{}_{max}$, $V^*{}_{1m}$ and $V^*{}_4$ were less correlated. Thus, the other shape variables have been disregarded. Within the temporal variables, only t_{10-25} were found to be correlated to t_{25-50}. Given that t_{10-25} is more correlated to the remaining parameters than t_{25-50}, the former one has been neglected. Consequently, selected variables for the ANN input vector (marked in green in the Fig. 3) are the following:

$$X = [\log({t_{25-50}}^{-1}), \log({t_{50-75}}^{-1}), \log({t_{75-max}}^{-1}), V^*{}_{max}, V^*{}_{1m}, V^*{}_4] \quad (3)$$

Every element of the vector of model inputs is normalized between −1 and 1; which makes the training faster.

4.3. ANN architecture

The ANN of this study is a feedforward network with six input neurons and one output neuron and full connectivity (see Fig. 5). The dimensions of the input and output layers are directly determined by the selected inputs (Eq. 3) and the choice of the desired output or target (herein the interfacial velocity). However, dimensions of the hidden layer and the number of layers have undergone an iterative process. While one hidden layer can identify simple patterns, two can guarantee recognition of more complex patterns. Usually, it is not recommended to go over three hidden layers. In this study, two hidden layers have been selected. Different types of transfer functions between neurons have been examined, obtaining the best results for linear (input layer), sigmoid (hidden layer 1 and 2) and linear (output layer). Other types of transfer functions are available in PyBrain (Schaul et al. 2010) and in the literature (Rojas 2013).

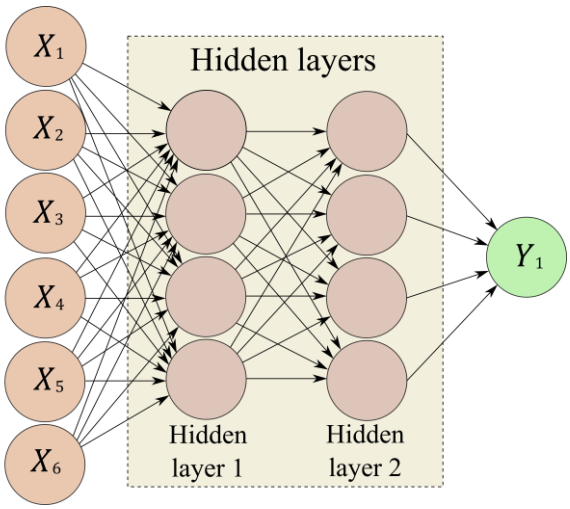

Figure 5. ANN architecture: feedforward network with full connectivity, 6 input neurons, 2 hidden layers and 1 output layer.

4.4. ANN training and testing

As ANNs are prone to overfitting the calibration data, cross-validation is generally used, as part of which the calibration data are divided into training and testing subsets (Maier et al. 2010). The available dataset (646 samples) has been divided in training and testing subsets with a proportion of 70 % and 30 % respectively (452 and 194 samples respectively). The training algorithm adjusts the parameters reducing the mean squared error (MSE, as defined by Bennett et al. 2013) for the training subset while tracking the effect upon the testing subset. When the error in the testing subset stops decreasing the training is stopped (see Fig. 6). The iterations are commonly called epochs.

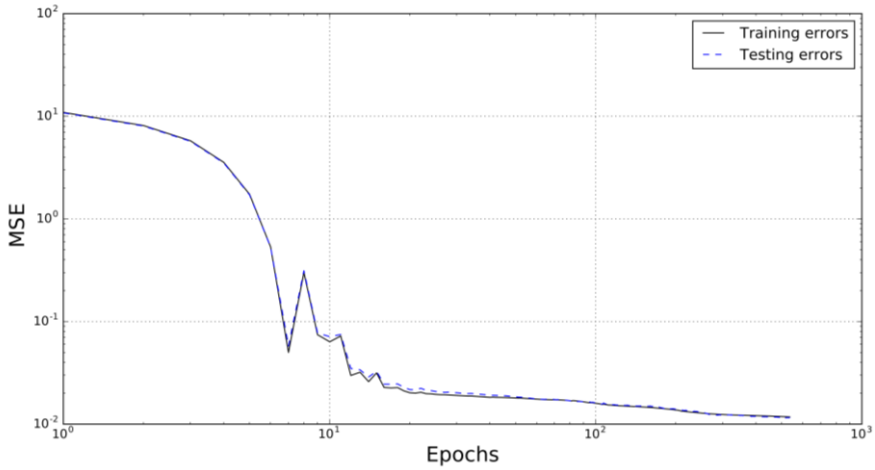

Figure 6. Training with cross validation for the ANN model. Mean squared error (MSE, as defined by Bennett et al. 2013).

The employed training algorithm is RProp- of Igel and Hüsken (2003) with all training samples with the same weight. Classic backpropagation algorithm has been also used resulting usually in a worst training.

5. RESULTS

Alternatively to the MSRE computed in the training process, the correlation coefficient (r) as defined by Bennet et al. (2013) has been computed to assess both Eq. 1 and ANN performance; which is commonly used for model evaluation. In Fig. 7, r values are shown for ANN training and testing datasets for a total number of 2541 trainings (21 per combination). It is clearly observed that all shown combinations provide a r value over 70 % for both training and testing datasets for all of the studied number of neurons in the hidden layers; and a maximum value of 88.9 % and 81.9 % respectively.

In Fig. 7 it can be also observed that higher number of neurons in the hidden layers improves the accuracy for the training datasets while it suddenly stabilizes for the testing dataset. As the number of samples does not increase, a smaller number of neurons for the same accuracy level might be desirable. Consequently, a combination of five neurons in the hidden layer one with five neurons in the hidden layer two has been selected to show the ANN results (see Fig. 8). In order to illustrate utility of the present ANN, results from Eq. 1 are also shown in Fig. 8.

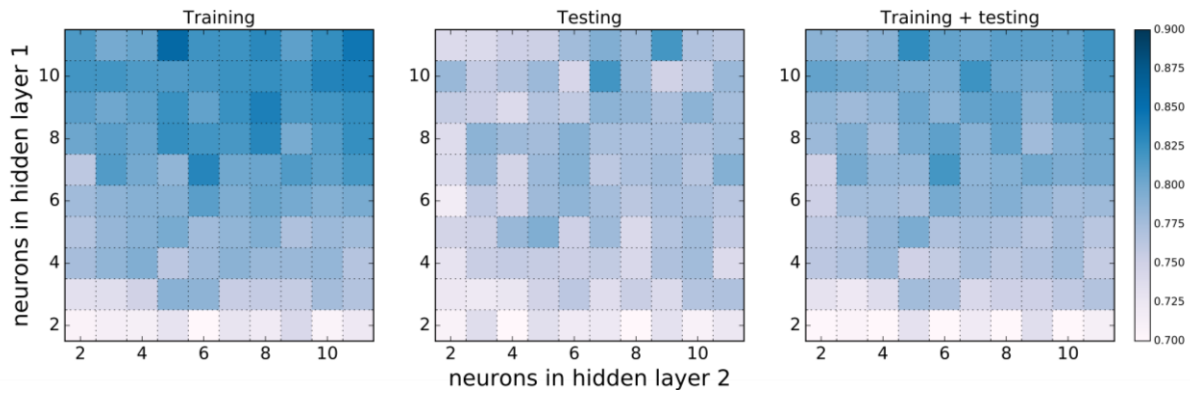

Figure 7. Best correlation coefficient for training (left), testing (center) and all dataset (right) after 21 trainings until convergence and different neurons number in the hidden layers.

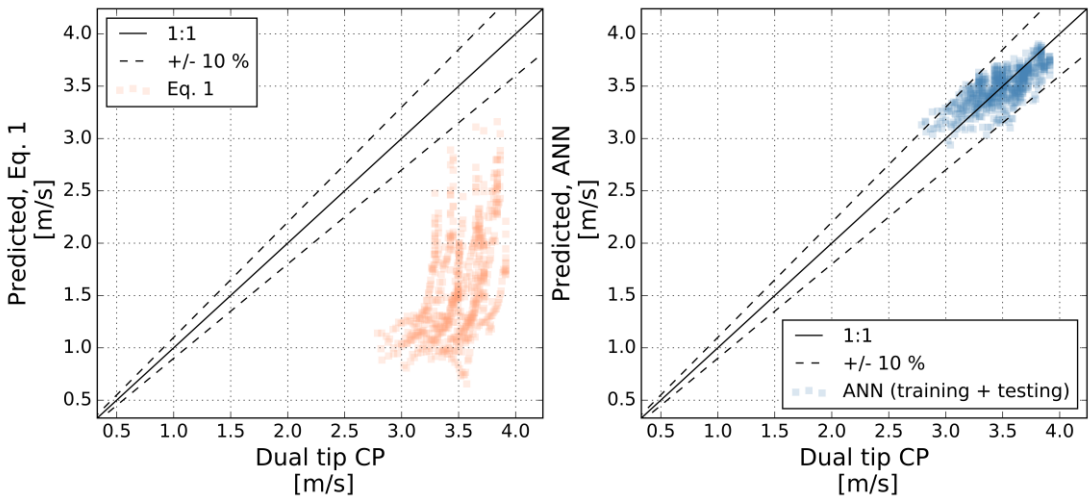

Figure 8. Dual tip conductivity probe (CP) measurements of Bung (2011) and predicted interfacial velocity of the quasilinear Eq. 1 (left) and the ANN (right).

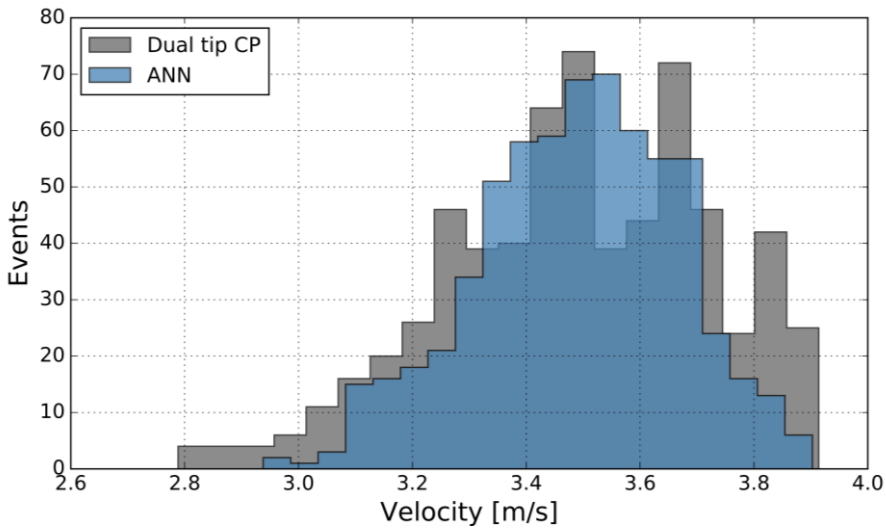

Figure 9. Interfacial velocities histograms for the cross-correlation based velocity of Bung (2011) and the ANN approach presented herein.

6. CONCLUSIONS

In this study, a large number of measurements with a single tip optical fibre probe have been performed in a 1V:2H stepped spillway. Measurements have been conducted every 2 mm at different steps, obtaining different velocities at regions of different aeration. After a correlation analysis (see Fig. 4), some irrelevant parameters have been discarded, finally selecting three temporal parameters and three phase function shape parameters as input for a feedforward ANN. Choice of these initially proposed parameters is based on previous studies observations, which showed that rising times are related to the interfacial velocities and that signature shape may depend on small geometrical defects occurring at the probes tips (Cartellier and Barrau 1998a, b).

When using an ANN approach, non-linear model flexibility allows reproducing complex patterns and detection of important relations which could remain unseen otherwise. The proposed ANN counts on two hidden layers and one output (the interfacial velocity). The number of neurons in the hidden layers has been the result of an iterative process, as shown in Fig. 7, where training performance has been studied accounting also for the dimension of the network thus avoiding over fitting.

In this study, improvement of the predictions has shown to be significant when compared to the initial proposed model. Accuracy enhancement of ANN model over the quasilinear approach (Eq. 1) can be observed in Figs. 8 and 9. Majority of ANN predictions fall within the +/− 10 error, showing higher difficulty to reproduce extreme values.

7. ACKNOWLEDGMENTS

Authors thank A2 Photonic Sensors for providing the instrumentation, installation recommendations and for their kind attention.

8. REFERENCES

Amador, A., Sánchez-Juny, M., and Dolz, J. (2006). Characterization of the non-aerated flow region in a stepped spillway by PIV. *Journal of Fluids Engineering*, 128(6), 1266–1273. doi:10.1115/1.2354529

André, S., Boillant, J.L., Schleiss, J.L. (2005). Two-Phase Flow Characteristics of Stepped Spillways. Discussion, Journal of Hydraulic Engineering, 131(5), 423-427. doi: 10.1061/(ASCE)0733-9429(2005)131:5(423)

Bennett, N. D., Croke, B. F., Guariso, G., Guillaume, J. H., Hamilton, S. H., Jakeman, A. J., Marsili-Libelli, S., Newham, L. T., Norton, J. P., Perrin, C. and Pierce, S. A. (2013). Characterising performance of environmental models. *Environmental Modelling & Software*, 40, 1-20. doi:10.1016/j.envsoft.2012.09.011

Boes, R., and Hager, W. H. (2003). Two-Phase Flow Characteristics of Stepped Spillways. *Journal of Hydraulic Engineering*, 129(9), 661-670. doi: 10.1061/(ASCE)0733-9429(2003)129:9(661)

Borges, J. E., Pereira, N. H., Matos, J., and Frizell, K. H. (2010). Performance of a combined three-hole conductivity probe for void fraction and velocity measurement in air–water flows. *Experiments in fluids*, 48(1), 17-31. doi: 10.1007/s00348-009-0699-1

Bung, D. B. (2011). Developing flow in skimming flow regime on embankment stepped spillways. *Journal of Hydraulic Research*, 49(5), 639-648. doi: 10.1080/00221686.2011.584372

Bung, D. B. (2013). Non-intrusive detection of air–water surface roughness in self-aerated chute flows. *Journal of Hydraulic Research*, 51(3), 322-329. doi: 10.1080/00221686.2013.777373

Bung, D. B., and Valero, D. (2015). Image Processing for Bubble Image Velocimetry in Self-aerated Flows. *E-proceedings of the 36th IAHR World Congress*, 28 June – 3 July, 2015, The Hague, the Netherlands. ISBN: 978-90-824846-0-1

Bung, D. B., and Valero, D. (2016a). Optical flow estimation in aerated flows. *Journal of Hydraulic Research*, 1-6. doi: 10.1080/00221686.2016.1173600

Bung, D. B., and Valero, D. (2016b). Application of the Optical Flow Method to Velocity Determination in Hydraulic Structure Models. Proc., *6th International Symposium on Hydraulic Structures*, Portland, Oregon, USA, 27-30 June 2016.

Carosone, F., Cenedese, A., and Querzoli, G. (1995). Recognition of partially overlapped particle images using the Kohonen neural network. *Experiments in Fluids*, 19(4), 225-232. doi: 10.1007/BF00196470

Cartellier, A. (1998). Measurement of gas phase characteristics using new monofiber optical probes and real-time signal processing. *Nuclear Engineering and Design*, 184(2-3), 393-408. doi: 10.1016/S0029-5493(98)00211-8

Cartellier, A., and Barrau, E. (1998a). Monofiber optical probes for gas detection and gas velocity measurements: conical probes. *International Journal of Multiphase Flow*, 24(8), 1265-1294. doi: 10.1016/S0301-9322(98)00032-9

Cartellier, A., and Barrau, E. (1998b). Monofiber optical probes for gas detection and gas velocity measurements: optimized sensing tips. *International Journal of Multiphase Flow*, 24(8), 1295-1315. doi: 10.1016/S0301-9322(98)00033-0

Chachereau, Y., and Chanson, H. (2011). Free-surface fluctuations and turbulence in hydraulic jumps. *Experimental Thermal and Fluid Science*, 35(6), 896-909. doi: 10.1016/j.expthermflusci.2011.01.009

Chanson, H., and Brattberg, T. (2002). Experimental study of the air–water shear flow in a hydraulic jump. *International Journal of Multiphase Flow*, 26(4), 583-607. doi:10.1016/S0301-9322(99)00016-6

Chanson, H. and Toombes, L. (2002). Air–water flows down stepped chutes: turbulence and flow structure observations. International Journal of Multiphase Flow, 28(11), 1737-1761. doi: 10.1016/S0301-9322(02)00089-7

Chanson, H. (2013). Hydraulics of aerated flows: qui pro quo?. *Journal of Hydraulic Research*, 51(3), 223-243.

Felder, S., and Chanson, H. (2011). Air–water flow properties in step cavity down a stepped chute. *International Journal of Multiphase Flow*, 37(7), 732-745. doi: 10.1016/j.ijmultiphaseflow.2011.02.009

Chen, P. –H., Yen, J. –Y., and Chen, J. –L. (1998). An artificial neural network for double exposure PIV image analysis. *Experiments in Fluids*, 24(5), 373-374. doi: 10.1007/s003480050185

Felder, S., and Chanson, H. (2014). Air–water flows and free-surface profiles on a non-uniform stepped chute. *Journal of Hydraulic Research*, 52(2), 253-263. doi: 10.1080/00221686.2013.841780

Felder, S., and Chanson, H. (2015). Phase-detection probe measurements in high-velocity free-surface flows including a discussion of key sampling parameters. *Experimental Thermal and Fluid Science*, 61, 66-78. doi: 10.1016/j.expthermflusci.2014.10.009

Hunter, J.D., 2007. Matplotlib: a 2D graphics environment. *Computing in Science & Engineering*, 9(3), 90-95. doi: 10.1109/MCSE.2007.55

Igel, C., and Hüsken, M. (2003). Empirical evaluation of the improved Rprop learning algorithms. *Neurocomputing*, 50, 105-123. doi: 10.1016/S0925-2312(01)00700-7

Kucukali, S., and Chanson, H. (2008). Turbulence measurements in the bubbly flow region of hydraulic jumps. *Experimental Thermal and Fluid Science*, 33(1), 41-53. doi: 10.1016/j.expthermflusci.2008.06.012

Leandro, J., Bung, D. B., Carvalho, R. (2014). Measuring void fraction and velocity fields of a stepped spillway for skimming flow using non-intrusive methods. *Experiments in Fluids*, 55:1732. doi: 10.1007/s00348-014-1732-6

Maier, H. R., Jain, A., Dandy, G. C., and Sudheer, K. P. (2010). Methods used for the development of neural networks for the prediction of water resource variables in river systems: Current status and future directions. *Environmental Modelling & Software*, 25(8), 891-909. doi:10.1016/j.envsoft.2010.02.003

Matos, J., and Meireles, I. C. (2014). Hydraulics of stepped weirs and dam spillways: Engineering challenges, labyrinths of research. *Proc., 5th International Symposium on Hydraulic Structures: Hydraulic Structures and Society-Engineering Challenges and Extremes*, Brisbane, Australia, 25-27 June 2014.

Meireles, I. C., Renna, F., Matos, J, and Bombardelli, F. A. (2012). Skimming, nonaerated flow on stepped spillways over roller compacted concrete dams. *Journal of Hydraulic Engineering*, 138(10), 870–877.

Meireles, I. C., Bombardelli, F. A., and Matos, J. (2014). Air entrainment onset in skimming flows on steep stepped spillways: an analysis. *Journal of Hydraulic Research*, 52(3), 375-385. doi: 10.1080/00221686.2013.87840

Misra, S. K., Thomas, M., Kambhamettu, C., Kirby, J. T., Veron, F., and Brocchini, M. (2006). Estimation of complex air–water interfaces from particle image velocimetry images. *Experiments in Fluids*, 40(5), 764-775. doi: 10.1007/s00348-006-0113-1

Murzyn, F., Mouaze, D., and Chaplin, J. R. (2005). Optical fibre probe measurements of bubbly flow in hydraulic jumps. International Journal of Multiphase Flow, 31(1), 141-154. doi: 10.1016/j.ijmultiphaseflow.2004.09.004

Neal, L. G., and Bankoff, L. G. (1963). A high resolution resistivity probe for determination of local void properties in gas-liquid flow. *AIChE Journal*, 9(4), 490-494. doi: 10.1002/aic.690090415

Nóbrega, J. D., Schulz, H. E., and Zhu, D. Z. (2014). Free surface detection in hydraulic jumps through image analysis and ultrasonic sensor measurements. *E-proccedings of the 5th IAHR International Symposium on Hydraulic Structures* (pp. 1-8). The University of Queensland. doi: 10.14264/uql.2014.42

Rojas, R. (1996). Neural networks: a systematic introduction. *Springer Science & Business Media.* doi: 10.1007/978-3-642-61068-4

Schaul, T., Bayer, J., Wierstra, D., Sun, Y., Felder, M., Sehnke, F., Rückstieß, T., and Schmidhuber, J. (2010). PyBrain. *The Journal of Machine Learning Research*, 11, 743-746.

Valero, D., and Bung, D. B. (2016). Development of the interfacial air layer in the non-aerated region of high-velocity spillway flows. Instabilities growth, entrapped air and influence on the self-aeration onset. *International Journal of Multiphase Flow*, 84, 66-74. doi:10.1016/j.ijmultiphaseflow.2016.04.012

Vejražka, J., Večeř, M., Orvalho, S., Sechet, P., Ruzicka, M. C., and Cartellier, A. (2010). Measurement accuracy of a mono-fiber optical probe in a bubbly flow. *International Journal of Multiphase Flow*, 36(7), 533-548. doi: 10.1016/j.ijmultiphaseflow.2010.03.007

Wang, H., Felder, S., and Chanson, H. (2014). An experimental study of turbulent two-phase flow in hydraulic jumps and application of a triple decomposition technique. *Environmental Fluid Mechanics*, 55:1775. doi: 10.1007/s00348-014-1775-8

Wang, H., and Chanson, H. (2015). Air entrainment and turbulent fluctuations in hydraulic jumps. Urban Water Journal, 12(6), 502-518. doi: 10.1080/1573062X.2013.847464

Wang, H., and Chanson, H. (2016). Experimental assessment of characteristic turbulent scales in two-phase flow of hydraulic jump: from bottom to free surface. *Environmental Fluid Mechanics*, 1-19. doi: 10.1007/s10652-016-9451-6

Zhang, G., and Chanson, H. (2016a). Interaction between free-surface aeration and total pressure on a stepped chute. *Experimental Thermal and Fluid Science*, 74, 368-381. doi:10.1016/j.expthermflusci.2015.12.011

Zhang, G., and Chanson, H. (2016b). Hydraulics of the Developing Flow Region of Stepped Spillways. I: Physical Modeling and Boundary Layer Development. *Journal of Hydraulic Engineering*, 04016015. doi: 10.1061/(ASCE)HY.1943-7900.0001138